Universität für Bodenkultur Wien
University of Natural Resources
and Life Sciences, Vienna

Doctoral Dissertation

Optical biosensing of biomarkers in blood and plasma enabled by biocompatible polymer architectures

submitted by

DI[in] Daria Ewa KOTLAREK, BSc

in partial fulfilment of the requirements for the academic degree

Doktorin der Bodenkultur (Dr.nat.techn.)

Vienna, November 2021

Supervisor:
Prof. Dr. Wolfgang Knoll
Department of Nanobiotechnology

AFFIDAVIT

I hereby declare that I have authored this dissertation independently, and that I have not used any assistance other than that which is permitted. The work contained herein is my own except where explicitly stated otherwise. All ideas taken in wording or in basic content from unpublished sources or from published literature are duly identified and cited, and the precise references included. Any contribution from colleagues is explicitly stated in the authorship statement of the published papers.

I further declare that this dissertation has not been submitted, in whole or in part, in the same or a similar form, to any other educational institution as part of the requirements for an academic degree.

I hereby confirm that I am familiar with the standards of Scientific Integrity and with the guidelines of Good Scientific Practice, and that this work fully complies with these standards and guidelines.

Vienna, October 2021 Daria Ewa KOTLAREK *(manu propria)*

SUPERVISORY TEAM AND REVIEWERS

SUPERVISORY TEAM

Dr. Jakub Dostalek, BioSensor Technologies, Austrian Institute of Technology, AIT, Vienna, Austria

Prof. Dr. Ulrich Jonas, Macromolecular Chemistry, University of Siegen, Germany

Prof. Dr. Wolfgang Knoll, Institute for Biophysics, BOKU, Vienna, Austria

REVIEWERS

Univ. Prof. Dr. Erik Reimhult, Institute of Biologically Inspired Materials, BOKU, Vienna, Austria

Prof. Dr. Souhir Boujday, NanoMaterials & Surfaces @ BioInterfaces, Sorbonne University, Paris, France

PREFACE

The research presented in this doctoral dissertation was conducted in the framework of the Marie Skłodowska-Curie Innovative Training Network BIOGEL, funded by European Union's Horizon 2020 research and innovation programme under grant agreement No 642787. The research was conducted at the Austrian Institute of Technology over the period from September 2015 to June 2019, in cooperation with Leibniz Institute for Interactive Materials (Aachen, Germany), Institute of Photonics and Electronics of the Czech Academy of Sciences (Prague, Czech Republic) and Institute of Molecules and Materials of Le Mans (Le Mans, France).

ACKNOWLEDGEMENTS

For thousands of years, humankind has been seeking the improvement of the welfare of the species. Each of us commits to serving and endeavor to advance essential areas for human beings like food production, housing, transportation, communication, or health. The most attractive and intriguing for me was how the new biotechnologies can elevate the quality of everyday life and extend the lifespan by better management and eradication of certain diseases that accompany humankind. To achieve this, a deeper understanding of the pathological processes needs to be acquired that would lead to the development of more effective and less deleterious drugs. Also, a faster and factual diagnosis enabled by sophisticated medical devices would aid adequate disease management and higher recuperation numbers.

Breakthrough ideas and inventions draw from a collective body of knowledge. Today I add this little brick of experimental work to the edifice of science, hoping that it will serve a good cause. Although my Ph.D. study was a long and sometimes bumpy way, it opened new horizons, strengthened my character, and brought beautiful memories that will be cherished forever. These, of course, would not be possible without my superiors, colleagues, friends, and family, whom I would like to thank with all my heart.

My deepest gratitude goes to Dr. Jakub Dostalek and the BST Group for scientific guidance, constant support, patience, extraordinary working atmosphere, and utmost - long-lasting friendships.

The profound appreciation goes to Prof. Wolfgang Knoll and the founders and members of the Marie Skłodowska-Curie ITN BIOGEL, for the possibility to contribute to this excellent program and for allowing me to witness the emergence of cutting-edge biotechnologies. The BIOGEL Crew - thank you all for an active exchange of ideas, inspiring discussions, and memorable events!

I would like to extend my warmest thanks to Cesar Rodriguez- Emmenegger and Mariia Vorobii for their genuine kindness in hosting and training me in the previously foreign field of research.

Sincere acknowledgments go to all Associates and Colleagues from AIT and other institutions for the valuable scientific input and the fruitful collaborations.

Last but not least, heartfelt thanks to my beloved Jarek and my family and friends for letting me follow my dreams and for their everlasting support.

TABLE OF CONTENT

LIST OF PUBLICATIONS

Publications that comprise the main part of this cumulative dissertation:

1. Kotlarek D, Curti F, Vorobii M, Corradini R, Careri M, Knoll W, Rodriguez-Emmenegger C, Dostalek J, "Surface plasmon resonance-based aptasensor for direct monitoring of thrombin in a minimally processed human blood." *Sensors and Actuators B: Chemical* 320 (2020): 128380, DOI: 10.1016/j.snb.2020.128380. Publication 1 - published
2. Kotlarek D, Fossati S, Venugopalan P, Gisbert Quilis N, Slaby J, Homola J, Lequeux M, Amiard F, Lamy de la Chapelle M, Jonas U and Dostalek J, "Actuated plasmonic nanohole arrays for sensing and optical spectroscopy applications." *Nanoscale* 12.17 (2020): 9756-9768, DOI: 10.1039/D0NR00761G, Publication 2 - published
3. Kotlarek D, Liu K, Gisbert Quilis N, Bernhagen D, Timmerman P, Kouwer P, Dostalek J, "Thin-Film Polyisocyanide-Based Hydrogels for Affinity Biosensors." *The Journal of Physical Chemistry C* (2021), DOI: 10.1021/acs.jpcc.1c02489, Publication 3 - published
4. Kotlarek D, Vorobii M, Ogieglo W, Knoll W, Rodriguez-Emmenegger C, Dostalek J, "Compact grating-coupled biosensor for the analysis of thrombin." *ACS sensors* 4.8 (2019): 2109-2116. DOI: 10.1021/acssensors.9b00827, Publication 4 - published

ABSTRACT

Thrombin is an important biomarker of thrombosis, a condition that can lead to ischemic stroke, heart failure, or pulmonary embolism. The appropriate treatment can prevent this morbidity, but a generic method for detecting this pathological state is missing. Fast detection of thrombin in blood using a compact biosensor would help monitor the hemostatic condition, tailor the anticoagulation therapy, and avoid thrombotic events. However, the unspecific interaction of complex matrices of biological samples with a biosensor surface complicates the readout and limits the application of this technology in clinical settings. To provide a way for quick analysis of thrombin directly in blood and plasma, this study searched for the optimal biosensor design, including chip architecture, antifouling coatings, detection assay with biorecognition elements, and optical readout. Ultimately, a biosensor chip was developed with tailored polymer brushes that are functionalized with DNA aptamer receptors. The presented surface coating proved superior resistance to fouling in comparison to standard surface modifiers. Direct label-free analysis of thrombin in biological samples and in the medically relevant concentration range was achieved by using a surface plasmon resonance biosensor. The designed sensor chip was implemented to a portable optical system that can be used outside the specialized laboratory and constitutes the first step towards a hand-held point-of-care device. The reported biosensor platform holds great promise as a diagnostic tool for monitoring the coagulation status of patients at risk of thrombosis. In addition, the used detection principle can be easily implemented to measure other essential biomarkers present in the blood.

KURZFASSUNG

Thrombin ist ein wichtiger Biomarker für Thrombose, eine Erkrankung, die zu ischämischem Schlaganfall, Herzinsuffizienz oder Lungenembolie führen kann. Die Sterblichkeit durch Thrombose kann durch entsprechende Behandlung verringert werden, jedoch fehlt derzeit eine generische Methode zum Nachweis. Eine schnelle Detektion im Blut mithilfe eines kompakten Biosensors könnte helfen, den hämostatischen Zustand zu überwachen, eine Antikoagulationstherapie anzupassen und dabei Thrombosen zu verhindern. Die unspezifische Interaktion komplexer biologischer Proben mit der Oberfläche eines Biosensors erschwert jedoch das Auslesen und schränkt die Anwendung dieser Technologie im klinischen Umfeld ein. Um eine schnelle Analyse von Thrombin direkt in Blut und Plasma zu ermöglichen, beschäftigt sich diese Dissertation mit dem optimalen Biosensordesign. Dabei wurden die Chiparchitektur, Antifouling-Beschichtungen, Assays mit verschiedenen Liganden und die Möglichkeiten für das optisches Auslesen berücksichtigt. Schließlich wurde ein Biosensor-Chip mit Polymerbürsten entwickelt, der mit DNA-Aptamer-Rezeptoren funktionalisiert ist. Die vorgestellte Oberflächenbeschichtung gegen Fouling erwies sich im Vergleich zu Standard-Oberflächenmodifikatoren als überlegen. Die direkte markierungsfreie Analyse von Thrombin in biologischen Proben und im medizinisch relevanten Konzentrationsbereich wurde mittels Oberflächenplasmonenresonanz-Biosensor erreicht. Der entwickelte Sensorchip wurde in ein tragbares optisches System eingebaut, das auch außerhalb spezialisierter Labors eingesetzt werden kann und den ersten Schritt hin zu einem kompakten Point-of-Care-Gerät darstellt. Die beschriebene Biosensor-Plattform ist ein vielversprechendes diagnostisches Instrument zur Überwachung des Gerinnungsstatus von thrombosegefährdeten Patienten. Darüber hinaus lässt sich das verwendete Detektionsprinzip für die Messung weiterer wichtiger Biomarker, die im Blut vorhanden sind, anpassen.

1. INTRODUCTORY OVERVIEW

1.1. HEMOSTASIS

Hemostasis (from Greek, "haeme" - blood and "stasis" - to stop) is a physiological process that maintains the uninterrupted flow of the blood inside the vascular system. In healthy individuals, this is achieved by a subtle interplay of procoagulant and anticoagulant mechanisms that, under normal circumstances, stay in equilibrium. However, in the case of vascular endothelium disruption, this delicate balance is rapidly shifted in favor of coagulation. The coagulation leads to stopping bleeding by forming the localized blood clot that seals the damaged vessel. In the final stage, the integrity of the endothelium is restored, and the clot is dissolved during the fibrinolysis (1). Any congenital or clinical disparity in the process might lead to a life-threatening hemorrhage (excessive bleeding) or thrombosis (formation of a persistent clot). Different manifestations of thrombotic events were estimated to affect approximately 2% of the population and account for 25% of deaths worldwide in 2010 (2) with significant medical costs (3). Notably, the frequency of the thrombotic events and the related economic burden can be efficiently lowered by the appropriate anticoagulation therapy. However, when the treatment is not accurately tailored to the overall health condition and co-administered medication, it results in an adverse effect of bleeding that remains a significant safety concern (4). The therapeutic outcomes of thrombosis-associated incidents can be dramatically improved by fully comprehending the complex mechanisms that govern the coagulation and inclusion of routine monitoring of patients' hemostatic state (5). In this section, the process of hemostasis with its possible complications leading to distinct morbidities, current methods of diagnosis, and patient monitoring are discussed.

1.1.1 Primary hemostasis

In physiological conditions, the reaction of our body to the tissue injury and accompanying bleeding constitutes a rapid trigger for highly controlled reactions that result within seconds to minutes in a stop of the blood loss (1). The immediate response at the site of vessel injury is a release of vasoconstricting peptides (endothelin), a subsequent vascular spasm that leads to a deceleration of the blood flow, and secretion of von Willebrand factor (vWF) by the activated endothelial cells (Figure 1a).

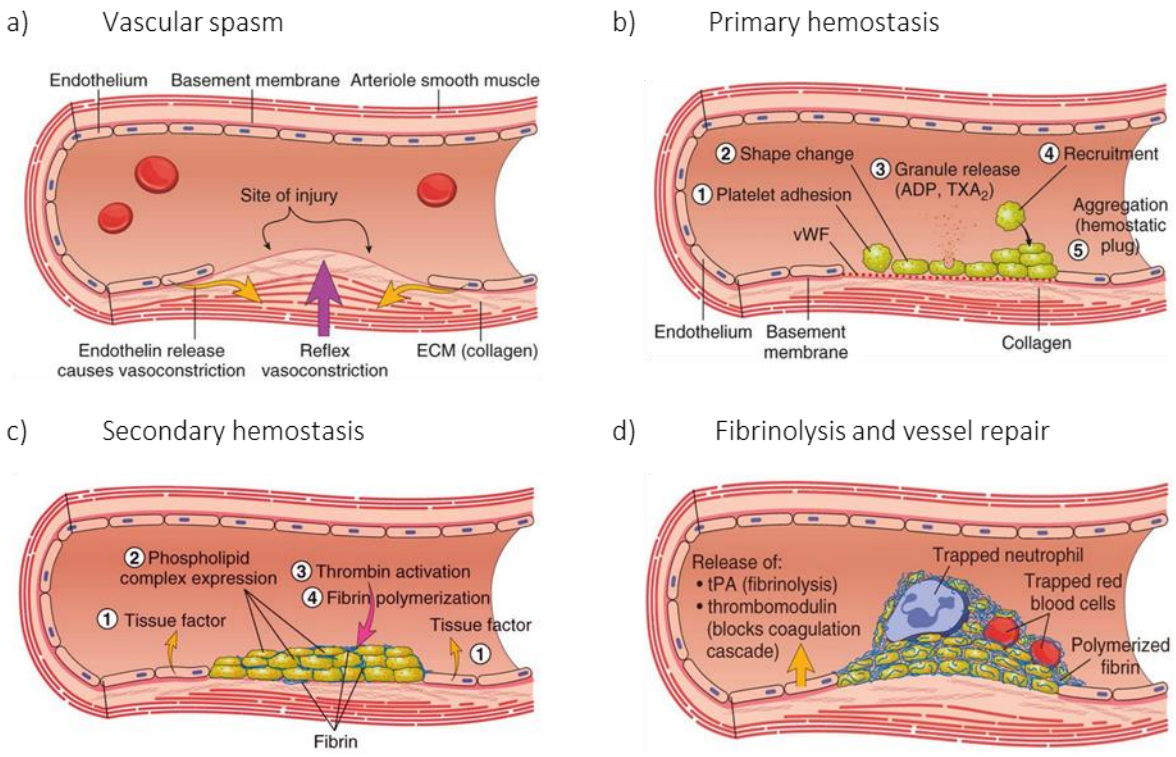

Figure 1. Stages of hemostasis. Modified from (6).

Following the loss of endothelium integrity, the components of an extracellular matrix (ECM), including collagen, get exposed to the vessel's lumen, initiating the primary hemostasis (Figure 1b). Firstly, the vWF binds to the subendothelial collagen and recruits circulating platelets to the site of injury. Next, platelets line the open endothelium by the interaction of their surface glycoproteins with collagen-bound vWF and collagen alone. At the same time, the glycoproteins contained in the intracellular compartment undergo the inside-out process, with the most important being integrin $\alpha_{IIb}\beta_3$ as its phosphorylation induces the conformational change that results in increased affinity to vWF and fibrinogen (7). The adhesion and platelet-mediated signaling induce platelet activation and change their morphology from discoid to irregular with multiple pseudopods. This shape alteration is essential to maximize the contact surface area with other activated platelets and endothelium and physically prevent the further escape of blood (8). Subsequently, platelets release thromboxane (TXA_2) that stimulates new platelets and recruits them to the injury site. Besides, platelets extricate the content of alpha and dense granules, releasing several molecules that contribute to the progress of hemostasis, e.g., vWF, fibrinogen, calcium, and ADP (Table 1). The released factors recruit additional platelets to the damaged site, whereas the integrin $\alpha_{IIb}\beta_3$ plays a crucial role in platelet aggregation and mass growth of the initial hemostatic plug. In summary, the primary hemostasis culminates in the formation of an initial platelet plug throughout platelet adhesion, activation, and aggregation. In the meantime, the secondary

hemostasis is initiated by the transfer of the phospholipids to the outer membrane of platelets and their interaction with calcium and clotting factors (7) (Figure 1c).

Table 1. Selected proteins and factors released by platelets during the degranulation process in the primary hemostasis (based on (7)).

Protein/factor	Type of granule	Function
histamine	dense granules	vasocontraction, enhancing TF expression
serotonin	dense granules	recruiting new platelets to the site of injury
ATP, ADP, inorganic diphosphate, inorganic phosphate	dense granules	support platelet adhesion and aggregation
VWF, fibrinogen, vitronectin	alpha granule	platelet adhesion, clot expansion, and stabilization
ionized calcium	dense granules	activation and assembly of coagulation factors upon binding to the phospholipids on the platelets' outer membrane
vascular endothelial growth factor, epidermal growth factor, platelet-derived growth factor	alpha granule	angiogenic factors that induce and stabilize the growth of new blood vessels
angiostatin, thrombospondin, endostatin	alpha granule	anti-angiogenic factors that induce vessel stability and maturation
platelet factor 4 (PF4), CCL5 (RANTES), interleukin-8 (IL-8)	alpha granule	immune modulators

1.1.2 Secondary hemostasis

The year 1964 brought a breakthrough in the coagulation research when two independent groups described the coagulation as a cascade of reactions of serine proteases where each enzyme precursor, once activated, serves as an activator of a downstream clotting factor (9,10). Two independent pathways were determined: intrinsic (surface-contact factors, all components present in the blood) and extrinsic (TF - Factor VII, which requires the subendothelial TF). Both merge on activation of Factor X in the common pathway to generate fibrin clot as an endpoint. The presented finding proved to be a significant advancement in better understanding of the *in vitro* coagulation tests: activated partial thromboplastin time (aPTT) for investigation of intrinsic pathway and prothrombin time (PT) for measuring the extrinsic pathway (11). The cascade model, however, does not fully reflect the hemostasis *in vivo* because neither pathway cannot compensate the other, as the model implies (12). To match the clinical observations, the coagulation cascade was revised and updated by a contribution of the cell surface in the so-called cell-based model of hemostasis in which three phases are distinguished: initiation, amplification, and propagation (Figure 2) (13).

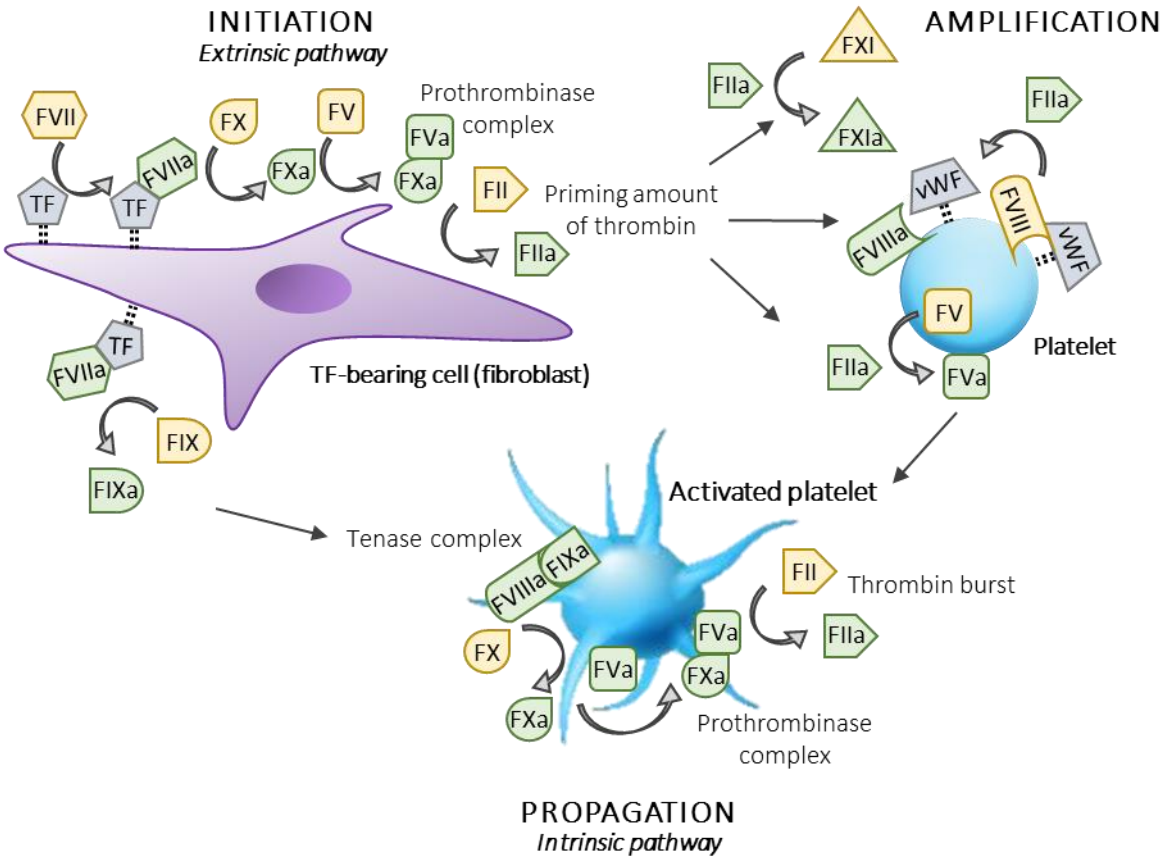

Figure 2. Cell-based coagulation model representing stages of secondary hemostasis: initiation, amplification, and propagation (based on (13)).

The initiation stage starts with trauma to tissue when the endothelium wall is damaged, and blood gets in contact with TF-bearing cells (e.g., sub-endothelial smooth muscle cells or fibroblasts) that do not interact with the everyday circumstances bloodstream. The coagulation is initiated by activating Factor VII by a cell-bound TF in the presence of calcium ions and subsequent complex formation that activates Factors IX and X. The activated Factor X (FXa) stimulates FV activation and the prothrombinase complex that produces only a limited number of thrombin molecules. This priming amount of thrombin is necessary to catalyze the reactions of the next stage of amplification. This phase takes place on platelet surfaces that have been anchored at the injury site by the interaction of their exterior glycoproteins with the ECM's collagen and vWF. The adherence process partially activates the platelets and allows them to stay close to the source of produced thrombin. Here, thrombin participates in the enhanced platelet adhesion and their final activation and the activation of circulating FXI, surface-bound FVIII, and FV that is released in the process of platelet degranulation onto their surface. High-affinity receptors of FIXa, FXa, and FXIa are expressed on activated platelets and presumably play a role in the appropriate assembly of the coagulation factors leading to large-scale production of thrombin in the propagation stage. At this stage, the FIXa diffuses from the vicinity of the TF-bearing cell and forms a

tenase complex with the surface-attached FVIIIa that stimulates circulating FX. Finally, FXa combines with FVa (prothrombinase complex), which leads to the burst of thrombin (FIIa) and subsequent formation and stabilization of the hemostatic fibrin clot (13). The cell-based model of coagulation proofs that extrinsic and intrinsic pathways are not redundant but rather complementary to each other by serving a diverse purpose and operating on distinct cellular surfaces.

1.1.3 Anticoagulant mechanisms

An essential feature of hemostasis is the confinement of the clot to the site of vessel injury maintained by the cellular receptors and high-affinity binding sites of the clotting factors. Besides, several anticoagulant mechanisms are employed to prevent the spreading of coagulation to systemic circulation and thrombosis. The aggregation of the platelets on the healthy endothelium is obstructed by the ADPase activity that removes the ADP molecules released from the activated platelets (13). Tissue factor pathway inhibitor (TFPI) regulates the initiation phase of secondary hemostasis by inhibiting FXa and TF-FVIIa complex. The circulating antithrombin III (ATIII) neutralizes FIX, FX, and FXI and thrombin once they leave the localized site of coagulation (14). In addition, thrombin activity is inhibited by the thrombomodulin (TM) attached to intact endothelial cells. Binding to TM interferes with the procoagulant activity of thrombin that, as a result, loses its ability to cleave fibrinogen and activate the platelets. In return, thrombin becomes 1000-fold more effective in activating the protein C. Activated protein C (APC) constitutes a potent regulator of the coagulation process mainly by irreversible proteolytic inactivation of FVa and FVIIIa, the components of the prothrombinase and tenase complexes, respectively (15). Besides ATIII, there are other circulating plasma protease inhibitors (serpins) that constitute a generic tool for inactivation of the activated clotting factors at the sites distant from the injury: heparin cofactor II, protein Z-dependent protease inhibitor, a1-protease inhibitor, protein C inhibitor, a2-antiplasmin and plasminogen activator inhibitor-1 (16).

1.1.4 Fibrinolysis

Fibrinolysis is an enzymatic process that disrupts the hemostatic clot by dissolving fibrin into fibrin degradation products (FDPs) (Figure 1d). It begins alongside the coagulation to limit the expansion of the clot and facilitate its clearance once the vessel wall is healed. The dissolution of fibrin is facilitated by plasmin formed from the proenzyme plasminogen by tissue-type plasminogen activator (tPA) or urokinase-type plasminogen activator (uPA) released by endothelial cells. The release of t-PA is promoted by tissue obstruction, thrombin, epinephrine, vasopressin, and strenuous exercise (8). Degraded fibrin enhances its decay by exposed C- terminal lysines that act as a cofactor in activating plasminogen primarily by tPA. On the other hand, removing C-terminal lysines by the thrombin-activatable inhibitor of fibrinolysis (TAFI) down-regulates the fibrinolysis. Other important regulators of

fibrinolysis are an inhibitor of tPA and uPA (plasminogen activator inhibitor type 1) and inhibitors of plasmin (a2-antiplasmin and a2-macroglobulin), respectively (17).

In conclusion, coagulation and fibrinolysis are two coexisting mechanisms confined spatially and temporarily by a multi-level regulatory system in physiological conditions. Therefore, the deficiency in any participating factors can lead to either thrombosis or bleeding, each severe health complication.

1.2. MANIFESTATIONS OF THROMBOSIS

Thrombosis is an uncontrolled blood clot formation in the lumen of an artery or vein, leading to vessel occlusion and obstruction of blood circulation. The mechanisms underlying arterial and venous thrombosis emergence vary and are reflected in the morphology of the thrombus (Figure 3) and the manifestation of the disease (18).

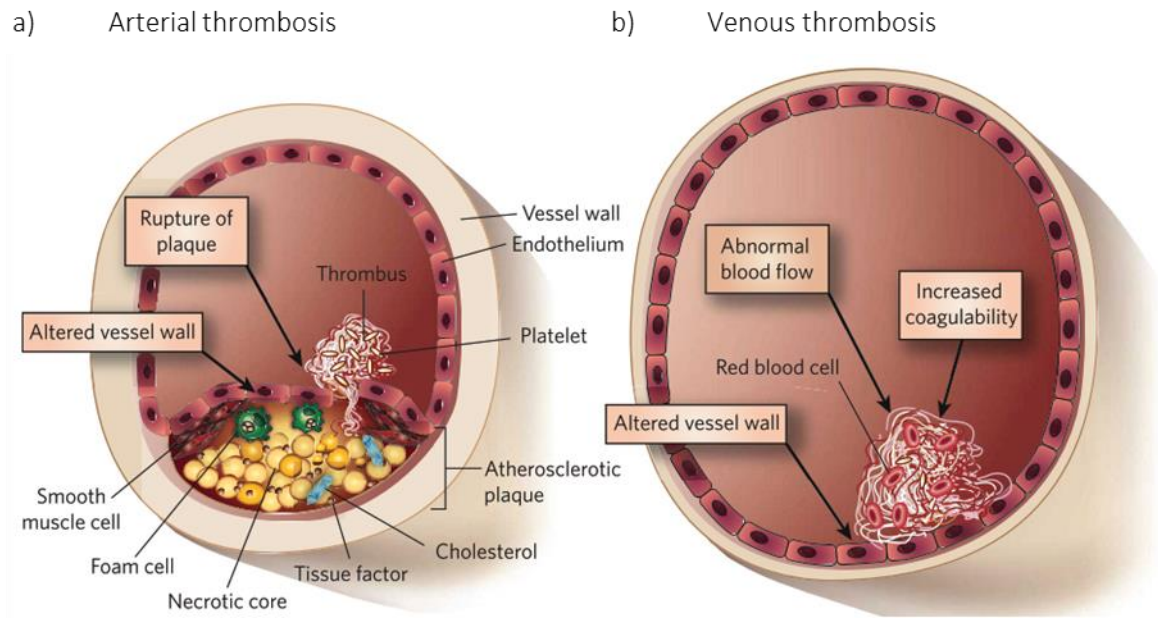

Figure 3. Formation of the pathologic thrombus in the lumen of a) an artery and b) a vein (modified from (18)).

1.2.1 Arterial thrombosis

The most severe manifestation of arterial thrombosis is an undesired clot formation in coronary or cerebral circulation leading to ischemic heart disease (IHD) or ischemic stroke (IS), respectively (19). Both of these morbidities are invariably the most common causes of death worldwide (data since 2000), accounting for 9 433 mln (IHD) and 5 781 mln (IS) deceased in 2016 and corresponding to the death rates of 126 per 100 000 population for IHD and 77 per 100 000 population for IS (20). Arterial thrombosis is triggered by the rapture of the atherosclerotic plaque (cholesterol deposits and lipid-laden

macrophages) and the resulting discontinuation of the endothelial wall (Figure 3a). The procoagulant proteins (collagen, vWF, and TF) get exposed to the blood leading to a subsequent buildup of the platelet-rich thrombus at the high shear flow. Unlike the hemostatic clot, the arterial thrombus proceeds onto the atherosclerotic plaque and propagates inside the lumen of the artery inducing local blood flow alterations. Downstream from the platelet plug, there is a formation of the additional fibrin- and red cells-rich thrombus in the zone of lower blood circulation. These events display a lack of spatial and temporal regulation of the primary and secondary clot, as it usually occurs in hemostasis (19). The main risk factors for arterial thrombosis include hypertension, high levels of low-density lipoprotein (LDL - cholesterol), diabetes, obesity, smoking, and advanced age (21). Antiplatelet drugs are the most commonly used agents for the prevention and treatment of arterial thrombosis. In addition, anticoagulants and fibrinolytic therapies play an essential role in managing the disease (19).

1.2.2 Venous thrombosis

Venous thrombosis manifests as deep vein thrombosis (DVT), its sequelae pulmonary embolism (PE) (collectively referred to as thromboembolism), and post-thrombotic syndrome. The DVT evolves upon pathologic formation of thrombus and obstruction of the blood flow in deep veins of the leg or, less frequently, upper extremities (22). PE is a complication of DVT, and it occurs once the thrombus breaks down and is circulated to the pulmonary artery (embolization). PE leads to hemodynamic instability ranging from asymptomatic to massive embolism, causing instant death (23). In addition, the patients often experience recurrent episodes of thromboembolism or a substantial post-thrombotic syndrome, a common chronic disease including pain, swelling, and sporadically ulceration of the leg (3). Thromboembolism constitutes the third most common cause of death from cardiovascular disease after a heart attack and stroke (24), with a mortality rate of 9.4–32.3 per 100 000 population (1998–2008) (2).

Contrary to arterial thrombosis, the venous clot typically emerges without damage to the endothelium and is triggered by factors described as Virchow's Triad (25): altered properties of the blood (thrombophilia), altered vessel wall, or abnormal blood flow. In contrast to the platelet-rich arterial plug, the venous thrombus is composed mainly of fibrin strands, red blood cells, and few platelets (so-called red thrombus) (Figure 3b) (18). The elevated risk for venous thrombosis is related to both genetic and environmental factors. Thrombophilia is a global term for congenital or acquired thrombotic disorders related to the excessive activity of the coagulation system caused either by increased levels of coagulation factors or lack of hemostatic regulators. The hereditary thrombophilia includes deficiencies in ATIII, protein C, and protein S and mutations in FV and prothrombin. The acquired coagulation abnormalities comprise antiphospholipid antibody syndrome, increased levels of

factors VIII, IX, XI, or fibrinogen and heparin-induced thrombocytopenia (8). Another potential route for the emergence of venous thrombosis is changes in the vessel wall. In physiological conditions, endothelium constitutes a surface with anticoagulant properties. However, the abnormal expression of pro- or anticoagulant factors can initiate the spontaneous formation of the clot. Besides, the low blood flow and shear stress (stasis) caused by immobility (hospitalization, long travel, sedentary lifestyle) negatively impact the natural antithrombotic and profibrinolytic functions of vascular cells (25). Other predisposing factors to venous thrombosis include major surgery, trauma, cancer, obesity and a history of deep vein thrombosis (22). Anticoagulant drugs such as low-molecular-weight heparin followed by vitamin K antagonists (VKAs) constitute a cornerstone of thromboembolism management (22).

1.2.3 Challenges and risks in the prevention of thrombosis

Thrombosis is a remarkable example of a disease that can be prevented (2,22,26). The appropriate anticoagulation therapy can avoid the formation of deadly blood clots. The established repertoire of anticoagulants includes oral vitamin K antagonists (VKAs), non-vitamin K antagonist oral anticoagulants (NOACs), heparins, and parenteral indirect activated FXa inhibitors (27,28). Despite these agents' high effectiveness and everyday use, some limitations have to be acknowledged, e.g., narrow therapeutic range, lack of a specific antidote, and variability in patient outcome. Notably, the anticoagulant agents target the partially shared pathways between the physiologic hemostasis and the pathological emergence of thrombus. Therefore, overtreatment is commonly associated with a side effect of severe bleeding (5).

Furthermore, adjusting the correct dose is troublesome because the patient outcome is highly dependent on age, environmental, and genetic factors. For instance, altered pharmacokinetics is reported for VKAs due to food-drug interactions, renal failure, or liver disease. On the other hand, heparin-based anticoagulants are associated with the potential development of heparin-induced thrombocytopenia (28). Furthermore, serious bleeding events were reported in 38 – 56% of extracorporeal life support (ECLS) patients, while thrombosis was noted in 13 – 31% (29, 30). For elective surgeries, anticoagulation therapy is typically discontinued in patients with atrial fibrillation and bridged with low-molecular-weight heparin (LMWH) to minimize the risk of bleeding and protect against stroke and systemic embolism (31). However, this strategy was reported to increase the risk for significant bleeding upon interruption of anticoagulation with dabigatran or warfarin (32). Besides, there is no established protocol for perioperative management of patients receiving long-term anticoagulation therapy or general anticoagulation scheme among different centers (33). The treatment can be improved by accurately quantifying the risk and tailored treatment aided by diagnostic testing for dosage adjustment. However, identifying individuals at high risk and implementing the safe and

effective anticoagulation strategy remains challenging due to the lack of a generic diagnostic method (19).

1.3. DIAGNOSIS OF THROMBOSIS

1.3.1 Screening blood tests

The measurement of clotting times (thrombin time, activated partial thromboplastin time, and prothrombin time) belongs to the routine blood diagnostic ordered for screening purposes of thrombotic and bleeding disorders. The assays measure the time it takes the sample of decalcified plasma to clot after adding the test-specific reagent (

Figure 4). Typically, testing of samples is performed on automated instruments with mechanical or optical detection of the fibrin clot (34).

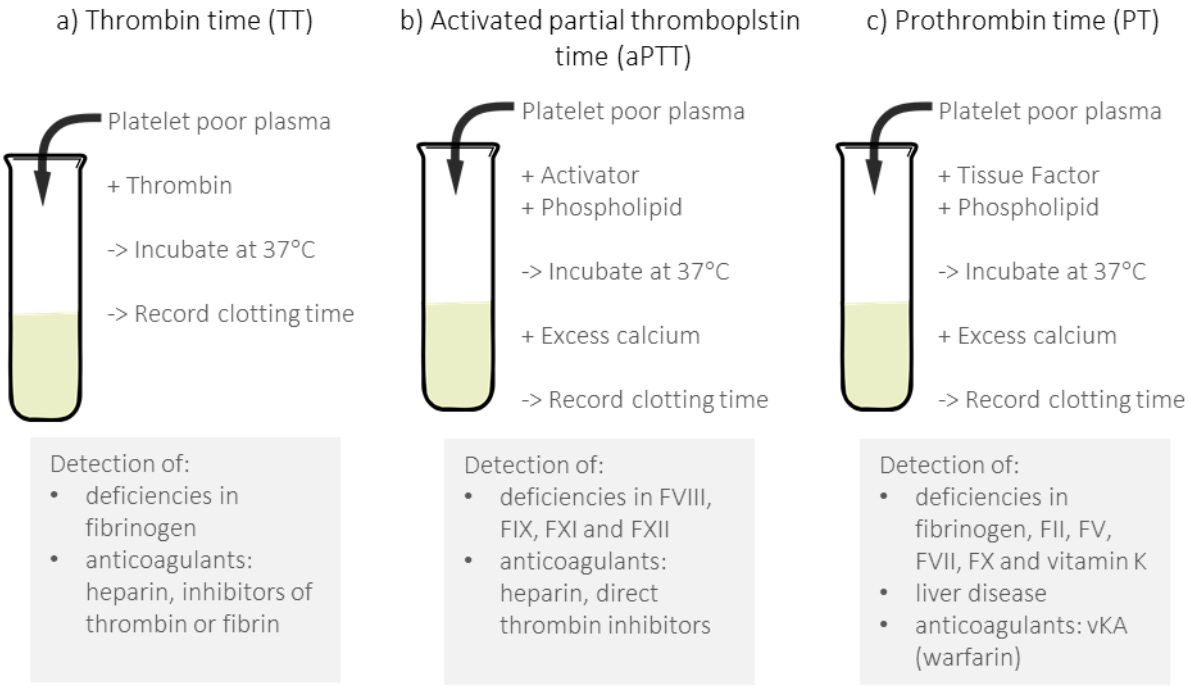

Figure 4. A schematic representation of the blood clotting tests (based on https://practical-haemostasis.com).

Thrombin time (TT) is the starting point in the clinical investigation for clotting abnormalities. In this test, the human or bovine thrombin is added to the citrated platelet-poor plasma. The TT result is represented as the time it takes the sample to form the stable clot. Although a typical TT result varies depending on the reagents and procedure used in each diagnostic center, it should be in the range of 13-15 seconds. The shortened TT has no clinical significance as it is related to the improper collection and processing of the sample in most cases. The prolonged TT indicates congenital or acquired

fibrinogen deficiencies or the presence of inhibitors against thrombin or fibrin. The TT is followed by other tests that lead to a more specific diagnosis (35).

Activated partial thromboplastin time (aPTT) deals with the activity of the factors from the intrinsic pathway. Firstly, the platelet-poor plasma is prepared from the blood sample collected in the presence of the chelation agent (e.g., sodium citrate). Then, the prepared sample is incubated at 37°C with Cephalin (a phospholipid substitute of the platelet phospholipids) and a contact activator (micronized silica or ellagic acid). The clotting is initiated after the addition of pre-warmed excess of calcium that reverses the anticoagulant action of the chelator and starts the clotting cascade of intrinsic and common pathways (34). The typical aPTT ranges from 27 to 35 seconds, but these reference times vary significantly between laboratories depending on the type of activator, duration of incubation, and analytical instrument. The term "partial" indicates the absence of the tissue factor in the thromboplastin reagent. Thus the aPTT cannot detect deficiencies in factor VII. The shortened aPPT times have minor clinical relevance, although some data suggest they can be indicators of recurrent thromboembolism (36). The prolonged times imply hereditary or acquired deficiencies in factors FVIII, FIX, FXI, and FXII or the presence of anticoagulants. The aPTT is commonly used for monitoring anticoagulation therapy with heparin and direct thrombin inhibitors (34).

Prothrombin time (PT) measures clotting time after adding thromboplastin (TF, phospholipid, and calcium) to the citrated platelet-poor plasma. The PT allows assessment of the extrinsic and common pathways, and therefore it is sensitive to fibrinogen deficiencies, FII, FV, FVII, FX. As most of the clotting factors are produced in the liver and undergo a vitamin K-dependent posttranslational modification that allows them to participate in the clotting reactions (8), the PT is useful in detecting liver disease, deficiencies in the vitamin K, and the presence of its antagonists such as warfarin (34). However, the typical PT results show significant interlaboratory variations, depending on the thromboplastin sensitivity and type of instrumentation. Historically, thromboplastin reagent was derived from tissues of different species, which was associated with variability of the results. However, the introduction of the recombinant thromboplastin to the market did not significantly improve the assay reproducibility. To overcome this problem, the World Health Organization introduced the international normalized ratio (INR) that normalizes the PT result with the value that refers to the sensitivity of the particular thromboplastin used in the measurement (36). Standardizing the test is especially important for monitoring the vKA anticoagulation because of the narrow therapeutic index of warfarin and the high risk of side effects. In addition, the introduction of PT/INR resulted in the emergence of self-monitoring devices for controlling warfarin therapy (37).

Although the aPTT and PT tests allow for the detection of deficiencies in the specific factors, they cannot reconstruct the complex interplay of coagulant and anticoagulant processes *in vivo*. Firstly, the

assays measure the clot formed when only about 5% of all physiologically relevant thrombin is generated. Secondly, they lack the cellular component of the coagulation (e.g., endothelial cells with thrombomodulin that is necessary to activate anticoagulant protein C). Therefore, these assays often fail to correlate the result with clinical symptoms, especially in the case of hypercoagulability or mild bleeding disorders (38,39). Besides, high interlaboratory variations make it difficult to compare the results between different centers. Thus, the diagnostic is vulnerable to errors in the determination of optimal doses of anticoagulants. For instance, the credibility of PT standardized with INR was undermined when a poor agreement among the results was observed for seven commercial reagents (40). Also, a comparison of self-monitoring devices based on PT/INR with laboratory values showed statistically significant differences with the trend towards overestimation on the lower end of the therapeutic scale for patients on anticoagulation (where: risk of thrombosis > 2-3 < risk of bleeding) (41). Therefore, methods that could measure a complete coagulation process and better reflect the complex interplay of the coagulant and anticoagulant processes have been pursued to provide a better insight into the functionality and pathologies of hemostasis (42).

1.3.2 Thrombin generation assay

The thrombin generation assay (TGA) measures thrombin generation kinetics at all stages of the coagulation process: initiation, amplification, propagation, and inhibition. As TGA can capture the interaction of pro- and anti-coagulatory factors, it is believed to reflect the condition of the respective hemostatic systems accurately. In addition, the assay records the intensity of fluorescence that originates from the cleavage of the fluorogenic substrate by thrombin in the recalcified plasma or whole blood after the addition of TF, phospholipids, and calcium (38) (Figure 5a). The measurement result is presented as a thrombogram with the main parameters described below (Figure 5b):

- Lag time – initiation phase – a small amount of thrombin is formed
- Upward slope – thrombin generation rate
- Time to peak and peak height – amplification and propagation phase – thrombin burst
- Endogenous thrombin potential (ETP) – the area under the curve reflecting total thrombin formed
- Downward slope – thrombin inactivation rates due to activation of coagulation inhibitors

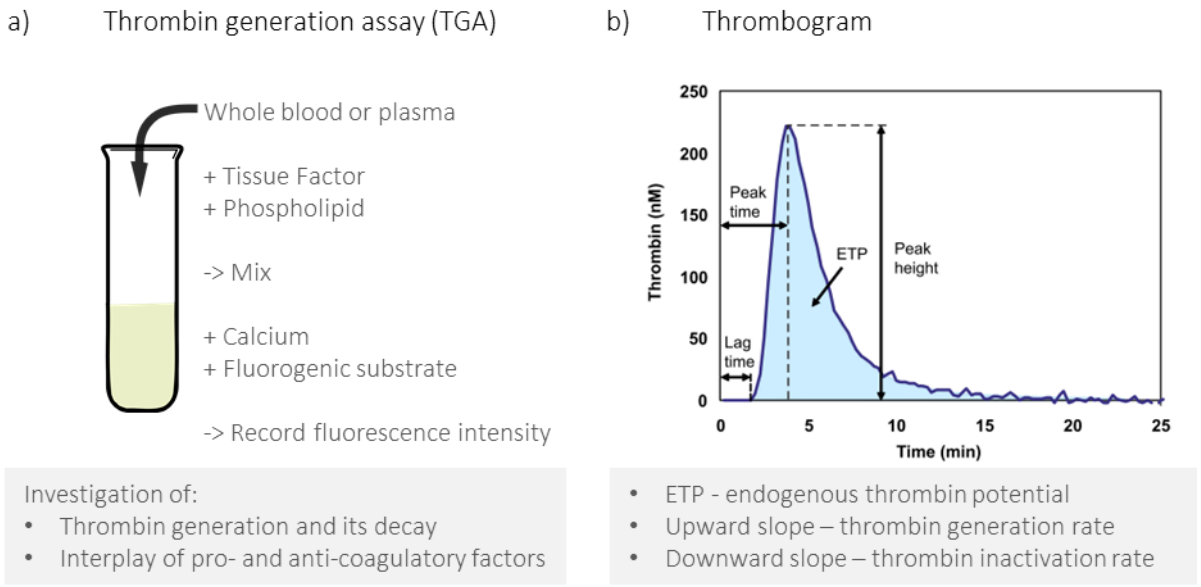

Figure 5. a) A schematic representation of thrombin generation assay and b) the resulting thrombogram with main parameters. Modified from (43).

To remove the intrinsic fluorescence of plasma samples, the calibrated automated thrombogram was introduced (CAT). In the CAT method, the plasma (or blood) sample is split into two portions. One portion is supplemented as in standard TGA (TF, phospholipids, calcium, and the fluorogenic substrate), while the second portion is used for calibration by adding α2-macroglobulin-thrombin complex and the fluorogenic substrate. Both samples are measured in parallel, and the fluorescence intensity of the thrombin-generating sample is compared to the calibrator sample with a known concentration of the exogenous thrombin (44).

As the thrombin is the final effector of the coagulation process, the thrombogram can reflect both hypo- and hypercoagulability, combined pathologies, and the action of anticoagulation treatment. Although TGA was automated to run multiple samples simultaneously, the standardization is still problematic and hampers the everyday use of TGA in the clinic (45).

1.3.3 Thromboelastography

Thromboelastography (TE) constitutes a global hemostasis test that investigates the viscoelastic properties of the coagulating and fibrinolytic blood under low shear stress. It was introduced by Dr. Hellmut Hartert in 1948 (46). Since then, technology emerged into two primary modalities: thromboelastography (TEG®) and thromboelastometry (ROTEM®) together with commercially available instrumentation. Both techniques measure the physical properties of a forming clot in whole blood via a suspended detection pin immersed in the sample. The measurement is performed in the disposable

cup that oscillates around the detection pin (TEG) or in an immobile cup with an oscillating suspended pin (ROTEM) (47) (Figure 6).

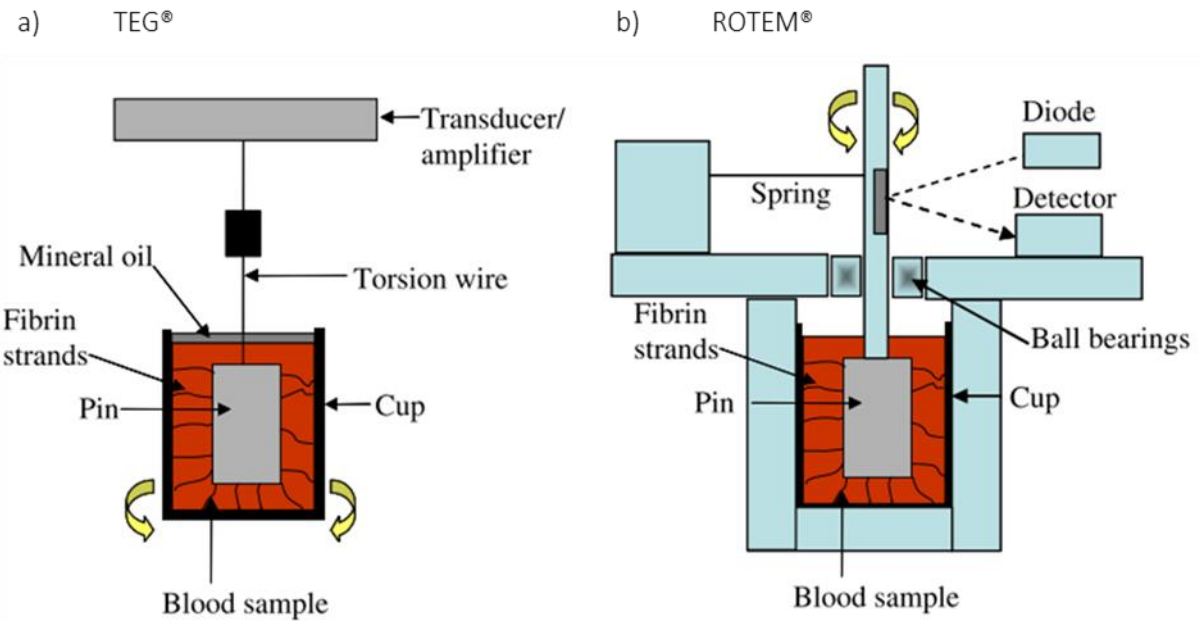

Figure 6. The working principle of a) TEG and b) ROTEM. Reprinted from (47).

During the measurement, the cup is heated to 37°C, and the coagulation activators are added (kaolin, TF). With the progression of the coagulation process, the sample's viscosity increases due to the development of the three-dimensional fibrin mesh over aggregated platelets. As a result, the clot starts to adhere to the cup inducing changes in pin's rotation - the amplitude of the detection pin motion scales with the viscoelasticity of the clot. As the process of fibrinolysis begins, the clot slowly dissolves, and the sample loses its viscosity resulting in a reduced rotation of the pin (48). The detected changes in pin motion are recorded in time and presented graphically as a thromboelastogram (Figure 7). In the analysis of the thromboelastogram, four parameters are taken into account: clot initiation (R time), clot formation rate (K time and Alpha angle), clot strength (maximum amplitude MA), and clot stability (lysis at 30 min). Depending on the existing coagulopathy, different shapes of thromboelastogram can be obtained. Moreover, different nomenclatures describe the same measurement parameters in TEG and ROTEM (49).

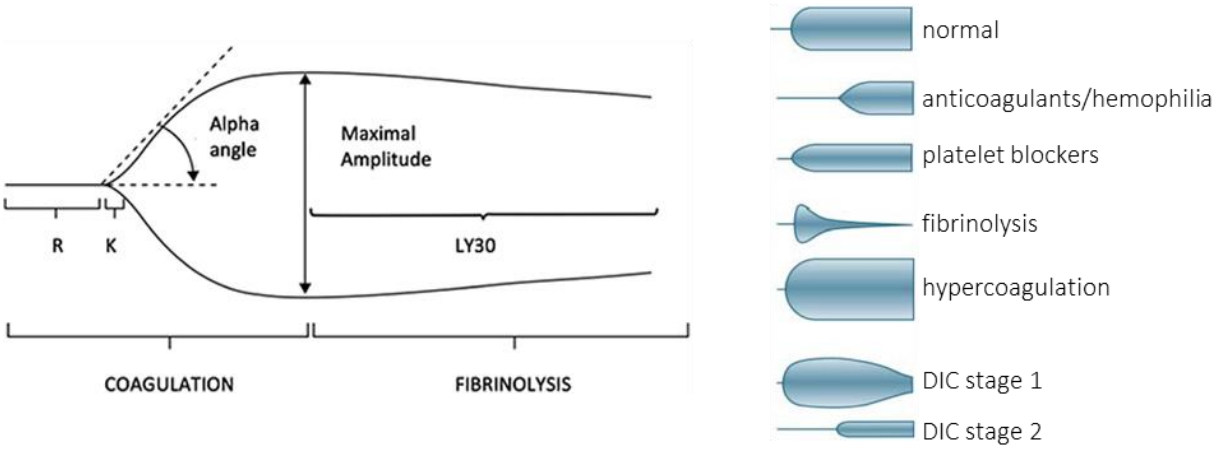

Components	Definition	Normal values	Problem
R time	time to start forming clot	5 – 10 minutes	coagulation factors
K time	time until clot reaches a fixed strength	1 – 3 minutes	fibrinogen
Alpha angle	speed of fibrin accumulation	53 – 72 degrees	fibrinogen
Maximum amplitude (MA)	highest vertical amplitude of the teg	50 – 70 minutes	platelets
Lysis at 30 minutes (LY30)	percentage of amplitude reduction 30 minutes after maximum amplitude	0 – 8%	excess fibrinolysis

Figure 7. In TEG measurement, the amplitude of the pin is recorded in time and presented as a thromboelastogram (top left). Different coagulation patterns are reflected in the particular shape of the thromboelastogram (top right), DIC - disseminated intravascular coagulation. The parameters describing each stage of clotting are presented in the table, modified from *www.tamingthesru.com* and *www.emdocs.net*.

The TE methods consider the function of platelets and therefore offer a global assessment of the hemostasis. Due to the commercially available instrumentation, both methods are used as a bedside device in emergency settings (e.g., trauma, massive bleeding) and in liver transplantation and cardiac surgeries for timely decision making and management of transfusions. Despite many advantages, some challenges remain, such as poor reproducibility and ambiguous results in the case of administration of low molecular weight heparin (LMWH), aspirin, or presence of post-cardiac bypass (33, 44). Notably, due to the lack of accuracy in testing trauma-induced coagulopathy, TEG-based methods were advised to be restricted to scientific use until the standardized protocol is developed (51).

1.3.4 Molecular markers of thrombin

Complex and often ambiguous data analysis of global coagulation assays boosted the development of new screening techniques directed towards measurements of single components of the hemostatic system, including molecular markers of thrombin: prothrombin fragment 1+2 (F1+2), fibrinopeptide A (FPA), and thrombin-antithrombin complex (TAT) (Figure 8). Multiple techniques can be used to detect every single component utilizing specific antibodies or aptamers and using ELISA and sensor technologies. The measured markers give an indirect overview of the generation of thrombin, its activity, and inhibition. It should be noted that levels of these markers do not predict the risk of coagulation or bleeding but rather describe the ongoing or past abnormal process (52).

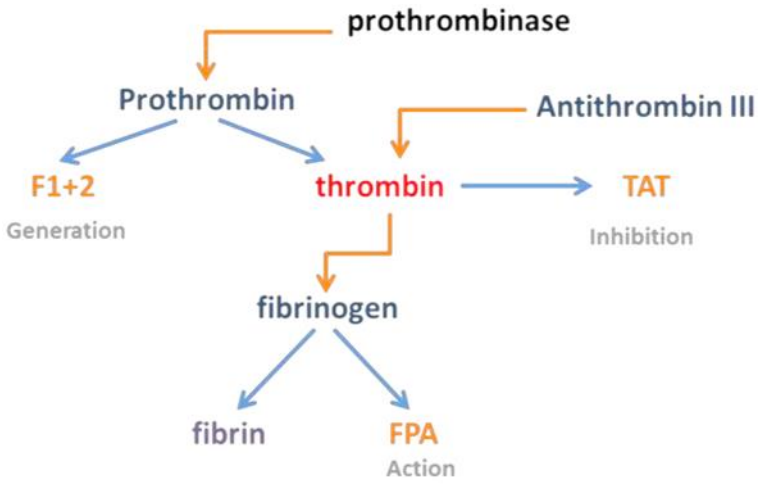

Figure 8. Formation of molecular markers of thrombin generation (F1+2), activity (FPA), and inhibition (TAT). Reprinted from (53).

For the generation of active thrombin enzyme, the inactive zymogen prothrombin is cleaved in the presence of FXa, FVa, phospholipids, and calcium ions (prothrombinase complex). Thus, the first proteolytic cleavage occurs at Arg271, producing prethrombin-2 and F1+2, or at Arg320, making meizothrombin. Then, the prethrombin is cleaved at Arg 320 to produce active thrombin, while the meizothrombin is processed at Arg 271 to liberate F1+2 and active thrombin (54). Therefore, the F1+2 is a molecular marker of thrombin generation, and it was proved to be helpful in the diagnosis of ongoing thrombotic stages such as DVT, DIC, myocardial and cerebral infarction, and for monitoring of anticoagulant therapy with VKAs (55).

FPA is a 16 amino acid peptide that is released during the cleavage of fibrinogen by active thrombin. Therefore, this marker reflects the amount of active (non-inhibited) thrombin in the blood. It has a short lifetime of 3-5 min (56), and therefore it is a reliable marker of the ongoing coagulation process. The processing of the fibrinogen by thrombin results in the generation of a fibrin monomer that has a strong

propensity to polymerization. Fibrin molecules are crosslinked by FXIIIa and form insoluble fibrin polymer, strengthening the initial hemostatic plug composed of platelets. The fibrin clot is degraded by plasmin during the fibrinolysis, which creates a heterogeneous group of fibrin degradation products such as D-dimers. The D-dimer tests are also commonly used as a strong indicator of past thrombotic conditions to diagnose PTE, DIC, DVT, and cancers (57).

The active thrombin is instantly inhibited by serpin antithrombin with a complex half-life of about 15 min. Glycosaminoglycan cofactors, e.g., heparin, increase antithrombin activity by enhancing the affinity of the interaction. Therefore, measuring the level of TAT complexes constitutes a complementary test to FPA. When FPA describes thrombin activity, TAT estimates thrombin inactivated by binding to its natural inhibitor antithrombin. (58).

1.3.5 Free thrombin as a biomarker of thrombosis

Despite multiple modalities of testing the condition of the coagulation system, there is still room for a more precise and direct method. The methods mentioned above can provide valuable information about the coagulation stage. However, to get a complete picture of hemostasis status and quantitatively assess the risk, the direct monitoring of thrombin concentrations would be beneficial. As thrombin is the ultimate enzyme in the coagulation cascade, it truly reflects different hemostatic stages. Therefore, it can be used as a marker to help the understanding of the actual state of the patient and account for better diagnostic, patient care, and outcome. A simple test measuring the amount of circulating free thrombin would help timely decision-making in intensive care units, surgeries, and self-monitoring at home. However, monitoring free-thrombin directly in the blood is problematic since it leads to coagulation because of present fibrinogen. Also, once it is generated, thrombin is almost instantly inhibited by antithrombin in physiological conditions.

1.4. SURFACE PLASMON RESONANCE SENSORS

During the past several decades, new diagnostic platforms have been pursued to provide a robust and cost-effective alternative for the already established methods in the clinics. Among multiple investigated techniques, affinity biosensors based on optical, electrochemical, calorimetric, and piezo-electric detection have received much attention. The most promising from these seem to be optical approaches based on surface plasmon resonance (SPR) and fluorescence as they provide sufficient sensitivity and limit of detection necessary for clinical applications. Moreover, the physical principles of these platforms are well understood (59). The history of the optical phenomenon of SPR dates back to 1902 when Robert Williams Wood described the uneven distribution of white light spectrum diffracted by a metallic diffraction grating (60). However, it was not until 1968 when the phenomenon was

thoroughly explained, and the methods for excitation of surface plasmons were demonstrated by Otto (61) and Kretschmann and Raether (62). Since then, the SPR has been extensively studied, becoming a basis for the emergence of the first SPR-based sensor in 1982 (63,64). Besides, the commercialized system Biacore™ was launched in 1990 by Pharmacia Biosensor AB in Sweden (65) and, up to now, is a leading technology for the automated investigation of kinetics and thermodynamics of biomolecular interactions. The phenomenon of excited surface plasmons on the metal-dielectric interface found a wide range of applications in the detection of chemical and biological species not only in the medical diagnostics (biomarkers detection) but also in the biotech and pharmaceutical industry (optimization of antibodies, investigation of drug-target interactions), food industry (detection of allergens and pathogens) and environmental monitoring (detection of pollutants and biohazards). This chapter discusses the principles of SPR, its various implementations, and its methodology.

1.4.1 Physical bases of SPR

SPR occurs when the energy of photons impinging the metal-dielectric interface is transformed into a collective oscillation of electron plasma in the metal that propagates along with the interface as the surface plasma wave (SPW) with the propagation constant β:

$$\beta = \frac{\omega}{c}\sqrt{\frac{n_m^2 n_d^2}{n_m^2+n_d^2}} \quad (1)$$

where ω is the angular frequency, c is the speed of light in a vacuum, n_d is the refractive index of the dielectric, and n_m is the refractive index of the metal (66). The propagation of the SPW is associated with the emergence of the evanescent electromagnetic wave (EW) that penetrates the two adjacent media in a perpendicular direction to the interface and decays exponentially while propagating. Due to the shorter penetration depth of the metal, 80 - 90% of the electromagnetic field energy is confined in the dielectric (67). The SPW in the visible part of the spectrum can be supported by several metals, from which silver and gold are the most commonly used. Table 2 compares the main characteristics of SPW propagating along with silver and gold interfaces at a wavelength of λ = 630 nm. From the physics point of view, silver has better features for application in SPR-based sensors because the SPW is less attenuated and has higher localization of the EW in the dielectric. However, silver is vulnerable to oxidation, and therefore gold was chosen as a standard coating of the SPR sensor chips (67).

Table 2. SPW propagation parameters for silver and gold at the wavelength λ = 630 nm, based on (67).

Metal supporting SPW	Silver	Gold
SPW propagation length (μm)	19	3
EW penetration depth into metal (nm)	24	29
EW penetration depth into dielectric (nm)	219	162
Concentration of EW in dielectric (%)	90	85

Equation 1 implicates that *β* depends on the optical properties of both the dielectric and the metal. Therefore, the EW that penetrates the dielectric can be employed to probe its variations induced by the binding of molecular species to the metal surface, resulting in a refractive index change. SPR-based biosensor technology takes advantage of this phenomenon because while the other parameters are constant, changes in the refractive index of the dielectric medium near the interface will alter the propagation constant *β.* From this, the SPR signal scales regardless of the identity of the interacting molecules but rather due to mass accumulated on the sensor surface. Therefore, for sensing applications, the biomolecular recognition elements (ligands) are immobilized on the sensor surface to achieve selective detection of analytes. Various biomolecular recognition elements have been used for SPR sensing, while the most common are antibodies, enzymes, aptamers, and nucleic acids. In the affinity biosensors, the interaction of the immobilized ligand and the analyte ensures the high specificity and sensitivity of the biosensor. Thus, depending on the ligand used, the plasmonic sensor can be designed to detect different kinds of analytes as antigens, enzymatic substrates, proteins, complementary strands of nucleic acids, etc.

Three main types of surface plasmons can be differentiated (Figure 9): propagating surface plasmons (PSP), localized surface plasmons (LSP), and long-range surface plasmons (LRSP).

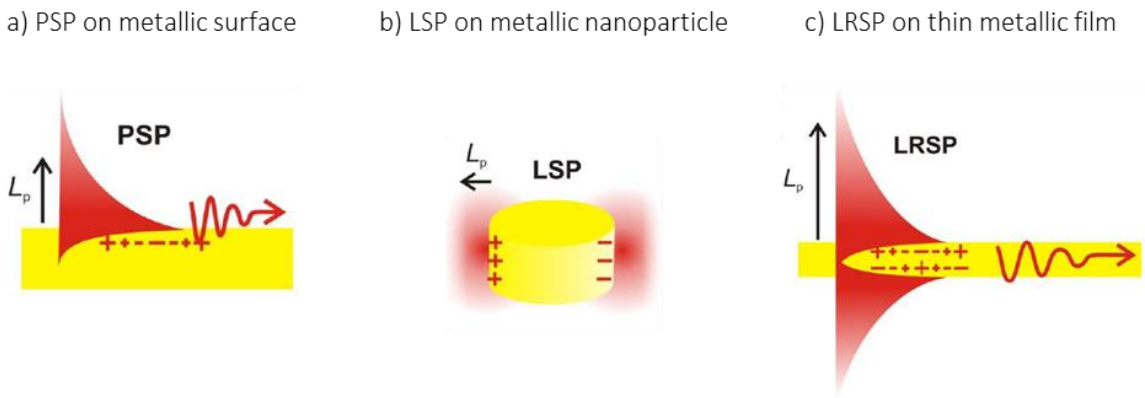

Figure 9. Three types of surface plasmon resonance, modified from (68).

PSPs emerge at the interface of a dielectric and a continuous layer of thin metal. PSPs allow for probing the molecular interactions up to L_p~200 nm from the metallic surface, and they are the first choice method for the investigation of binding events of biomolecules such as antibodies. On the other hand, LSPs are excited on plasmonic nanostructures such as metallic nanoparticles or arrays of metallic nanoparticles, nanoholes, or nanopillars attached to the solid support. LSPs are accompanied by the electron cloud that oscillates collectively, leading to the electric field's concentration near the metallic surface (L_p up to tens of nanometers). Thus, LSPs are utilized for the enhancement of sensitivity and probing of small molecules. In contrast, LRSP can be excited when the continuous thin metallic layer is suspended between two dielectrics with a similar refractive index. In this case, the electromagnetic field is confined on both sides of the metal and penetrates the dielectric in opposite directions. As a result, a stronger EW is created to measure larger species such as cells or thick layers of molecules up to 1 um from the surface (69). Notably, different types of surface plasmons can be combined on one SPR sensor chip to achieve better sensitivity or multiplexing.

1.4.2 Light coupling methods

The incident optical wave must be phase-matched with the PSP waves along the metal surface to excite PSP modes. Indeed, this is impossible to achieve with an optical wave directly impinging at the metal surface as the magnitude of the wave vector of light is consistently lower than that of PSPs. Therefore, the excitation beam light vector needs to be enhanced by using a coupler. One commonly used approach is the so-called Kretschmann configuration of attenuated total reflection method (ATR). Here, a substrate with high refractive index n_p is coated by a thin metallic film, and contacted with dielectric with refractive index n_d, see Figure 10. A light beam that is incident at the metal film from the high refractive index glass slide above the critical angle can generate an evanescent field that penetrates the film. At the outer interface between the metal and lower refractive index dielectric, PSPs can be excited as the high index glass allows to achieve the phase-matching condition that holds:

$$\frac{2\pi}{\lambda} n_p \sin(\theta) = Re\{\beta\}, \quad (2)$$

where λ is a wavelength and θ is the angle of incidence.

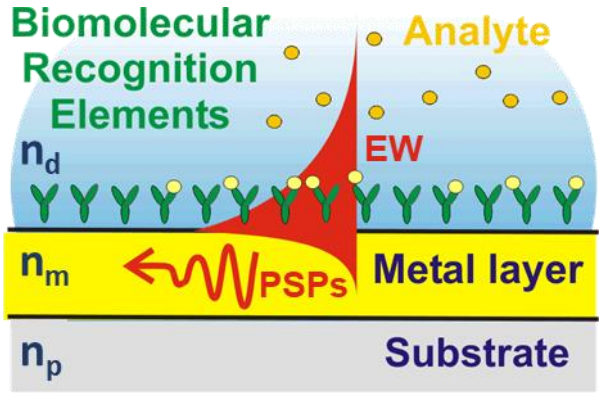

Figure 10. A schematic representation of the Kretschmann configuration with high refractive index substrate n_p, propagating surface plasmons (PSPs), and evanescent wave (EW) at the metal-dielectric interface with refractive indices of n_m and n_d. Detection of an analyte (yellow) by biomolecular recognition elements (green) immobilized on the sensor surface is shown.

In practice, the ATR configuration with Kretschmann geometry is implemented by using a high refractive index glass prism, as presented in Figure 11a. Then, a light beam is launched to the prism and made totally internally reflected (TIR) at the prism base with an optically matched glass substrate carrying a thin metallic film. The angle of incidence θ is tuned above the critical angle $\theta_{C,}$ and the generated evanescent field penetrates through the metal film to excited surface plasmons. Figure 11b illustrates the excitation of surface plasmons by using the optical waveguide, which also relies on ATR. In the classical configuration of this method, the optical fiber that is composed of the core (refractive index n_{core}) coated with plasmon-supporting metal is immersed in a dielectric (refractive index $n_d < n_{core}$). As a result, the light propagating inside the core undergoes TIR and excites surface plasmons.

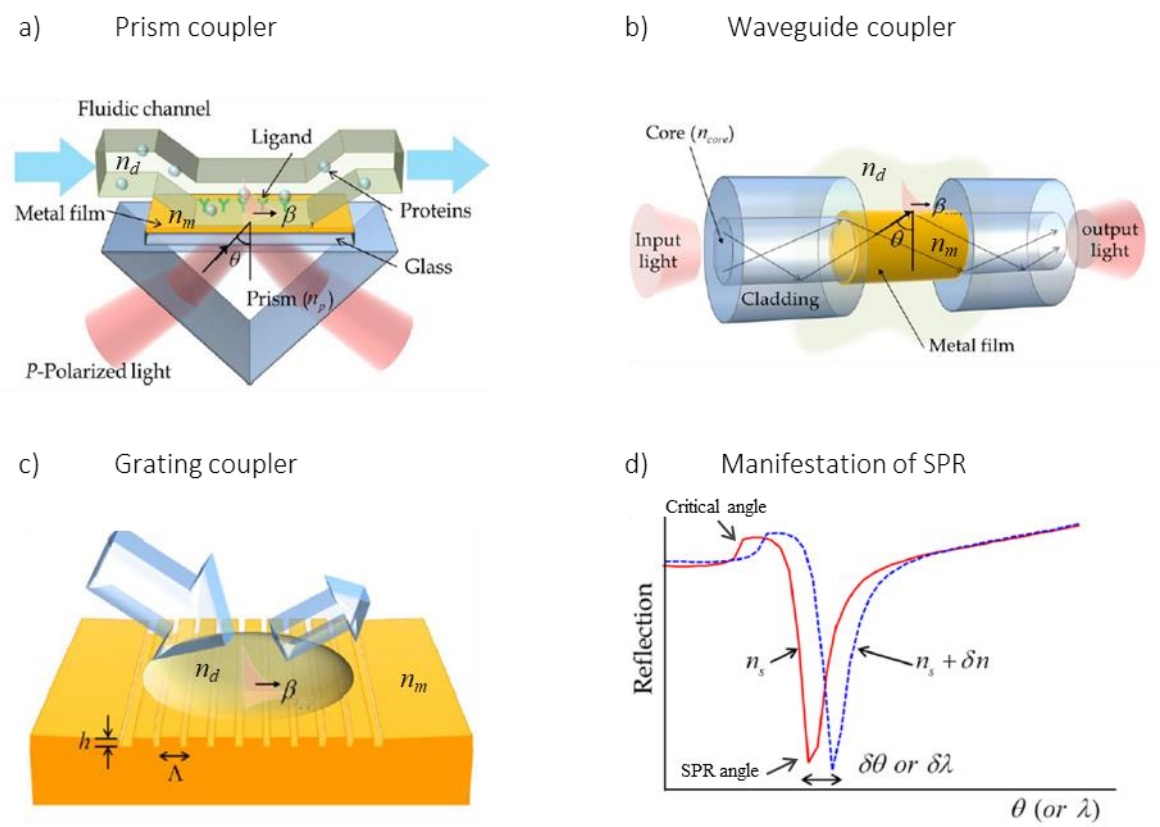

Figure 11. Excitation of surface plasmons by using a) a prism coupler in Kretschmann configuration, b) waveguide, and c) metallic grating. d) Manifestation of SPR as a resonant dip in the reflectivity spectrum.

A distinct type of coupler utilizes diffraction-based phase-matching, as presented in Figure 11c. In this configuration, a light beam directly hits a periodically corrugated surface of a metallic grating. It becomes coupled to a series of diffraction orders that travel in the far-field or form evanescent waves propagating along its surface through diffraction. The energy of the optical wave can be transformed into the surface plasmons when a part of the diffracting light with a wave vector that is parallel to the surface grating matches with the propagation constant of the surface plasmon wave for specific diffraction order m:

$$\frac{2\pi}{\lambda} n_d \, sin(\theta) + \, m\frac{2\pi}{\Lambda} = \pm Re\,\{\beta\}\,, \tag{3}$$

where Λ is the grating period.

In the SPR sensors, refractive index changes occurring on their surface are monitored as variations in polarization and phase shift, resonant angle shift, and resonant wavelength shift. The SPR angle shift

monitoring is the most commonly used detection method in the SPR biosensors (70). As it is illustrated in Figure 11d, the SPR is manifested as a characteristic dip in the reflected light spectrum since the energy of photons is consumed by PSPs at the SPR angle/SPR wavelength, where the phase-matching condition is fulfilled ($\delta\vartheta$ or $\delta\lambda$ depending on the SPR setup). Therefore, the position of the SPR dip is sensitive to the changes in refractive index on the metal-dielectric interface. This allows for monitoring the mass accumulating on the surface due to molecular binding events and therefore sensing.

1.4.3 Plasmonic nanostructures

Recent progress in nanofabrication methods such as electron-beam lithography, focused ion beam milling, photolithography, and soft lithography has paved the way for the realization of metallic nanostructures with strictly controlled dimensions in shape, size, and spacing (71) (Figure 12). Metallic nanostructures can also facilitate light coupling to surface plasmons supported at their surface – LSPs. They provide means to manipulate light by tight confinement to subwavelength volume and therefore became increasingly employed in biosensing. LSPs typically confine their energy on sharp or bent metallic edges of metallic nanoparticles. Moreover, such LSP resonances can form more complex hybrid modes when interacting with PSPs on the planar metallic surface of nanostructure arrays or become diffractively coupled LSPs and establish surface lattice resonances.

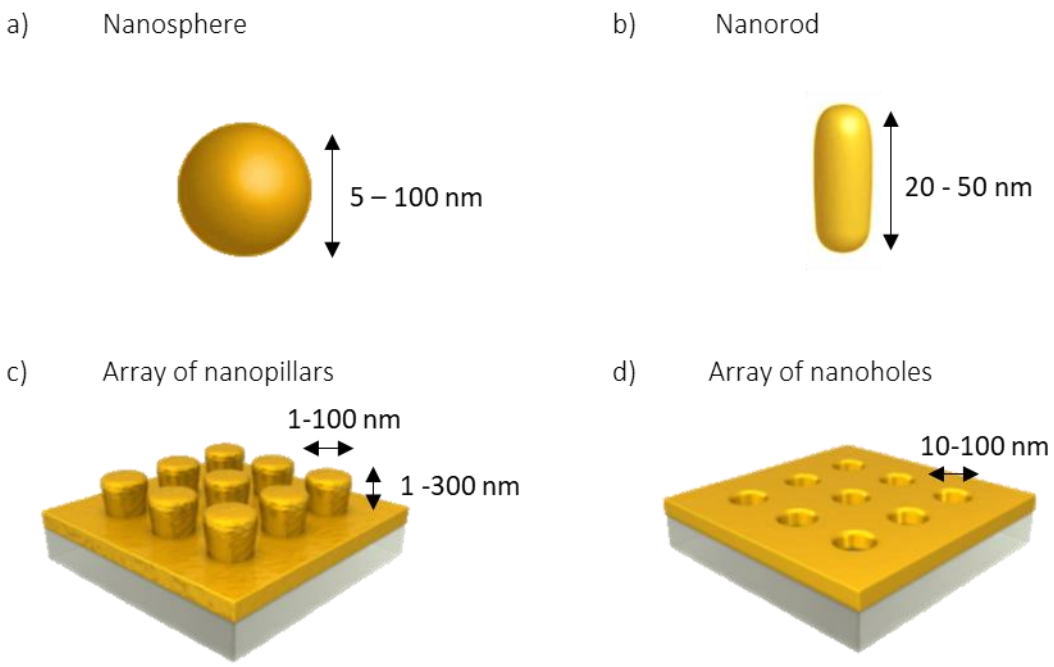

Figure 12. Various shapes and dimensions of nanostructures are available for excitation of LSPs, and coupled LSPs and PSPs resonances.

In addition, the optical properties of the nanostructures can be enriched by interfacing them with inorganic and organic materials to actuate resonant coupling (72). Metallic nanostructures composed of nanoparticles (NPs), nanopillars, nanoholes in multiple geometrical variations have captivated substantial interest due to their potential applications in miniaturized devices such as photonic circuits, sensors, and diagnostic systems (73).

1.4.4 Operation of SPR-based biosensors

An example of an SPR biosensor system with Kretschmann configuration is depicted in Figure 13. The sensor chip is optically matched to a prism mounted on the rotation stage that allows for the control of the angle of incidence θ. At the metallic surface of the sensor chip, a microfluidic cell is clamped to transport the analyzed liquid samples across its surface. The optical system is composed of a light source, polarizer, chopper, and detector. The binding that manifests as a change in the refractive index (and the corresponding change in the SPR) is converted into an electrical signal processed by dedicated hardware and software into readable data. The data can be recorded as the angular scans when the change of the surface optical properties is represented as a shift in the SPR angle. Otherwise, the angle can be kept constant, and the changes in the reflectivity intensity can be recorded in time, resulting in the SPR sensorgram.

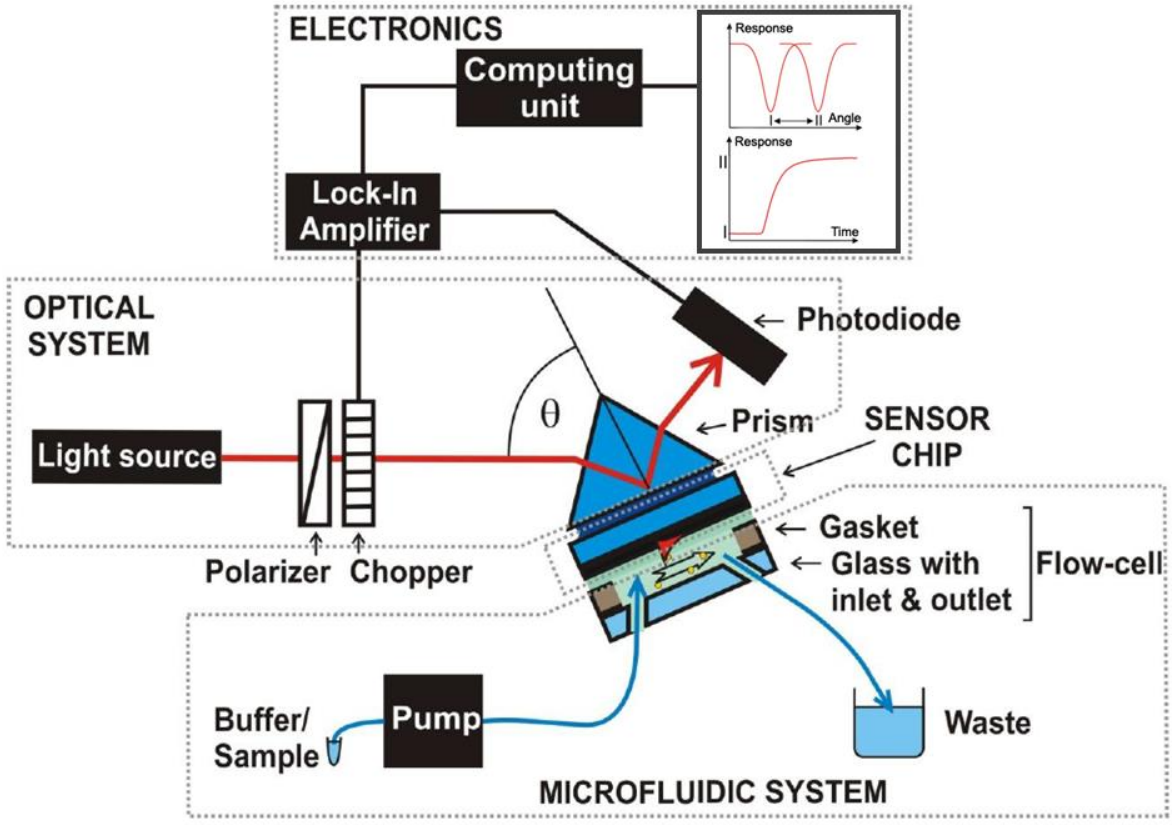

Figure 13. The main components of the SPR sensor system are microfluidics, sensor chip, optics, and electronics.

SPR technology allows for the real-time monitoring of molecular interactions, represented in the form of sensorgrams. Figure 14 shows a representative example of such sensorgram acquired for affinity binding experiment on the sensor chip. The experiment starts with a running buffer to establish the baseline in the SPR signal. Subsequently, the interacting analyte is injected and let interact with the sensing layer that is pre-functionalized with BRE. The binding of the target analyte from the liquid sample to its affinity partner immobilized at the sensor surface manifests as an increase of the SPR signal in the so-called association phase. A plateau is reached after a sufficiently long time when the association and dissociation event rates are in equilibrium. Finally, running buffer flows over the surface, and a gradual dissociation of the bound analyte molecules is observed as a decrease of the SPR signal. The regeneration buffer can be used to completely remove affinity-bound molecules from the surface and get back to the original baseline level.

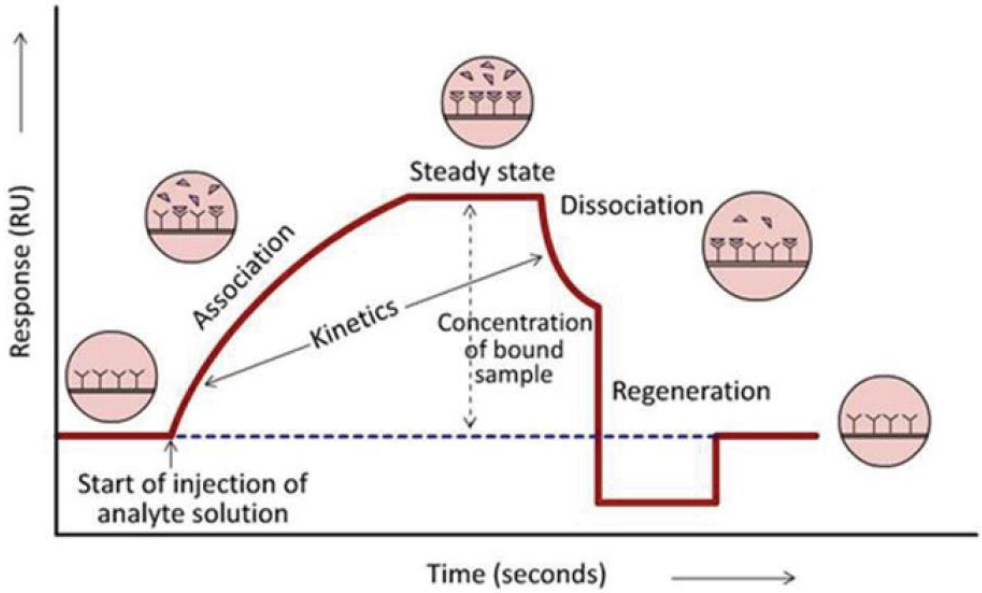

Figure 14. Example of an SPR sensorgram illustrating the changes in the signal during subsequent stages of the assay. The association of molecules is represented by an increase of SPR response (RU) from the initial baseline. The equilibrium is reached when there is a balance between the association and dissociation of the complex. The decrease in SPR response represents the dissociation of the complex. Reprinted from (74).

1.5. ANTI-FOULING BIOINTERFACES

Direct monitoring of affinity binding events without using labels represents a vital advantage of the SPR biosensor technology. However, it also imposes a challenge of assuring the sensor specificity as it is solely provided by the proper design of the sensor surface. This is inherent to the measurement principle as the SPR signal shifts with refractive index changes of the surface due to the respective surface mass accumulation. Therefore, the SPR-based biosensors cannot differentiate between the specific response

originating from the analyte and nonspecific interactions of other components present in the tested sample. These nonspecific interactions can occur between the sample and biorecognition elements due to the overlap of binding sites or between the sample and the SPR chip surface. Both can lead to a high background signal and false positives. In addition, the reduction of detection window and surface activity can be observed due to the blocking of available binding sites (75). This phenomenon is especially troublesome when the detection needs to be performed in multicomponent biological samples like plasma and blood that, apart from biomarkers, are rich in various other abundant chemical species and cells. The complex matrices of these samples render the sensor surfaces fouling that is described as nonspecific and irreversible adsorption of proteins on the solid interfaces (76). Protein fouling is a multistep process that starts with attracting high-mobility proteins that are subsequently replaced by the bigger species with a higher affinity to the surface (Vroman effect) (77). This phenomenon is driven by polar or hydrophobic interactions, hydrogen bonding, and van der Waals forces (78). Proteins can adhere to virtually any surface (79), taking into account the abundance of amino acid residues with various physicochemical properties as well as a possibility of conformational change of already adsorbed proteins [that can further increase the affinity of protein to the surface, primarily via hydrophobic interactions (80)]. Therefore, a vast majority of SPR-based methodologies are developed based on detection in single-compound solutions in buffer media to eliminate the propensity of the surface to fouling. Often, such proof-of-concept methods have insufficient capacity to produce reliable data in the real-life samples and thus, are not applicable in clinics. Notably, a direct detection of biomarkers in (ideally minimally processed) biological fluids lays in the tremendous interest of modern diagnostics as it can provide a valuable medical information in the instant and thus, shorten time to diagnosis. In order to limit the contribution of the nonspecific adsorption to the detection signal, the reference surface that does not contain the biorecognition elements was introduced to account for the nonspecific adsorption on the SPR chip surface. This method enables eliminating the contribution of the nonspecific signal, however, does not prevent the fouling. Therefore, in order to reduce the nonspecific interactions originating from a complex biological samples a pre-separation techniques of biomarkers were applied (81) or a number of antifouling coatings were implemented (76). Among the most commonly used coatings of gold sensor chips are self-assembled monolayers (SAMs) of oligoethylene glycol (OEG)-alkanethiols, polyethylene glycol (PEG), polymer brushes and hydrogels. This chapter discusses the preparation of the biosensor coatings that prevent nonspecific interactions with the surface, their types and architectures.

1.5.1 Preparation methods of thin anti-fouling layers

1.5.1.1 "Grafting to"

The antifouling surfaces can be prepared using the "grafting to" or "grafting from" approaches. "Grafting to" utilizes preformed molecules such as short polymer chains that spontaneously adsorb to the surface in the process of physisorption or chemisorption. The assembly of molecules occurs due to a favorable gain of free energy, and it is governed by the diffusion, molecular crowding, quality of the solvent, and the properties of the surface (e.g., purity, roughness). During the physisorption, elements forming the antifouling layer attach to the surface via common physical interactions, e.g., ionic, hydrophobic, dipole-dipole attraction, H-bonding, and van-der Waals forces. In general, this approach does not require the presence of any specific anchor group. However, the composition of the polymer can be optimized for such an interaction to occur more efficiently in particular conditions. For instance, Figure 15a shows the physisorption of diblock copolymer while in a given solvent, one block preferentially interacts with the surface, and the second block with the solvent facilitating the self-assembly. Nevertheless, the quality (growth and composition) of the physisorbed layer is difficult to control, and such interface based on relatively weak electrostatic interactions is susceptible to removal, e.g., by the thermodynamically more beneficial solvent (82).

These limitations can be overcome by preparing molecules with the terminal groups that are reactive towards the sensor surface and undergo the process of chemisorption. This approach utilizes the preformed molecules, but contrary to physisorption, the end reactive group assembly via a covalent linkage directly on the surface or interacts with the surface-bound complementary functional group (Figure 15b). A typical implementation is a photochemical "grafting to", whereas the photoreactive groups are incorporated in the polymer chain and sometimes on the surface. Irradiation with light leads to the covalent bonding of polymer and the substrate and the polymer crosslinking (83). As a result, the sensor coatings formed via chemisorption or photoreaction are more stable than the physisorbed layers.

Nevertheless, problems with the layer homogeneity and relatively low grafting densities can arise due to the steric hindrances created by big polymer chains and their partial physisorption leading to masking the reactive spots on the surface. In "grafting to" methods, the preformed polymers can be fully characterized beforehand, resulting in lower molecular dispersity (82). However, they provide layers with lower maximum thickness.

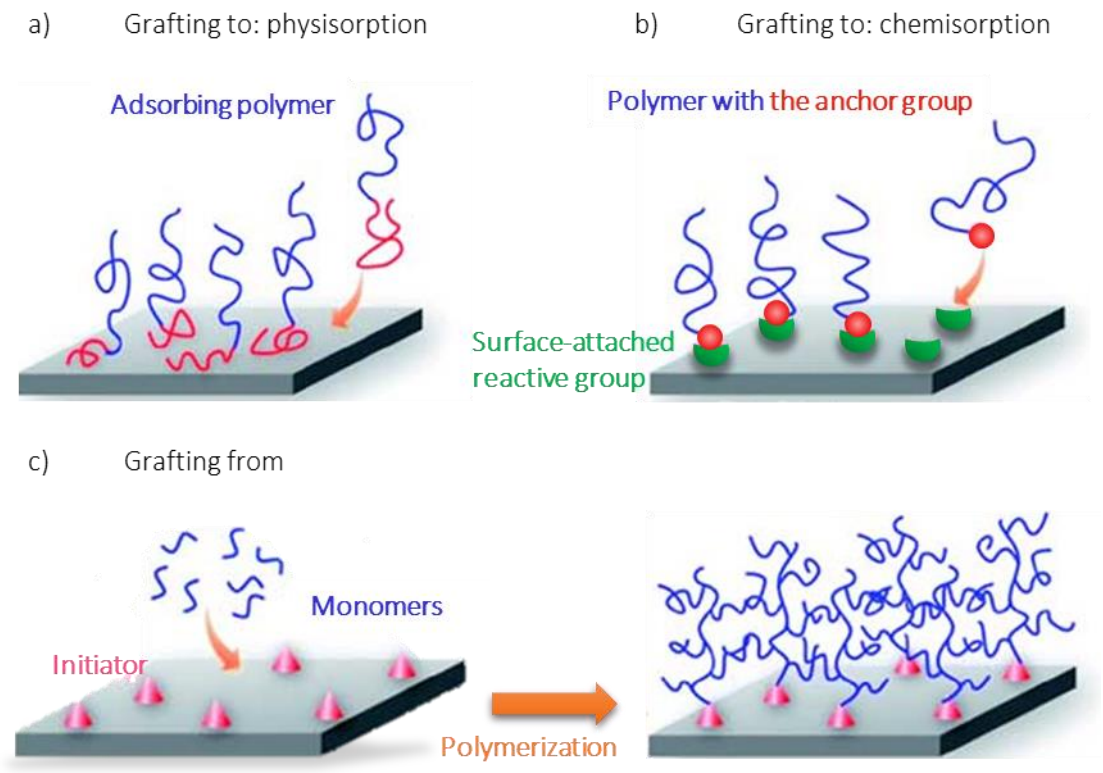

Figure 15. Preparation of the antifouling layers on the sensor chip surface by a "grafting to" approach: a) physisorption, b) chemisorption, and c) "grafting from" method. Modified from (84).

1.5.1.2 "Grafting from"

To increase the grafting density and improve quality of the antifouling layers, there were investigated the "grafting from" methods based on *in situ* surface-initiated polymerization (SIP), resulting in homogenous layers of polymer coatings on the sensor surface (Figure 15c) (85). In this approach, the growth of the polymer is initiated from the surface-attached reactive initiator, and it depends on the availability and diffusion of the monomers, reactivity of the reaction centers during the propagation process, and conditions of the polymerization reaction (time, temperature, ambient) (82). The most common synthetic methodologies include free-radical polymerizations (surface-initiated atom transfer radical polymerization (SI-ATRP), surface-initiated reversible-addition fragmentation chain transfer (SI-RAFT) polymerization, surface-initiated nitroxide-mediated polymerization (SI-NMP) and surface-initiated photoiniferter-mediated polymerization (SI-PIMP)), polymerizations using 2,2,6,6-tetramethyl- 1-piperidyloxy (TEMPO), ring-opening metathesis polymerization (ROMP), cationic polymerization and anionic polymerization (86). The SIP method can provide high quality, densely packed, and homogenous antifouling layers primarily due to small molecular entities such as monomers and catalysts (instead of whole polymer chains), providing a lack of steric hindrance and thick layers. The main drawbacks of the "grafting from" method are complicated synthetic approaches and the possibility of the broader mass distribution due to the side reactions (85).

1.5.1.3 Coating methods

Thin polymer layers can also be deposited on the solid sensor surface using physical coating methods (Figure 16). There are two main strategies: deposition of the polymer layer followed by the crosslinking or crosslinking during the deposition and growth of the polymer network (83). Electrospinning (or its modification electrospraying) uses the capillary tube (needle) filled with the solution of the polymer. Once a high voltage is applied to the system, the electrically charged jet of the polymer fibers or particles breaks up from the needle and deposits on the substrate. The advantage of electrospinning is its versatility, as it can be used for virtually any soluble polymer. However, a fine-tuning of the deposition parameters is necessary to obtain the reproducible polymer layers (87).

Spin coating is another valuable method for the creation of thin and homogenous polymer layers. In this method, a substrate is placed onto a spin coater's rotating stage, and the appropriate volume of the polymer solution is dropped on the top. Upon the substrate rotation, the centrifugal force acts on the coating fluid, spreading it over the substrate. The film's thickness depends on the polymer concentration, initial acceleration, and rotation speed. The advantage of the spin coater is the low polymer amount needed. However, there is a substantial loss of the material during the process. The spin coating is primarily applicable for small samples, as sufficient rotational force to get the thin and homogenous layer cannot be applied to the large area substrates (87).

For the coating of the large surface areas, the dip-coating approach is beneficial where the substrate is immersed in a solution. The substrate is left in the solution for minutes to hours to allow the adsorption of the polymer molecules and then removed and dried by solvent evaporation. This approach enables obtaining highly uniform layers. However, a substantial amount of the polymer is needed. The thickness is impacted by several parameters such as attraction forces between the polymer and the substrate, immersion time, polymer concentration, and the number of coating cycles. In addition, since the polymers are physisorbed to the surface, the adhesion strength can be relatively low (87).

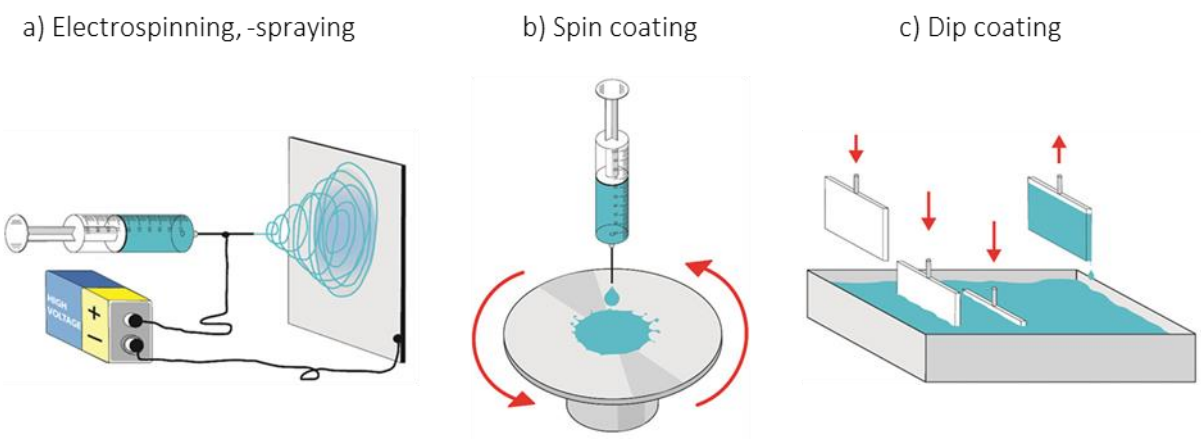

Figure 16. Polymer coating methods a) electrospinning or electrospraying, b) spin coating, and c) dip coating. Modified from (87).

Also, various micropatterning techniques can be used for the deposition of structured layers of polymer materials such as nanoimprint lithography (88), photolithography (89), hot/soft embossing (90), and many others.

1.5.2 Self-assembled monolayers of alkanethiols

Due to their availability and ease of preparation from the solution or vapor phase, SAMs of alkanethiols, alkane dithiols, and dialkyl(di)sulfides conjugated to (oligo)ethylene glycol (OEG) constitute a widely used toolbox for conferring the antifouling properties of the sensor interface. Each molecule of SAM contains three building blocks (Figure 17a): the headgroup, spacer, and the terminal group (91). The headgroup contains an atom of sulfur that guides the spontaneous self-assembly to the gold surface by chemisorption. The spacer is composed of the hydrocarbon chain of various lengths C11 – C15 that through the van der Waals and hydrophobic forces promotes the upright position of each molecule and ensures efficient packing. The self-assembly of alkanethiols is a multistep process (Figure 17b) that can take up to several hours or even days to be completed and involves an i. initial physisorption through the van der Waals interactions, ii. lying down phase where most of the surface is covered by the horizontally physisorbed molecules, iii. transition to the upright position by chemisorption of sulfur to gold and loss of the hydrogen atom, iv. standing up configuration resulting in an ordered and packed SAM. In the process of SAM formation, the intermolecular interactions compete with the interactions with the metallic surface, finally forming a uniform layer of closely packed molecules in a standing up position (91).

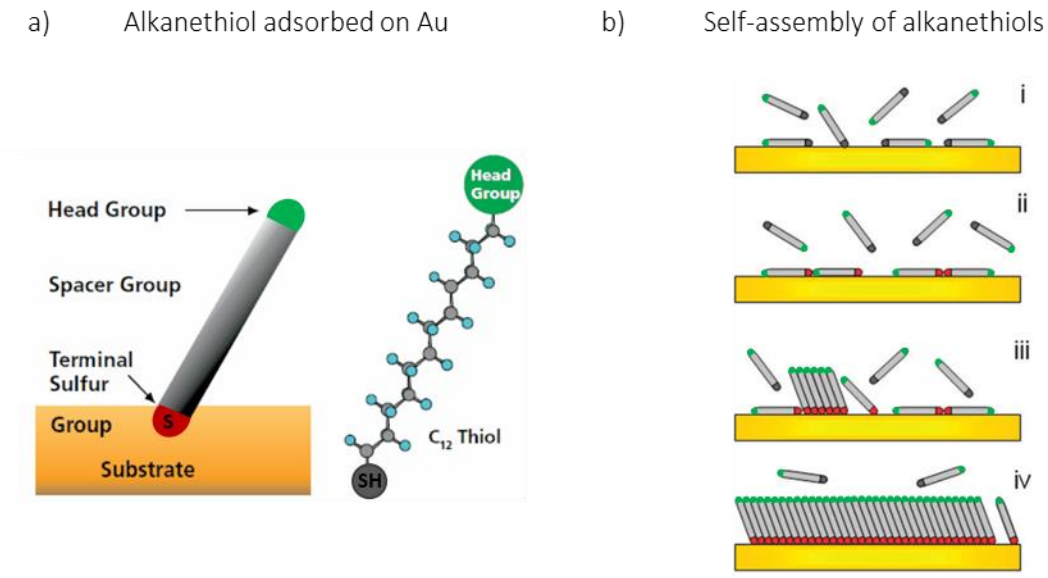

Figure 17. a) Schematic of the alkanethiol molecule chemisorbed on gold. The three building blocks of alkanethiol are shown in the picture. b) Phases of alkanethiols self-assembly: i. physisorption, ii. lying down phase, iii. initiation of the chemisorption and standing up phase, iv. standing up phase of closely packed alkanethiol molecules. Modified from (91).

Typically, the alkane chain is extended by 3-6 units of ethylene glycol terminated with the functional group that can be utilized for a covalent attachment of the biorecognition elements on the top of the SAM layer. The packing of the surface can be controlled by adjusting the alkanethiols' concentration and optimizing the conditions of their preparation. Besides, a mixture of hydroxy- and carboxy-terminated thiols are applied to regulate the density of the biorecognition elements attached via, e.g., amine coupling involving carboxylic groups. Notably, the thickness of such SAM is only about 2.5 nm and can be used for sensors based on LSP with a highly localized evanescent field that probes interactions up to a few tens of nanometers from the surface (79). The antifouling properties of OEG alkanethiol SAM emerge from their packing density and the hydrophilicity of the oligoether chains and terminal -OH groups. The OEG alkanethiols are the most straightforward anti-fouling coating for proof-of-concept experiments with single protein solutions. However, they lack the resistance to fouling from more complex biological fluids (76,92).

1.5.3 Hydrogels

Hydrogels hold a prominent position among the organic materials integrated into biosensing devices due to their unique chemical and physical characteristics. Hydrogels can be composed of small molecules, particles, or polymer chains that are either chemically or physically crosslinked to form a network that highly swells in water (83). The hydrogel matrix's number and type of crosslinks determine its mechanical properties and mesh size (ξ). Chemical links are made through the covalent bonds and typically provide better chemical stability than the physical ones based on hydrogen bonding and

hydrophobic and electrostatic interactions. The mesh size constitutes a space between the polymer chains available for the diffusion of the molecules through the matrix (Figure 18).

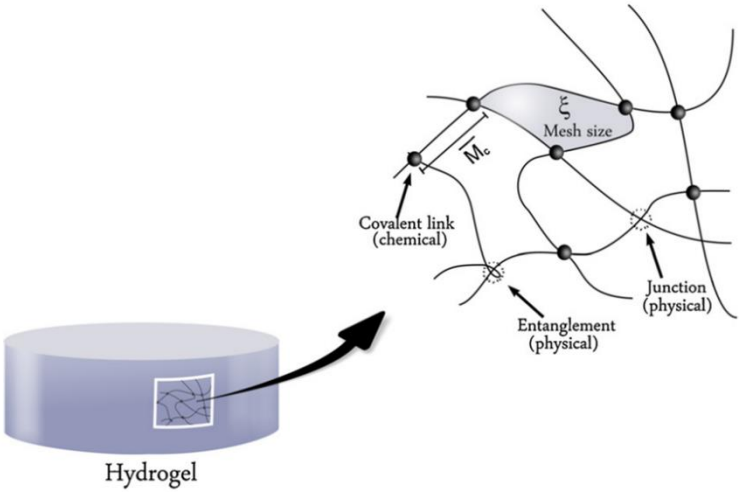

Figure 18. Schematic representation of the hydrogel matrix with the mesh size ξ, and present chemical and physical links and chain entanglements. The $\overline{M}_c$ indicates the average molecular weight between the crosslinking points. Reprinted from *(93)*.

The main hydrogel formats are presented in Figure 19 and can be classified as bulk 3D materials, small microgel particles with the advantage of large surface area, thin hydrogel layers (~100 nm – 10 µm) attached to the solid support, and surface-attached polymer brushes.

On the molecular level, due to the uneven distribution of the chains concentration, their length, and non-uniform crosslinking, the spatial and topological inhomogeneities can arise in the hydrogel network. Therefore, various methods are used to study the topology and the physicochemical properties of the hydrogel structures, such as contact angle measurements, ellipsometry, SPR combined with optical waveguide spectroscopy (OWS), atomic force microscopy (AFM), small-angle X-ray, neutron, and dynamic light scattering and fluorescence spectroscopy (83).

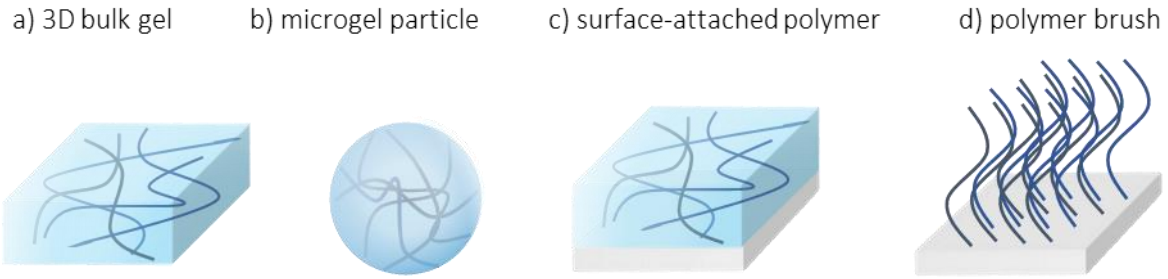

Figure 19. Schematic representation of different hydrogel formats a) 3D bulk gel, b) microgel particle, c) surface-attached polymer network, d) polymer brush. Modified from (83).

The water uptake by hydrogel materials can vary from a few up to 99% (w/w) without a polymer dissolving (94). A large amount of water makes the hydrogels compatible with the biological systems

and renders their bioinert properties. Therefore, hydrogels are widely employed in various biomedical applications such as tissue fillers (95), scaffolds for tissue engineering (96), wound dressings (97), contact lenses (98), drug delivery systems (99), and bioanalytical devices (100).

1.5.3.1 Mechanism of swelling

Upon contact with the solvent, the hydrogel swells, expanding its volume even up to several orders of magnitude. The process of swelling is guided by the osmotic pressure that is built inside the highly hydrophilic matrix. The degree of swelling is dependent on the chemical composition of the gel, quality of the solvent, and a crosslinking degree as typically the highly crosslinked polymers have smaller mesh sizes and swell less. In the first phase of the swelling process, the molecules of water diffuse into the hydrogel. As they penetrate the matrix, the hydration of the polymer chains occurs, leading to their relaxation. Subsequently, the hydrated polymer chains stretch away, leading to a volumetric change of the system. The stretching of the polymer chains induces elastic retractive forces as a counterforce to the network expansion. The degree of swelling is determined by the balance between the osmotic pressure and the retractive elastic forces leading to the swelling to the maximal degree at the so-called equilibrium water content. When these forces meet a balance, the swelling stops, and the equilibrium is reached (93). Flory and Rehner first explained this phenomenon in the theory of swelling of the neutral isotropic polymer. The free energy of the hydrogel with the Gaussian distribution of polymer chain length and the tetrafunctional branching units can be expressed by:

$$\Delta G = \Delta G_{el} + \Delta G_{mix} \quad \text{(Eq. 4)}$$

where ΔG_{el} is the free energy of elastic retractive forces and ΔG_{mix} is the free energy of polymer and solvent mixing (94). Assuming the equal swelling in all directions, the mesh size ξ of the swollen hydrogel network can by calculated as:

$$\xi = v_{2,s}^{-1/3}\left(\frac{2C_N\overline{M_c}}{M_r}\right)^{1/2} l \quad \text{(Eq. 5)}$$

where $v_{2,s}$ is the polymer volume fraction in the fully swollen state, l is the length of the bond along the backbone chain, C_N is the Flory characteristic ratio, $\overline{M}_c$ is a molecular weight of the polymer chain between crosslinks, and M_r is a molecular weight of the polymer repeat unit (93).

1.5.3.2 Stimuli-responsive hydrogels

In advanced hydrogel materials, swelling and shrinking of the network can be triggered and controlled by external stimulus, e.g., temperature, pH, light, pressure, electric or magnetic field, and presence of biomolecules as depicted in Figure 20 (95). Upon exposure to the stimulus, these materials undergo volume-phase transition, leading to rapid changes in the network morphology such as swelling, collapsing, or solution-to-gel transition.

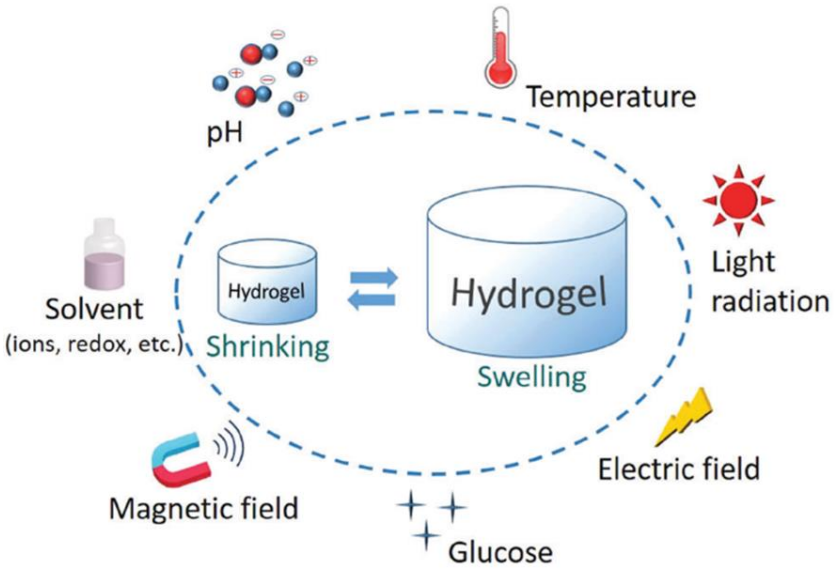

Figure 20. Different types of stimuli for responsive hydrogel materials. Copied from (96).

The responsive properties are inherent to the chemical composition of the hydrogel. For instance, the anionic and cationic hydrogels were designed with acidic or basic pendant groups to induce responsiveness to the pH changes (97). In the low pH, the acidic groups of the anionic hydrogel are protonated, and in the absence of the counterions, the hydrogel network becomes hydrophobic, leading to the removal of water and shrinking. In the alkaline pH, however, the acidic groups are deprotonated, the number of fixed charges increases the electrostatic repulsions between the chains and the hydrophilicity leading to the expansion of the hydrogel matrix. Cationic hydrogels exhibit similar behavior with the opposite trend (93). The other well-recognized class of responsive materials constitutes hydrogels sensitive to the thermal stimulus. These polymers can be divided into upper critical solution temperature (UCST) gels that are swollen above the UCST point and lower critical solution temperature (LCST) polymers that swell below the LCTS (Figure 21).

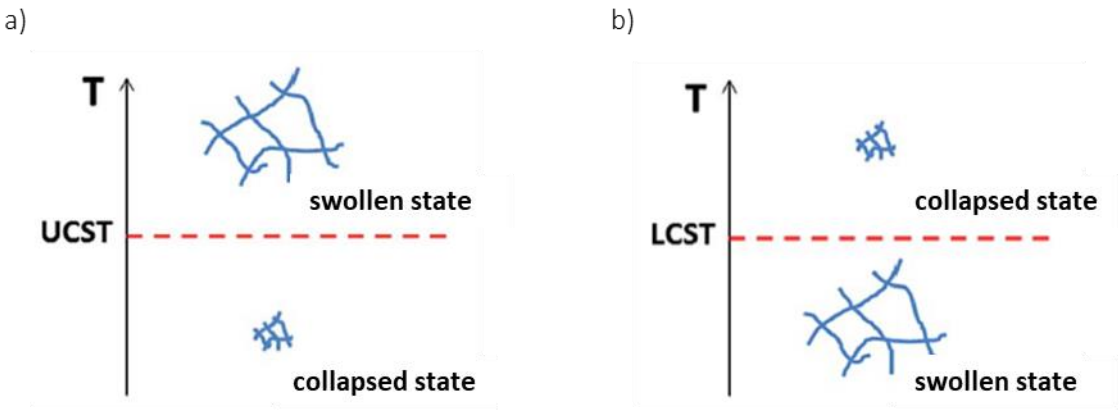

Upper Critical Solution Temperature (UCST)	Lower Critical Solution Temperature (LCST)
poly(acrylic acid)	N-methylacrylamide
polyacrylamide	N,N-dimethylacrylamide
poly(acrylamide-co-butyl methacrylate)	N- isopropylacrylamide

Figure 21. The difference between (a) the UCST and (b) the LCST polymers with examples of the respective materials. Modified from (98).

This temperature-dependent behavior can be explained by the differences in the strength of the intermolecular interaction below and above the critical solution temperature point. For instance, below the LCST, the interaction between polymer and water is stronger than the one between polymer chains defining the swollen state of the hydrogel. However, when the temperature increases above the LCST, the polymer's hydrophobic parts become exposed due to the higher mobility of water molecules at a higher temperature. In this situation, the clustering of the non-polar elements and removal of water from the network is more energetically favorable and results in the collapsing of the polymer (93).

The mechanical work performed by the responsive hydrogels that is associated with swelling and collapsing has been exploited for the design of miniature valve systems (99), pumps (100), actuators (101), and microrobots (102). In addition, the stimuli-responsive hydrogels were utilized to actuate the optical signal in optical affinity SPR-based sensors (72,103,104).

1.5.3.3 Origin of hydrogel materials

Various hydrogel materials of a synthetic or a biological origin and numerous functionalities have been used for sensing applications (83,105). Natural hydrogels, including polysaccharides and polypeptides (e.g., dextran, cellulose, alginate, chitosan, agarose, collagen, hyaluronic acid, and fibrin), are non-toxic materials with a good bio-compatibility and offer a low cost of preparation. However, they generally exhibit shorter shelf-life, worse mechanical properties, lower water uptake, and poor stimulus-

responsive characteristics (106). These shortcomings led to new synthetic materials that can be readily tailored towards a specific stimulus and sensor readout. Gels based on polyacrylate and polyvinyl derivatives are most commonly exploited in optical sensors and are responsive to temperature changes to control their volume and refractive index (107). The polypyrrole, polyaniline, and poly(ethylenedioxy) thiophene are conductive polymers exploited for electrochemical sensing (108–110). Synthetic hydrogels typically provide better mechanical stability and longer degradation time.

In addition, to combine the advantages of both hydrogel classes mentioned above, the natural hydrogels were modified with synthetic additives (e.g., nanofibers (111), nanoparticles (112–114) and carbon materials (115–117), and nature-mimicking hydrogels were synthetized (118–120) to obtain an improved cytotoxic profile, mechanical stability, degree of swelling and controlled reaction to various stimuli.

1.5.3.4 Polymer brushes

Polymer brushes are hydrogel-related surface modifiers that were researched to armor the sensor interface with antifouling properties. They are densely grafted macromolecule chains composed of one or more types of monomers. Brushes are attached to the surface via one end, while the second terminus stretches away, creating a closely packed polymeric layer (82). Contrary to the canonical hydrogels matrices of interconnected polymers, the polymer brushes do not need to be crosslinked as their topography is mainly determined by the surface attachment and the intermolecular non-covalent interactions between the chains. The theoretical studies and experimental observation of polymer brushes have shown that tethered polymers exhibit different properties than bulk systems. A grafting density (σ) is a critical factor that governs the physical and morphological properties of the layer as well as the resistance to fouling. The three regimes of polymer brushes were identified: a mushroom, moderate- and high-density brush (Figure 22), in which the thickness of the layer correlates with the grafting density through the scaling law:

$$h \propto N \times \sigma^{v} \quad \text{(Eq. 6)}$$

where h is the height of the polymer layer, N corresponds to the degree of polymerization, and v is an exponent that varies from 0 to 1 with the solvent quality and grafting density σ (e.g., in a moderate-density regime $v \approx 0.3$ in a good solvent and $v \approx 0.8$ in a poor solvent). The mushroom regime is maintained in the low grafting densities σ when the average distance between two grafting sites D is larger than two times the radius of gyration R_g of the polymer chains ($D > 2R_g$), and $v \approx 0$. In this situation, the polymer layer achieves the lowest height h as the long polymer chains are electrostatically attracted to the empty sites on the surface. However, when σ increases and D approaches or is smaller than 2Rg, the chains transit to moderate or high-density regimes. When the grafting sites are in very close proximity, the chains stretch away from the surface to avoid energetically not favorable contact with each other and

to maximize the polymer-solvent interactions. In these conditions, the height of the polymer layer reaches the maximum in the presence of a good solvent (121).

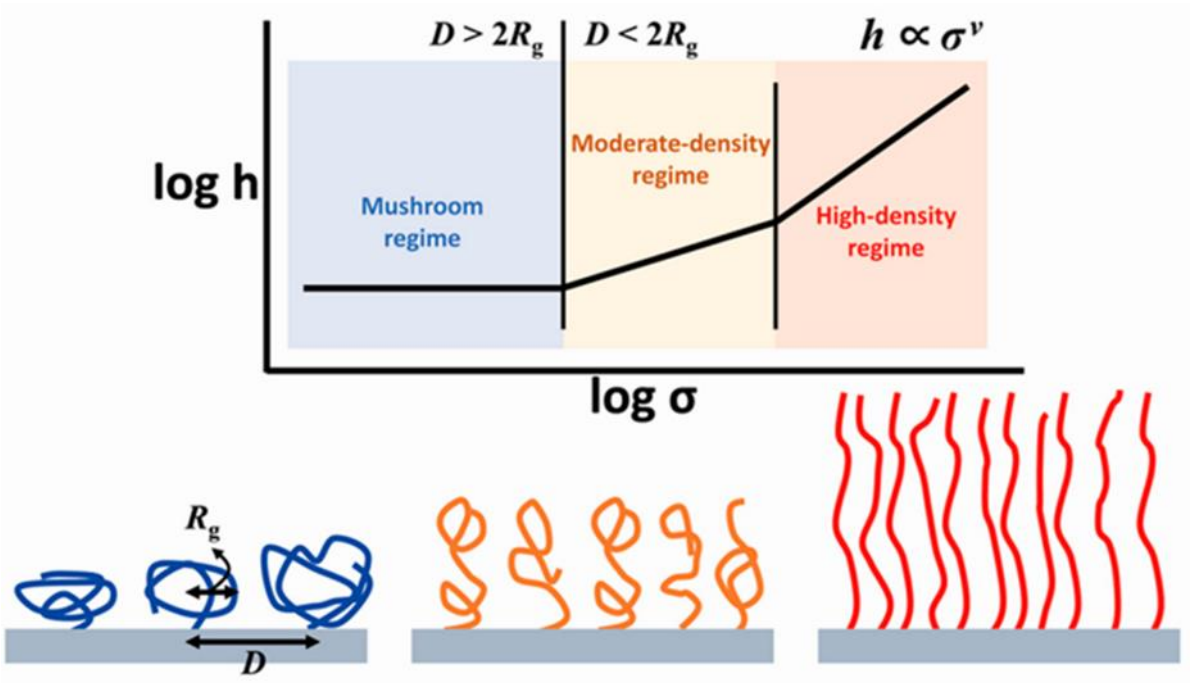

Figure 22. The three regimes of polymer brushes are mushroom, moderate-density, and high-density. The height of the polymer layer *h* depends on the grafting density *σ,* and it is theoretically described in the scaling law. The figure was copied from (121).

Also, the grafting density *σ* impacts the antifouling properties of the polymer layer. It was observed that in low *σ* (mushroom regime), the proteins and cells penetrate the polymer chains and interact with the sensor surface via van der Waals forces. However, the solvated brushes generate an entropic penalty in the highly stretched regime that prevents trespassing to the underlying substrate. In this case, the repulsive interactions strongly dominate, enforcing the resistance to the interfering biological matter (122).

Polymer brushes on the solid surfaces can be prepared by both the “grafting to” and “grafting from” approaches. However, only limited grafting densities were achieved with the first method. Therefore, multiple types of SIP have been developed to grow uniform quality antifouling layers on different substrate types and with various grafting densities and polymer growth kinetics. Depending on the application, different compositions and architectures of the polymer brushes can be designed, including a homopolymer, block copolymer, mixed brush or mixed molecular weight chains grafting, or chemical gradient polymer brush (Figure 23).

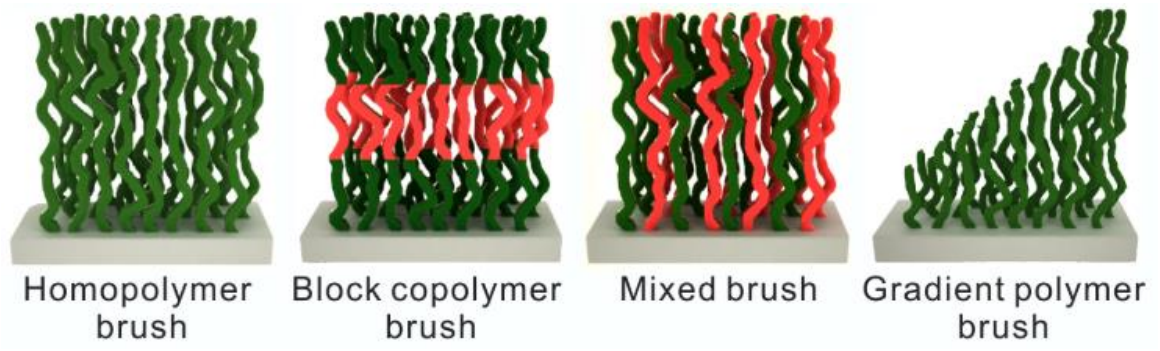

Figure 23. Various architectures of polymer brushes, reprinted from (123).

1.5.3.5 Hydrogel optical waveguide spectroscopy

The appropriate selection of hydrogel building blocks, chemically reactive groups and crosslinking parameters allows for tailoring hydrogel materials for specific applications in the field of biosensors as functional coatings (124), large capacity binding matrices (125), and actuators (126). One of the implementations of these materials into sensing is realized by hydrogel optical waveguide spectroscopy (HOWS). In this method, a metallic substrate is coated with a thin hydrogel layer. If this hydrogel layer's refractive index and thickness are sufficiently high, the surface-attached film can support propagation of the guided optical waves traveling inside the hydrogel matrix. These waves are confined in the polymer layer between the reflective metallic surface and the upper dielectric with a lower refractive index in the total internal reflection condition. The propagation constant β of the hydrogel waveguide modes depends on the refractive indices of the metal, hydrogel, and the dielectric as well as the polymer thickness and can be determined by solving the dispersion relation:

$$\tan(\kappa d_h) = \frac{\gamma_d n_h^2/\kappa n_d^2 + \gamma_m n_h^2/\kappa n_m^2}{1-(\gamma_d n_h^2/\kappa n_d^2)(\gamma_m n_h^2/\kappa n_m^2)} \quad \text{(Eq. 7)}$$

where d_h - thickness of the hydrogel layer; n_h, n_d, n_m – refractive indices of the hydrogel, dielectric, and metal, respectively; $\kappa^2 = k_0^2 n_h^2 - \beta^2$, $\gamma_m^2 = \beta^2 - k_0^2 n_m^2$ and $\gamma_d^2 = \beta^2 - k_0^2 n_d^2$ – transverse propagation constants in the hydrogel film, metal, and liquid, respectively (127).

The HOWS is commonly implemented using the Kretschmann configuration in which the metal- and the polymer-coated substrate is optically matched to a high refractive index prism (n_p). In this case, a monochromatic light beam under TIR can resonantly couple to the surface plasmon mode (SP) and the hydrogel waveguide mode (HW) (Figure 24a). The field intensity of the SP mode is confined close to the metallic surface, and it decays into the hydrogel matrix. On the other hand, the evanescent field of the HW mode is concentrated in the hydrogel, and it decays into the adjacent dielectric. The distinct dips manifest the excitation of these two modes in the reflectivity spectrum at the specific angles θ_{HW} and θ_{SP} (Figure 24b), which grows with the rise of the refractive index of the hydrogel and the adjacent dielectric. Such guided waves can be excited with both transverse magnetically and transverse

electrically polarized light, and their number increase with the thickness and the refractive index of the hydrogel.

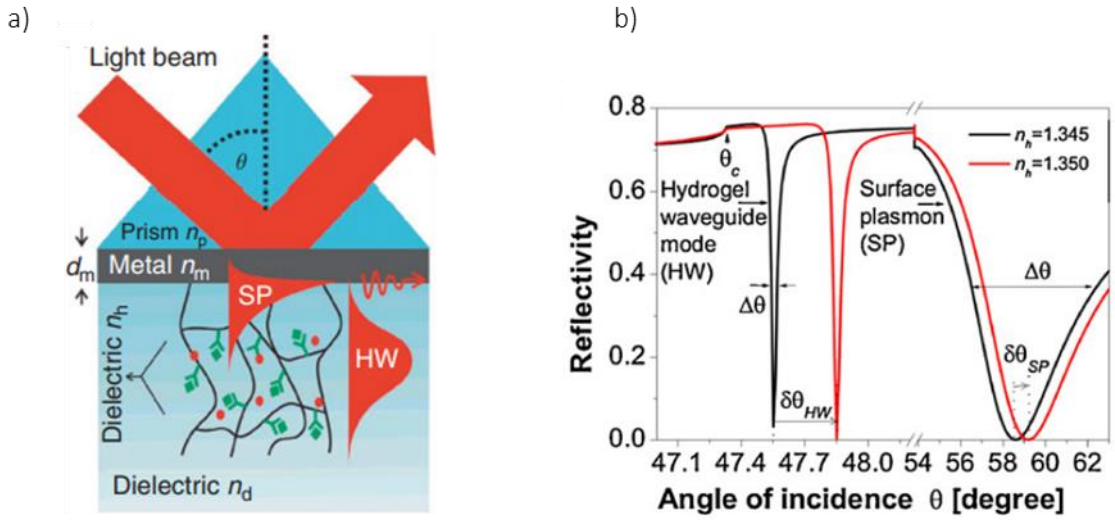

Figure 24. a) The Kretschmann configuration for the excitation of SP and HW modes, reprinted from (128). b) A simulated shift of the resonant angles θ_{HW} and θ_{SP} due to the change of the refractive index of the hydrogel film from n_h=1.345 to n_h=1.350, reprinted from (125).

The HOWS is a powerful tool for investigating the properties of the hydrogel layers, such as refractive index, thickness, and swelling ratio. Moreover, it provides means to employ hydrogel as a sensing element to observe molecular interactions. Notably, the excitation of the HW mode with a narrow resonant dip offers an order of magnitude better resolution of the refractive index measurements than a standard SP mode. In addition, the 3-D hydrogel matrix provided a 5-fold lower limit of detection of IgG molecules than the conventional SPR using a 2-D self-assembled monolayer in the model immunoassay. Even higher enhancement can possibly be achieved with molecules smaller than IgG that can rapidly diffuse inside the hydrogel matrix (125).

1.6. APTAMERS

The aptamer is a synthetic single-stranded DNA or RNA oligonucleotide that can recognize and specifically bind to a chosen molecular target with a high affinity. Therefore, it can serve as a biomolecular recognition element of the SPR sensor. The unique oligonucleotide sequence of the aptamer can be identified in an *in vitro* selection and amplification process called SELEX (Systematic Evolution of Ligands by Exponential Enrichment) that was introduced independently by two groups: Ellington and Szostak (129) and Tuerk and Gold (130) in 1990. The target can be virtually any organic or inorganic compound (dye, drug, vitamin) or a larger biomolecule, e.g., nucleic acid, peptide, protein, or whole cell. Aptamers bind their targets by adopting three-dimensional structures, e.g., loops, hairpins,

triplexes, and quadruplexes, creating unique interfaces for strong interaction with the target by structural compatibility, hydrogen bonding, and electrostatic and van der Walls interactions. The aptamer selection process starts with generating a pool of ~10^{15} fully or partially randomized nucleic acid sequences. Each sequence has a fixed length of *n* nucleotides flanked by constant regions in 5' and 3' ends. These regions serve as primers in the polymerase chain reaction (PCR) (and reverse transcriptase (RT)-PCR in case of RNA libraries) that is used to create multiple copies of each sequence in the amplification step. The library is incubated at elevated temperature and then slowly cool down to achieve conformational equilibration of single-stranded oligonucleotides folded into three-dimensional structures. Then, the prepared pool of oligonucleotides is incubated with the immobilized target molecule on an affinity chromatography column or paramagnetic beads to allow the oligonucleotides to interact with the target. The unbound sequences are washed away from the column, leaving behind the oligonucleotides that specifically interacted with the target. These specific sequences are eluted from the column using denaturing conditions, causing the loss of binding conformation and detaching from the target molecule. These oligonucleotides are again amplified by PCR and used in the next cycle of SELEX until the oligonucleotide with the highest affinity will be finally selected and sequenced (Figure 25).

The rounds of SELEX are systematically repeated until about 100% of the library will be bound to the immobilized target. Although the SELEX technology aims to select a specific and high-affinity aptamer candidate, it is a lengthy and laborious process that can take several weeks. Besides, SELEX is susceptible to failure due to incomplete library, retention of the nonspecific binders, accumulation of the amplification artifacts, and inadequate selection conditions. To overcome these limitations and speed up the selection of target-specific aptamers, substantial improvements (131) or alternative platforms were introduced, such as High-Fidelity SELEX (132) and computational modeling approaches (133). Also, different chemical variants of the libraries are now available such as modified nucleotides (134), locked nucleic acid aptamers (135), and peptide aptamers (136) to improve the stability, enhance the resistance to nucleases and expand the chemical properties.

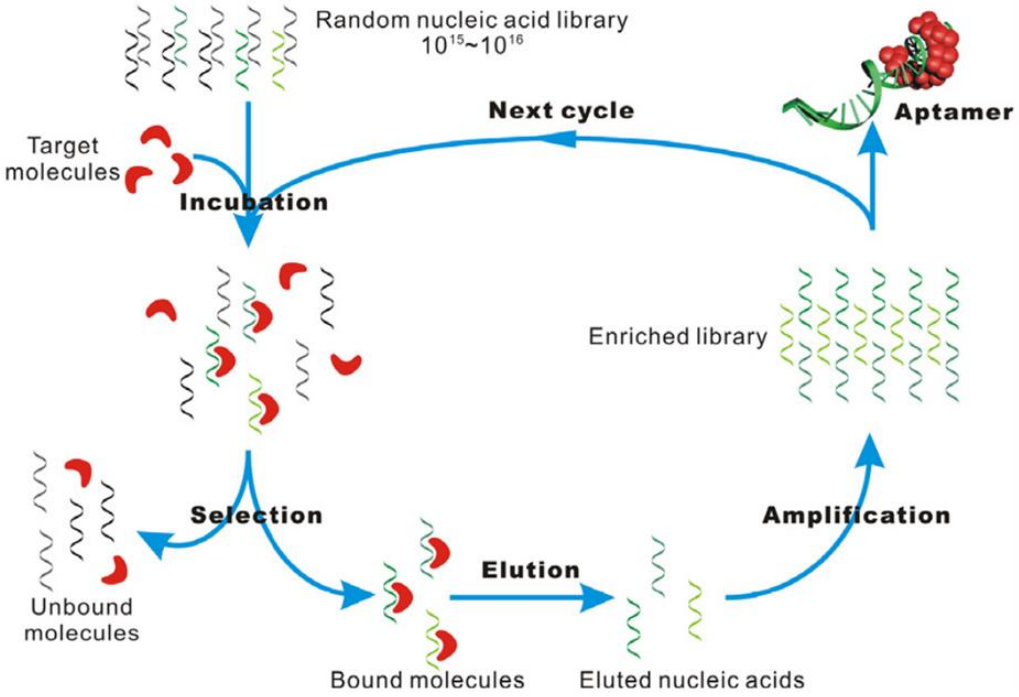

Figure 25. Process of Systematic Evolution of Ligands by Exponential Enrichment (SELEX), reprinted from (137).

Depending on the application, the potencies of aptamers can vary from a subnanomolar to a micromolar range. The high binding affinities enabled the use of aptamers as a substitute for the antibodies. Yet, aptamers offer advantages over antibodies such as smaller size, good stability throughout a wide range of temperatures and pH, low immunogenicity, and ease of production. Once selected for a specific target, the sequence can be chemically synthesized and modified with functional groups on a commercial basis. The comparison of aptamers and antibodies is presented in Table 3. Aptamers found multiple applications as therapeutics, delivery vectors in targeted therapies, and diagnostics and analytical tools, e.g., purification, bioimaging, and biosensors (138).

Table 3. Comparison of aptamers and antibodies (reprinted from (53)).

Aptamers	Antibodies
Selection	
SELEX: *In vitro* Any target (~ 50% success) *In vitro* conditions	**Cellular immune response in animal host:** *In vivo* Non-toxic, immunogenic target Physiologic conditions
Production	
Chemical solid-phase synthesis: Scalable	**Immune response in animal host:** Low amount

Cost-effective Reproducible No batch-to-batch variation Non-contaminated Easy to add functionalities	Expensive Batch-to-batch variation Impurities Difficult to add functionalities
Properties	
High affinity High specificity Non-immunogenic Intra- and extracellular action Small size Flexible Stability (pH, temperature) Reversible denaturation Nuclease degradation Long shelf-life	High affinity High specificity Immunogenic Extracellular action Large size Non-flexible Sensitive to conditions Irreversible denaturation

1.6.1 Aptamers for detection of thrombin

The fact that thrombin constitutes a common factor in both pathways keeping the delicate balance between clot formation and bleeding predispose it as a molecule of particular interest in controlling the hemostasis. However, thrombin-receptor binding might trigger clotting of the sample and subsequent fouling of the sensor. For this reason, the biorecognition element used in the biosensing of thrombin has to be carefully chosen. It should not only bind to thrombin but also block its coagulation activity. For this purpose, aptamers are well-suited candidates. Thrombin harbors two spatially separated binding pockets, which can be efficiently blocked by optimized HD1 (139) and HD22 (140) DNA aptamer sequences. HD1 aptamer binds to exosite I of thrombin and blocks the cleavage of fibrinogen to fibrinopeptides and subsequent formation of fibrin network as well as thrombin-induced aggregation of platelets. HD22 aptamer is specific to exosite II and inhibits the activation of factors V/VIII. The DNA sequence of the aptamer can be manipulated through a custom order to obtain functional groups that mediate attachment to a solid surface (e.g., aptamer+spacer+thiol to bind gold). These features of aptamers provide means for successful use in SPR-based detection of thrombin, including the sandwich format of the assay.

REFERENCES

1. Sira J, Eyre L. Physiology of haemostasis. Anaesth Intensive Care Med [Internet]. 2016;17(2):79–82. Available from: http://dx.doi.org/10.1016/j.mpaic.2015.11.004
2. Wendelboe AM, Raskob GE. Global Burden of Thrombosis: Epidemiologic Aspects. Circ Res. 2016;118(9):1340–7.
3. MacDougall DA, Feliu AL, Boccuzzi SJ, Lin J. Economic burden of deep-vein thrombosis, pulmonary embolism, and post-thrombotic syndrome. Am J Heal Pharm. 2006;63(20 SUPPL.):5–15.
4. Eikelboom J, Merli G. Bleeding with Direct Oral Anticoagulants vs Warfarin: Clinical Experience. Am J Med [Internet]. 2016;129(11):S33–40. Available from: http://dx.doi.org/10.1016/j.amjmed.2016.06.003
5. Barr D, Epps QJ. Direct oral anticoagulants: a review of common medication errors. J Thromb Thrombolysis [Internet]. 2019;47(1):146–54. Available from: http://dx.doi.org/10.1007/s11239-018-1752-9
6. Periayah MH, Halim AS, Saad AZM. Mechanism action of platelets and crucial blood coagulation pathways in Hemostasis. Int J Hematol Stem Cell Res. 2017;11(4):319–27.
7. Reyes Gil M. Overview of the Coagulation System [Internet]. Third Edit. Transfusion Medicine and Hemostasis. Elsevier Inc.; 2019. 559–564 p. Available from: https://linkinghub.elsevier.com/retrieve/pii/B978012813726000091X
8. Palta S, Saroa R, Palta A. Overview of the coagulation system. Indian J Anaesth. 2014;58(5):515–23.
9. Macfarlane RG. An enzyme cascade in the blood clotting mechanism and its function as a biochemical amplifier. Nature. 1964;202(4931):498–9.
10. Davie, E. W., & Ratnoff OD. Waterfall sequence for intrinsic blood clotting. Science (80-). 1964;145(3638):1310–2.
11. Suchman AL, Griner PF. Diagnostic uses of the activated partial thromboplastin time and prothrombin time. Ann Intern Med. 1986;104(6):810–6.
12. Hoffman M, Monroe DM. Coagulation 2006: A Modern View of Hemostasis. Hematol Oncol Clin North Am. 2007;21(1):1–11.
13. Hoffman M, Iii DMM, Riddel JP, Aouizerat BE, Miaskowski C, Lillicrap DP, et al. A Cell-based Model of Hemostasis " For Internal Educational Purposes Only . Not for Dissemination ." " For Internal Educational Purposes Only . Not for Dissemination ." Arterioscler Thromb Vasc Biol. 2003;24(3):797–811.
14. Butenas S, Mann KG. Review : Blood coagulation. Biochem. 2002;67(1):3012.
15. Dahlbäck B, Villoutreix BO. Regulation of blood coagulation by the protein C anticoagulant pathway: Novel insights into structure-function relationships and molecular recognition. Arterioscler Thromb Vasc Biol. 2005;25(7):1311–20.
16. Rau JC, Beaulieu LM, Huntington JA, Church FC. Serpins in thrombosis, hemostasis and fibrinolysis. J Thromb Haemost. 2007;5(SUPPL. 1):102–15.
17. Saes JL, Schols SEM, van Heerde WL, Nijziel MR. Hemorrhagic disorders of fibrinolysis: a clinical review. J Thromb Haemost. 2018;16(8):1498–509.
18. Mackman N. Triggers, targets and treatments for thrombosis. Nature. 2008;451(7181):914–8.
19. Jackson SP. Arterial thrombosis-insidious, unpredictable and deadly. Nat Med. 2011;17(11):1423–36.
20. Global Health Estimates 2016: Deaths by Cause, Age, Sex, by Country and by Region, 2000-2016. Geneva;
21. Previtali E, Bucciarelli P, Passamonti SM, Martinelli I. Risk factors for venous and arterial thrombosis. Blood Transfus. 2011;9(2):120–38.
22. Kyrle PA, Eichinger S. Deep vein thrombosis. Lancet. 2005;365(9465):1163–74.
23. Agarwal R, Varma S. Acute pulmonary embolism. East J Med. 2009;14(2):57–68.
24. Goldhaber SZ, Bounameaux H. Pulmonary embolism and deep vein thrombosis. Lancet [Internet]. 2012;379(9828):1835–46. Available from: http://dx.doi.org/10.1016/S0140-6736(11)61904-1
25. Wolberg, A. S., Aleman, M. M., Leiderman, K., & Machlus KR. Procoagulant Activity in Hemostasis and Thrombosis: Virchow's Triad Revisited. Anesth Analg. 2012;114(2):275.
26. Hachey KJ, Sterbling H, Choi DS, Pinjic E, Hewes PD, Munoz J, et al. Prevention of postoperative venous thromboembolism in thoracic surgical patients: Implementation and evaluation of a Caprini risk assessment protocol. J Am Coll Surg [Internet]. 2016;222(6):1019–27. Available from: http://dx.doi.org/10.1016/j.jamcollsurg.2015.12.003
27. Husted S, De Caterina R, Andreotti F, Arnesen H, Bachmann F, Huber K, et al. Non-vitamin K antagonist oral anticoagulants (NOACs): No longer new or novel. Thromb Haemost. 2014;111(5):781–2.
28. Miyares MA, Davis K. Newer oral anticoagulants: A review of laboratory monitoring options and reversal

agents in the hemorrhagic patient. Am J Heal Pharm. 2012;69(17):1473–84.
29. Dalton HJ, Garcia-Filion P, Holubkov R, Moler FW, Shanley T, Heidemann S, et al. Association of bleeding and thrombosis with outcome in extracorporeal life support. Pediatr Crit Care Med. 2015;16(2):167–74.
30. Mazzeffi M, Greenwood J, Tanaka K, Menaker J, Rector R, Herr D, et al. Bleeding, Transfusion, and Mortality on Extracorporeal Life Support: ECLS Working Group on Thrombosis and Hemostasis. Ann Thorac Surg. 2016;101(2):682–9.
31. Kearon C, Hirsh J. Management of anticoagulation before and after elective surgery. 1997;
32. J.D. D, J.S. H, M. B, J.W. E, M.D. E, M. F, et al. Perioperative bridging anticoagulation during dabigatran or warfarin interruption among patients who had an elective surgery or procedure: Substudy of the RE-LY trial. Thromb Haemost [Internet]. 2015;113(3):625–32. Available from: http://th.schattauer.de/en/contents/current-issue/issue/special/manuscript/23790/download.html%5Cnhttp://ovidsp.ovid.com/ovidweb.cgi?T=JS&PAGE=reference&D=emed17&NEWS=N&AN=603146059
33. Arachchillage DR, Passariello M, Laffan M, Aw TC, Owen L, Banya W, et al. Intracranial Hemorrhage and Early Mortality in Patients Receiving Extracorporeal Membrane Oxygenation for Severe Respiratory Failure. Semin Thromb Hemost. 2018;44(03):276–86.
34. Levy JH, Szlam F, Wolberg AS, Winkler A. Clinical use of the activated partial thromboplastin time and prothrombin time for screening: A review of the literature and current guidelines for testing. Clin Lab Med. 2014;34(3):453–77.
35. Ignjatovic V. Thrombin Clotting Time. In: Monagle P, editor. Haemostasis Methods in Molecular Biology (Methods and Protocols). New York: Humana Press; 2013. p. 131–8.
36. Ng VL. Prothrombin Time and Partial Thromboplastin Time Assay Considerations. Clin Lab Med [Internet]. 2009;29(2):253–63. Available from: http://dx.doi.org/10.1016/j.cll.2009.05.002
37. Heneghan C, Alonso-Coello P, Garcia-Alamino JM, Perera R, Meats E, Glasziou P. Self-monitoring of oral anticoagulation : a systematic review and meta-analysis. Lancet. 2006;367(9508):404–11.
38. Hemker HC, Al Dieri R, Beguin S. Thrombin generation assays: Accruing clinical relevance. Curr Opin Hematol. 2004;11(3):170–5.
39. Nair SC, Dargaud Y, Chitlur M, Srivastava A. Tests of global haemostasis and their applications in bleeding disorders. Haemophilia. 2010;16(SUPPL. 5):85–92.
40. Horsti J, Uppa H, Vilpo JA. Poor Agreement among Prothrombin Time International Normalized Ratio Methods: Comparison of Seven Commercial Reagents. 2005;560:553–60.
41. Gosselin R, Owings JT, White RH, Hutchinson R, Branch J, Mahackian K, et al. A comparison of point-of-care instruments designed for monitoring oral anticoagulation with standard laboratory methods. Thromb Haemost. 2000;83(5):698–703.
42. Van Veen JJ, Gatt A, Makris M. Thrombin generation testing in routine clinical practice: Are we there yet? Br J Haematol. 2008;142(6):889–903.
43. Castoldi E, Rosing J. Thrombin generation tests. Thromb Res [Internet]. 2011;127(SUPPL. 3):S21–5. Available from: http://dx.doi.org/10.1016/S0049-3848(11)70007-X
44. Hemker HC, Giesen P, Aldieri R, Regnault V, Smed E De, Wagenvoord R. 1 CAT Hemker 2002. 2002;249–53.
45. Hemker HC. The application of thrombin generation in real life clinical situations. Thromb Res [Internet]. 2015;136(1):3–4. Available from: http://dx.doi.org/10.1016/j.thromres.2015.04.010
46. Hartert H. Blutgerinnungsstudien mit der Thrombelastographie, einem neuen Untersuchungsverfahren. Klin Wochenschr. 1948;26(37–38):577–83.
47. Lindahl TL, Ramström S. Methods for evaluation of platelet function. Transfus Apher Sci [Internet]. 2009;41(2):121–5. Available from: http://dx.doi.org/10.1016/j.transci.2009.07.015
48. Shaydakov ME, Sigmon DF BJ. Thromboelastography (TEG). In: StatPearls [Internet] [Internet]. StatPearls Publishing; 2019. Available from: https://www.ncbi.nlm.nih.gov/books/NBK537061/
49. Burton AG, Jandrey KE. Use of Thromboelastography in Clinical Practice. Vet Clin North Am - Small Anim Pract [Internet]. 2020;50(6):1397–409. Available from: https://doi.org/10.1016/j.cvsm.2020.08.001
50. Park MS, Martini WZ, Dubick MA, Salinas J, Butenas S, Kheirabadi BS, et al. Thromboelastography as a better indicator of postinjury hypercoagulable state than prothrombin time or activated partial thromboplastin time. J Trauma. 2009;67(2):266–76.
51. Hunt H, Stanworth S, Curry N, Woolley T, Cooper C, Ukoumunne O, et al. Thromboelastography (TEG) and thromboelastometry (ROTEM) for trauma-induced coagulopathy in adult trauma patients with bleeding. Cochrane Database Syst Rev [Internet]. 2015;(2). Available from: INJ

52. Nair SC, Dargaud Y, Chitlur M, Srivastava A. Tests of global haemostasis and their applications in bleeding disorders. Haemophilia [Internet]. 2010;16(SUPPL. 5):85–92. Available from: http://www.embase.com/search/results?subaction=viewrecord&from=export&id=L359258891%0Ahttp://dx.doi.org/10.1111/j.1365-2516.2010.02304.x
53. Trapaidze A. Integration of thrombin-binding aptamers in point-of-care devices for continuous monitoring of thrombin in plasma. 2015; Available from: https://tel.archives-ouvertes.fr/tel-01174364/document
54. Introduction H. Prothrombin fragment F1 +2. :217–22.
55. Ota S, Wada H, Abe Y. Elevated Levels of Prothrombin Risk of Thrombosis. Clin Appl Thromb. 2008;14(3):279–85.
56. Nossel HL, Yudelman I, Canfield RE, Butler VP, Spanondis K, Wilner GD, et al. Measurement of fibrinopeptide A in human blood. J Clin Invest. 1974;54(1):43–53.
57. Horan JT, Francis CW. Fibrin degradation products, fibrin monomer and soluble fibrin in disseminated intravascular coagulation. Semin Thromb Hemost. 2001;27(6):657–66.
58. Crawley JTB, Zanardelli S, Chion CKNK, Lane DA. The central role of thrombin in hemostasis. J Thromb Haemost. 2007;5(s1):95–101.
59. Zheng R, Cameron BD. Surface plasmon resonance: Recent progress toward the development of portable real-time blood diagnostics. Expert Rev Mol Diagn. 2012;12(1):5–7.
60. Wood RW. On a remarkable case of uneven distribution of light in a diffraction grating spectrum. Proc Phys Soc London. 1902;18(1):269–75.
61. Otto A. Excitation of nonradiative surface plasma waves in silver by the method of frustrated total reflection. Zeitschrift für Phys. 1968;216(4):398–410.
62. Kretschmann E, Raether H. Radiative Decay of Non Radiative Surface Plasmons Excited by Light. Zeitschrift fur Naturforsch - Sect A J Phys Sci. 1968;23(12):2135–6.
63. Nylander C, Liedberg B, Lind T. Gas detection by means of surface plasmon resonance. Sensors and Actuators. 1982;3(C):79–88.
64. Liedberg B, Nylander C, Lunström I. Surface plasmon resonance for gas detection and biosensing. Sensors and actuators. 1983;4:299–304.
65. Liedberg B, Nylander C, Lundström I. Biosensing with surface plasmon resonance - how it all started. Biosens Bioelectron. 1995;10(8).
66. Dostálek, J., Huang, C. J., & Knoll W. Surface plasmon resonance-based biosensors. In: Jenkins ATA, Foersch R, Schoenherr H, editors. Advanced surface design for biomaterial and life science applications. Weinheim: Wiley-VCH; 2009. p. 29–49.
67. Homola J, Yee SS, Gauglitz G. Surface plasmon resonance sensors: review. Sensors Actuators B Chem. 1999;54:3–15.
68. Dostalek J. Encyclopedia of Nanotechnology. Encycl Nanotechnol. 2016;1–11.
69. Kasry A, Dost J, Knoll W. Platform for Biosensors. :2–11.
70. Tokel O, Inci F, Demirci U. Advances in plasmonic technologies for point of care applications. Chem Rev. 2014;114(11):5728–52.
71. Henzie J, Lee J, Lee MH, Hasan W, Odom TW. Nanofabrication of plasmonic structures. Annu Rev Phys Chem. 2009;60:147–65.
72. Sharma N, Keshmiri H, Zhou X, Wong TI, Petri C, Jonas U, et al. Tunable Plasmonic Nanohole Arrays Actuated by a Thermoresponsive Hydrogel Cushion. J Phys Chem C. 2016;120(1):561–8.
73. Tokonami S, Yamamoto Y, Shiigi H, Nagaoka T. Synthesis and bioanalytical applications of specific-shaped metallic nanostructures: A review. Anal Chim Acta [Internet]. 2012;716:76–91. Available from: http://dx.doi.org/10.1016/j.aca.2011.12.025
74. Jain P, Arora D, Bhatla SC. Surface Plasmon Resonance Based Recent Advances in Understanding Plant Development and Related Processes. Biochem Anal Biochem. 2016;05(04).
75. Monolayers S, Brushes P. Self-Assembled Monolayers and Polymer Brushes in Biotechnology: Current Applications and Future Perspectives. 2005;2427–48.
76. Rodriguez-Emmenegger C, Brynda E, Riedel T, Sedlakova Z, Houska M, Alles AB. Interaction of blood plasma with antifouling surfaces. Langmuir. 2009;25(11):6328–33.
77. Vroman L, Adams AL, Fischer G, Munoz P. Interaction of high molecular weight kininogen, factor XII, and fibrinogen in plasma at interfaces. Blood. 1980;55(1):156–9.
78. Andrade JD. Surface and Interfacial Aspects of Biomedical Polymers: Volume 1 Surface Chemistry and Physics. Springer Science & Business Media; 2012.
79. Vaisocherová H, Brynda E, Homola J. Functionalizable low-fouling coatings for label-free biosensing in

complex biological media: advances and applications. Anal Bioanal Chem. 2015;407(14):3927–53.
80. Ostuni E, Chapman RG, Holmlin RE, Takayama S, Whitesides GM. A survey of structure-property relationships of surfaces that resist the adsorption of protein. Langmuir. 2001;17(18):5605–20.
81. Stern E, Vacic A, Rajan NK, Criscione JM, Park J, Bojan R, et al. Label-free biomarker detection from whole blood. Nat Nanotechnol. 2010;5(2):1–11.
82. Naphthalate E. Polymer brushes. 11:114–34.
83. Mateescu A, Wang Y, Dostalek J, Jonas U. Thin hydrogel films for optical biosensor applications. Membranes (Basel). 2012;2(1):49–69.
84. Bhosale R, Gangadharappa HV, Moin A, Gowda DV, Osmani R. Grafting Technique with Special Emphasis on Natural Gums: Applications and Perspectives in Drug Delivery. Nat Prod J. 2015;5(2):124–39.
85. Zhao B, Brittain WJ. Polymer brushes : surface-immobilized macromolecules. 2000;25(February):677–710.
86. Lavanant L, Paripovic D, Schu N, Sugnaux C, Tugulu S, Klok H. <Intiator.Pdf>. 2009;5437–527.
87. Song J, Winkeljann B, Lieleg O. Biopolymer-Based Coatings: Promising Strategies to Improve the Biocompatibility and Functionality of Materials Used in Biomedical Engineering. Adv Mater Interfaces. 2020;7(17).
88. Lee BK, Lee HY, Kim P, Suh KY, Seo JH, Cha HJ, et al. Stepwise self-assembly of a protein nanoarray from a nanoimprinted poly(ethylene glycol) hydrogel. Small. 2008;4(3):342–8.
89. Hahn MS, Taite LJ, Moon JJ, Rowland MC, Ruffino KA, West JL. Photolithographic patterning of polyethylene glycol hydrogels. Biomaterials. 2006;27(12):2519–24.
90. Kobel S, Limacher M, Gobaa S, Laroche T, Lutolf MP. Micropatterning of hydrogels by soft embossing. Langmuir. 2009;25(15):8774–9.
91. Vericat C, Vela ME, Benitez G, Carro P, Salvarezza RC. Self-assembled monolayers of thiols and dithiols on gold: New challenges for a well-known system. Chem Soc Rev. 2010;39(5):1805–34.
92. Benesch J, Svedhem S, Svensson SCT, Valiokas R, Liedberg B, Tengvall P. Protein adsorption to oligo(ethylene glycol) self-assembled monolayers: experiments with fibrinogen, heparinized plasma, and serum. J Biomater Sci Polym Ed. 2001;12(6):581–97.
93. Buenger D, Topuz F, Groll J. Hydrogels in sensing applications. Prog Polym Sci [Internet]. 2012;37(12):1678–719. Available from: http://dx.doi.org/10.1016/j.progpolymsci.2012.09.001
94. White EM, Yatvin J, Grubbs JB, Bilbrey JA, Locklin J. Advances in smart materials: Stimuli-responsive hydrogel thin films. J Polym Sci Part B Polym Phys. 2013;51(14):1084–99.
95. Gibas I, Janik H. Review : Synthetic Polymer Hydrogels for Biomedical. 2010;4(4).
96. Fu LH, Qi C, Ma MG, Wan P. Multifunctional cellulose-based hydrogels for biomedical applications. J Mater Chem B. 2019;7(10):1541–62.
97. Dai S, Ravi P, Tam KC. pH-Responsive polymers: Synthesis, properties and applications. Soft Matter. 2008;4(3):435–49.
98. Augé A, Zhao Y. What determines the volume transition temperature of UCST acrylamide-acrylonitrile hydrogels? RSC Adv. 2016;6(74):70616–23.
99. Yu Q, Bauer JM, Moore JS, Beebe DJ. Responsive biomimetic hydrogel valve for microfluidics. Appl Phys Lett. 2001;78(17):2589–91.
100. Kwon GH, Jeong GS, Park JY, Moon JH, Lee SH. A low-energy-consumption electroactive valveless hydrogel micropump for long-term biomedical applications. Lab Chip. 2011;11(17):2910–5.
101. Lee BP, Konst S. Novel hydrogel actuator inspired by reversible mussel adhesive protein chemistry. Adv Mater. 2014;26(21):3415–9.
102. Li H, Go G, Ko SY, Park JO, Park S. Magnetic actuated pH-responsive hydrogel-based soft micro-robot for targeted drug delivery. Smart Mater Struct [Internet]. 2016;25(2):27001. Available from: http://dx.doi.org/10.1088/0964-1726/25/2/027001
103. Endo T, Ikeda R, Yanagida Y, Hatsuzawa T. Stimuli-responsive hydrogel-silver nanoparticles composite for development of localized surface plasmon resonance-based optical biosensor. Anal Chim Acta. 2008;611(2):205–11.
104. Toma M, Jonas U, Mateescu A, Knoll W, Dostalek J. Active control of SPR by thermoresponsive hydrogels for biosensor applications. J Phys Chem C. 2013;117(22):11705–12.
105. Tavakoli J, Tang Y. Hydrogel based sensors for biomedical applications: An updated review. Polymers (Basel). 2017;9(8):1–25.
106. Ahmed EM. Hydrogel: Preparation, characterization, and applications: A review. J Adv Res [Internet]. 2015;6(2):105–21. Available from: http://dx.doi.org/10.1016/j.jare.2013.07.006
107. Lee YM, Kim SH, Cho CS. Synthesis and swelling characteristics of pH and thermoresponsive

interpenetrating polymer network hydrogel composed of poly(vinyl alcohol) and poly(acrylic acid). J Appl Polym Sci. 1996;62(2):301–11.
108. Brahim S, Narinesingh D, Guiseppi-Elie A. Polypyrrole-hydrogel composites for the construction of clinically important biosensors. Biosens Bioelectron. 2002;17(1–2):53–9.
109. Zhai D, Liu B, Shi Y, Pan L, Wang Y, Li W, et al. Highly sensitive glucose sensor based on pt nanoparticle/polyaniline hydrogel heterostructures. ACS Nano. 2013;7(4):3540–6.
110. Sobkowiak M, Gabrielsson R, Inganäs O, Milczarek G. Amperometric detection of iron (III) on electroconductive hydrogel based on polypyrrole and alkoxysulfonated poly(3,4-ethylenedioxythiophene) (PEDOT-S). Synth Met [Internet]. 2014;194:170–5. Available from: http://dx.doi.org/10.1016/j.synthmet.2014.04.028
111. Jang J, Lee J, Seol YJ, Jeong YH, Cho DW. Improving mechanical properties of alginate hydrogel by reinforcement with ethanol treated polycaprolactone nanofibers. Compos Part B Eng [Internet]. 2013;45(1):1216–21. Available from: http://dx.doi.org/10.1016/j.compositesb.2012.09.059
112. Hu W, Chen S, Li X, Shi S, Shen W, Zhang X, et al. In situ synthesis of silver chloride nanoparticles into bacterial cellulose membranes. Mater Sci Eng C [Internet]. 2009;29(4):1216–9. Available from: http://dx.doi.org/10.1016/j.msec.2008.09.017
113. Oun AA, Rhim JW. Carrageenan-based hydrogels and films: Effect of ZnO and CuO nanoparticles on the physical, mechanical, and antimicrobial properties. Food Hydrocoll [Internet]. 2017;67(June):45–53. Available from: http://dx.doi.org/10.1016/j.foodhyd.2016.12.040
114. Peralta Ramos ML, González JA, Albornoz SG, Pérez CJ, Villanueva ME, Giorgieri SA, et al. Chitin hydrogel reinforced with TiO2 nanoparticles as an arsenic sorbent. Chem Eng J. 2016;285:581–7.
115. Cirillo G, Curcio M, Spizzirri UG, Vittorio O, Tucci P, Picci N, et al. Carbon nanotubes hybrid hydrogels for electrically tunable release of Curcumin. Eur Polym J [Internet]. 2017;90(December 2016):1–12. Available from: http://dx.doi.org/10.1016/j.eurpolymj.2017.03.011
116. Bhattacharyya S, Guillot S, Dabboue H, Tranchant JF, Salvetat JP. Carbon nanotubes as structural nanofibers for hyaluronic acid hydrogel scaffolds. Biomacromolecules. 2008;9(2):505–9.
117. Chen Y, Pötschke P, Pionteck J, Voit B, Qi H. Smart cellulose/graphene composites fabricated by: In situ chemical reduction of graphene oxide for multiple sensing applications. J Mater Chem A. 2018;6(17):7777–85.
118. Zhu, J., Tang, C., Kottke-Marchant, K., & Marchant RE. Design and Synthesis of Biomimetic Hydrogel Scaffolds with Controlled Organization of Cyclic RGD Peptides. Bioconjug Chem. 2009;20(2):333–9.
119. Moon, J. J., Saik, J. E., Poche, R. A., Leslie-Barbick, J. E., Lee, S. H., Smith, A. A., Dickinson, M.E & West JL. Biomimetic hydrogels with pro-angiogenic properties. Biomaterials. 2010;31(14):3840–7.
120. Kouwer PHJ, Koepf M, Le Sage VAA, Jaspers M, Van Buul AM, Eksteen-Akeroyd ZH, et al. Responsive biomimetic networks from polyisocyanopeptide hydrogels. Nature [Internet]. 2013;493(7434):651–5. Available from: http://dx.doi.org/10.1038/nature11839
121. Kim M, Schmitt SK, Choi JW, Krutty JD, Gopalan P. From Self-Assembled Monolayers to Coatings: Advances in the Synthesis and Nanobio Applications of Polymer Brushes. 2015;1346–78.
122. Brittain WJ, Minko S. A structural definition of polymer brushes. J Polym Sci Part A Polym Chem. 2007;45(16):3505–12.
123. Kim W, Jung J. Polymer brush: A promising grafting approach to scaffolds for tissue engineering. BMB Rep. 2016;49(12):655–61.
124. Zhang T-D, Zhang X, Deng X. Applications of protein-resistant polymer and hydrogel coatings on biosensors and biomaterials. Ann Biotechnol. 2019;1(2).
125. Wang Y, Huang CJ, Jonas U, Wei T, Dostalek J, Knoll W. Biosensor based on hydrogel optical waveguide spectroscopy. Biosens Bioelectron. 2010;25(7):1663–8.
126. Ionov L. Hydrogel-based actuators: Possibilities and limitations. Mater Today [Internet]. 2014;17(10):494–503. Available from: http://dx.doi.org/10.1016/j.mattod.2014.07.002
127. Dostalek J, Wang Y, Huang CJ, Knoll W. Evanescent wave biosensors with a hydrogel binding matrix. Handb Biofunctional Surfaces. 2013;360–408.
128. Dostálek J, Knoll W. Plasmonics. In: Polymer Science: A Comprehensive Reference. Amsterdam: Elsevier B.V.; 2012. p. 647–59.
129. Ellington AD, Szostak JW. In vitro selection of RNA molecules that bind specific ligands. Nature. 1990;346(6287):818–22.
130. Tg90 [Internet]. 2004. p. 1–7. Available from: papers2://publication/uuid/EF348D9B-CCD3-4ED1-B6E7-0B7E96F68C4C

131. Murphy MB, Fuller ST, Richardson PM, Doyle SA. An improved method for the in vitro evolution of aptamers and applications in protein detection and purification. Nucleic Acids Res. 2003;31(18):1–8.
132. Ouellet E, Foley JH, Conway EM, Haynes C. Hi-Fi SELEX: A high-fidelity digital-PCR based therapeutic aptamer discovery platform. Biotechnol Bioeng. 2015;112(8):1506–22.
133. Krüger A, Zimbres FM, Kronenberger T, Wrenger C. Molecular modeling applied to nucleic acid-based molecule development. Biomolecules. 2018;8(3):1–17.
134. Meek KN, Rangel AE, Heemstra JM. Enhancing aptamer function and stability via in vitro selection using modified nucleic acids. Methods [Internet]. 2016;106:29–36. Available from: http://dx.doi.org/10.1016/j.ymeth.2016.03.008
135. Renee K. Mosing and Michael T. Bowser. Chapter 3 Isolating Aptamers Using Capillary Electrophoresis–SELEX (CE–SELEX) [Internet]. Available from: www.springer.com/series/7651
136. Reverdatto S, Burz D, Shekhtman A. Peptide Aptamers: Development and Applications. Curr Top Med Chem. 2015;15(12):1082–101.
137. Song S, Wang L, Li J, Fan C, Zhao J. Aptamer-based biosensors. TrAC - Trends Anal Chem. 2008;27(2):108–17.
138. Proske D, Blank M, Buhmann R, Resch A. Aptamers - Basic research, drug development, and clinical applications. Appl Microbiol Biotechnol. 2005;69(4):367–74.
139. Bock, L. C., Griffin, L. C., Latham, J. A., Vermaas, E. H., & Toole JJ. Selection of single-stranded DNA molecules that bind and inhibit human thrombin. Nature. 1992;355(6360):564–6.
140. Tasset DM, Kubik MF, Steiner W. Oligonucleotide inhibitors of human thrombin that bind distinct epitopes. J Mol Biol. 1997;272(5):688–98.
141. Sai TP, Raychaudhuri AK. Adhesion behaviour of self-assembled alkanethiol monolayers on silver at different stages of growth. J Phys D Appl Phys. 2007;40(10):3182–9.

2. RESEARCH GOAL AND THE OUTLINE OF THE THESIS

The general research goal of this study encompasses the development of a plasmonic biosensor device that allows for rapid and sensitive detection of thrombin in human blood and plasma for timing medical diagnostics and tailored treatment. This aim was realized through the following specific tasks:

1. Optimization of the detection assay
2. Fabrication of the plasmonic nanostructures for faster and sensitive detection
3. Testing biocompatible materials for sensor coating
4. Compact reader implementation

Each task was accomplished and described in the published manuscripts that constitute the basis for the "Results" section of this thesis:

1. Kotlarek D, Curti F, Vorobii M, Corradini R, Careri M, Knoll W, Rodriguez-Emmenegger C, Dostalek J, "Surface plasmon resonance-based aptasensor for direct monitoring of thrombin in a minimally processed human blood." *Sensors and Actuators B: Chemical* 320 (2020): 128380
2. Kotlarek D, Fossati S, Venugopalan P, Gisbert Quilis N, Slaby J, Homola J, Lequeux M, Amiard F, Lamy de la Chapelle M, Jonas U and Dostalek J, "Actuated plasmonic nanohole arrays for sensing and optical spectroscopy applications." *Nanoscale* 12.17 (2020): 9756-9768.
3. Kotlarek D, Liu K, Gisbert Quilis N, Bernhagen D, Timmerman P, Kouwer P, Dostalek J, "Thin-Film Polyisocyanide-Based Hydrogels for Affinity Biosensors." *The Journal of Physical Chemistry C* (2021).
4. Kotlarek D, Vorobii M, Ogieglo W, Knoll W, Rodriguez-Emmenegger C, Dostalek J, "Compact grating-coupled biosensor for the analysis of thrombin." *ACS sensors* 4.8 (2019): 2109-2116.

The first subsection, "Optimization of the detection assay" (Publication 1), is devoted to the validation process of aptamer affinities upon their incorporation onto two distinct surface architectures: SAM of alkanethiols and polymer brushes by using SPR setup with a prism coupler in Kretschmann configuration. Further, the aptamers were tested for their activity against the thrombin proenzyme (prothrombin) as it can potentially be a source of a false positive detection signal. Finally, the operation of the sensors based on SAM of alkanethiols and polymer brushes was demonstrated in the biological sample of human blood and compared to the detection of thrombin in the spiked buffer solutions.

The next part, entitled "Fabrication of plasmonic nanostructures for faster and sensitive detection" (Publication 2), focuses on a novel sensor architecture that is based on the metallic nanohole arrays (NHA) combined with a thermo-responsive hydrogel. This work was motivated by the possibility of

sensor miniaturization by using a nanostructured gold layer and a simplified detection system based on the detection of the transmitted light instead of using bulky sensors mounted on the prism coupler. Furthermore, the implementation of the hydrogel layer served for tuning of distinct plasmonic modes and as a sample reservoir.

The following subsection, "Testing biocompatible materials for sensor coating" (Publication 3), is dedicated to the investigation of a new type of hydrogel based on polyisocyanide (PIC). Due to its unique properties like gelation at around room temperature and stress-stiffening featuring by natural polymers, PIC constitutes a new class of biomimetic and fully synthetic polymers with potential applications in the field of sensing. Notably, a complete solubility in water and the temperature-induced gelation of the polymer constitutes much milder conditions for encapsulation of the biorecognition elements in the 3D matrices compared to, e.g., UV-crosslinkable pNIPAAm. In this study, the PIC polymer was implemented for the first time as a sensor coating and affinity binding matrix, and its optical, physiochemical, and anti-fouling properties were tested using the SPR instrument.

Finally, a complete and portable device for detecting thrombin in undiluted human blood plasma is presented in the last part of this chapter, "Compact reader implementation" (Publication 4). The developed detection system draws from the anti-fouling surface architecture based on polymer brushes and a simplified detection system based on grating-coupled SPR. This sensor setup constitutes the first step towards a point-of-care device for thrombin monitoring outside the specialized laboratories.

3. RESULTS

3.1. OPTIMIZATION OF THE DETECTION ASSAY

Surface plasmon resonance-based aptasensor for direct monitoring of thrombin in a minimally processed human blood

Daria Kotlarek[a], Federica Curti[a,b], Mariia Vorobii[c], Wolfgang Knoll[a], Cesar Rodriguez-Emmenegger*[,c], Jakub Dostálek*[,a]

[a] Biosensor Technologies, AIT-Austrian Institute of Technology GmbH, Konrad-Lorenz-Straße 24, 3430 Tulln an der Donau, Austria

[b] Department of Chemistry, Life Sciences and Environmental Sustainability, University of Parma, Parco Area Delle Scienze, 17/A, 43124, Parma, Italy

[c] DWI – Leibniz Institute for Interactive Materials and Institute of Technical and Macromolecular Chemistry, RWTH Aachen University, Forckenbeckstraße 50, 52074 Aachen, Germany

Corresponding Authors

* Jakub Dostalek, PhD, E-mail: jakub.dostalek@ait.ac.at. Phone: +43 (0) 50550 4470, Fax: +43 (0) 50550 4450

* Cesar Rodriguez-Emmenegger, PhD, E-mail: rodriguez@dwi.rwth-aachen.de. Phone: +49 (0) 241 80-23362, Fax: +49 (0) 241 80-23301.

ABSTRACT

Optical affinity biosensors are pursued for timely monitoring of thrombin in human blood, which is of urgent need in tailored anticoagulation therapies. However, the unspecific deposition of molecules, cells, and aggregates from the blood at their surface (also termed fouling) severely hinders their development and impedes the deployment of this technology to everyday clinical practice. We addressed this challenge by designing a surface plasmon resonance (SPR) sensor chip with an antifouling polymer brush architecture and incorporated thrombin aptamer bioreceptors. Poly[(N-(2-hydroxypropyl)-methacrylamide)-co-(carboxybetaine methacrylamide)] brushes were synthesized on gold sensor chip surface via photo-induced single-electron transfer living radical polymerization and postmodified with three thrombin aptamers (HD1 short, HD1, and HD22). The affinity interaction of the aptamer bioreceptors with thrombin (as well as with other molecules present in the blood) was investigated, and changes in performance when incorporated into the polymer brushes were measured.

The combination of brushes and aptamer bioreceptors allowed for the analysis of medically relevant concentrations of thrombin in the 10% blood by direct SPR detection format. This is the first time that the optical affinity biosensor has been demonstrated for label-free analysis of biomarkers in minimally processed human blood without a need for pre-separation steps. We believe that this system constitutes a basis for future affinity biosensor applications suitable for clinical settings and can be readily adapted to detect a range of important biological markers.

Keywords: surface plasmon resonance; polymer brushes; antifouling surface; aptamers; thrombin; whole human blood; point-of-care

HIGHLIGHTS

- Antifouling polymer brushes with incorporated aptamer ligands specific to thrombin
- Changes in the affinity interaction of three established aptamers on thiol SAM and polymer brushes architectures investigated
- Superior antifouling properties of functionalized brushes compared to SAM beneficial for direct label-free surface plasmon resonance detection principle
- Direct rapid detection of thrombin in 10% human blood at clinically relevant concentrations in 15 min

Introduction

Thrombin is an essential enzyme of hemostasis, and it keeps at check bleeding by initiating coagulation in healthy individuals. Its misbalance may lead to hemorrhage or thrombosis - severe conditions that are accompanied by excessive bleeding, pulmonary embolism, stroke, or myocardial infarction [1,2]. Therefore, the concentration of thrombin in the blood is an important marker in clinical practice. It dictates the anticoagulation strategy to be followed for patients subjected to cardiac surgery, extracorporeal membrane oxygenation therapy, and even dialysis. Notably, the lack of means to monitor changes in the concentration of this biomarker directly results in the administration of higher doses of anticoagulants. Although the anticoagulation may later be reversed (if some indirect test shows that the levels of thrombin are too low), this often causes a window of time in which the patient may suffer hemorrhages. New biosensor technologies for rapid analysis of thrombin constitute a promising tool to prevent hemostatic complications, tailor the anticoagulation therapy, and guide the timely decision making in the operating room. However, the unspecific interaction of blood-derived constituents with the surface of affinity biosensors (fouling) hinders the readout of the specific sensor signal and it is arguably the most limiting factor hampering their progress in the clinical applications [3].

The vast majority of reported label-free biosensor concepts with rapid direct detection format were demonstrated for the analysis of target analytes in buffer or diluted blood serum or plasma [4,5]. These results are only a pre-step towards the direct detection in minimally or unprocessed whole blood, which represents the most challenging medium [6]. In order to overcome the problem of sensor fouling, there was implemented pre-separation of blood components by using a two-stage microfluidic platform [7], microfilter [8], continuous-flow diffusion filter [9] or by applying a centrifugal force [10]. In addition, there was pursued research on an alternative strategy to minimize the blocking of sensor surface with blood constituents based on coatings with antifouling properties including self-assembled monolayers (SAMs) with oligo(ethylene glycol) chains (OEG) [11,12], tethered zwitterionic groups [13] and grafting polymer chains forming brushes [14]. OEG-SAMs are formed by tightly packed ordered molecules that carry short OEG headgroups oriented towards the sample. The hydration of OEG moieties provides sufficient repellence from model matrices comprising proteins such as human serum albumin (HSA), fibrinogen, lysozyme, and immunoglobulin G (IgG) that are the most abundant constituents of blood. However, these SAMs fail to resist fouling when they are brought in contact with more complex biological media such as blood plasma and serum [15–17]. Improved resistance to fouling was achieved when the head-group of the SAM comprised zwitterionic groups. For instance, zwitterionic peptides were shown to prevent the unspecific protein adsorption from 2% serum [13] and 1% human whole blood [18]. Such advanced performance is attributed to the ability of zwitterionic groups to structure water, which generates an enthalpic barrier to fouling. This barrier, however, cannot fully prevent adsorption of less diluted blood and undiluted blood plasma when introduced to SAM-based architectures. To date, further increased resistance to fouling has been achieved by several types of hydrophilic polymer brushes. This type of biointerface takes advantage of high-density polymer chains grafted to the sensor surface to prevent fouling by a combination of an enthalpic barrier, strong solvation, and an entropic penalty. The utilization of various hydrophilic polymer brushes has been reported, but among them, only several types fully prevented the fouling from undiluted blood plasma. Currently, the best antifouling performance has been achieved with zwitterionic carboxybetaines [methacrylate [19], acrylamide [20] and methacrylamide (CBMAA) [21]] and *N*-2-hydroxypropyl methacrylamide (HPMA) brushes [22].

Although the described biointerfaces were showed to repel blood plasma proteins, their properties often change when implemented to an affinity biosensor that requires their post-modification with bioreceptors. The chemical procedures employed in the ligation of the bioreceptor to the polymer brushes lead to irreversible changes in their structure and a concomitant loss of their antifouling performance [23]. To circumvent this problem, two antifouling monomers (CBMAA and HPMA) were statistically copolymerized in molar ratio 17:3 in order to provide only a small fraction of the side chains

for the ligation of bioreceptors. This approach resulted in the minimal changes in the chemical structure of the polymer brushes and allowed preserving their antifouling properties. This concept was implemented in several surface plasmon resonance (SPR) – based sensors for the analysis of biological samples using the protein bioreceptors such as hepatitis B surface antigen-HBsAg or anti-fetuin-A IgY antibody [24–26].

In our recent work [27], we presented a compact SPR sensor device based on a gold-coated grating that was modified by poly(HPMA-*co*-CBMAA) brushes with HD1 aptamer and used for detection of thrombin in undiluted human plasma. In this approach, the optical probing is utilized through the analyzed sample, which is not suitable for the analysis of blood samples with large constituents that absorb and scatter light. Herein, we therefore further extended this work for the analysis of 10% human blood and investigate options to improve the performance of the sensor by using different thrombin DNA aptamer sequences that recognize two distinct binding sites of thrombin (exosite I and II). The DNA aptamers constitute an attractive alternative to the protein recognition elements as they can be engineered in a test tube and mass-produced by chemical synthesis [28]. In addition, aptamers exhibit better storage stability, and often their interaction with target molecules is reversible allowing for a facile regeneration of the sensor surface [29]. The HD1 short, HD1 and HD22 aptamers were incorporated in poly(HPMA-*co*-CBMAA) brushes on a surface of SPR sensor with Kretschmann configuration of attenuated total reflection method, where the optical probing is performed from the opposite side to the analyzed sample. The importance of biointerface engineering and cross-reactivity of the used aptamers with abundant proteins present in the blood (HSA, IgG, and prothrombin) is demonstrated in order to enable rapid analysis of minimally processed blood samples. Such biointerface was tailored for label-free and rapid detection of thrombin at clinically relevant concentrations in human blood samples diluted to 10%. According to our knowledge, this is the first label-free affinity biosensor that can be operated in such a manner.

Materials and methods

Materials and reagents

Thrombin aptamers were custom synthesized by Integrated D NA Technologies (Belgium). There were used two variants of each aptamer, either with amine or with biotin terminal group (HD1 short: amino modifier C6 5'-TTT TTG GTT GG-3', M_W = 3.6 kDa; biotin 5'-TTT TTT TTT TGG TTG G-3', M_W = 5.3 kDa; HD1: amino modifier C6 5'-TTT TTG GTT GGT GTG GTT GG-3', M_W = 6.5 kDa; biotin 5'-TTT TTT TTT TGG TTG GTG TGG TTG G-3', M_W = 8.2 kDa; scrambled biotin 5'-TTT TTT TTT TGG TGG TGG TTG TGG T-3' M_W = 8.2 kDa; HD22: amino modifier C6 5'-TTT TTA GTC CGT GGT AGG GCA GGT TGG GGT GAC T-3', M_W = 10.9 kDa; biotin 5'-TTT TTT TTT TAG TCC GTG GTA GGG CAG GTT GGG GTG ACT-3', M_W = 12.5 kDa).

Thrombin purified from human plasma (M_W = 37 kDa) was obtained from Enzo Life Sciences (Switzerland). Human Prothrombin Native Protein (M_W = 72 kDa) and Human Immunoglobulin G (M_W = 150 kDa) were purchased from Thermo Scientific (Germany). The single donor whole human blood was obtained from Innovative Research (USA). Biotinylated alkane OEG-thiol (thiol-OEG-biotin, SPT-0012D) and (11-mercaptoundecyl) triethyleneglycol (thiol-OEG-OH, SPT-0011) were purchased from SensoPath Technologies Inc. (USA). 1-Ethyl-3-(3-dimethylaminopropyl)-carbodiimide (EDC), *N*-hydroxysuccinimide (NHS) and neutravidin protein were purchased from Thermo Scientific (Austria). Acetic acid, sodium acetate, sodium chloride, HEPES, Tween 20, argatroban monohydrate (M_W = 526.65 g/mol), Human Serum Albumin (HSA, M_W = 6.6 kDa) and Hellmanex III were purchased from Sigma-Aldrich (Austria). Phosphate buffer saline tablets (PBS: 140 mM NaCl, 10 mM phosphate, 3 mM KCl, pH 7.4) came from Calbiochem (Germany). All buffer solutions were prepared by using ultrapure water (arium pro, Sartorius Stedim, Germany). PBS Tween (PBST) was prepared by adding Tween 20 (0.05%) to PBS solution. 10 mM sodium acetate buffer (SA, pH 5) was prepared from acetic acid and sodium acetate. The HEPES buffer was used with the pH adjusted by NaOH (pH 7.5). Extra dry dimethyl sulfoxide (DMSO, 99.7+%) was acquired from Acros Organic (Germany). Tris[2-(dimethylamino)ethyl]amine (Me_6TREN, 99+%) were obtained from Alfa Aesar (Germany). Copper (II) bromide ($CuBr_2$, 99.999% trace metal basis) was purchased from Sigma Aldrich (Germany). Initiator, ω-mercaptoundecyl bromoisobutyrate [30], and monomer, *N*-(2-hydroxypropyl) methacrylamide (HPMA) [31], were synthesized according to the procedures published before. Monomer, (3-methacryloylaminopropyl)-(2-carboxyethyl)-dimethylammonium (carboxybetaine methacrylamide, CBMAA), was synthesized using a modified version of the procedure reported earlier [16], Ethanol (EtOH) came from VWR Chemicals (Germany). Milli-Q water was obtained using an Elga US filter Purelab Plus UF purification system (PL5113 02) (UK).

Preparation of SPR sensor chips

BK7 glass substrates (Carl Roth, Austria) and LASFN9 glass substrates (Hellma GmbH, Germany) were cleaned by subsequent sonication in a 1% aqueous solution of Hellmanex III, in ultrapure water and in ethanol. Then, chromium (2 nm thickness) and gold (50 nm thickness) layers were deposited on their top by vacuum thermal evaporation (HHV AUTO 306 from HHV LTD, UK) in vacuum better than 10^{-6} mBar. In addition, commercial SPR sensor chips already coated with thin gold film (XanTec bioanalytics GmbH, Germany) were used. For the experiments with thiol SAM biointerface, the BK7 glass and XanTec SPR sensor chips were overnight immersed in 1 mM ethanolic solution of thiol-OEG-biotin and thiol-OEG-OH (molar ratio 1:4) in order to form mixed SAM. The LASFN9 glass substrates coated with gold were used for the experiments with polymer brushes. The polymer brushes of poly(HPMA-*co*-CBMAA) were synthesized by photo-induced single-electron transfer living radical polymerization (SET-

LRP). For the formation of SAM of initiator, gold-coated LASFN9 glass substrates were immersed overnight in 2.4 mM ethanolic solution of *ω*-mercaptoundecyl bromoisobutyrate. For the polymerization, 5.99 g (41.89 mmol) of HPMA and 1.79 g (7.39 mmol) of CBMAA were dissolved in 28 mL of dry DMSO. Simultaneously, a stock solution of the catalyst was prepared by dissolving 8.7 mg (39 µmol) of $CuBr_2$ and 62.5 µL (233.8 µmol) of Me_6TREN in 10 mL of dry DMSO. Both flasks were kept in the dark by wrapping them with aluminum foil. After the complete dissolution of all components, 1.2 mL of stock catalyst solution was mixed with dissolved monomers and degassed by bubbling N_2 for 1 h. Subsequently, polymerization solution was transferred to previously degassed (purging with N_2 for 30 min) vials containing gold-coated LASFN9 glass substrates with SAM of the initiator. The polymerization was conducted for 17 min by irradiating the vials inside a UV-reactor, consisting of a nail-curing device (four 9 W lamps, λ_{max} = 65 nm) kept at room temperature by fanning with a ventilator. After polymerization, the reaction was stopped by exposing a reaction mixture to air and adding DMSO. The samples were removed from the reactor and washed twice with EtOH and Milli-Q water and dried by blowing with N_2.

SPR biosensor instruments

Two SPR sensor instruments that rely on the Kretschmann configuration of the attenuated total reflection method with angular interrogation were used in the presented work. The affinity interaction analysis was performed by using a Reichert SR7000DC system with an integrated SR7120 autosampler instrument. XanTec sensor chips were used in this instrument and surface plasmons were resonantly excited at a wavelength of 780 nm. As this instrument was not suitable for the studies on sensor chips with the polymer brushes (the increased refractive index of the brushes shifted the SPR out of the measurable range), additional in-house developed SPR spectrometer that utilizes same type angular spectroscopy of surface plasmons was employed. The SPR sensor chip carrying either the mixed thiol-OEG/biotin SAM or poly(HPMA-*co*-CBMAA) brushes was optically matched to the LASFN9 glass prism by using a refractive index matching oil (Cargille Inc., USA) and mounted on a rotation stage to control the angle of incidence ϑ. The beam from HeNe laser at a wavelength of 633 nm that was coupled to the 90° LASFN9 glass prism in order to resonantly excite surface plasmons (Figure 1a). The intensity of the reflected beam was measured as a function of angle of incidence $R(\vartheta)$ or time $R(t)$ at an angle ϑ that was fixed close to the SPR dip [on the resonance edge with the highest slope in $R(\vartheta)$]. The instrument was controlled by dedicated software (Wasplas, Max Planck Institute for Polymer Research, Mainz, Germany). A flow-cell with a 5 µL reaction chamber made from a thin PDMS gasket (thickness of 100 µm from Specialty Silicone Products, Inc., USA, cut by Institute of Photonics and Electronics, Czech Academy of Sciences) was clamped against the SPR chip surface. Analyzed liquid samples were flowed by using a

Tygon tubing and a peristaltic pump (Ismatec, Germany) with a flow rate of 50 mL min^{-1}. In order to compare the SPR sensor signal from the two SPR instruments, the response *R* was converted to refractive index units (RIU) by a calibration step with the bulk refractive index changes upon the flow of aqueous solutions spiked with 1, 2 and 4 wt% of sucrose (inducing bulk refractive index increase of Δn_s = 1.4 × 10^{-3}; 2.8 × 10^{-3}; 5.6 × 10^{-3} RIU, respectively).

Immobilization of the thrombin aptamer

The immobilization of thrombin aptamers was performed *in situ* on the SPR sensor chips that were previously modified with either mixed thiol-OEG/biotin SAM or poly(HPMA-*co*-CBMAA) brushes. The SPR sensor chip carrying the mixed thiol SAM was firstly rinsed with PBS buffer (pH 7.4) for 5 min in order to establish a baseline in the SPR signal *R*(*t*). Then 50 μg·mL^{-1} neutravidin dissolved in PBS was flowed over the surface for 90 min in order to conjugate to the biotin moieties tethered at the sensor surface. The excess of neutravidin was rinsed off by using PBS for 5 min and finally, 1 μM solution of biotinylated aptamer (HD1 short, HD1 or HD22) in PBS was reacted with the sensor surface for 15 min and then washed with PBS for 5 min. The immobilization of aptamers on the poly(HPMA-*co*-CBMAA) brushes was carried out by amine coupling. The baseline in the SPR signal *R*(*t*) was established upon the 5 min flow of PBS (pH 7.4) that was then replaced with SA buffer for 5 min (pH 5.0). Subsequently, the carboxylic moieties of the betaine monomer in the poly(HPMA-*co*-CBMAA) brushes were activated by a freshly prepared aqueous solution of EDC (0.4 M) and NHS (0.1 M) for 10 min. The activated polymer film was shortly rinsed with SA (pH 5.0) and HEPES buffer (pH 7.5) and then 1 μM solution of aptamer (HD1 short, HD1 or HD22) with the amine terminal group was flowed over the surface for 30 min in order to form covalent bonds with the chains of polymer brushes. Subsequently, the unbound aptamers were rinsed off with HEPES (pH 7.5) and the functionalized sensor surface was incubated in PBS for 90 min in order to let the unreacted active ester groups hydrolyze.

Assay for interaction analysis and detection in buffer and blood samples

The SPR sensor chips functionalized with aptamer bioreceptors were used for the affinity capture of thrombin from either PBS or whole human blood diluted to 10% with PBS. The same protocol was adopted for the interaction study of aptamers with other proteins that may interfere with the thrombin binding including HSA, IgG, and prothrombin. Since the addition of exogenous thrombin to the whole blood containing fibrinogen would trigger its coagulation, we supplemented the analyzed samples with the anticoagulant argatroban (38 μM concentration). Firstly, the baseline in the SPR sensor signal *R*(*t*) was established upon the flow of PBS(T) for 5 min. Then, the analyzed sample spiked with investigated biomolecules was flowed over the surface and the reaction time was set to 30-60 min (in affinity

interaction study) or to 15 min (in rapid detection experiment). The sensor surface was afterward rinsed with PBS(T) for 30 min (in affinity interaction study) or 5 min (in rapid detection experiment) and subsequently regenerated with an aqueous solution of 2 M NaCl for 2 min followed by the rinsing with PBS(T). The control experiment was performed analogously on the non-functionalized surface or on the surface with anchored aptamers exhibiting scrambled sequence.

Calculation of surface mass density

A model was established in order to determine surface mass density Γ of covalently immobilized aptamers and affinity captured thrombin from measured changes in SPR signal $R(t)$ acquired in RIU for sensor chips with mixed thiol-OEG/biotin SAM and polymer brushes architectures. The surface mass density was calculated by using the formula $\Gamma = (n_p - n_s) \cdot d_p / (\partial n / \partial c)$, [32] where n_p and n_s are the refractive indices of oligonucleotide/protein layer and an aqueous sample, respectively, and d_p corresponds to the thickness of the oligonucleotide/protein layer. The factor $\partial n / \partial c$ = 0.2 mm^3 mg^{-1} relates the changes in refractive index and concentration of biomolecules bound to the surface [33]. As the probing surface plasmon field (that evanescently decay from the gold surface) responds differently to molecular binding occurring at a short distance of 3 nm (for thiol SAM) and long distance of 42 nm (for polymer brushes), the used respective converting factors $\Gamma / \delta R$ are different. Further, we used the factors of $\Gamma/\delta R$= 510 ng mm^{-2} RIU^{-1} for SAM and $\Gamma/\delta R$ = 450 ng mm^{-2} RIU^{-1} for polymer brushes interface. These factors where obtained for the probing SPR wavelength of 633 nm from Fresnel reflectivity-based simulations implemented in Winspall software (Max Planck Institute for Polymer Research, Germany) as described in the supporting information.

Evaluation of SPR binding kinetics

The association binding rate k_{on} and dissociation binding rate k_{off} describing the interaction between thrombin in a liquid sample and aptamers immobilized on mixed thiol-OEG/biotin SAM were obtained by the analysis of measured SPR sensorgrams. Thrombin was dissolved in PBS at a concentration of c = 5, 10, 15, 20, 35, 50, 100 and 500 nM and these samples were sequentially flowed over the sensor surface that was functionalized with HD1 short (60 min reaction time), HD1 (30 min reaction time), and HD22 (30 min reaction time) in order to affinity bind and followed by 30 min rinsing with the PBS to dissociate from the surface. In between the analysis of samples with different thrombin concentrations, the sensor chip was regenerated with 2 M NaCl. The sensorgrams $R(t)$ acquired by using the XanTec SPR chip and Reichert SPR instrument were fitted with a 1:1 binding model that was implemented in Prism 8 (GraphPad Software) and by a model taking into account diffusion-limited kinetics in Scrubber 2 (BioLogic Software). For details of the fitting model, the reader is referred to the SI.

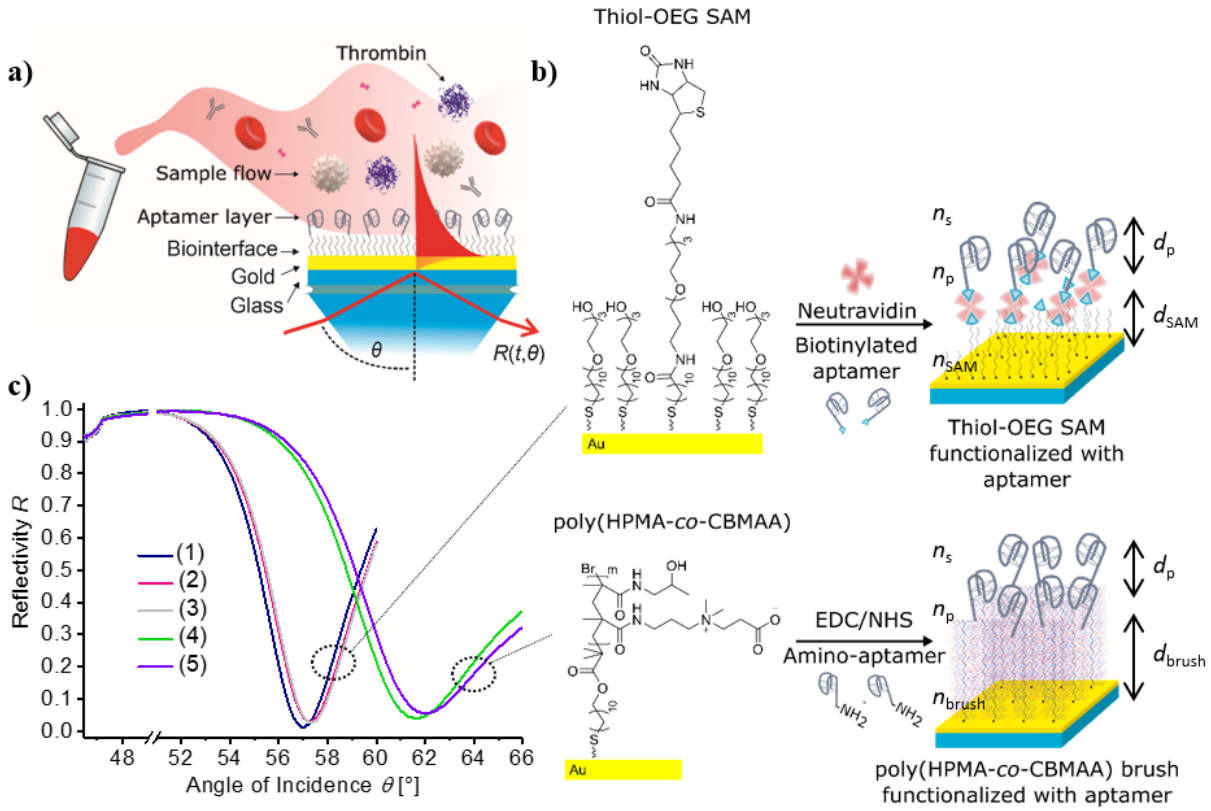

Figure 1. a) The schematic of the SPR sensor chip that is modified with b) thiol-OEG SAM or poly(HPMA-*co*-CBMAA) architecture in order to couple thrombin aptamer at its surface. c) Angular reflectivity SPR spectra acquired at the wavelength of 633 nm on SPR sensor chip carrying (1) thiol-OEG SAM, (2) thiol-OEG SAM with neutravidin, (3) thiol-OEG SAM with neutravidin and immobilized aptamer HD22 compared to that measured on (4) pristine polymer brushes and (5) polymer brushes functionalized with aptamer HD22.

Results and discussion

Immobilization of thrombin aptamers

In order to enable direct detection of thrombin in minimally processed whole blood, there was pursued a biointerface architecture based on poly(HPMA-*co*-CBMAA) brushes that specifically bind target thrombin analyte from the analyzed sample at the sensor surface by the use of aptamer bioreceptors, see Figure 1a. In order to benchmark the performance of this biointerface, additional regular mixed thiol SAM modification with OEG-OH and OEG-biotin headgroups [32] was used. As Figure 1b illustrates, we investigated these sensing surfaces in conjunction with three thrombin aptamer bioreceptors – HD1 short, HD1 and HD22 – that were anchored at the sensor surface by using amine coupling on poly(HPMA-*co*-CBMAA) brushes via a biotin tag for mixed thiol-OEG/biotin SAM interface.

The immobilization procedure was monitored by SPR and both reflectivity curves $R(\vartheta)$ before and after the bioreceptor immobilization and the SPR signal kinetics $R(t)$ upon the surface reaction were acquired. The example presented in Figure 1c shows that resonant excitation of surface plasmons on mixed thiol-

OEG/biotin SAM surface with incorporated biotin moieties manifests itself as a dip in $R(\vartheta)$ centered at an angle of incidence of ϑ = 57.00° (1). The SPR angle changes to ϑ = 57.28° (2) after the conjugation of neutravidin with the biotin headgroups on thiol SAM and it further shifts to ϑ = 57.33° when the immobilization of the biotinylated aptamer HD22 is carried out (3). For the SPR chip carrying the pristine poly(HPMA-*co*-CBMAA) brushes, the SPR occurs at a higher angle of ϑ = 61.60° (4) because of the increased thickness of the polymer brush layer (d_{brush}~42.0 nm measured by ellipsometry, SI, Figure S1) in comparison to the SAM architecture (~ 3.0 nm, SensoPath manufacturer catalog). The covalent coupling of the amine-terminated aptamer HD22 to carboxylic groups present at the chains of polymer brushes leads to the additional shift of SPR angle to ϑ = 62.00° (5).

SPR sensor kinetics $R(t)$ were recorded upon the immobilization of aptamer bioreceptors on the poly(HPMA-*co*-CBMAA) brushes and mixed thiol-OEG/biotin SAM. The sensor response ΔR in RIU was acquired for all three aptamers from the respective kinetics of SPR sensor signal $R(t)$ and it was subsequently converted to changes in surface mass density Γ and surface density (by dividing these values with a respective molecular weight of biomolecules - MW) as can be seen in the overview presented in Table 1. The SPR sensor response of ΔR = 137, ΔR = 317, ΔR = 549 µRIU was measured for the coupling of HD1 short, HD1 and HD22 aptamers, respectively, on the mixed thiol-OEG/biotin SAM architecture. These data were obtained from the kinetics presented in Figure S3a and they stand in a good agreement with the previously reported values [34,35]. The SPR sensor response was 8 - 11 times higher on the poly(HPMA-*co*-CBMAA) brushes yielding ΔR = 1536, ΔR = 2409 and ΔR = 4361 µRIU for HD1 short, HD1, and HD22 aptamers, respectively, as determined from data in Figure S3b. These results translate to a surface density of Γ/MW=0.013 pmol mm^{-2}, 0.020 pmol mm^{-2} and 0.022 pmol mm^{-2} for HD1 short, HD1 and HD22 respectively, on the mixed thiol-OEG/biotin SAM surface. Interestingly, the density ratio of the aptamer to the tetrafunctional neutravidin (which served as a linker between the biotin groups in the SAM and aptamer biotin terminal group) was in all cases close to one. This confirms that the density of these bioreceptors was controlled by the density of immobilized neutravidin linker (Γ = 0.019 pmol mm^{-2} determined from measured SPR sensor response of ΔR = 2289 µRIU).

The immobilization of aptamers on poly(HPMA-*co*-CBMAA) brush biointerface allowed to reach a substantially higher surface density of Γ/MW=0.194 pmol mm^{-2}, 0.168 pmol mm^{-2} and 0.182 pmol mm^{-2} for HD1 short, HD1 and HD22 respectively. This is the result of the organization of chains in the brushes at the interface which is less rigid than in SAMs allowing access not only to the last monomer units but to others in the last thermal blob. Furthermore, while in SAMs the immobilization of the aptamer required a very bulky neutravidin, in brushes the immobilization was direct which enhances further the binding sites available. Importantly, the chemical design of the selected brushes can provide efficient means to compensate for the negative charge introduced by the aptamer immobilization (which often

leads to undesired unspecific interactions). The balance between the carboxylate groups and the quaternary ammonium from the betaine monomer guarantees the initial neutral zeta potential of the polymer brush structure. Upon the activation, with the carbodiimide crosslinking agent the carboxylate groups are turned to the active esters that lead to establishing of weakly positive zeta potential. This results in the electrostatic attraction of the negatively charged aptamer molecules that is reflected in the rapid kinetics within the first 3 min of the reaction (see Figure S3b). The gradual incorporation of the aptamers introduces to the polymer brushes negative charge that slows down the reaction by Coulombic interaction. Moreover, the slower part of the reaction kinetics occurring after 3 min can be attributed to the immobilization of the aptamers deeper in the poly(HPMA-*co*- CBMAA) brush structure, which is affected by the hindered molecular diffusion in the crowded polymer brushes structure.

Table 1. Comparison of the surface mass density (middle columns) and respective surface density *Γ*/*MW* (right columns) of immobilized aptamers on thiol-OEG SAM and polymer brushes (upper part) and surface density of thrombin that is affinity captured in saturation at these biointerfaces (bottom part).

	Thiol-PEG SAM	Polymer brushes	Thiol-PEG SAM	Polymer brushes	Thiol-PEG SAM	Polymer brushes
Aptamer	**μRIU**		**pg/mm²**		**pmol/mm²**	
HD 1 short	137 ± 19	1536 ± 240	70 ± 10	691 ± 108	0.013 ± 0.002	0.194 ± 0.030
HD1	317 ± 23	2409 ± 603	162 ± 12	1083 ± 271	0.020 ± 0.001	0.168 ± 0.042
HD22	549 ± 19	4361 ± 750	280 ± 10	1960 ± 337	0.022 ± 0.001	0.182 ± 0.031
Thrombin	**μRIU**		**pg/mm²**		**pmol/mm²**	
HD 1 short	208 ± 3	-	106 ± 2	-	0.003 ± 0.001	-
HD1	510 ± 74	1393 ± 44	260 ± 38	626 ± 20	0.007 ± 0.001	0.017 ± 0.001
HD22	374 ± 25	662 ± 329	191 ±13	298 ± 148	0.005 ± 0.001	0.008 ± 0.004

Thrombin-aptamer affinity interaction analysis

The characteristics of affinity interaction between thrombin and the aptamers HD1 short, HD1, and H22 were determined by the use of SPR for mixed thiol-OEG/biotin SAM. For this purpose, PBS was spiked with a concentration of thrombin of *c*=5, 10, 15, 20, 35, 50, 100 and 500 nM and flowed sequentially over the sensor surface with a regeneration step applied between each cycle. The measured SPR signal *R*(*t*) for the association and dissociation phases was fitted with a kinetic model as can be seen in Figure 2. This model assumed the 1:1 interaction between the analyte and the ligand and simultaneous fitting of measured curves for all concentrations was performed using non-linear regression. For the truncated version of HD1 aptamer (HD1 short), the obtained association rate of $k_{on} = 1.7 \cdot 10^6\,M^{-1}s^{-1}$ and dissociation rate $k_{off} = 21 \cdot 10^{-3}\,s^{-1}$ (according to our knowledge measured for the first time) yields an

equilibrium dissociation constant of K_d = 12 nM. The interaction of longer HD1 and HD22 aptamers exhibited higher affinity and therefore an additional mass transfer coefficient k_m had to be introduced to the fitting. However, the association and dissociation binding rates for HD1 aptamer were not possible to accurately determine from the acquired data, and only equilibrium dissociation constant of K_d <5 nM could be estimated for HD1 and HD22 aptamers (see the summary in Figure 2a). In comparison with literature, the herein reported values of equilibrium dissociation constant K_d are in the lower range of reported values. It is worth noting these values vary over a wide range from 1.19 nM [36] to 171 nM [37] for HD1 aptamer and from 2.4 nM [38] to 110 nM [37] for HD22.

a)

K_d [nM]	Thrombin	Prothrombin
HD 1 short	12	-
HD1	<5	39±9
HD22	<5	>1000

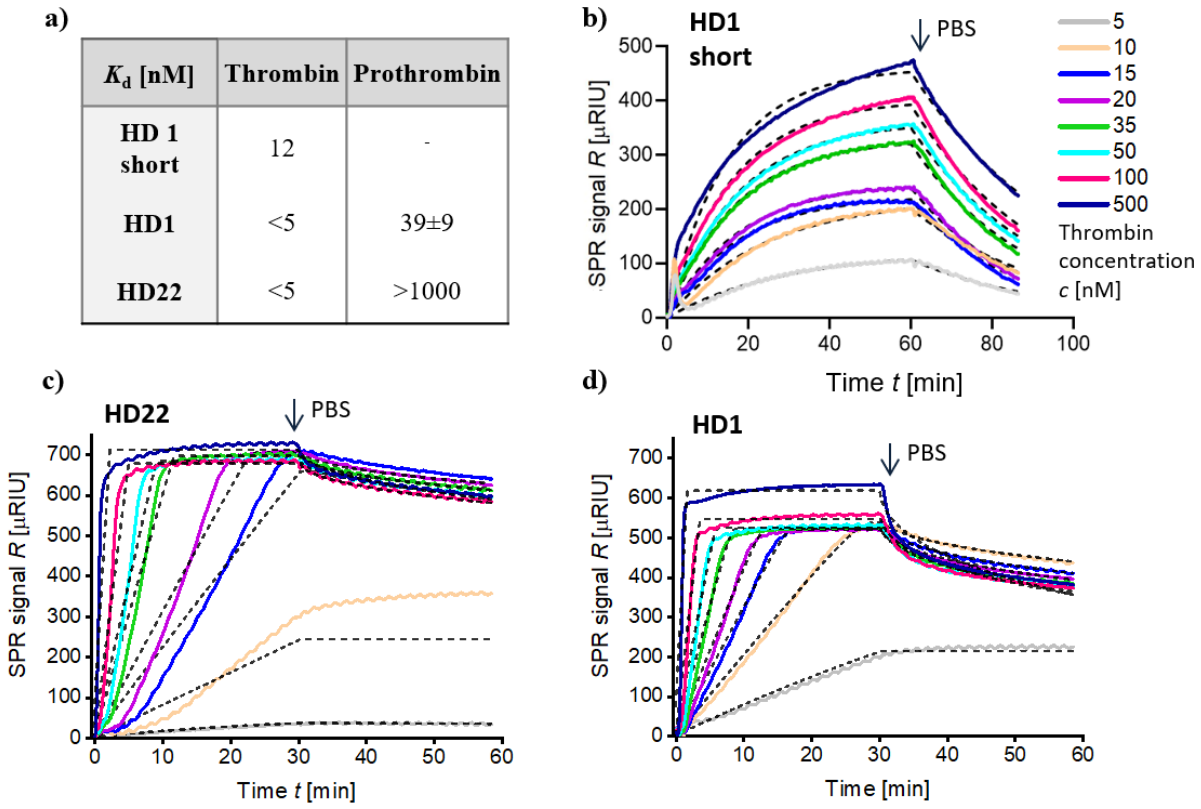

Figure 2. Global analysis measurement affinity binding rates of thrombin with three aptamer ligands. a) The table summarizes the determined equilibrium dissociation affinity constants and the graphs show the SPR sensorgrams for the interaction of analyte concentration c=5; 10; 15; 20; 35; 50; 100 and 500 nM on the sensor surface with thiol-OEG SAM functionalized with b) HD1 short, c) HD22 and d) HD1 aptamers. The solid lines present experimental data and dashed lines show the fitted curves. The arrows indicate the end of the association phase and the beginning of the dissociation phase.

Specificity of thrombin-aptamer affinity interaction

In order to verify the specificity of the used aptamers HD1 and HD22, their interaction with abundant biomolecules that constitutes human blood was observed with SPR. These include human serum albumin (HSA), human immunoglobulin G (hIgG), and prothrombin. In the blood of healthy donors, HSA

is present at about 500 µM concentration, hIgG at 80 µM and prothrombin at 1.4 µM [39]. It is worth noting that prothrombin is structurally related to thrombin and HD1 aptamer recognizes the thrombin exosite I and II, while HD22 aptamer affinity binds solely to exosite II [36]. SPR affinity interaction study showed that HD1 also binds to prothrombin with the equilibrium dissociation constant of K_d=37 nM, while HD22 did not interact with this prothrombin (aptamers were attached via biotin tag to dextran polymer chains anchored to the gold surface) [36].

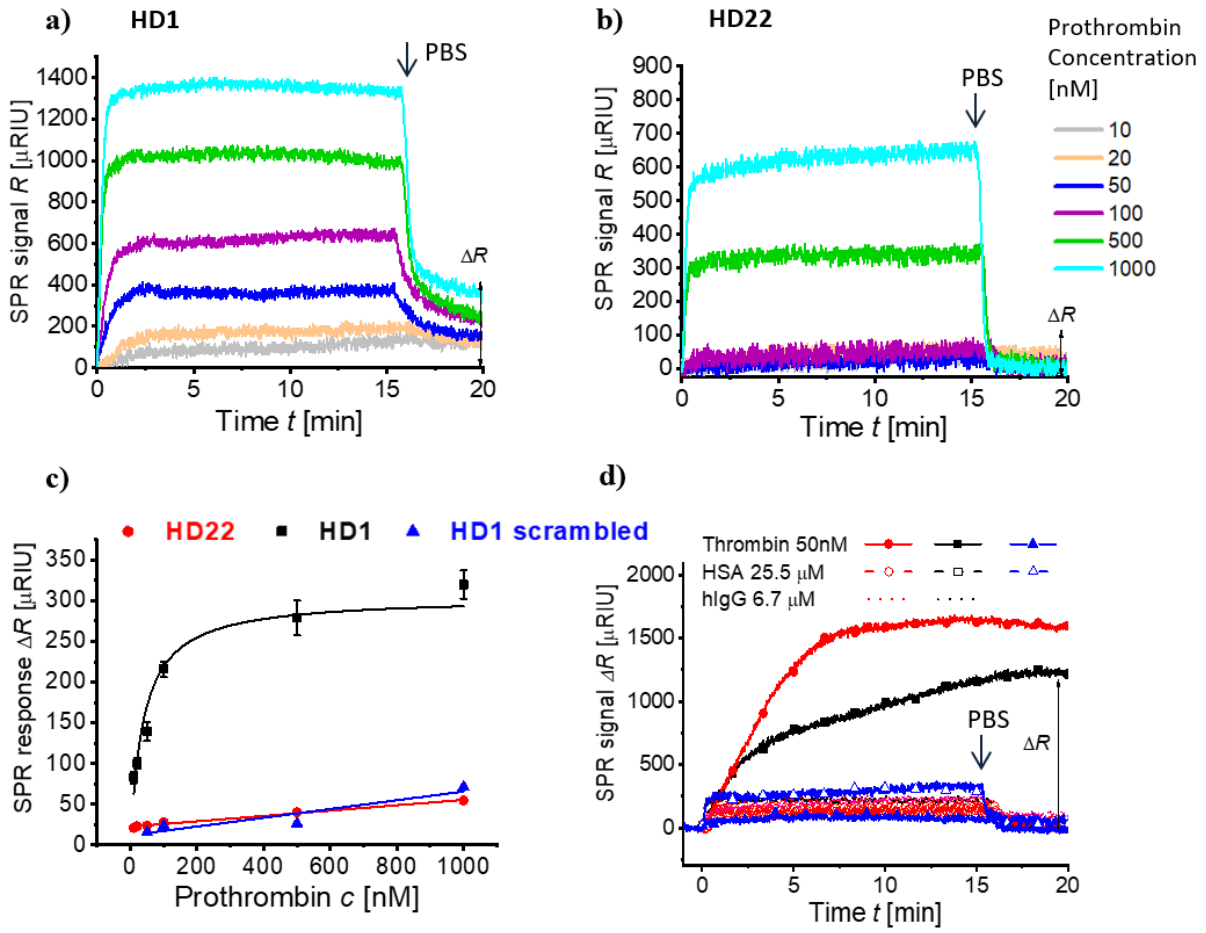

Figure.3 Specificity binding measurements of prothrombin, HSA and hIgG. The graphs show the SPR sensorgrams for the interaction with prothrombin at a concentration of *c*=10, 20, 50, 100, 500 and 1000 nM on the sensor surface with thiol-OEG SAM functionalized with a) HD1 and b) HD22 aptamers. c) The respective calibration curves are established. d) The interaction of HSA at 25.5 µM and hIgG at *c*=6.7 µM.

Further, we investigated potential interference of thrombin direct assay with HD1 and HD22 aptamers through the affinity binding to HSA, hIgG, and prothrombin and thiol-OEG-OH/biotin SAM was employed. The SPR kinetics data presented in Fig. 3a and Fig. 3b reveals measurable affinity interaction of prothrombin with HD1 aptamer and no specific interaction for HD22 aptamer at prothrombin concentrations below 100 nM, respectively. The SPR signal change Δ*R* measured after 5 min rinsing of

the surface that was exposed to prothrombin samples are plotted in Fig.3c. For the aptamer HD1, the plot is fitted with the Langmuir isotherm curve (as the association phase reached equilibrium) and the affinity dissociation constant of K_d = 39 ± 9 nM was determined. The dependence of ΔR on the surface of HD22 aptamer could be fitted with linear function and indicates that the respective K_d is above the used concentration rate. Moreover, a similar trend was observed for scrambled HD1 aptamer sequence which suggests that the small response may originate from unspecific sorption to the used thiol-OEG-OH/biotin SAM. In Fig.3d, there can be found the interaction of HD1 and HD22 with HSA and hIgG compared to that with thrombin. These findings show a negligible response for HSA at a concentration of 25.5 μM and hIgG at 6.7 μM. For the HSA, the same experiment was performed on the surface with a scrambled sequence of HD1 aptamer and a similar response suggests that the measured negligible change in SPR signal is attributed to unspecific sorption to the used thiol SAM-based biointerface.

Rapid detection of thrombin in buffer and blood samples

Sensor chips with poly(HPMA-*co*-CBMAA) brushes and mixed thiol-OEG/biotin SAM surface architectures were postmodified with the aptamers and their ability to specifically capture thrombin from 10 % diluted whole blood and resist fouling was evaluated with direct SPR detection format. As can be seen in the acquired SPR kinetics data presented in Figure 4, the injection of 10 % blood sample (with the endogenous thrombin present below pM concentration for healthy donors [40] into the sensor is accompanied by a rapid increase in the SPR signal $R(t)$ on both types of surfaces, which can be attributed to a change in bulk refractive index n_s. On the surface with the polymer brushes, this SPR signal change is less pronounced as the surface plasmon evanescent field exponentially decays with the distance from the gold surface. Compared to a thinner layer of mixed thiol SAM of 3 nm (according to the provider of thiol-OEG-biotin), the hydrated brushes occupy up to 42 nm (as measured with ellipsometry, see Figure S1) to which the penetration of blood constituents is hindered. After 2.5 minutes, a slower gradual increase in the SPR signal $R(t)$ occurs due to the sorption of blood compounds to the surface. The 10% blood was flowed over the surface for 15 min and then the sensor surface was rinsed with PBS and the SPR signal $R(t)$ rapidly drops as the bulk refractive index n_s decreases. After an additional 5 min rinsing the SPR signal levels at a value that is higher than the original baseline by ΔR_0 = 1.60 and 2.1 mRIU on the brushes and 1.85 and 2.7 mRIU on the thiol-OEG SAM carrying HD22 and HD1 aptamers, respectively. This change is attributed to the unspecifically adsorbed molecules and cross-reaction of aptamers with abundant constituents in blood. The more pronounced response to this blank sample for the HD1-modified biointerface compared to that carrying HD22 aptamer can be attributed to HD1 affinity to prothrombin. Importantly, these molecules can be fully removed from the surface of the poly(HPMA-*co*-CBMAA) brushes by the regeneration step while on the mixed thiol-

OEG/biotin SAM only 80% of the adsorbed mass density Γ was released. This observation can be explained by electrostatic interaction of blood components with negatively charged aptamers and affinity binding of prothrombin being the main origin of the binding on the surface of polymer brushes. Both these interactions can be disrupted by using a high concentration of Na^+ ions that shield the negative charge of the aptamers [41]. In the case of functionalized mixed thiol-OEG/biotin SAM, there is a coexisting effect of irreversible protein adsorption (fouling) that cannot be prevented in the performed experiments.

In the subsequent second detection cycle, a 10 % diluted blood sample was spiked with thrombin at a concentration of 20 nM and allowed to interact with the investigated biointerface architectures by using the same protocol. Measured SPR signal kinetics presented in Figure 4 shows that the slope of the gradual increase of the SPR signal $R(t)$ is substantially steeper on the poly(HPMA-*co*-CBMAA) brushes and it levels at a higher value of ΔR = 2.3 and 3.8 mRIU after the rinsing of the surface with immobilized aptamer HD22 and HD1, respectively. Importantly, on the thiol-OEG SAM, the SPR signal change does not substantially differ from that measured for a blank sample proving that this interface becomes blocked by the blood constituents and that it cannot be used for direct SPR analysis of such complex biofluid. Interestingly, HD1 short aptamer lost the ability to affinity capture the thrombin analyte after its incorporation to the poly(HPMA-*co*-CBMAA) brushes (data not shown) and thus it was not used in further experiments.

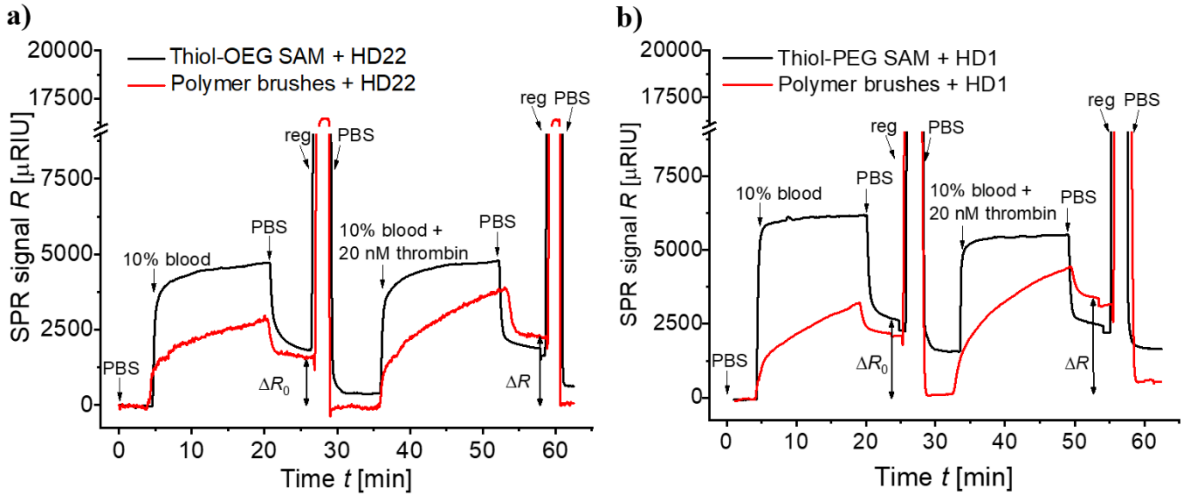

Figure 4. SPR sensor signal showing the interaction kinetics of blood compounds and thrombin in 10 % diluted whole blood on the sensor chip carrying thiol-OEG-SAM (black) or polymer brushes (red) functionalized with a) HD22 and b) HD1 thrombin aptamer.

Based on these observations, the functionalized poly(HPMA-*co*-CBMAA) brushes and HD1 and HD22 aptamers were employed for establishing a biosensor for the rapid direct detection of thrombin in 10% human blood samples. This biosensor was calibrated by using the developed protocol and 10% human blood samples containing $c = 0$, 5, 10, 15, 20 nM thrombin were sequentially injected with a regeneration step between detection cycles, see Figure 5a. The sensor response ΔR was determined as a difference in the SPR signal $R(t)$ before and after the flow of the analyzed liquid sample that was allowed to interact with the immobilized aptamer at the sensor surface for 15 min. The change in the SPR signal ΔR was acquired after 5 min of rinsing with PBS. ΔR was plotted versus thrombin concentration c and fitted with a function $\Delta R = \Delta R_0 + \Delta R_{max} \cdot c / K_d / (1 + c / K_d)$, where ΔR_0 states for the change after the flow of a blank sample, ΔR_{max} is the response in saturation, and the parameter K_d corresponds to the equilibrium dissociation affinity constant. The error bar was determined as a standard deviation of at least three independent measurements. The SPR response ΔR of each sample was compensated with respect to the blank sample ΔR_0 and plotted against the analyzed concentration c in order to establish the calibration curves. The obtained data are presented in Figure 5b for the immobilized aptamers HD1 and HD22 and calibration curves measured for 10% blood samples are compared to those obtained with model samples when PBS was spiked with the target thrombin analyte.

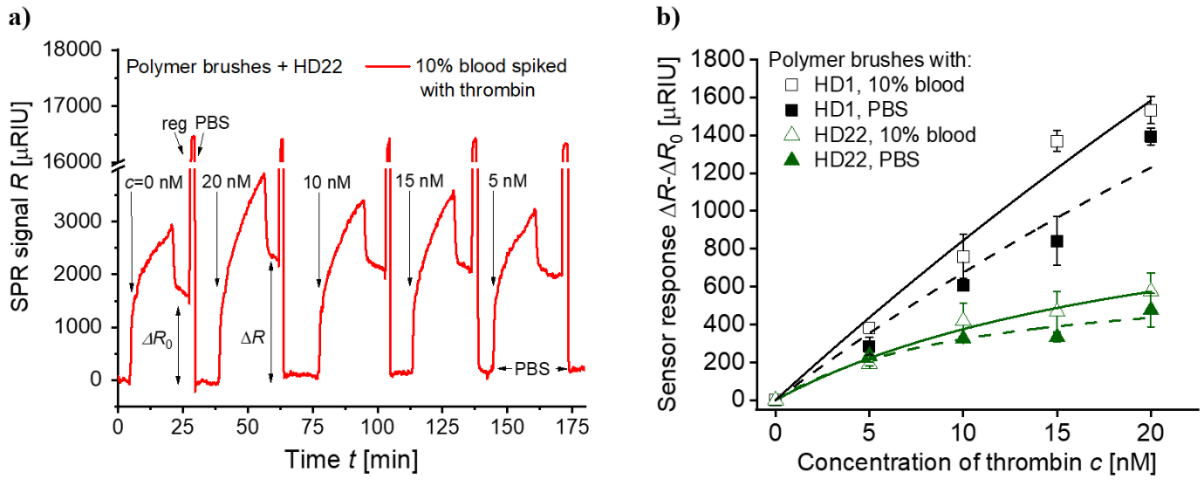

Figure 5. a) SPR sensor signal showing the kinetics of the affinity binding of thrombin from 10% diluted whole blood at a concentration of c=0, 5, 10, 15 and 20 nM on the sensor chip carrying polymer brushes functionalized with thrombin aptamer HD22. b) The calibration curves for detection of thrombin in PBS and 10% diluted whole blood established for polymer brushes functionalized with HD1 and HD22 aptamers.

Interestingly, the response of the SPR sensor to the presence of thrombin in 10% blood is higher than that for thrombin dissolved in PBS. The SPR response ΔR-ΔR_0 is increased by about 10% for HD22-

functionalized polymer brushes and by 20% for the polymer brushes with the attached HD1 aptamer. The reason for this observation can be attributed to the potential activation of prothrombin by the captured thrombin (despite the used anticoagulant argatroban that prevents the coagulation in the bulk solution). This effect is less pronounced for HD22 aptamer as it does not exhibit affinity to prothrombin and it captures only thrombin by its exosite II with K_d<5 nM. Contrary to HD22, the aptamer HD1 interacts with thrombin exosite I with K_d<5 nM and also binds prothrombin with K_d=39 nM. However, these interaction characteristics (measured with biotin-tagged aptamers in mixed thiol SAM surface) are probably substantially changed when aptamer bioreceptors are immobilized on poly(HPMA-*co*-CBMAA) brushes. The fitting of the obtained calibration curves with the Langmuir isotherm function yielded much higher effective values of K_d = 140.0 ± 6.5 and 22.5 ± 10.4 nM for HD1 and HD22 aptamer, respectively, for both PBS and 10% blood. This discrepancy can be partially attributed to the fact the used reaction time of 15 min did not allow for reaching equilibrium in the surface reaction (particularly for low thrombin concentrations *c*), which may be in addition slowed down by diffusion of the target analyte through the brushes polymer chains carrying higher density of aptamer ligands that the thiol SAM-based architecture (see Table.1). Moreover, the affinity interaction of aptamers is expected to be very sensitive to its local environment as it is reflected in the large variety of K_d values reported in the literature [36–38]. The presence of densely packed polymer chains constituting the brushes likely impacts the secondary structure of the aptamers necessary for the affinity interaction or leads to the steric hindrances and impeded access of thrombin molecules to the aptamer binding sites.

The limit of detection (LOD) was determined as a concentration where the fitted calibration curve intersects with the three times the standard deviation of the SPR sensor signal $\sigma(R[t])$. The used sensor instrument allowed for the measurement of bulk refractive index changes with the standard deviation of $\sigma=2\times10^{-5}$ RIU on the surface with poly(HPMA-*co*-CBMAA) brushes. It translates to LOD = 0.7 and 0.9 nM for HD1 aptamer-based sensor operated for detection of thrombin in 10% blood and PBS, respectively. For the HD22 aptamer, the achieved LOD was higher and reached 1 and 1.2 nM for 10% blood and PBS. The limit of detection in complex 10% blood is better than in PBS for both biointerfaces and it can be potentially explained by the cross-reaction with prothrombin and its potential interaction with a high surface concentration of affinity captured thrombin. In addition, let us note the previous work showed that HD1 aptamer (immobilized via biotin tag to the streptavidin-modified open dextran-based binding matrix) cannot be used for detection of thrombin in diluted blood plasma due to its cross-reaction with other biomolecules [36]. Contrary to this work, the herein presented results indicate that when incorporated to poly(HPMA-*co*-CBMAA) polymer brushes both aptamers HD1 and HD22 can serve for specific direct detection of thrombin in minimally processed 10% blood.

Giving the fact that the coagulation process occurs when the level of thrombin in the blood exceeds 5 – 20 nM [42], the obtained LOD = 0.7 nM for the direct rapid assay with HD1 aptamer in ten times diluted whole blood is in the lower part of this concentration range that indicates the risk of thrombosis. It is worth noting that the reported experiments focused on the investigation of the new antifouling biointerface by using a versatile home-built SPR instrument with limited accuracy (refractive index resolution of σ=1.4×10^{-5} RIU when operated with thiol SAM). In order to improve the LOD, another commercially available SPR sensor instruments with refractive index resolution at 10^{-7} level [43] are available and potentially applicable with the reported sensor chip biointerface architecture.

Conclusions

Thrombin aptamer bioreceptors HD1 and HD22 were successfully immobilized on poly(HPMA-*co*-CBMAA) brushes and utilized for the detection of thrombin in 10% whole human blood. The affinity interaction parameters of the aptamers on the novel polymer brush architecture were compared with a standard modification based on mixed thiol-OEG-OH/biotin SAM that was functionalized with the same aptamer sequences. The poly(HPMA-*co*-CBMAA) brushes allowed for immobilizing a higher density of the aptamers at the surface and provided antifouling properties enabling repeating direct detection of thrombin in 10% whole blood by using regeneration in between the analysis cycles. Moreover, the limit of detection achieved for polymer brush architecture with HD1 aptamer is sufficient for the prediction of a thrombotic event and diagnosis of thrombosis. We believe that this work opens doors to the development of new diagnostic tools for rapid and direct detection of biomarkers in the minimally processed blood leading to guided therapeutic decision making and personalized treatment.

Supporting Information

The Supporting Information contains ellipsometry measurements of refractive index and thickness of polymer brush, characteristic of the SPR sensor, fitting parameters, and sensorgrams of aptamer immobilization and detection of thrombin in 10% human blood.

Author Contributions

All authors have given approval to the final version of the manuscript.

Acknowledgment

D.K. received funding from the European Union's Horizon 2020 research and innovation programme under grant agreement No 642787, Marie Sklodowska-Curie Innovative Training Network BIOGEL. J.D. was supported by Lower Austria project IKTHEUAP number WST3-F-5030820/010-2019. CR-E and M.V.

acknowledge the support of the Deutsche Forschungsgemeinschaft (DFG) in the framework of the priority programme 2014 “Towards an Implantable Lung", project numbers: 346972946. Authors would like to thank Dr. Wojciech Ogieglo for conducting the ellipsometry measurements.

References

[1] B. Siegerink, A. Maino, A. Algra, F.R. Rosendaal, Hypercoagulability and the risk of myocardial infarction and ischemic stroke in young women, J. Thromb. Haemost. 13 (2015) 1568–1575. https://doi.org/10.1111/jth.13045.

[2] D.A. Wilkinson, A.S. Pandey, B.G. Thompson, R.F. Keep, Y. Hua, G. Xi, Injury mechanisms in acute intracerebral hemorrhage, Neuropharmacology. (2018) 240–248. https://doi.org/10.1016/j.neuropharm.2017.09.033.

[3] C. Blaszykowski, S. Sheikh, M. Thompson, Surface chemistry to minimize fouling from blood-based fluids, Chem. Soc. Rev. 41 (2012) 5599–5612. https://doi.org/10.1039/c2cs35170f.

[4] O. Tokel, F. Inci, U. Demirci, Advances in plasmonic technologies for point of care applications, Chem. Rev. 114 (2014) 5728–5752. https://doi.org/10.1021/cr4000623.

[5] S. Sang, Y. Wang, Q. Feng, Y. Wei, J. Ji, W. Zhang, Progress of new label-free techniques for biosensors: A review, Crit. Rev. Biotechnol. 36 (2016) 465–481. https://doi.org/10.3109/07388551.2014.991270.

[6] C. Rodriguez-Emmenegger, M. Houska, A.B. Alles, E. Brynda, Surfaces resistant to fouling from biological fluids: towards bioactive surfaces for real applications, Macromol. Biosci. 12 (2012) 1413–1422. https://doi.org/10.1002/mabi.201200171.

[7] E. Stern, A. Vacic, N.K. Rajan, J.M. Criscione, J. Park, R. Bojan, D.J. Mooney, M.A. Reed, T.M. Fahmy, Label-free biomarker detection from whole blood, Nat Nanotechnol. 5 (2010) 1–11. https://doi.org/10.1038/nnano.2009.353.Label-free.

[8] H.K. Chang, F.N. Ishikawa, R. Zhang, R. Datar, R.J. Cote, M.E. Thompson, C. Zhou, Rapid, label-free, electrical whole blood bioassay based on nanobiosensor systems, ACS Nano. 5 (2011) 9883–9891. https://doi.org/10.1021/nn2035796.

[9] B.S. Ferguson, D.A. Hoggarth, D. Maliniak, K. Ploense, R.J. White, N. Woodward, K. Hsieh, A.J. Bonham, M. Eisenstein, T. Kippin, K.W. Plaxco, H.T. Soh, Real-time, aptamer-based tracking of circulating therapeutic agents in living animals, Sci. Transl. Med. 5 (2013) 213ra165. https://doi.org/10.1371/journal.pone.0178059.

[10] C.E. Nwankire, A. Venkatanarayanan, T. Glennon, T.E. Keyes, R.J. Forster, J. Ducrée, Label-free impedance detection of cancer cells from whole blood on an integrated centrifugal microfluidic platform, Biosens. Bioelectron. 68 (2015) 382–389. https://doi.org/10.1016/j.bios.2014.12.049 LK.

[11] B. Zhu, T. Eurell, R. Gunawan, D. Leckband, Chain-length dependence of the protein and cell resistance of oligo (ethylene glycol)-terminated self-assembled monolayers on gold, J Biomed Mater Res. 56 (2001) 406–416. https://doi.org/10.1002/1097-4636(20010905)56:3<406::aid-jbm1110>3.0.co;2-r.

[12] C.M. Xing, F.N. Meng, M. Quan, K. Ding, Y. Dang, Y.K. Gong, Quantitative fabrication, performance optimization and comparison of PEG and zwitterionic polymer antifouling coatings, Acta Biomater. 59 (2017) 129–138. https://doi.org/10.1016/j.actbio.2017.06.034.

[13] M. Cui, Y. Wang, M. Jiao, S. Jayachandran, Y. Wu, X. Fan, X. Luo, Mixed self-assembled aptamer and newly designed zwitterionic peptide as antifouling biosensing interface for electrochemical detection of alpha-fetoprotein, ACS Sensors. 2 (2017) 490–494. https://doi.org/10.1021/acssensors.7b00103.

[14] A. De Los Santos Pereira, S. Sheikh, C. Blaszykowski, O. Pop-Georgievski, K. Fedorov, M. Thompson, C. Rodriguez-Emmenegger, Antifouling polymer brushes displaying antithrombogenic surface properties, Biomacromolecules. 17 (2016) 1179–1185. https://doi.org/10.1021/acs.biomac.6b00019.

[15] J. Benesch, S. Svedhem, S.C.T. Svensson, R. Valiokas, B. Liedberg, P. Tengvall, Protein adsorption to oligo(ethylene glycol) self-assembled monolayers: experiments with fibrinogen, heparinized plasma, and serum, J. Biomater. Sci. Polym. Ed. 12 (2001) 581–597. https://doi.org/10.1163/156856201316883421.

[16] C. Rodriguez-Emmenegger, E. Brynda, T. Riedel, Z. Sedlakova, M. Houska, A.B. Alles, Interaction of blood plasma with antifouling surfaces, Langmuir. 25 (2009) 6328–6333. https://doi.org/10.1021/la900083s.

[17] O. Pop-Georgievski, Š. Popelka, M. Houska, D. Chvostová, V. Proks, F. Rypáček, Poly(ethylene oxide) layers grafted to dopamine-melanin anchoring layer: Stability and resistance to protein adsorption, Biomacromolecules. 12 (2011) 3232–3242. https://doi.org/10.1021/bm2007086.

[18] G. Wang, X. Su, Q. Xu, G. Xu, J. Lin, X. Luo, Antifouling aptasensor for the detection of adenosine triphosphate in biological media based on mixed self-assembled aptamer and zwitterionic peptide, Biosens. Bioelectron. 101 (2018) 129–134. https://doi.org/10.1016/j.bios.2017.10.024.

[19] Z. Zhang, T. Chao, S. Chen, S. Jiang, Superlow fouling sulfobetaine and carboxybetaine polymers on glass slides, Langmuir. 22 (2006) 10072–10077. https://doi.org/10.1021/la062175d.

[20] W. Yang, H. Xue, W. Li, J.Z. And, S. Jiang, Pursuing "zero" protein adsorption of poly(carboxybetaine) from undiluted blood serum and plasma, Langmuir. 25 (2009) 11911–11916. https://doi.org/10.1021/la9015788.

[21] C. Rodriguez-Emmenegger, B.V.K.J. Schmidt, Z. Sedlakova, V. Šubr, A.B. Alles, E. Brynda, C. Barner-Kowollik, Low temperature aqueous living/controlled (RAFT) polymerization of carboxybetaine methacrylamide up to high molecular weights, Macromol. Rapid Commun. 32 (2011) 958–965. https://doi.org/10.1002/marc.201100176.

[22] C. Zhao, L. Li, J. Zheng, Achieving highly effective nonfouling performance for surface-grafted poly(HPMA) via atom-transfer radical polymerization, Langmuir. 26 (2010) 17375–17382. https://doi.org/10.1021/la103382j.

[23] H. Vaisocherová, V. Ševců, P. Adam, B. Špačková, K. Hegnerová, A. de los Santos Pereira, C. Rodriguez-Emmenegger, T. Riedel, M. Houska, E. Brynda, J. Homola, Functionalized ultra-low fouling carboxy- and hydroxy-functional surface platforms: functionalization capacity, biorecognition capability and resistance to fouling from undiluted biological media, Biosens. Bioelectron. 51 (2014) 150–157. https://doi.org/10.1016/j.bios.2013.07.015.

[24] T. Riedel, F. Surman, S. Hageneder, O. Pop-Georgievski, C. Noehammer, M. Hofner, E. Brynda, C. Rodriguez-Emmenegger, J. Dostálek, Hepatitis B plasmonic biosensor for the analysis of clinical serum samples, Biosens. Bioelectron. 85 (2016) 272–279. https://doi.org/10.1016/j.bios.2016.05.014.

[25] T. Riedel, S. Hageneder, F. Surman, O. Pop-Georgievski, C. Noehammer, M. Hofner, E. Brynda, C. Rodriguez-Emmenegger, J. Dostálek, Plasmonic hepatitis B biosensor for the analysis of clinical saliva, Anal. Chem. 89 (2017) 2972–2977. https://doi.org/10.1021/acs.analchem.6b04432.

[26] Z. Riedelová, P. Májek, K. Pečánková, J. Kučerová, F. Surman, A. De Los Santos Pereira, T. Riedel, SPR biosensor for quantification of fetuin-A as a promising multibiomarker, 67 (2018) 367–375. https://doi.org/10.33549/physiolres.933982.

[27] D. Kotlarek, M. Vorobii, W. Ogieglo, W. Knoll, C. Rodriguez-Emmenegger, J. Dostalek, Compact grating-coupled biosensor for the analysis of thrombin, ACS Sensors. 4 (2019) 2109–2116. https://doi.org/10.1021/acssensors.9b00827.

[28] S. Song, L. Wang, J. Li, C. Fan, J. Zhao, Aptamer-based biosensors, Trends Anal. Chem. 27 (2008) 108–117. https://doi.org/10.1016/j.trac.2007.12.004.

[29] K.M. You, S.H. Lee, A. Im, S.B. Lee, Aptamers as functional nucleic acids: in vitro selection and biotechnological applications, Biotechnol. Bioprocess Eng. 8 (2003) 64–75. https://doi.org/10.1007/BF02940259.

[30] D.M. Jones, A.A. Brown, W.T.S. Huck, P. Street, C. Cb, Surface-initiated polymerizations in aqueous media: effect of initiator density, Langmuir. 18 (2002) 1265–1269. https://doi.org/10.1021/la011365f.

[31] K. Ulbrich, V. Šubr, J. Strohalm, D. Plocová, M. Jelínková, B. Říhová, Polymeric drugs based on conjugates of synthetic and natural macromolecules, J. Control. Release. 64 (2000) 63–79. https://doi.org/10.1016/S0168-3659(99)00141-8.

[32] W. Knoll, M. Liley, D. Piscevic, J. Spinke, M.J. Tarlov, Supramolecular architectures for the functionalization of solid surfaces, Adv. Biophys. 34 (1997) 231–251. https://doi.org/10.1016/S0065-227X(97)89642-6.

[33] C. Stenberg, E., Persson, B., Roos, H., & Urbaniczky, Quantitative determination of surface concentration of protein with surface plasmon resonance using radiolabeled proteins, J. Colloid Interface Sci. 143 (1991) 513–526. https://doi.org/doi.org/10.1016/0021-9797(91)90284-F.

[34] J. Vidic, M. Pla-Roca, J. Grosclaude, M.A. Persuy, R. Monnerie, D. Caballero, A. Errachid, Y. Hou, N. Jaffrezic-Renault, R. Salesse, E. Pajot-Augy, J. Samitier, Gold surface functionalization and patterning for specific immobilization of olfactory receptors carried by nanosomes, Anal. Chem. 79 (2007) 3280–3290. https://doi.org/10.1021/ac061774m.

[35] I. Mihai, A. Vezeanu, C. Polonschii, C. Albu, G.L. Radu, A. Vasilescu, Label-free detection of lysozyme in wines using an aptamer based biosensor and SPR detection, Sensors Actuators, B Chem. 206 (2015) 198–204. https://doi.org/10.1016/j.snb.2014.09.050.

[36] A. Trapaidze, J.P. Hérault, J.M. Herbert, A. Bancaud, A.M. Gué, Investigation of the selectivity of thrombin-binding aptamers for thrombin titration in murine plasma, Biosens. Bioelectron. 78 (2016) 58–66. https://doi.org/10.1016/j.bios.2015.11.017.
[37] P.H. Lin, R.H. Chen, C.H. Lee, Y. Chang, C.S. Chen, W.Y. Chen, Studies of the binding mechanism between aptamers and thrombin by circular dichroism, surface plasmon resonance and isothermal titration calorimetry, Colloids Surf., B. 88 (2011) 552–558. https://doi.org/10.1016/j.colsurfb.2011.07.032.
[38] J. Müller, D. Freitag, G. Mayer, B. Pötzsch, Anticoagulant characteristics of HD1-22, a bivalent aptamer that specifically inhibits thrombin and prothrombinase, J. Thromb. Haemost. 6 (2008) 2105–2112. https://doi.org/10.1111/j.1538-7836.2008.03162.x.
[39] S. Butenas, C. Van't Veer, K.G. Mann, "Normal" thrombin generation, Blood. 94 (1999) 2169–2178. https://doi.org/10.1182/blood.V94.7.2169.419k22_2169_2178.
[40] J. Müller, T. Becher, J. Braunstein, P. Berdel, S. Gravius, F. Rohrbach, J. Oldenburg, G. Mayer, B. Pötzsch, Profiling of active thrombin in human blood by supramolecular complexes, Angew. Chemie - Int. Ed. 50 (2011) 6075–6078. https://doi.org/10.1002/anie.201007032.
[41] T. Hianik, V. Ostatná, M. Sonlajtnerova, I. Grman, Influence of ionic strength, pH and aptamer configuration for binding affinity to thrombin, Bioelectrochemistry. 70 (2007) 127–133. https://doi.org/10.1016/j.bioelechem.2006.03.012.
[42] K.G. Mann, S. Butenas, K. Brummel, The dynamics of thrombin formation, Arterioscler. Thromb. Vasc. Biol. 23 (2003) 17–25. https://doi.org/10.1161/01.ATV.0000046238.23903.FC.
[43] M. Piliarik, J. Homola, Surface plasmon resonance (SPR) sensors: approaching their limits?, Opt. Express. 17 (2009) 16505. https://doi.org/10.1364/OE.17.016505.

Supporting information

Simulations of SPR changes for surface mass density determination

Surface mass density of Γ = 4.2 ng·mm^{-2} was obtained for a full packed monolayer of thrombin captured by paramers d_p = 5 nm, n_p = 1.50 and n_s = 1.33. For the short distance of such layer from the gold sensor surface of 3 nm (assumed for thiol-OEG SAM d_{SAM} = 3 nm, n_{SAM} = 1.46](141)) the respective shift in the SPR dip of $\Delta\vartheta$ = 0.95 deg was determined for the probing SPR wavelength of 633 nm by using Fresnel reflectivity model (implemented in the tool Wasplas, Max Planck Institute for Polymer Research in Mainz, Germany). For the longer distance of 42 nm corresponding to the thickness the brush architecture (d_{brush} = 42 nm, n_{brush} = 1.42, Figure S1), smaller shift of SPR angle of $\Delta\vartheta$ = 0.75 deg was simulated. The bulk refractive index sensitivity for these two geometries was determined as S_b = 116.6 deg RIU^{-1} for the thiol-OEG SAM and S_b = 81 deg RIU^{-1} poly(HPMA-*co*-CBMAA) brush system, respectively. The sensor response described in bulk refractive index changes RIU is equal to $\delta R = \Delta\vartheta / S_b$ enabling to obtain the conversion factor as $\Gamma / \delta R = \Gamma / S_b \cdot \Delta\vartheta$.

Ellipsometry measurements of diblock polymer brush

The thickness and refractive index of the dry and swollen film of poly(HPMA-co-CBMAA) brushes was determined in the ellipsometry measurement by using a spectroscopic ellipsometer M2000 (J.A.Woollam Co., USA) operated in a rotating compensator mode. The measurements were performed at room temperature with a Xe-arc lamp at angles of incidence 65, 70 and 75° and wavelength range

350–1000 nm. The thickness and refractive index of the polymer brushes were determined by fitting the data to the transparent Cauchy-type optical dispersion model in a CompleteEASE software (Figure S1).

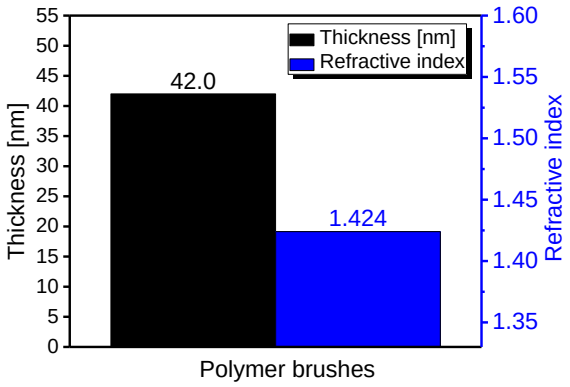

Figure S1 A thickness and a refractive index of the polymer brushes determined for the swollen brush layer.

Comparison of the sensitivity and resolution of the sensor carrying thiol-OEG or polymer brush interface

The instrument sensitivity S=43.1 vs. S=23.4 RIU^{-1} and the refractive index resolution 2×10^{-5} RIU vs. 1.4×10^{-5} RIU was evaluated from the refractometric experiment with sucrose for the SPR sensor chips that were modified with thiol-OEG SAM vs. poly(HPMA-*co*-CBMAA) brushes, respectively (Figure. S2). The apparent decrease of the sensitivity and resolution upon synthesis of the polymer brushes can be related to their layer thickness (~ 42 nm in comparison to ~ 3 nm of thiol-OEG SAM) and the decay of the evanescent field of surface plasmons with the distance from the surface (L_p ~ 100 nm).

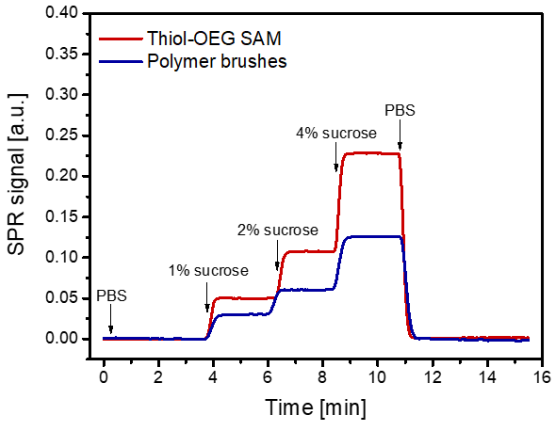

Figure S2 The sensorgram showing SPR signal to 1, 2 and 4% sucrose solutions by using SPR chip coated with thiol-OEG SAM (red) and SPR chip modified with poly(HPMA-co-CBMAA) brushes (blue).

Model for binding kinetics

The global analysis of the kinetic parameters of thrombin – aptamer interaction was performed in Prism 8 (GraphPad Software) by using nonlinear regression method of the "association than dissociation" function implemented in the program following the definition:

Radioligand=HotNM*10^{-9}
K_{ob}=[Radioligand] * K_{on}+K_{off}
K_d=K_{off}/K_{on}
Eq=B_{max}*radioligand/(radioligand + K_d)
Association=Eq*(1-exp(-1*K_{ob}*X))
YatTime0 = Eq*(1-exp(-1*K_{ob}*Time0))
Dissociation= YatTime0*exp(-1*K_{off}*(X-Time0))
Y=IF(X<Time0, Association, Dissociation) + NS
Set parameters:
HotNM (concentration of thrombin in nM) constant equal to = 5; 10; 15; 20; 35; 50; 100 or 500 nM
Time0 (time at which dissociation was initiated) constant equal to = 30 for HD1 and HD22 or 60 min for HD1 short
k_{on} = must be greater than 0
k_{off} = must be greater than 0
B_{max} = must be less than 1000 µRIU (1000 RU)
NS (nonspecific binding) = constant equal 0

Immobilization of thrombin aptamers

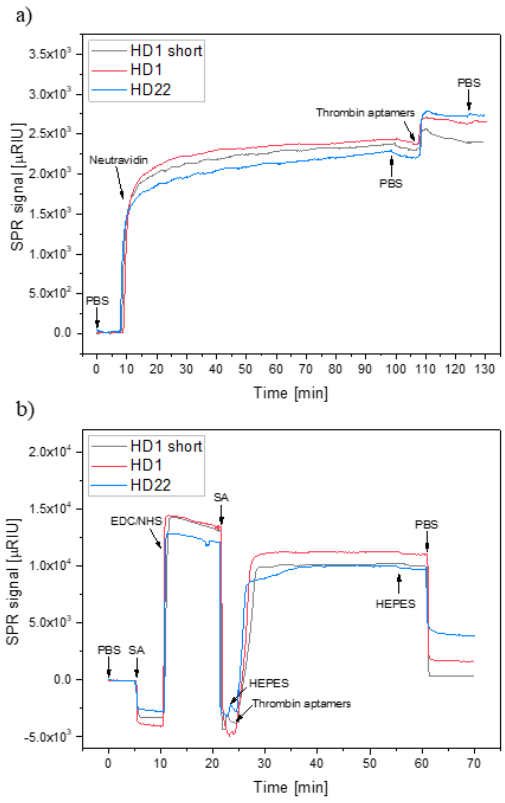

Figure S3 Sensorgrams showing immobilization of thrombin aptamers on a) thiol-OEG SAM and b) poly(HPMA-co-CBMAA) brushes.

3.2. FABRICATION OF PLASMONIC NANOSTRUCTURES FOR FASTER AND SENSITIVE DETECTION

Actuated Plasmonic Nanohole Arrays for Sensing and Optical Spectroscopy Applications

Daria Kotlarek[a], Stefan Fossati[a], Priyamvada Venugopalan[a,b,c], Nestor Gisbert Quilis[a], Jiří Slabý[d], Jiří Homola[d], Médéric Lequeux[e], Frédéric Amiard[f], Marc Lamy de la Chapelle[f], Ulrich Jonas[g], Jakub Dostálek[a]

[a] Biosensor Technologies, AIT-Austrian Institute of Technology GmbH, Konrad-Lorenz-Straße 24, 3430 Tulln an der Donau, Austria. E-mail: Jakub.dostalek@ait.ac.at.

[b] CEST Kompetenzzentrum für elektrochemische Oberflächentechnologie GmbH, TFZ, Wiener Neustadt, Viktor-Kaplan-Strasse 2, 2700 Wiener Neustadt, Austria

[c] Current address: NYU Abu Dhabi, Saadiyat Campus, P.O. Box 129188, Abu Dhabi, United Arab Emirates

[d] Institute of Photonics and Electronics, Academy of Sciences of the Czech Republic, Chaberská 57, 18251, Praha 8, Czech Republic

[e] Université Paris 13, Sorbonne Paris Cité, Laboratoire CSPBAT, CNRS, (UMR 7244), 74 rue Marcel Cachin, 93017 Bobigny, France

[f] Institut des Molécules et Matériaux du Mans (IMMM - UMR CNRS 6283), Avenue Olivier Messiaen, 72085 Le Mans cedex 9, France

[g] Macromolecular Chemistry, Department Chemistry-Biology, University of Siegen, Adolf Reichwein-Strasse 2, Siegen 57076, Germany

ABSTRACT

We report on new approach to rapidly actuate plasmonic characteristics of thin gold film perforated with nanohole arrays that are coupled with arrays of gold nanoparticles. The near-field interaction between localized and propagating surface plasmon modes supported by the structure is actively modulated by changing the distance between nanoholes and nanoparticles and by variations in refractive index symmetry of the structure. It is utilized by the use of thin responsive hydrogel cushion that is allowed to swell and collapse by a temperature stimulus. A detailed experimental study of changes and interplay of localized and propagating surface plasmons is complemented by numerical simulations. We demonstrate that the interrogation of resonant optical excitation to these modes allows for the label-free SPR observation of binding of biomolecules and that it is applicable for *in situ* SERS studies of low molecular weight molecules attached in the gap between nanoholes and nanoparticles.

Introduction

Metallic nanohole arrays (NHA) attracted increasing attention after the Ebbesen's observation of extraordinary optical transmission[1] that is assigned to surface plasmon-mediated light tunneling through periodically arranged subwavelength pores. Since then, NHA structures found their use in diverse application areas including optical filters,[2,3] amplification of weak spectroscopy signals such as fluorescence[4,5] and Raman scattering,[6,7,8,9] in second-harmonic generation,[10] and particularly in sensing. Up to date, NHA-based sensors were utilized for the direct optical probing of proteins,[11,12–14] exosomes,[15] viruses,[16,17] bacteria,[18] and even cancer cells[19,20] and organelles.[21] Moreover, NHA enabled studies on lipid membranes that span over the holes[22] and allow for the facile incorporation of membrane proteins for interaction studies with drug candidates.[16,23]

NHA structures enable to strongly confine electromagnetic field inside the subwavelength nanoholes[24] due to the excitation of two types of surface plasmon modes: propagating surface plasmons (PSPs that are also referred as to surface plasmon polaritons) traveling along the metal surface and localized surface plasmons (LSPs) that occur at the sharp edges of the holes. The coupling to these modes can be tailored for specific purposes by controlling the structure geometry including hole shape, diameter, and lateral periodic or quasi-periodic spacing.[25] In addition, a more complex spectrum of supported plasmonic modes can be utilized by the coupling complementary geometries that support LSP modes at similar wavelengths based on the Babinet's principle.[26] When NHA geometry is combined with the complementary metallic nanoparticles (NP) arrays, additional LSP resonance is introduced and it can near-field couple with the NHA.[27] Moreover, NHA structures that comprise stacks of perforated metallic films[28] and NHA+NP structure with a defined lateral offset of NPs with respect to the nanohole center[29] were investigated. Such perturbation of symmetry was shown to allow for turning LSP with dark mode characteristics to bright LSP mode[30] and thus providing means for decreased damping. It is worth of noting that also arranging the metallic nanoholes and nanoparticles in periodic arrays allows to decrease damping of plasmonic modes by their diffraction coupling through forming so called surface lattice resonances.[31]

Perforated metal layer structures with NHA have been recently prepared by a range of lithography processes. In top-down approaches, a variety of geometries become accessible using focused ion beam milling (FIB) or electron beam lithography (EBL).[32,33] Nanoimprint lithography and template stripping[34] were used to partially alleviate the limited throughput of EBL and FIB by the replication of NHA structure from pre-fabricated templates. Alternatively, NHAs were also prepared using bottom-up approaches, mostly relying on the colloid particle self-organization.[35] Using sub-monolayer surface coverage of colloids, the colloid particles were used as a mask for the preparation of sparse and disordered nanoholes while dense monolayers of colloids were employed to create ordered arrays of

nanoholes.[28,29,36] This approach allows the control of the pattern period *Λ* by the size of colloid particles and the hole diameter *D* can be independently adjusted by using an isotropic etching of the assembled particles before the metal deposition. The technique was further extended for the preparation of nanoholes on cavities[37] and there was also adopted a lift-off approach of the NHA membrane for its subsequent transfer to more complex structures with multiple stacked patterned metallic layers.[28]

Typically, NHAs used for sensing applications are prepared by stripping-based techniques or by lithographic methods directly on non-permeable solid support which is loaded to a microfluidic device.[38,39] Analyzed liquid sample is then flowed over the perforated NHA surface with closed-ended pores where the liquid flow velocity is equal to zero and, consequently, the transport of molecules to and inside the pores is dominantly driven by slow diffusion.[40,41] To overcome this limitation, a flow-through assay format, in which the analyte solution is transported internally across the nanoporous film, was pursued.[8,16,41,42] However, these works typically rely on NHA structure prepared on thin nitride membranes that requires multiple lithography steps and complicates the utilization of sensing experiments.

This work reports on a new type of NHA+NP structure that is supported by a thermo-responsive hydrogel cushion. It is made from an N-isopropylacrylamide hydrogel material that can expand and contract in an aqueous environment thereby actuating the plasmonic properties of metallic nanostructures.[43–45] In the reported architecture, the hydrogel cushion accommodates arrays of gold NPs, which are located below the NHA and their mutual distance *g* can be on demand actuated (Figure 1).

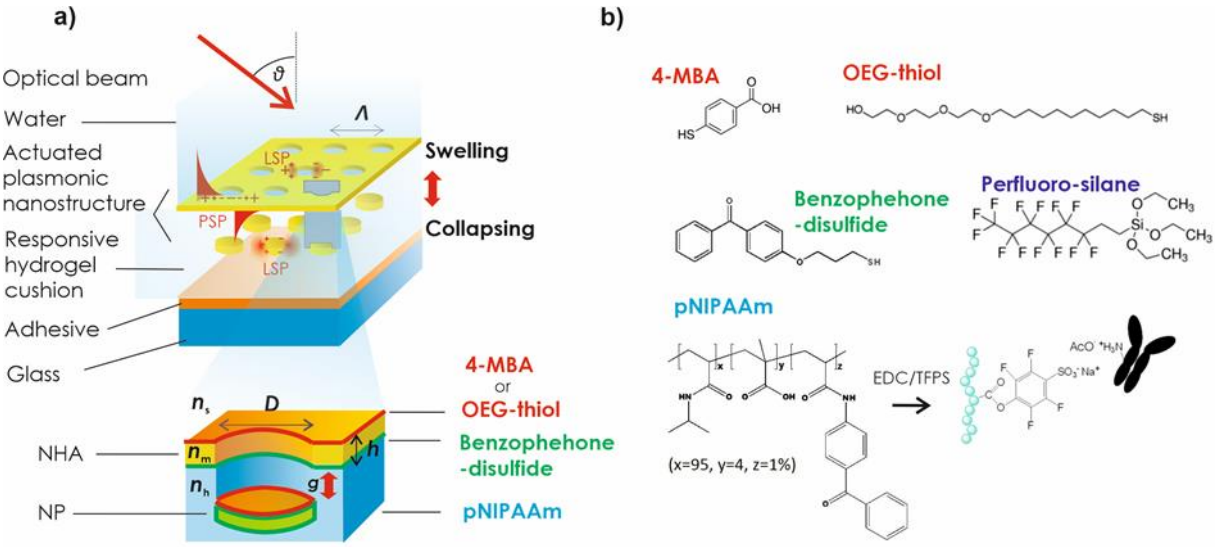

Figure 1. a) Schematics of plasmonic nanostructure composed of periodic nanohole arrays (NHA) coupled with arrays of nanoparticles (NP) by the use of responsive hydrogel cushion implemented by materials with chemical structure shown in b).

Herein, we investigate the spectrum of supported PSP and LSP modes and their actuating by temperature-induced reversible swelling and collapsing of hydrogel cushion. In addition, the hydrogel can serve as a three-dimensional binding matrix for the immobilization of biofunctional molecules and the applicability of the structure for SPR (surface plasmon resonance) and SERS (surface-enhanced Raman scattering) detection is demonstrated with the use of plasmonic modes that probe the open pores, through which aqueous samples can be actively flowed.

Results and Discussion

We developed a method to prepare the nanostructure geometry that combines thin gold film perforated with NHA and arrays of gold NP that are suspended in a thin layer of poly(N-isopropyl acrylamide) (pNIPAAm) - based hydrogel. It serves as a responsive cushion which responds to temperature changes as pNIPAAm exhibits lower critical solution temperature (LCST) of 32 ˚C. Below its LCST it is hydrophilic and contains large amounts of water in its polymer network structure. When increasing temperature above the LCST, it abruptly collapses by expelling water. In the used geometry (Figure 1a), the pNIPAAm-based hydrogel cushion was allowed to swell and collapse by diffusion of water through the NHA pores and its volume changes were utilized for active control of a distance *g* between the NHA and the NP. In addition, the hydrogel was made from a terpolymer that carries pendant groups attached to its backbone enabling its post-modification with biofunctional molecules (Figure 1b) for the application in optical spectroscopy and biosensors.[46] It is worth noting that this thermo-responsive hydrogel cushion allows for controlled opening and closing of the nanohole arrays pores and that switching to the open state is accompanied by rapid diffusion of water that drags contained biomolecules through the pores where a plasmonic hotspot occurs. The spectrum of plasmonic modes probing the pores of the structure and their near field coupling is detailly investigated as follows.

Preparation of NHA+NP structure with hydrogel cushion

The NHA+NP structure featuring actively tunable plasmonic properties has been prepared by a combination of UV nanoimprint lithography (UV-NIL) and template-stripping (Figure 2a). Arrays of nanopillars cast to transparent Ormostamp material were used as a template. AFM observation of the structure topography showed that the arrays of nanopillars exhibited a diameter of D=100 nm, their height was of 100 nm, and they were arranged in rectangular arrays with a period set to Λ=460 nm (Figure 2b).

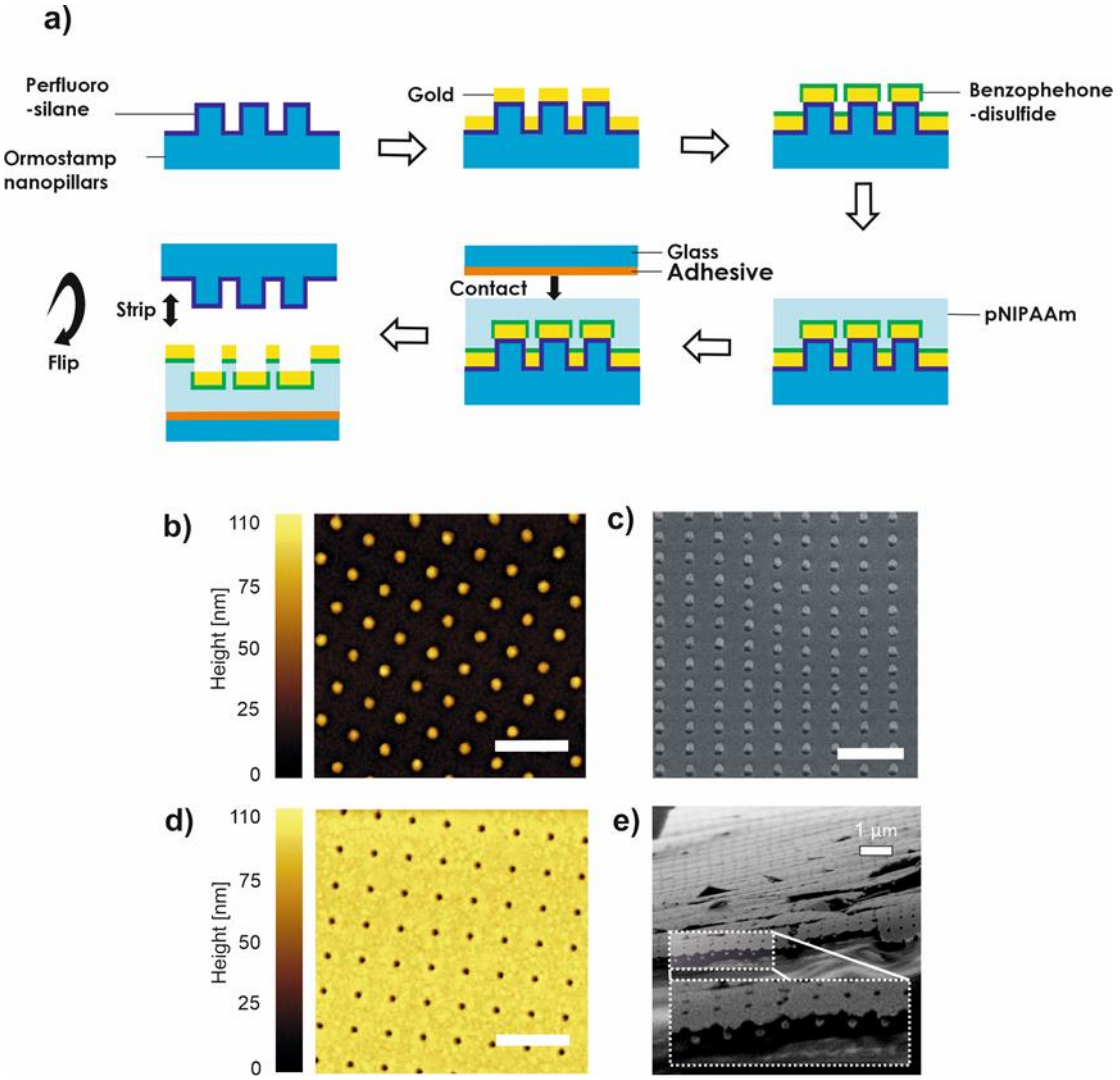

Figure 2. a) Schematics of the preparation steps of the investigated NHA+NP nanostructure, b) AFM image of template with arrays of nanopillars cast to Ormostamp, c) SEM image after coating of the template with 50 nm thick gold layer, d) AFM image of the topography of stripped surface with gold NHA, and d) SEM image of a broken edge of the NHA+NP structure tethered to a solid surface via the responsive pNIPAAm-based polymer. All scale bars are 1 µm in length.

Arrays of OrmoStamp nanopillars were then activated by UV-ozone treatment and modified with perfluoro-silane by using vapor deposition in order to reduce their surface energy. Subsequently, the nanopillars with a perfluoro-silane anti-adhesive layer were coated by a gold layer with a thickness of h=50 nm. SEM observation (presented in Figure 2c) reveals that the gold deposition led to the formation of a continuous layer which is protruded by the nanopillars and their top is capped by gold that is not connected to the bottom continuous gold layer. Afterward, the outer gold surface was modified by a self-assembled monolayer of photo-active benzophenone-disulfide and subsequently coated with the pNIPAAm-based terpolymer layer. This terpolymer carries the same photo-reactive benzophenone groups at its backbone (see Figure 1b) and upon the irradiation with UV light these chains were simultaneously covalently crosslinked and attached to the gold via the benzophenone-disulfide linker.

Then, the outer surface of the crosslinked pNIPAAm-based polymer was pressed against a glass substrate with a soft adhesive layer (Ostemer resin pre-cured with UV light) that was afterwards thermally cured overnight at a temperature of 50°C. Finally, the assembly was stripped at the Ormostamp – gold interface (treated with anti-adhesive layer) in order to yield a structure with a thin gold film perforated by NHA that are attached to pNIPAAm-based crosslinked polymer networks and comprise underneath embedded gold NPs spatially separated from the perforated continuous gold film. The AFM topography image in Figure 2d shows that the pores exhibit the same diameter *D* as the nanopillars and SEM image of an edge of the structure in Figure 2e confirms that below the NHA there are present arrays of gold NPs (that were stripped from the top of OrmoStamp pillars). It is worth noting that the distortions of the surface that are visible in Figure 2e are a result of breaking the sample to obtain the cross-section image.

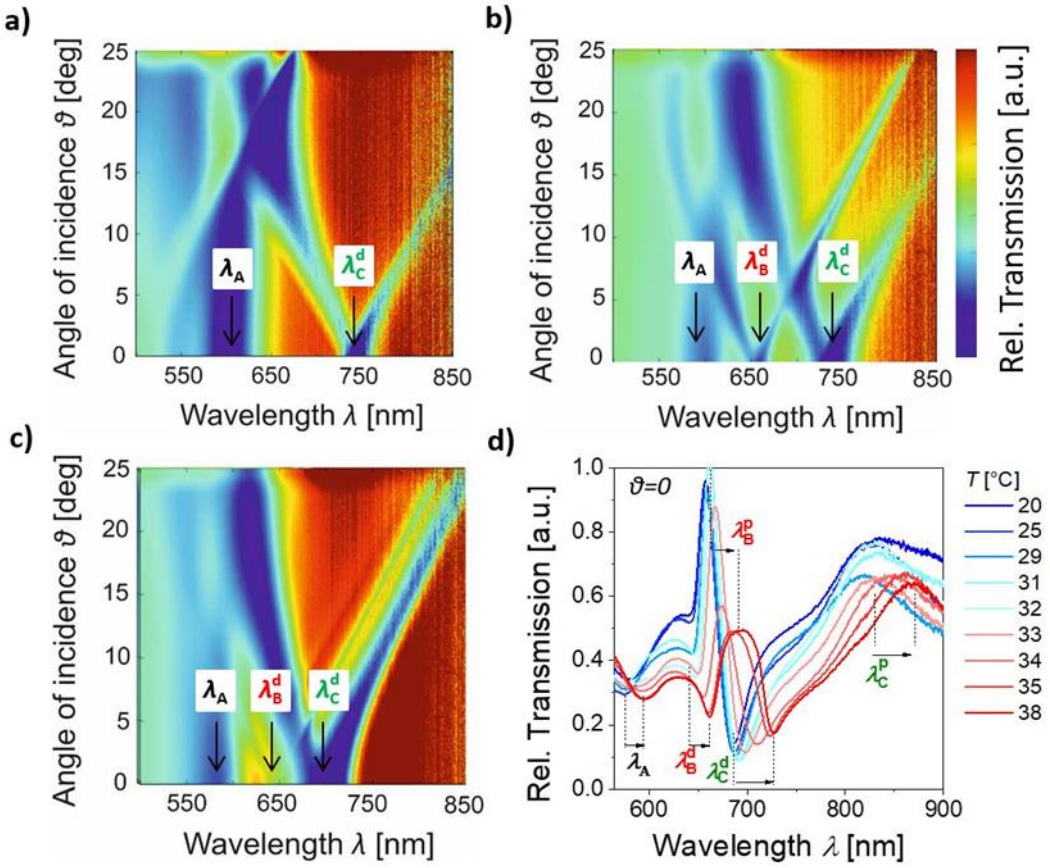

Figure 3. Measured dependence of wavelength transmission spectra on angle of incidence ϑ for NHA+NP structure in contact with a) air (n_s=1, n_h=1.48), b) for the collapsed state of the pNIPAAm-based cushion that is in contact with water at *T*=40 °C (n_s=1.33, n_h=1.48), and c) for the swollen state of pNIPAAm cushion in water at *T*=22 °C (n_s=1.33, n_h=1.37). d) Comparison of wavelength transmission spectra for ϑ and NHA+NP structure in contact with water with varied temperature *T*. The transmission spectra were normalized with those measured for flat structure not perforated Au film.

Optical observation of plasmonic modes

The spectrum of LSP and PSP modes supported by the prepared nanostructure was investigated with the use of optical transmission measurements. In order to distinguish between diffraction coupling to dispersive PSP modes (traveling along the gold film) and non-dispersive LSP resonances (supported by the pores in NHA+NP nanostructure), transmission spectra were measured by a collimated beam impinging at the NHA+NP structure at angles between ϑ=0 to 25 deg. The transmitted beam emitted from halogen light bulb was then analyzed with a spectrometer in wavelength range of λ=500-850 nm. Firstly, the wavelength-angular dependence of transmission was measured for a structure that was dry and in contact with air (with refractive index of n_s=1). As presented in Figure 3a, the acquired spectrum shows that the excitation of non-dispersive resonance is manifested as a dip in centered at a wavelength of λ_A=600 nm. Moreover, additional dispersive mode occurs and its excitation is associated with a dip in the transmission spectrum at λ_C^d=750 nm that splits when the angle of incidence ϑ deviates from zero. Secondly, the structure was clamped to a flow-cell and water (with refractive index of n_s=1.33) was flowed over its surface that was kept at a temperature of T=40°C. This temperature is above the LCST of pNIPAAm and thus this material exhibits hydrophobic properties preventing diffusion of water into polymer networks through the NHA pores. As refractive index of the dielectric above the structure n_s increases, a new dispersive dip resonance centered at a wavelength of λ_B^d=650 nm appears while the resonance features λ_A and λ_C^d do not change (Figure 3b).

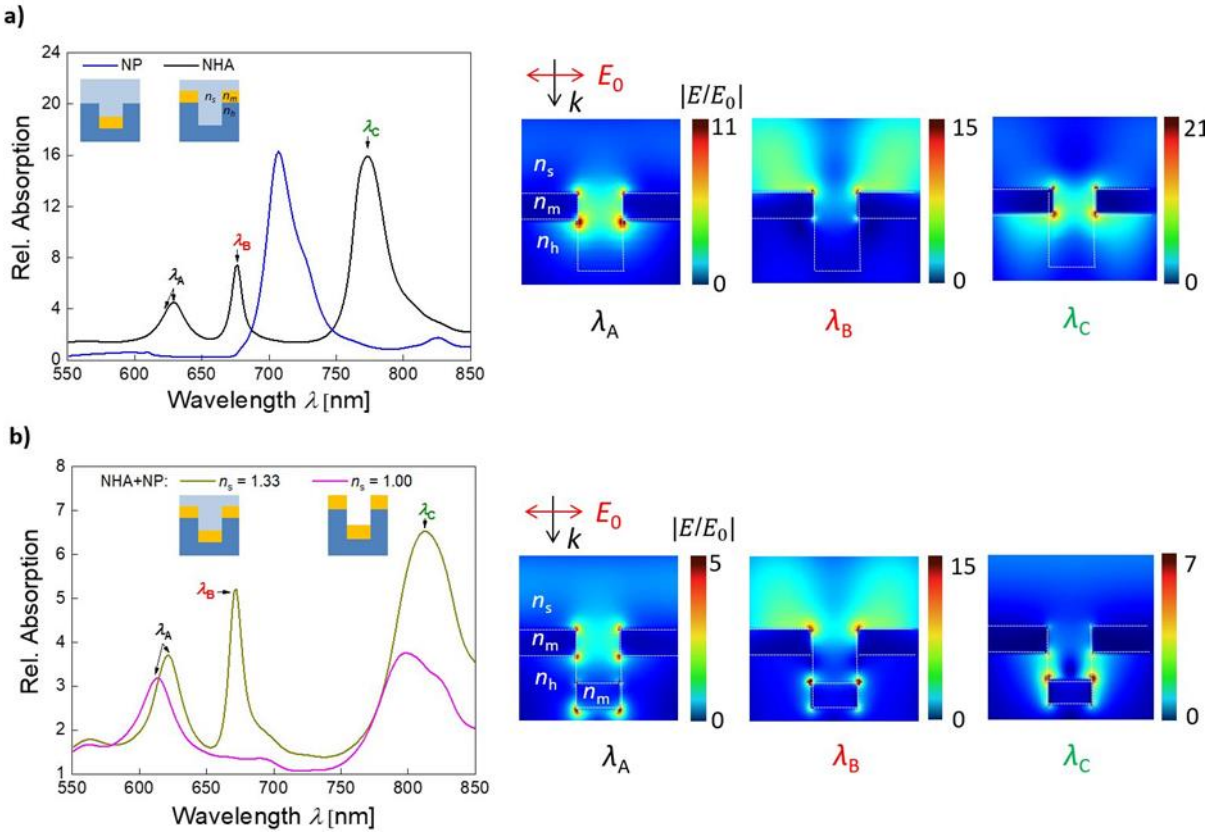

Figure 4. Simulations-based investigation of the spectrum of supported plasmonic modes: the absorption spectra were obtained for normally incident beam at a) structure with a thin gold film perforated with arrays of nanoholes (NHA), with arrays of cylindrical nanoparticle (NP), and for the combined geometry (NHA+NP) with superstrate refractive indices n_s=1 1.33 and substrate refractive index n_h=1.47. b) The absorption spectrum simulated for the NHA+NP geometry for superstrate refractive indices n_s=1 and 1.33. The substrate refractive index was of n_h=1.47, gap distance between NP and NHA was of g=50 nm, period of Λ=460 nm, diameter averaged between D=100-120 nm, and the height of h=50 nm. The cross-section of spatial distribution of the electric field amplitude was simulated for the plasmonic modes as indicated in the inset.

Thirdly, the structure in contact with water was cooled to T=22 °C, which is below the pNIPAAm LCST. Then, there occurred a strong blueshift of λ_A and λ_C^d resonances in the transmission spectrum and also much weaker spectral shift of λ_B^d accompanied with a decreased coupling efficiency at this wavelength (Figure 3c). These observation indicates that the resonances at λ_A and λ_C^d are associated with the coupling to surface plasmon modes that confine electromagnetic field at the inner side of the structure in contact with the pNIPAAm-based hydrogel (with refractive index of n_h=1.47 at T=22 ˚C and n_h=1.37 at T=40 ˚C, see supporting information Figure S1). The resonance λ_B^d probes the upper part of the structure in contact with the water (n_s=1.33) that changes its refractive index with temperature much less than pNIPAAm. As the resonances at λ_B^d and λ_C are dispersive, they can be attributed to PSP modes travelling at the upper or bottom god interface of gold film, respectively. The non-dispersive nature of λ_A resonance indicates it can be ascribed to LSP mode.

More detailed dependence of transmission spectra on temperature T was measured for the normal angle of incidence ϑ=0 (Figure 3d). These spectra were measured by with a different lightsource (supercontinuum laser) in order to extend the wavelength range to 900 nm and it allowed us to observe additional feature that manifests itself as a transmission peak at λ_C^p=810 nm. Moreover, it shows more clearly that close to λ_B^d there appears a peak at a wavelength λ_B^p. It is worth to note that measured transmission spectra were normalized with those obtained for flat 50 nm thick gold film that exhibit rapidly decreasing transmission with wavelength in the red and near infrared part of spectrum. Therefore, the measurement of absolute values of transmission was not possible and only relative values are presented.

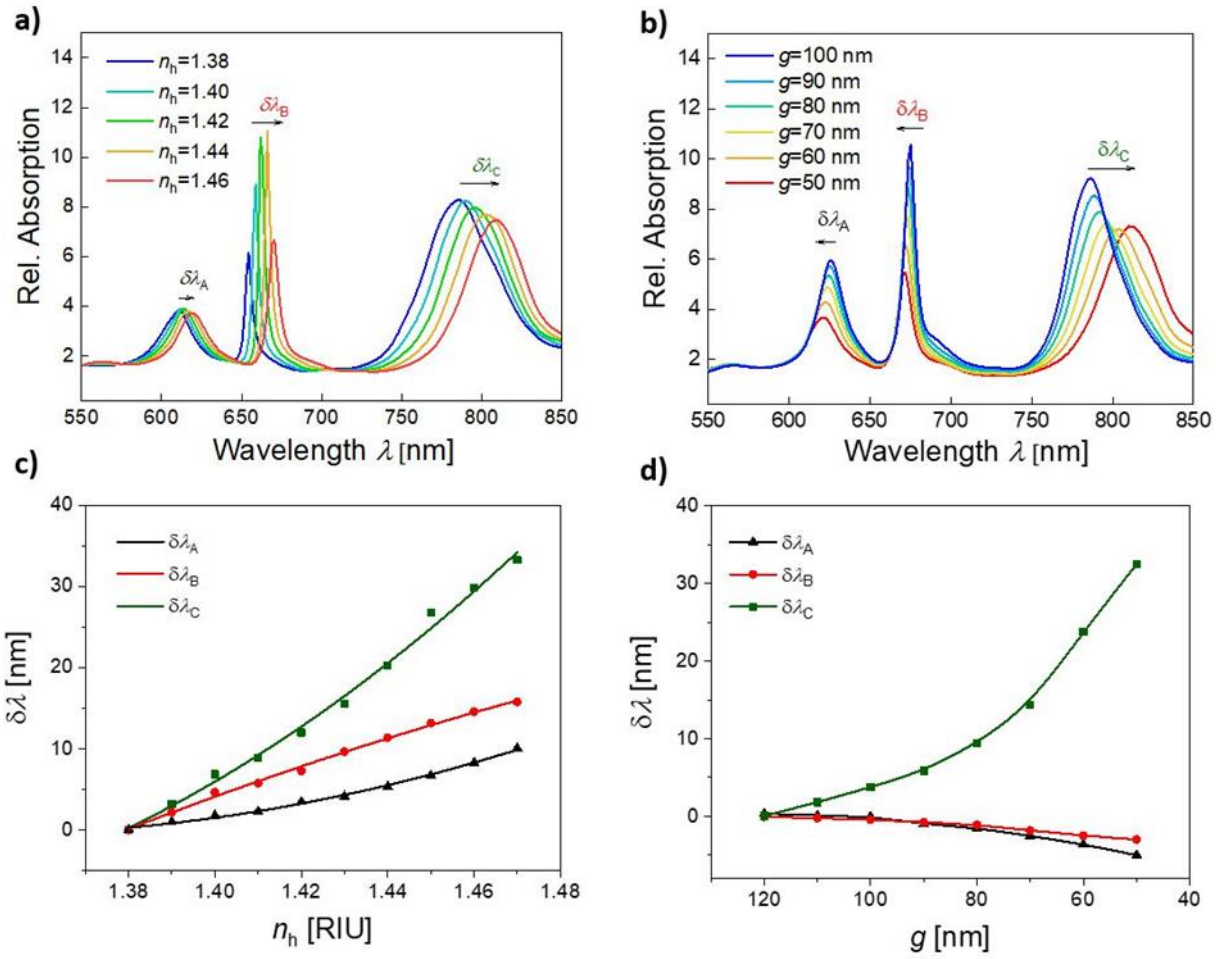

Figure 5. Simulated absorption spectra for the structure NHA+NP for varied a) refractive index of substrate n_h and b) distance g between NHA and NP. From these spectra, the spectral shift of three resonant features are determined for changes c) in n_h and d) in g. The superstrate refractive index was set to n_s=1.33, the substrate refractive index for b) and d) was of n_h=1.47, gap distance between NP and NHA for a) and c) was set as g=50 nm, period was Λ=460 nm, diameter averaged between D=100-120 nm, height h=50 nm.

Identification of plasmonic modes aided by simulations

The observed five resonant features experimentally observed in transmission spectra were identified by using numerical finite difference time domain (FDTD) simulations. This model was employed for the calculation of absorption wavelength spectra and near-field distribution of electromagnetic field occurring in the structure upon a plane wave is normally impinging at its surface. The simulations of absorption spectra allowed us distinguishing between the excitation of LSP and PSP modes (that is accompanied with damping) from other features occurring in transmission spectrum that are related to interference between multiple specular and non-specular diffracted beams and their falling after the horizon in the superstrate or substrate. As shown in Figure 4a (blue curve), we firstly analyzed a structure composed of only arrays of cylindrically shaped nanoparticles – NPs (with a height of *h*=50 nm, diameter averaged over *D*=100-120 nm, and period of *Λ*=460 nm) embedded between dielectrics with

the refractive indices n_h=1.47 and n_s=1.33. The simulated spectrum reveals that the resonance associated with the coupling to LSP on arrays of NPs is manifested as a strong absorption peak at a wavelength of about 707 nm. The complementary NHA structure was composed of a 50 nm thick gold film that is perforated with arrays of cylindrical nanoholes exhibiting the same diameter D and that is sandwiched between same dielectrics with refractive indices n_h=1.47 and n_s=1.33. The absorption spectrum in Figure 4a (red curve) shows three resonances occurring at wavelengths of λ_A=630 nm, λ_B=676 nm, and λ_C=774 nm. At these wavelengths, the near-field distribution of electric field amplitude $|E|$ (normalized with that of the incidence plane wave $|E_0|$) was simulated as can be found in the right part of Figure 4a. These plots reveal that the resonance at wavelength λ_A exhibit characteristics of dipolar LSP mode that confines the field inside the nanohole. The resonance at a longer wavelength λ_B exhibits a more delocalized field profile on the top interface of the gold film with the superstrate n_s=1.33 which confirms it is due to first-order diffraction coupling to traveling PSP mode at this surface. The resonance at NIR wavelength λ_C is accompanied with the confinement of the electric field intensity at the bottom gold layer interface with the dielectric n_h=1.47, which peaks at the mouth of the pore and its distribution suggests the main origin lays in the first-order diffraction coupling to PSPs traveling along the bottom gold film interface. Let us note that these simulations were carried out for the mouth of nanopores filled by a dielectric with refractive index n_s, as the fabrication procedure involving stripping from arrays of nanopillars suggests this geometry (see Figure 2a).

The simulations in Figure 4b (brown curve) reveal that the short wavelength resonance is blue-shifted to λ_A=621 nm, the middle resonance is blue-shifted to λ_A=672 nm, and the long-wavelength resonance is red-shifted to λ_C=813 nm after the coupling of the nanohole arrays with the cylindrical nanoparticle arrays (NHA+NP). In these simulations, the gap distance between the bottom edge of the nanopore and the upper surface of the cylindrically shaped nanoparticle was set to g=50 nm, which corresponds to the difference between the nanopillar height of 100 nm and the thickness of the gold layer of h=50 nm (see Figure 1 and 2). When the refractive index of the superstrate is decreased from n_s=1.33 (representing water) to n_s=1 (representing air), the middle-wavelength resonance vanishes, see Figure 4b (green curve). This observation agrees with the measurements presented in Figure 3 and it confirms that the middle resonance occurs due to the first-order diffractive coupling the PSP mode at the outer gold layer surface, which is most sensitive to variations in refractive index on the upper interface (superstrate n_s). In addition, such a refractive index decrease leads to a slight blue shift in λ_A and λ_C as the field distribution corresponding to these resonances also partially probe the dielectric n_s. The spatial profile of the near field-enhanced electric field amplitude in the right part of Figure 4b shows that the presence of gold disk nanoparticles slightly perturbs the nanohole LSP resonance at λ_A as the field is dragged to the bottom part of the disk nanoparticle. The resonance at λ_B due to the PSPs traveling on

the top interface only weakly couples with the disk nanoparticle, contrary to the bottom PSP mode λ_C that exhibits field distribution much stronger confined in the gap.

Interestingly, the performed simulations predict that only three plasmonic modes are supported in the investigated wavelength range (Figure 4b, brown curve) when the geometry of NHA (with three plasmonic modes, black curve Figure 4a) and NP arrays (with one mode, blue curve in Figure 4a) are combined in order to yield the experimentally investigated structure NHA+NP. However, we identified five features in the experimental transmission data presented Figure 3 which is more than the number of predicted plasmonic modes. The discrepancy between the simulated absorption spectra and experimentally measured specular transmission can be explained by a Fano resonance shape of the two measured transmission features. The middle wavelength peak at λ_B^p and dip at λ_B^d can be attributed to the excitation of a single PSP mode at the interface of the structure with superstrate n_s and its asymmetric can be ascribed to an interference with additional waves generated by the structure in a broader wavelength range (previously observed for related plasmonic nanostructure by simulations[3]). Similarly, the long wavelength peak at λ_C^p and dip at λ_C^d can be attributed to the excitation of a PSP mode at the opposite interface of the structure with superstrate n_h.

In the next step, we performed more detailed simulations in order to reveal the spectral detuning of the resonances by the refractive index changes of the bottom dielectric n_h and the distance g between the gold NPs and NHA. These simulations represent the expected effect of the swelling and collapsing of the pNIPAAm-based hydrogel cushion. In general, the increased swelling is assumed to be accompanied with a prolongation of the distance g, a decreased polymer volume content and consequent decrease in the refractive index n_h. Figures 5a and b show the results for the refractive index n_h gradually increasing from 1.38 to 1.46 and the distance g varied between 50 and 100 nm, respectively. The increase in the substrate refractive index n_h leads to a redshift of all three resonances (Figure 5a) in line with the experimental data presented in Figure 3d. For small changes in refractive index, the variations in the resonant wavelengths can be assumed linear and the determined refractive index sensitivity of $\delta\lambda_B/\delta n_h$=190 nm/RIU and $\delta\lambda_C/\delta n_h$=390 nm/RIU were obtained from simulated data. These values are in the range reported for another SPR sensor configuration that utilizes grating coupling to PSP modes.[47] The lower sensitivity of $\delta\lambda_A/\delta n_h$=90 nm/RIU for the LSP mode is also in accordance to the previous observations on LSPR.[44] Similarly, we obtained the refractive index sensitivity of the three plasmon modes to changes in the refractive index of the superstrate n_s as $\delta\lambda_A/\delta n_s$=137 nm/RIU, $\delta\lambda_B/\delta n_s$=260 nm/RIU and $\delta\lambda_C/\delta n_s$=83 nm/RIU from data presented in Figure S2. Apparently, the highest sensitivity is observed for the mode at λ_B that is ascribed to propagating PSP at the outer interface where its field is dominantly confined.

The simulated spectra for varied gap distance *g* are presented in Figure 5b. They show more complex behavior and apparently the resonances λ_A and λ_B are weakly blue-shifted when increasing the distance *g* while the λ_C is strongly red-shifted. These changes exhibit non-linear behavior and for the shorter distances *g,* they are more pronounced than for the long-distance *g*. Therefore, this observation can be attributed to the near field coupling between the gold NPs and NHA, which is particularly pronounced for the resonance λ_C with its field tightly confined in the gap (see right part of Figure 4b). Interestingly, for long distance *g,* an increase in the absorption close to the wavelength of 700 nm occurs, which may be due to the re-occurrence of the LSP resonance supported by gold NP arrays not coupled with NHA presented in Figure 4a.

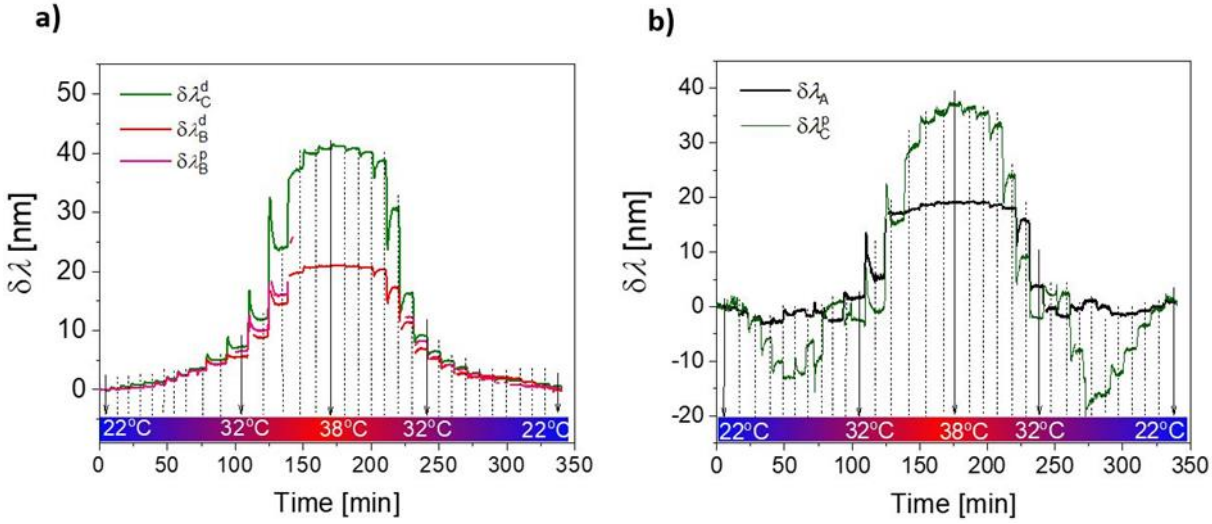

Figure 6. Dependence of spectral position of plasmonic features plotted as function of time for varied temperature from T=22°C to T=38°C: a) gradual variations of spectral positions of dips λ_B^d, λ_C^d and peak at λ_B^p and b) anomalous variations of spectral positions of dip λ_A and peak λ_C^p.

Actuating of plasmonic modes

The swelling and collapsing of the pNIPAAm-based hydrogel cushion by the varying temperature around its LCST were further exploited for actuating the plasmonic modes supported by the prepared structure NHA+NP. In this experiment, we changed the temperature in the range *T*=20-38 °C and tracked the resonant positions of all identified spectral features: transmission dip at λ_A=577 nm due to the LSP in the nanoholes, spectral dip at λ_B^d=641 nm and peak at λ_B^p=658 nm that were ascribed to Fano resonance of PSPs on the top NHA surface, and spectral dip at λ_C^d=684 nm and peak at a wavelength of λ_C^p=825 nm attributed to Fano resonance of PSP at the bottom NHA surface coupled with arrays of NPs (measured at temperature *T*=20 °C). The obtained response was measured in time upon a step-wise increasing and decreasing temperature *T* by the analysis of spectra presented in Figure 3d. The obtained time kinetics in Figure 6 show that the changes are reversible. The features presented in Figure 6a show

a gradual increase in spectral position when increasing temperature *T*. The Fano resonance features λ_B^d and λ_B^p exhibit similar shifts and the maximum change of about 20 nm occurs when raising the temperature from *T*=22 ˚C to 38 ˚C. The highest slope of the shift occurs close to pNIPAAm LCST of 32 ˚C. At higher temperatures the spectral shift of the peak was not possible to track due to the fact that it becomes weakly pronounced. The spectral dip λ_C^d shows same trend and reaches stronger maximum shift of 40 nm for temperature increase from *T*=22 ˚C to 38 ˚C.

Interestingly, the dependence of λ_A and λ_C^p shows different behavior. When increasing temperature from *T*=22 ˚C, initial decrease occurs with a local maximum at *T*=29 ˚C, then it decreases again and above pNIPAAm LCST it rapidly increases and shifts by about 20 nm. The peak position λ_C^p shows a complementary trend and it strongly decreases by 15 nm when increasing temperature from 22 ˚C to 27 ˚C and then it increases and has a local maximum at 30 ˚C and when passing the LCST it rapidly redshifts by 38 nm. These anomalous dependencies can be explained by a competing effect of the near field coupling (which is dominantly controlled by distance *g* and exhibit non-linear dependence, see Figure 5d) and refractive index change that shifts the resonance linearly (see Figure 5c). The anomalous changes occur below the pNIPAAm LCST, which indicates that the distance *g* is not directly proportional to the swelling degree of the hydrogel cushion layer and other effects such as filling the pores with the swelling polymer networks can occur.

Local probing of molecular binding events

In order to explore the potential of the developed hybrid nanostructure for applications in (bio)sensing, we employed the resonances for local probing of molecular binding events at its specific parts. In the first experiment, we directly monitored the binding of biomolecules in the pNIPAAm-based hydrogel cushion from the associated refractive index changes. These changes detune SPR wavelengths, at which there occurs the excitation of modes probing different sub-parts of the structure. After the stripping of the structure, the outer gold surface and the mouth of the pores were passivated by the thiol SAM with polyethylene glycol (PEG) groups. Then, the pNIPAAm-based hydrogel cushion was post-modified *in-situ* by covalent coupling of mouse immunoglobulin G - mIgG. The spectral positions of resonances at λ_A and λ_C^d were monitored by tracking there spectral detuning upon the surface reactions as can be seen in Figure 7a. These two resonances were selected as they probe different parts of the structure and they are well pronounced in the transmission spectrum. In order to activate the carboxylic groups within the hydrogel cushion, they were reacted with EDC/TFPS and then a solution with mIgG was flowed over the surface from the time 45 to 120 min. After rinsing with a buffer at time 120 min, the resonance λ_C^d shifted by 6 nm due to the covalent coupling of mIgG, while the resonance λ_A showed a much weaker shift of about 0.5 nm. This observation proves that the mIgG molecules can diffuse through the pores

and bind to the underneath swollen hydrogel (probed at λ_C^d) while they do not attach to the pores (probed at λ_A). Then, series of PBS solutions with sucrose dissolved at a concentration of 2, 4 and 8 % was flowed over the surface in order to change the bulk refractive index by 2.8, 5.6 and 11.2 × 10^{-3} RIU. These low molecular weight molecules do not interact with the structure but freely diffuse to the pNIPAAm-based hydrogel and thus change the refractive index on both sides of the superstrate n_s as well as substrate hydrogel cushion n_h. From the measured shifts in λ_A and λ_C^d, the sensitivity of these resonances was determined as $d\lambda_A/d_n$=218 nm/RIU and $d\lambda_C^d/d_n$ 454 nm/RIU. These values are close to the predicted sum of the sensitivities $d\lambda/dn_s$ and $d\lambda/dn_h$ and it supports the fact that the refractive index changes at both interfaces of the permeable thin gold film.

In the second experiment, we tested the structure as a substrate for SERS detection. Then, we probed the upper and bottom interfaces by a laser beam focused from the superstrate or substrate side by a lens with a numerical aperture of 0.5. The laser beam exhibited wavelength of λ=785 nm that is close to the resonance observed at λ_C^p associated with the confinement of the incident field in the gap between the NHA and NP (see Figure 4b). In this experiment, we directly used a structure that was stripped and compared the acquired Raman (Stokes-shifted) spectra with those acquired for the same structure where the upper gold surface and the pore mouth was modified with Raman-active 4-MBA monolayer (see schematics in Figure 1b). The results presented in Figure 7b show a series of Raman peaks in the spectral range 800 – 1800 cm^{-1} for the pristine striped structure that was probed from the bottom substrate through the pNIPAAm-based cushion. These peaks can be ascribed to the benzophenone molecules at the inner gold interface as their spectral positions are close to what is reported in previous works.[48] After modifying the pore mouth and the upper gold interface with 4-MBA, additional two peaks occur at 1071 cm^{-1} (aromatic ring breathing, symmetric C-H in-plane bending, C-S stretching) and 1581 cm^{-1} (aromatic ring C-C stretching, asymmetric C-H in-plane bending). These spectral positions are in vicinity to those observed previously for this molecule.[48,49]

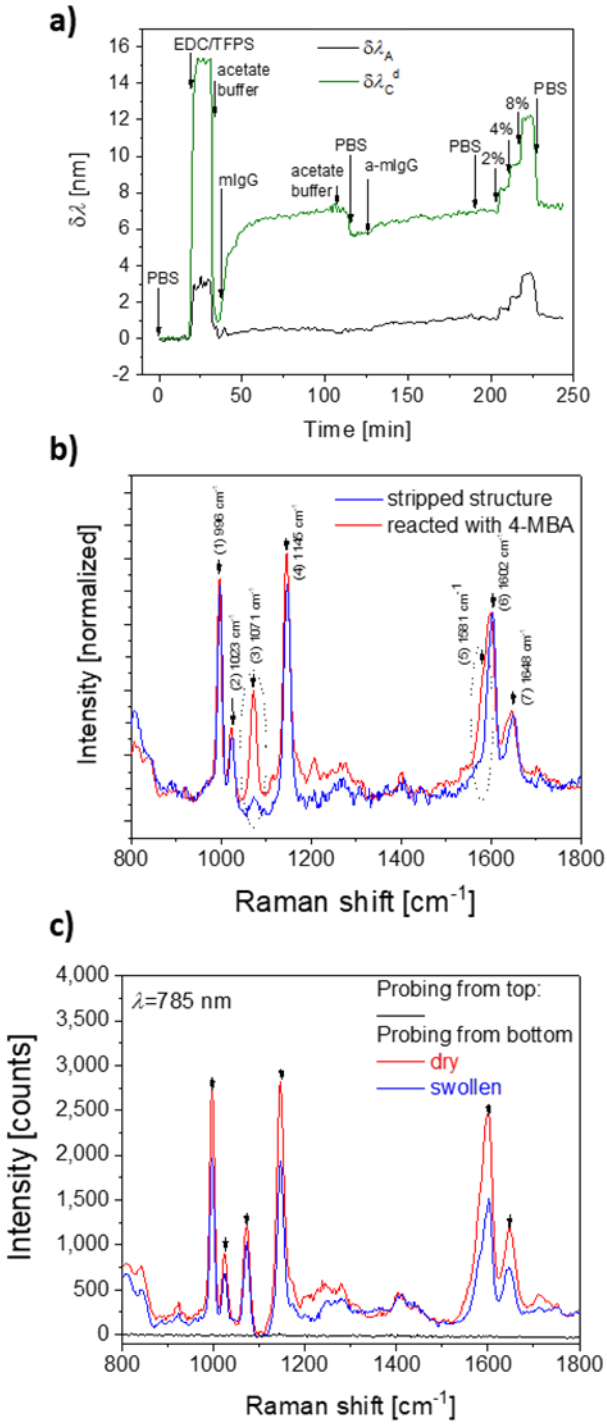

Figure 7. a) The probing of covalent coupling of immunoglobulin G molecules (IgG) to pNIPAAm hydrogel polymer networks with plasmonic modes centred at λ_A and λ_C^d, b) SERS spectra measured before and after the post modification of stripped area of gold with 4-MBA, as measured with the laser wavelength of 785 nm. The structure NHA+NP was swollen in water. c) Comparison of acquired Raman spectra from the top (dry NHA+NP structure) and bottom (swollen and dry NHA+NP structure).

Finally, the comparison of the Raman peaks intensity was carried out for the probing from the top (through the superstrate) and from the bottom (through the pNIPAAm cushion substrate). As can be seen in Figure 7c, the Raman peaks were observed only for the probing from the bottom, where the mode at λ_C^p can be efficiently excited with the laser beam at the wavelength of 785 nm. In addition, the spectral tuning of this mode by collapsing and swelling the structure leads to variations in the Raman peak intensities. An increase in the Raman peaks intensity by about 45% by collapsing the structure (by drying) with respect to the geometry when the hydrogel cushion is swollen in water. This can be attributed to potentially stronger field intensity enhancement in the gap between the nanopore in the NHA and the bottom metallic nanoparticle as well as to a shift of the resonance at λ_C^p to its optimized spectral position with respect to the excitation wavelength and Raman scattered peaks, which was observed to provide most efficient SERS.[50–55]

Conclusions

We developed a new approach for the preparation of hybrid plasmonic nanostructure that can be actuated and consists of arrays of nanoholes in a thin gold film that is connected to arrays of gold nanoparticles by a responsive hydrogel cushion attached to a solid substrate. We explored the spectrum of plasmonic modes supported by the structure and identified their origin due to the resonant excitation of three localized surface plasmons (confined in the nanopores and at the surface of nanoparticles) and diffractive coupling to propagating surface plasmons (traveling along the upper and bottom interface of the thin gold film). By swelling and collapsing of the hydrogel cushion, the characteristics of these modes can be changed on-demand and the field confinement as well as resonant wavelength (up to 50 nm shifts) can be actively actuated. Among others, the near-field coupling between the nanoparticles and nanoholes was observed and the simulations predict that it leads to strong confinement of the electromagnetic field in the respective gap in the near-infrared part of the spectrum. This is particularly attractive for biosensing applications as demonstrated by SPR observation of attachment of 160 kDa IgG molecules inside the structure and SERS measurement of low molecular weight Raman active 4-MBA molecules immobilized in the pore mouth. In addition, the structure can offer a unique opportunity to open and close the pores by swelling and collapsing of the hydrogel cushion. The pores can be thus switched between the dead-end geometry and open state when water molecules are actively driven through the pores dragging dissolved biomolecules across the plasmonic hotspot by diffusion.

Experimental

Materials

OrmoStamp® resin was purchased from Micro Resist Technology GmbH (Germany). The Ostemer 322 Crystal Clear was purchased from Mercene Labs AB (Sweden). Polydimethylsiloxane Sylgard 184 (PDMS) was obtained from Dow Corning (USA). Trichloro (1H,1H,2H,2H-perfluorooctyl) silane (perfluoro-silane), dimethyl sulfoxide (DMSO) and 1-Ethyl-3-(3-dimethylaminopropyl)carbodiimide (EDC) were obtained from Sigma Aldrich (Germany). (11-mercaptoundecyl) triethyleneglycol (PEG-thiol, SPT-0011) was purchased from SensoPath Technologies Inc. (USA). pNIPAAm based terpolymer composed of N-isopropylacrylamide, methacrylic acid, and 4-methacryloyloxybenzophenone (in a ratio of 94:5:1), benzophenone-disulfide and 4-sulfotetrafluorophenol (TFPS) were synthesized in our laboratory as previously reported.[56,57] IgG from mouse serum (mIgG, I 5381) and Tween 20 (P9416) was purchased from Sigma Aldrich (Austria), phosphate-buffered saline (PBS) and sodium acetate were obtained from VWR Chemicals (Austria). Goat anti-mouse IgG (a-mIgG, A11375) was acquired from Life Technologies, (Eugene OR, US).

UV-Nanoimprint lithography

A template structure bearing arrays of nanopillars was fabricated from a silicon master that carried a 1 cm^2 rectangular arrays of nanoholes with a diameter of D = 90 nm, depth 260 nm, and period Λ = 460 nm, fabricated by Temicon GmbH (Germany). 200 µL of OrmoPrime was spin-coated on a cleaned BK7 glass substrate at 4000 rpm for 60 s and hard-baked at 150 °C for 5 min. The BK7 substrate coated with OrmoPrime was contacted with the silicon master by using a drop of OrmoStamp and let still for 10 min in order to spread over the structure and fill the pores. The OrmoStamp was cured by using UV light at λ = 365 nm with the irradiation dose of 1 J/cm^2 (UV lamp Bio-Link 365, Vilber Lourmat). Then, the silicon master was carefully detached, leaving the BK7 substrate with an imprinted pattern of nanopillars in OrmoStamp resin. The fabricated arrays nanopillars were treated with UV-ozone for 5 min in order to remove the excess of OrmoStamp and activate the surface for silanization. An anti-adhesive layer was deposited on the Ormostamp structure in an argon atmosphere by using 13 µL of trichloro (1H,1H,2H,2H-perfluorooctyl) silane in a desiccator (volume 5.8 L) heated to T=250°C for 20 min. A 50 nm thin layer of gold was deposited on the arrays of nanopillars serving as a template by vacuum thermal evaporation (HHV AUTO 306 from HHV LTD) at a deposition rate of 2 Å s^{-1} in a vacuum better than 10^{-6} mbar. Each sample comprised a nanostructured region and a flat region for reference in the optical measurements.

Deposition of the responsive polymer

The Ormostamp arrays of nanopillars coated with 50 nm of gold were incubated overnight in the 1 mM solution of benzophenone-disulfide in DMSO in order to form a self-assembled monolayer serving as a linker. Then, the structure was coated with a uniform layer of pNIPAAm-based terpolymer by spin-coating 3 wt% ethanolic solution of the polymer at a spin rate of 2000 rpm for 1 min. The layer of the pNIPAAm-based terpolymer was dried overnight in a vacuum at 50 °C yielding a thickness of 230 nm. The resulting polymer film was crosslinked via the benzophenone moieties by UV light at λ=365 nm with the irradiation dose of 10 J/cm^2.

Template stripping

A drop of Ostemer epoxy was spread on cleaned BK7 glass by contacting it with a flat piece of PDMS and irradiating with UV-light at λ=365 nm (2 J/cm^2). The PDMS block was peeled-off leaving a glass substrate with a flat layer of a pre-cured Ostemer epoxy on its top. Then, the Ostemer surface was pressed against the template coated with crosslinked pNIPAAm-based film and incubated overnight at 50 °C in order to allow for the attachment to the pNIPAAm-based surface via its epoxy groups. Due to the pre-curing step, the Ostemer did not penetrate the pNIPAAm polymer network layer. Finally, the BK7 substrate with a layer of Ostemer was used to strip off the pNIPAAm-based film with the layer of gold from the template modified with the thin anti-adhesive layer.

Morphological characterization

Atomic force microscopy (AFM) measurements of the patterned structures in the air were acquired in tapping mode by using PPP-NCHR-50 tips (Nanosensors, Switzerland) and the PicoPlus instrument (Molecular Imaging, Agilent Technologies, USA). In addition, a scanning electron microscope (Zeiss Supra 40 VP (Carl Zeiss Microscopy GmbH, Germany) was used for imaging of a longitudinal and cross-section interfaces of the nanostructures at electron high tension EHT = 5 kV. Height, diameter and lateral spacing of the nanoscale features were determined by the Gwyddion free software (version 2.47 from gwyddion.net).

Optical configuration for angular-wavelength transmission measurement

Transmission optical spectra were acquired by using a polychromatic light beam emitted from a halogen lamp (LSH102 LOT-Oriel, Germany) that was coupled to a multimode optical fiber and collimated with a lens. It was made incident at the structure and the transmitted beam was collected by a lens to another multimode optical fiber and delivered to a spectrometer (HR4000, Ocean Optics, USA). The obtained transmission spectra were normalized with that obtained on a reference flat 50 nm thick gold film. A

flow-cell with a Peltier element[58] that was connected to the controller from Wavelength Electronics Inc. (USA) was clamped against the investigated structure in order to control the temperature of the liquid flowed over its surface. Deionized water was flowed through employing a peristaltic pump from Ismatec (Switzerland). The investigated structure with a flow cell was mounted on a rotation stage driven by a stepper motor from Huber GmbH (Germany) to control the angle of incident light ϑ. The transmission spectra were recorded by in-house developed Labview software and processed by using a dedicated Python script.

Tracking of resonant wavelengths

Polychromatic light emitted from supercontinuum laser source (WhiteLaser Micro, Fianium, UK) was collimated and the beam was expanded and spectrally filtered by a long-pass filter. The beam was made incident at normal angle onto the structure mounted in the temperature stabilized flow cell. The transmitted beam was collected by a GRIN lens to a multimode fiber and delivered to an input of a spectrometer (S2000, Ocean Optics, USA). The acquired transmission spectra were normalized by that measured for a reference flat gold film (thickness of 50 nm) and analyzed by a software SPR UP developed at the Institute of Photonics and Electronics, Czech Academy of Sciences.

Finite-difference time-domain simulations

FDTD simulations were done using Lumerical FDTD Solutions software. The geometry of nanoparticle arrays was described by using Cartesian coordinates with the *x*- and *y*- axis in the plane and with *z*-axis perpendicular to the plane of the arrays. An infinite array was considered in the simulations by choosing periodic boundary conditions (symmetric or anti-symmetric) along the *x* and *y* axis and by using perfectly matched layers (PML) above and below the structure. For the field profile simulations, the simulation mesh was set to 2 nm over the volume of the unit cell. A transmission monitor was placed 0.4 μm below the nanoparticle arrays and a 2D monitor in the *xz*-plane was employed for simulating near field distribution of the electric field intensity. The structure was illuminated by normally incident plane wave with its polarization set along the *x*-direction. Optical constants of Au were taken from CRC optical data tables (450-950 nm). In order to take into account the deviations of the experimental geometry from the (idealized) simulated one, the diameter *D* was varied in the range 100-120 nm and respective optical response averaged.

Immunoassay experiment

The substrate carrying the NHA+NP structure was clamped against a transparent flow-cell and loaded to an optical system for tracking of SPR dips in transmission spectrum. A polychromatic optical beam

was made incident at a normal angle of incidence ϑ=0 at the structure and by the analysis of transmitted light spectrum, variations in the resonant wavelengths were monitored in time. These variations were determined by fitting the acquired spectrum with polynomial function as reported before[47] and which allows to measured spectral shifts of dip or peak features with the accuracy 0.1-0.01 nm, depending on the coupling strength and noise in the transmission spectrum. Firstly, the baseline in the resonant wavelength kinetics was established upon a flow of PBS for 20 min. Then, a mixture of EDC/TFPS dissolved in water at concentrations 75 and 21 mg/mL, respectively, was flowed over the structure for 10 min in order to activate the carboxylic moieties of pNIPAAm hydrogel. The surface was quickly rinsed with acetate buffer pH 5 and reacted with a solution of 50 µg/mL mouse IgG in the same buffer for 60 min to covalently attach the mIgG molecules to the polymer chains. Finally, the structure was rinsed with PBS following by the flow of PBS spiked with 2, 4 and 8 % sucrose (Δn=2.8 × 10^{-3}, 5.6 × 10^{-3} and 11.2 × 10^{-3} RIU, respectively).

SERS experiments

The NHA+NP was incubated overnight in 1 mM ethanolic solution of 4-mercaptobenzoic acid to form a self-assembled monolayer of SERS-active molecules. Prior to the experiment, the structure was rinsed with ethanol and dried. The SERS experiments were performed by using an Xplora Raman microspectrometer (Horiba Scientific, France) with a ×50 long working distance objective (numerical aperture of 0.5) was used. The laser beam at λ=785 nm was focused at the investigated NHA+NP structure. The spectrum was accumulated for 20 s.

Conflicts of interest

There are no conflicts to declare.

Acknowledgements

DK acknowledges funding from the European Union's Horizon 2020 research and innovation programme under grant agreement No 642787, Marie Sklodowska-Curie Innovative Training Network BIOGEL. SF, JS, JD, JH and UJ were supported by European Union's Horizon 2020 research and innovation programme under grant agreement no 633937, project ULTRAPLACAD. PV, ML, and MDLC are grateful for the financing from the project jointly funded by Agence Nationale de la Recherche (ANR) and Austrian Science Fund (FWF) under the grant agreements ANR-15-CE29-0026 and I 2647, respectively. SF and JD received support by the Austrian Research Promotion Agency (FFG) with grant agreement No. 861578 (ERANET project PLABAN). JS and JH acknowledge financial support from the Czech Science

Foundation, grant agreement #19-02739S. The Raman analysis was performed at the Vibrational Spectroscopy platform of the IMMM, Université du le Mans.

Notes and references

1. P. A. Ebbesen, T. W., Lezec, H. J., Ghaemi, H. F., Thio, T., & Wolff, *Nature*, 1998, **391**, 667–669.
2. M. Najiminaini, F. Vasefi, B. Kaminska and J. J. L. Carson, *Sci. Rep.*, 2013, **3**, 1–7.
3. M. S. Ahn, T. Chung and K. H. Jeong, *Nanoscale*, 2018, **10**, 6313–6317.
4. A. G. Brolo, S. C. Kwok, M. G. Moffitt, R. Gordon, J. Riordon and K. L. Kavanagh, *J. Am. Chem. Soc.*, 2005, **127**, 14936–14941.
5. Q. Zhang, L. Wu, T. I. Wong, J. Zhang, X. Liu, X. Zhou, P. Bai, B. Liedberg and Y. Wang, *Int. J. Nanomedicine*, 2017, **12**, 2307–2314.
6. A. G. Brolo, E. Arctander, R. Gordon, B. Leathem and K. L. Kavanagh, *Nano Lett.*, 2004, **4**, 2015–2018.
7. N. Zheng, P., Cushing, S. K., Suri, S., & Wu, *Phys. Chem. Chem. Phys.*, 2015, **17**, 21211–21219.
8. S. Kumar, S. Cherukulappurath, T. W. Johnson and S. Oh, *Chem. Mater.*, 2014, **26**, 6523–6530.
9. T. Wu and Y. W. Lin, *Appl. Surf. Sci.*, 2018, **435**, 1143–1149.
10. S. P. Sahu, A. Mahigir, B. Chidester, G. Veronis and M. R. Gartia, *Nano Lett.*, 2019, **19**, 6192–6202.
11. M. E. Stewart, N. H. Mack, V. Malyarchuk, J. A. N. T. Soares, T.-W. Lee, S. K. Gray, R. G. Nuzzo and J. A. Rogers, *Proc. Natl. Acad. Sci. U. S. A.*, 2006, **103**, 17143–17148.
12. A. A. Yanik, A. E. Cetin, M. Huang, A. Artar, S. H. Mousavi and A. Khanikaev, *PNAS*, 2011, **108**, 11784–11789.
13. M. Nakamoto, K., Kurita, R., Niwa, O., Fujii, T., & Nishida, *Nanoscale*, 2011, **3**, 5067–5075.
14. H. Li, X., Soler, M., Özdemir, C. I., Belushkin, A., Yesilköy, F., & Altug, *Lab Chip*, 2017, **17**, 2208–2217.
15. H. Im, H., Shao, H., Park, Y. I., Peterson, V. M., Castro, C. M., Weissleder, R., & Lee, *Nat. Biotechnol.*, 2014, **32**, 490–495.
16. H. Yanik, A. A., Huang, M., Kamohara, O., Artar, A., Geisbert, T. W., Connor, J. H., & Altug, *Nano Lett.*, 2010, **10**, 4962–4969.
17. J. A. Jackman, E. Linardy, D. Yoo, J. Seo, W. B. Ng, D. J. Klemme, N. J. Wittenberg, S. H. Oh and N. J. Cho, *Small*, 2016, **12**, 1159–1166.
18. C. Gomez-Cruz, J., Nair, S., Manjarrez-Hernandez, A., Gavilanes-Parra, S., Ascanio, G., & Escobedo, *Biosens. Bioelectron.*, 2018, **106**, 105–110.
19. L. Tu, X. Li, S. Bian, Y. Yu, J. Li, L. Huang, P. Liu, Q. Wu and W. Wang, *Sci. Rep.*, 2017, **7**, 11020.
20. S. K. Lim, J. T., Yoon, Y. S., Lee, W. Y., Jeong, J. T., Kim, G. S., Kim, T. G., & Lee, *Nanoscale*, 2017, **9**, 17224–17232.
21. S. H. Kumar, S., Wolken, G. G., Wittenberg, N. J., Arriaga, E. A., & Oh, *Anal Chem.*, 2015, **87**, 1973–11977.
22. F. Jonsson, M. P., Jönsson, P., Dahlin, A. B., & Höök, *Nano Lett.*, 2007, **7**, 3462–3468.
23. L. Plucinski, M. Ranjan, W. R. Arnold, A. Ameen, T. Chang, A. Hsiao, G. Logan and A. Das, *Biosens. Bioelectron.*, 2016, **75**, 337–346.
24. W.-C. Liu and T. D. Ping, *Phys. Rev. B*, 2002, **65**, 155423.
25. F. J. Garcia-Vidal, L. Martin-Moreno, T. W. Ebbesen and L. Kuipers, *Rev. Mod. Phys.*, 2010, **82**, 729–787.
26. M. Horak, V. Krapek, M. Hrton, A. Konecna, F. Ligmajer, M. Stoeger-Pollach, T. Samoril, A. Patak, Z. Edes, O. Metelka, J. Babocky and T. Sikola, *Sci. Rep.*, , DOI:10.1038/s41598-019-40500-1.
27. L. Wang, B. Xu, W. Bai, J. Zhang, L. Cai, H. Hu and G. Song, *Plasmonics*, 2012, **7**, 659–663.
28. C. Stelling and M. Retsch, *Adv. Mater. Interfaces*, 2018, **5**, 1–7.
29. R. Mohammadi, M. Ochs, A. Andrieu-Brunsen and N. Vogel, *J. Phys. Chem. C*, 2020, **124**, 2609–2618.
30. M. Hentschel, T. Weiss, S. Bagheri and H. Giessen, *Nano Lett.*, 2013, **13**, 4428–4433.
31. V. G. Kravets, A. V Kabashin, W. L. Barnes and A. N. Grigorenko, *Chem. Rev.*, 2018, **118**, 5912–5951.
32. J. F. Masson, M. P. Murray-Méthot and L. S. Live, *Analyst*, 2010, **135**, 1483–1489.
33. C. Escobedo, *Lab Chip*, 2013, 13, 2445–2463.
34. H. Im, S. H. Lee, N. J. Wittenberg, T. W. Johnson, N. C. Lindquist, P. Nagpal, D. J. Norris and S. H. Oh, *ACS Nano*, 2011, **5**, 6244–6253.
35. S. H. Lee, K. C. Bantz, N. C. Lindquist, S.-H. Oh and C. L. Haynes, *LANGMUIR*, 2009, **25**, 13685–13693.
36. B. Ai, Y. Yu, H. Möhwald, G. Zhang and B. Yang, *Adv. Colloid Interface Sci.*, 2014, 206, 5–16.
37. J. Junesch, T. Sannomiya and A. B. Dahlin, *ACS Nano*, 2012, **6**, 10405–10415.
38. H. Im, J. N. Sutherland, J. A. Maynard and S.-H. Oh, *Anal Chem.*, 2012, **84**, 1941–1947.

39. S. H. Barik, A., Otto, L. M., Yoo, D., Jose, J., Johnson, T. W., & Oh, *Nano Lett.*, 2014, **14**, 2006–2012.
40. J. Dostálek and W. Knoll, *Plasmonics*, 2012, vol. 2.
41. Y. Zhao, G. Gaur, S. T. Retterer, P. E. Laibinis and S. M. Weiss, *Anal. Chem.*, 2016, **88**, 10940–10948.
42. C. Escobedo, A. G. Brolo, R. Gordon and D. Sinton, *Anal Chem.*, 2010, **82**, 10015–10020.
43. N. Sharma, C. Petri, U. Jonas and J. Dostalek, *Opt. Express*, 2016, **24**, 2457.
44. N. Gisbert Quilis, M. van Dongen, P. Venugopalan, D. Kotlarek, C. Petri, A. Moreno Cencerrado, S. Stanescu, J. L. Toca Herrera, U. Jonas, M. Möller, A. Mourran and J. Dostalek, *Adv. Opt. Mater.*, 2019, **7**, 1–11.
45. N. Sharma, H. Keshmiri, X. Zhou, T. I. Wong, C. Petri, U. Jonas, B. Liedberg and J. Dostalek, *J. Phys. Chem. C*, 2016, **120**, 561–568.
46. A. Aulasevich, R. F. Roskamp, U. Jonas, B. Menges, J. Dostálek and W. Knoll, *Macromol. Rapid Commun.*, 2009, **30**, 872–877.
47. A. T. Reiner, N. G. Ferrer, P. Venugopalan, R. C. Lai, S. K. Lim and J. Dostálek, *Analyst*, 2017, **142**, 3913–3921.
48. Y. Fleger, Y. Mastai, M. Rosenbluh and D. H. Dressler, *Surf. Sci.*, 2009, **603**, 788–793.
49. N. G. Quilis, M. Lequeux, P. Venugopalan, I. Khan, W. Knoll, S. Boujday, M. L. de la Chapelle and J. Dostalek, *Nanoscale*, 2018, **10**, 10268–10276.
50. S. J. Lee, Z. Guan, H. Xu and M. Moskovits, *J. Phys. Chem. C*, 2007, **111**, 17985–17988.
51. M. Chirumamilla, A. Gopalakrishnan, A. Toma, R. Proietti Zaccaria and R. Krahne, *Nanotechnology*, 2014, **25**, 235303.
52. N. Guillot and M. L. de la Chapelle, *J. Quant. Spectrosc. Radiat. Transf.*, 2012, **113**, 2321–2333.
53. N. Guillot, B. Fremaux, H. Shen, O. Péron, E. Rinnert, T. Toury and M. Lamy De La Chapelle, *Appl. Phys. Lett.*, 2010, **97**, 023113.
54. S. Kessentini, D. Barchiesi, C. D'Andrea, A. Toma, N. Guillot, E. Di Fabrizio, B. Fazio, O. M. Maragó, P. G. Gucciardi and M. Lamy De La Chapelle, *J. Phys. Chem. C*, 2014, **118**, 3209–3219.
55. F. J. Colas, M. Cottat, R. Gillibert, N. Guillot, N. Djaker, N. Lidgi-Guigui, T. Toury, D. Barchiesi, A. Toma, E. Di Fabrizio, P. G. Gucciardi and M. L. De La Chapelle, *J. Phys. Chem. C*, 2016, **120**, 13675–13683.
56. P. W. Beines, I. Klosterkamp, B. Menges, U. Jonas and W. Knoll, *Langmuir*, 2007, **23**, 2231–2238.
57. K. Sergelen, C. Petri, U. Jonas and J. Dostalek, *Biointerphases*, 2017, **12**, 051002.
58. M. Toma, U. Jonas, A. Mateescu, W. Knoll and J. Dostalek, *J. Phys. Chem. C*, 2013, **117**, 11705–11712.

Supporting information

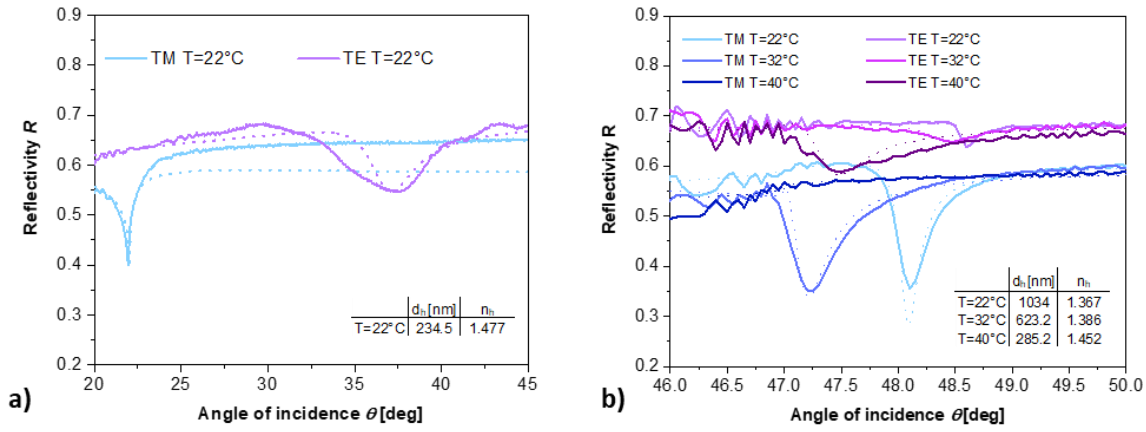

Figure S1. Measurement of thickness and the refractive index of a flat pNIPAAm-based polymer layer on a gold surface a) in a dry state and b) in water by using optical waveguide spectroscopy. Solid lines represent the measured angular scans and dashed curves are the fitted data.

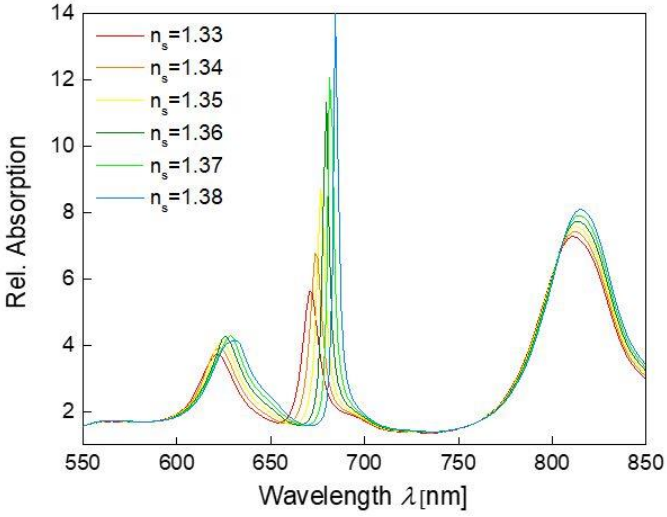

Figure S2. Simulated absorption spectra for the structure NHA+NP for the varied refractive index of superstrate ns the substrate refractive index was of nh=1.47, the gap distance between NP and NHA was set as g=50 nm, the period was Λ=460 nm, diameter averaged between D=100-120 nm, height h=50 nm.3.3. Testing antifouling materials for sensor coating.

3.3. TESTING BIOCOMPATIBLE MATERIALS FOR SENSOR COATING

Thin Film Polyisocyanide-based Hydrogels for Affinity Biosensors

Daria Kotlarek,[†] Kaizheng Liu,[‡] Nestor G. Quilis,[†] Dominik Bernhagen,[¶] Peter Timmerman,[¶] Paul Kouwer,[‡*] Jakub Dostalek[†§*]

[†] Biosensor Technologies, AIT-Austrian Institute of Technology GmbH, Konrad-Lorenz-Straße 24, 3430 Tulln an der Donau, Austria

[‡] Radboud University, Institute for Molecules and Materials, Heyendaalseweg 135, 6525 AJ Nijmegen, The Netherlands

[¶] Pepscan Therapeutics, Zuidersluisweg 2, 8243 RC Lelystad, the Netherlands

[§] FZU-Institute of Physics, Czech Academy of Sciences, Na Slovance 2, Prague 182 21, Czech Republic

Keywords: hydrogel, affinity biosensor, biocompatibility, self-assembly, optical waveguide spectroscopy, plasmonics

ABSTRACT

A new type of hydrogel thin film that can be post-modified with biofunctional molecules is investigated for possible applications in evanescent wave optical affinity biosensors. This material is based on a polyisocyanide (PIC) copolymer that self-assembles into a fibrous polymer network. It is covalently tethered to a solid transducer surface and its swelling gives rise to a hydrogel layer with a thickness up to several micrometers, as characterized by a combination of surface plasmon resonance (SPR) and optical waveguide spectroscopy (OWS). Thin PIC-based hydrogel films with pendant functional biomolecules give access to serve in label-free affinity sensing strategies. In this work, we demonstrate the PIC-based affinity binding matrix through an avidin coupling of functional biomolecules and immunoassay-based detection, which can be readily expanded to other types of assays and target analytes. In addition, the stable PIC matrix proves to be resistant to fouling, even in the presence of complex biological fluids such as blood plasma or serum.

Introduction

Hydrogels are materials composed of chemically or physically crosslinked polymer chains forming a three-dimensional network that can accommodate large amounts of water. The uptake of water by such polymer network occurs without dissolving its structure and it is accompanied by strong volumetric expansion.[1] On-demand swelling and contraction of such polymer networks can be achieved for a sub-

class of (mostly synthetic) responsive hydrogels by applying external stimulus, e.g. temperature,[2] pH,[3] light,[4] pressure,[5] electric or magnetic fields[6] or through specific interactions with (bio)molecules.[7] Besides, the chemical inertness of many hydrogels renders their excellent biocompatibility and minimized non-specific interactions with proteins and cells in complex biological environments. All these features form the basis for widespread hydrogel applications in areas including detection and analysis of chemical and biological species.[8]

Among various bioanalytical tools, evanescent wave optical biosensors and particularly those based on surface plasmon resonance (SPR) have become an established technology for the label-free detection and interaction analysis of (bio)molecules. The sensing principle is based on probing the sensor surface carrying biorecognition elements for affinity capture of target species by using a confined electromagnetic field of surface plasmons.[9] Notably, the utilization of a hydrogel-based binding matrix on the surface of SPR-based sensors improves their performance by matching the volume that is optically probed with that where biorecognition elements are

immobilized. In this approach, the sensing regime is extended from conventionally used two-dimensional architectures (e.g. based on self-assembled monolayers) to the three-dimensional systems that allow for the capture of more analyte molecules from the analyzed liquid sample and that provide an environment that better mimic the natural conditions in biomolecular interaction studies.[10,11] Along with these advancements, other modalities of optical transduction were introduced to SPR-based sensors as the thin hydrogel films at the sensor surface can also act as an optical waveguide. Optical waveguide spectroscopy (OWS)[12] and its combination with fluorescence spectroscopy[13] were employed for optical probing of highly swollen hydrogel films through which their open structure biomolecules can rapidly diffuse and affinity bind. In addition, stimuli-responsive hydrogels were utilized for the actuation of the optical signal in optical affinity SPR-based sensors,[14-16] while their inert chemical nature was exploited for the design of antifouling sensor coatings enabling the detection of biomarkers in complex biological media.[17-19]

Up to now, hydrogels derived from natural polymers, including polysaccharides and polypeptides (e.g. dextran, cellulose, alginate, chitosan, agarose, collagen, hyaluronic acid, and fibrin) were mostly explored for sensing applications, capitalizing on their porous architectures, non-toxicity and cost-efficient preparation. However, they typically lack stimulus-responsive characteristics,[20] which limits the implementation of additional functionalities based on the active tuning of their structure. Recently, a new responsive synthetic and highly biomimetic gel based on oligo(ethylene glycol)-grafted polyisocyanides (PICs) was developed. The glycol tails introduce a strong thermoresponsive behavior in the material, with a reversible sol-gel transition at T_{gel} ~ 18 °C that can be adjusted by the tail length.[21] The helical architecture of PIC is stabilized by the peptidic hydrogen bonds creating stiff polymer chain

bundles providing mechanical strength. Moreover, the polymer can be endowed with additional functional groups for the conjugation with biomolecules (e.g. RGD peptides for enhanced cell adhesion[22]) or crosslinkers. The PIC hydrogel exhibits a stress-stiffening behavior that is wide-spread in biopolymer matrices, however rare in synthetic materials. For instance, stress-stiffening of PIC was reported to play an important role in the commitment of stem-cell fate.[23] Due to the biomimetic properties and thermally-induced gelation temperature, PIC hydrogel was used as a bulk material and applied for wound dressing,[22] 3D cell cultures, and tissue engineering[24] and as an injectable scaffold.[25]
In this contribution, we report on the use of PIC polymers as a matrix for online biosensing in complex bioenvironments. Thin hydrogel films were attached to a solid SPR chip through facile PIC click conjugation chemistry and functionalized with biotin for subsequent biofunctionalization. The swelling of the biomolecule-functionalized PIC hydrogel thin films was observed by OWS combined with SPR. The combination of these evanescent-wave techniques with fluorescence spectroscopy was utilized to measure diffusion and affinity binding of biomolecules inside the hydrogel. The possible implementation of this novel material in bioassays and its resistance to fouling from bodily fluids such as blood plasma is demonstrated.

Experimental section

Materials

Dibenzocyclooctyne (DBCO)-EG4-biotin conjugate was obtained from Sigma Aldrich (Germany). Neutravidin and rabbit anti-mouse IgG (H+L) antibody conjugated with Alexa Fluor 647 were purchased from Thermo Scientific (Austria). Biotinylated mouse IgG was obtained from Abcam (UK). Phosphate buffer saline tablets (PBS: 140 mM NaCl, 10 mM phosphate, 3 mM KCl, pH=7.4) were obtained from Calbiochem (Germany). Normal pooled human serum, plasma, and single donor whole human blood were obtained from Innovative Research (USA). All buffer solutions were prepared by using ultrapure water (arium pro, Sartorius Stedim, Germany). Isocyanide monomers were obtained from Chiralix. Absolute ethanol (99.5%) was purchased from Fisher Scientific. Nickel(II)perchlorate hexahydrate was obtained from Sigma-Aldrich.

Synthesis of PIC co-polymer

The polyisocyanides were synthesized according to an established protocol.[26] Briefly, the isocyanide monomers (3% carrying an azide group for post-functionalization) were dissolved in freshly distilled toluene, then the catalyst $Ni(ClO_4)_2 \cdot 6H_2O$ (0.1 mg mL^{-1} in freshly distilled toluene/absolute ethanol, 9:1 in volume) was added, and the toluene was added to set the final isocyanide concentration

to 50 mg mL^{-1}. The ratio between Ni^{2+} and total monomer concentration was 1:2000 to yield polymers with a molecular weight around 500 kg/mol as determined by viscometry.

Synthesis of DBCO-linker

Dibenzocyclooctyne-EG4-SH (DBCO)-thiol linker for attachment to gold was synthesized as follows. Cysteamonium chloride ($HS(CH_2)_2NH_3Cl$) was dissolved in dimethylformamide (DMF) at c = 4 mM. Next, 0.9 eq DBCO-PEG4-NHS and 10 eq diisopropylethylamine (DIPEA) were added to the solution. The mixture was allowed to react on a rotating mixer for 24 h and quenched with 10% TFA/DMSO to pH < 4. Finally, the product was diluted with purified (MilliQ) water and further purified with HPLC.

Preparation of thin PIC films

The SPR sensor chips were prepared on BK7 glass substrates. Vacuum thermal evaporation (HHV AUTO 306 from HHV LTD) was used for the deposition of the 2 nm layer of chromium followed by a 50 nm layer of gold. The metal deposition rate was 2 Å s^{-1} in a vacuum better than 10^{-6} mbar. The gold surface of the prepared substrates was immersed in an ethanolic solution of 1 mM DBCO-thiol to form a self-assembled monolayer (SAM). After overnight incubation, the substrates were rinsed with copious amounts of ethanol to remove the excess of unbound DBCO-thiol, dried in the stream of air, and placed on ice for at least 15 min. The 4 mg/ml stock solution of gelled PIC hydrogel was cooled below its gelation temperature T_{gel} (for the used copolymer of 15 °C). The obtained fluid polymer solution was diluted in cold ultrapure water to yield a concentration of c = 0.5, 1.0, 2.0, and 4.0 mg/mL. Then, 200 µL of each solution was pipetted on a separately cooled substrate with the DBCO-thiol SAM. The PIC solution on the top of such an SPR sensor chip was left on ice for 30 min to allow for click reaction between the azide groups carried by the PIC chains and the DBCO moieties at the gold surface, which typically occurs in several minutes.[27] Afterwards, the SPR sensor chip was spun at 1000 rpm for 30 s in order to yield a thin homogenous polymer film that was allowed to slowly reach room temperature. After 30 min, a dry surface of PIC film was obtained and additional layers of the polymer were prepared by repeating the procedure with lowered spin rate to 500 rpm.

Optical setup

An in-house developed sensor instrument relying on angular interrogation of SPR and surface plasmon-enhanced fluorescence (SPFS) was used, see Figure 1. A monochromatic beam (λ_{ex} = 632.8 nm, 2 mW) was transverse magnetically (TM) or transverse electrically (TE) polarized by a polarizer (POL). The linearly polarized light beam

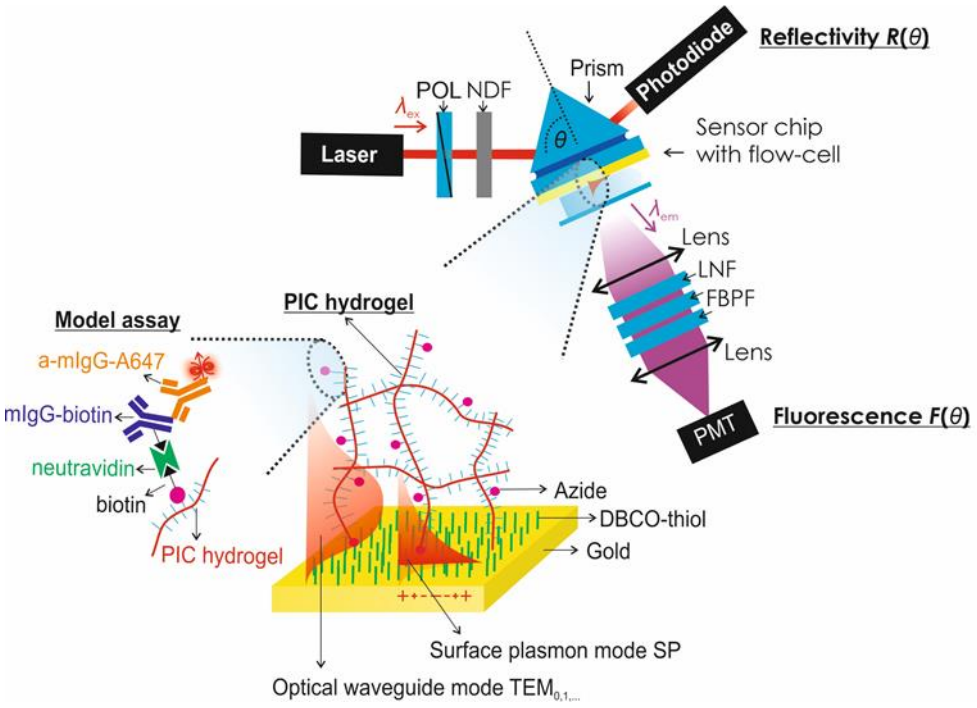

Figure 1. Optical setup employed for the combined surface plasmon resonance (SPR), optical waveguide spectroscopy (OWS), and fluorescence spectroscopy for the characterization and monitoring of affinity binding events inside the PIC-based thin hydrogel films.

passed through a chopper and was coupled to the 90° LASFN9 glass prism that was mounted on a rotation stage to control the angle of incidence ϑ. The SPR chip with a layer of attached PIC-based hydrogel was optically matched to the prism base by using an immersion oil (Cargille Inc., USA). The intensity of the beam R that reflected at the SPR sensor chip surface was measured as a function of angle of incidence ϑ by a photodiode connected to a lock-in amplifier (EG&G, USA). Liquid samples were transported over the SPR sensor chip surface at the flow rate of 50 mL min^{-1} by using a flow-cell connected to a Tygon tubing and a peristaltic pump (Ismatec, Germany). Fluorescence light emitted from the sensor surface in the perpendicular direction was collected through the flow-cell made from a transparent glass substrate. It was excited by the evanescent field on the sensor surface at a wavelength λ_{ex} and the emitted beam at wavelengths close to λ_{em}=670 nm was collected by the lens. It was then spectrally cleaned by a notch filter (LNF, the central stop-band wavelength of 632.8 nm, XNF-632.8-25.0M, CVI Melles Griot, USA) and two bandpass filters (FBPF, transmission wavelength λ=670 nm, 670FS10-25, Corporation Optical Filter, USA). The fluorescence intensity F was measured by a photomultiplier (H6240-01, Hamamatsu, Japan) that was connected to a counter (53131A, Agilent, USA). To minimize the bleaching of emitters, the intensity of the excitation laser beam at λ_{ex} was reduced to 1% by using a neutral-density filter (NDF, Linos Plano Optics). The angular reflectivity spectra $R(\vartheta)$ and fluorescence intensity $F(\vartheta)$ were recorded by a Wasplas software (Max Planck Institute for Polymer Research, Mainz, Germany).

Observation of thin PIC-based hydrogel layers

Thin layers of the PIC-based hydrogel were investigated in contact with air and water by using SPR combined with OWS. The thickness d_h and refractive index n_h of swollen hydrogel films and thickness $d_{h\text{-}dry}$ and refractive index $n_{h\text{-}dry}$ of dry hydrogel films were determined by fitting the reflectivity scans in TM and TE polarization $R(\vartheta)$ with a Fresnel reflectivity-based model implemented in Winspall software (Max Planck Institute for Polymer Research, Germany). A "box" approximation was used in which the layers were assumed homogeneous and a possible density gradient in the direction perpendicular to the surface was omitted. The swelling ratio *SR* of the PIC-based hydrogel layers was calculated from the experimentally found thickness of the hydrated and dry layers:

$$SR = \frac{d_{\mathrm{h}}}{d_{\mathrm{h-dry}}}. \qquad (1)$$

The respective polymer volume fraction *f* was obtained from the effective medium theory as[17]:

$$f = \frac{(n_h^2 - {n_{\mathrm{b}}}^2)\,({n_{\mathrm{h-dry}}}^2 + 2{n_{\mathrm{b}}}^2)}{({n_{\mathrm{h}}}^2 + 2{n_{\mathrm{b}}}^2)\,({n_{\mathrm{h-dry}}}^2 - {n_{\mathrm{b}}}^2)}, \qquad (2)$$

where n_b = 1.334 states the refractive index of buffer (PBS)[12] in contact with the polymer film, n_h and $n_{h\text{-}dry}$ are the refractive indices of the hydrated and the dried PIC layers, respectively. The surface mass density Γ of the PIC-based hydrogel layer loaded with biomolecules was determined as[28]:

$$\Gamma = (n_{\mathrm{h}} - n_{\mathrm{b}}) \times d_{\mathrm{h}} \times \frac{\partial c}{\partial n}, \qquad (3)$$

where we used for the coefficient describing the changes in refractive index with the concentration of proteins $\frac{\partial n}{\partial c} = 0.2\ \mu\mathrm{L/mg}$.[29]

AFM analysis of PIC-based hydrogel layers

The topography of dry PIC-based polymer layers was measured by using atomic force microscopy (PicoPlus from Molecular Imaging, Agilent Technologies, Germany) with tapping mode tips PPP-NCHR-50 (Nanosensors, Switzerland). The obtained images were processed in the open-source software Gwyddion (version 2.47 from gwyddion.net).

Post-modification of PIC-based hydrogel

Firstly, the SPR sensor chip carrying the PIC-based hydrogel layer was loaded to the SPR sensor instrument (Figure 1). The surface was rinsed with PBS for 5 min and then 200 µM DBCO-biotin dissolved in PBS was reacted with the PIC hydrogel layer for 30 min. The excess of DBCO-biotin was removed by rinsing the sensor chip with PBS for 5 min. Subsequently, a solution of 200 µM neutravidin was placed on top of the PIC hydrogel layer for 90 min and rinsed with PBS for 5 min. Then, biotinylated mouse IgG dissolved in PBS at a concentration of 50 µg/mL was allowed to bind to the PIC-based hydrogel matrix for 30 min. Finally, PBS with 2 µg/mL of rabbit anti-mouse IgG (that was tagged with the fluorescent dye Alexa Fluor-647) was flowed over the PIC-based hydrogel for 30 min followed by rinsing with PBS for 5 min.

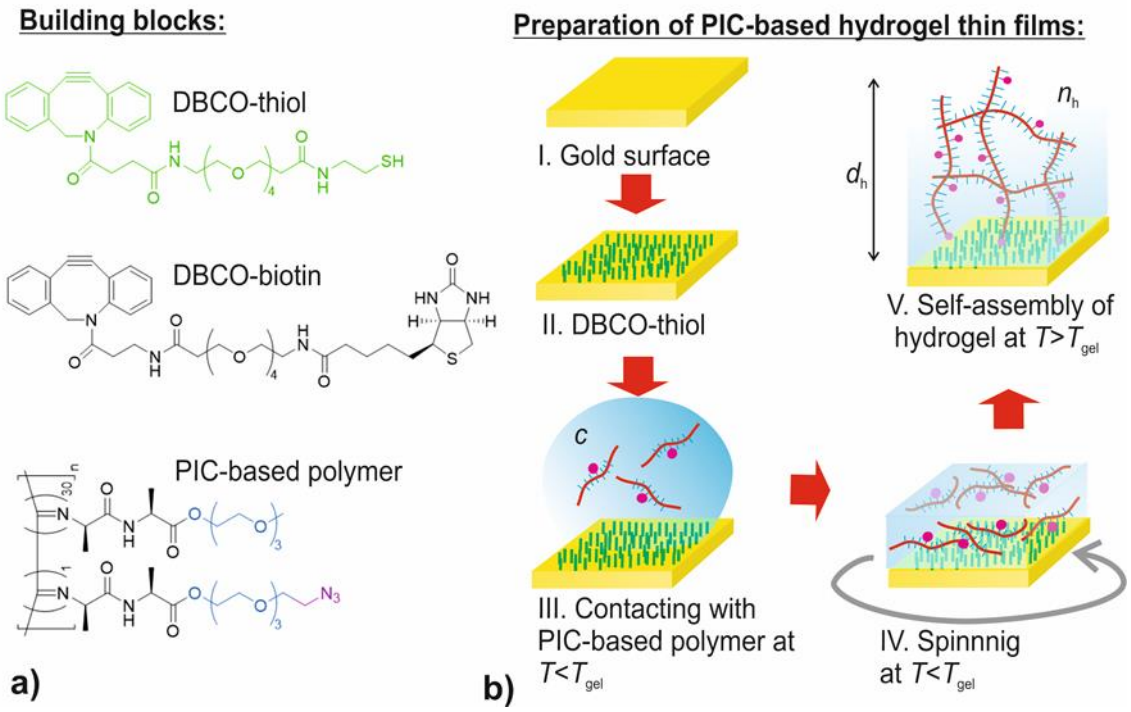

Figure 2. a) Overview of used linkers and PIC-based copolymer and b) the preparation of thin PIC-based hydrogel film.

Results and discussion

Preparation of PIC-based hydrogel layers

In order to graft the PIC hydrogel to the SPR sensor chip, its gold-coated surface was firstly reacted with a glycol linker carrying thiol group and dibenzocyclooctyne head group (DBCO-thiol), see Figure 2a. The DBCO-thiol was allowed to form a self-assembled monolayer [30] for the subsequent attachment of the PIC-based gel layer. As illustrated in Figure 2b, the PIC-based polymer was dissolved in water that was

cooled down below the gelation temperature T_{gel} and the solution was contacted with the DBCO-modified gold surface. The PIC-based polymer in the solution reacted with the DBCO groups at the surface via its attached azide groups to establish a permanent graft. After the grafting reaction, the substrate with the polymer solution on its top was spun in order to form a thin hydrated layer. This layer was slowly heated to temperature T=22 °C in 30 min, which is above the PIC polymer T_{gel}, and thus the bundling of the polymer chains and respective gel formation can occur before it dries. The concentration of PIC polymer in the aqueous solution was varied between 0.5-4 mg/mL to control the thickness and density of the PIC polymer-based film. The thickness of the dried film $d_{h\text{-}dry}$ was determined by SPR measurement from a shift of the SPR dip in the measured reflectivity spectrum $R(\vartheta)$ that was fitted with the Fresnel reflectivity-based model. As Figure 3a shows, SPR occurs at an angle of ϑ_{SP} = 25.8° on a bare gold surface (control without PIC-based polymer layer). After the coating with the PIC layer, the SPR angle shifts to a higher angle (reaching up to ϑ_{SP} = 35.68° for the 4 mg/mL PIC solution). The analysis of measured spectra $R(\vartheta)$ allowed for determining the film thickness $d_{h\text{-}dry}$ in the range of 4-40 nm as presented in Figure 3b. It is worthy of noting that the film thickness $d_{h\text{-}dry}$ can be further increased by repeating the coating procedure. As it is shown in Figure 3b, repeated deposition of the PIC-polymer from 4 mg/mL by using the same procedure with a decreased spin rate of 500 rpm yielded an increased thickness of $d_{h\text{-}dry}$ = 103 and 143 nm for two and three deposition cycles, respectively.

A previous study of the bulk PIC hydrogel structure showed that in average 7 helical polymer chains form a bundle with a diameter of 7.5 nm.[31] It was observed that the concentration of the polymer does not impact the bundle's diameter but rather their abundance and, as a result, the pore size of the hydrogel matrix. Indeed, this observation was later confirmed by a confocal fluorescence imaging that showed a heterogeneous structure of interconnected fibrils with a pore size reaching 1 to 10 µm depending on the concentration.[32] Refractive index of the herein prepared dry PIC polymer-based films was determined as $n_{h\text{-}dry}$ = 1.4624, which is below the value obtained for dense biopolymers and indicates that the structure comprises voids induced by the bundling of individual chains due to the forming of a network. The topography of dry PIC polymer-based dry layer prepared from 4 mg/mL solution was characterized by using atomic force microscopy (see Figure S1). Our analysis of the thin polymer films revealed that the surface of the dry PIC-based polymer layer exhibits an rms roughness of ± 4.2 nm and we did not observe the fine structure of polymer bundles. The reason can be attributed to the fact that the bundles are rather densely packed in the investigated dry polymer layer.

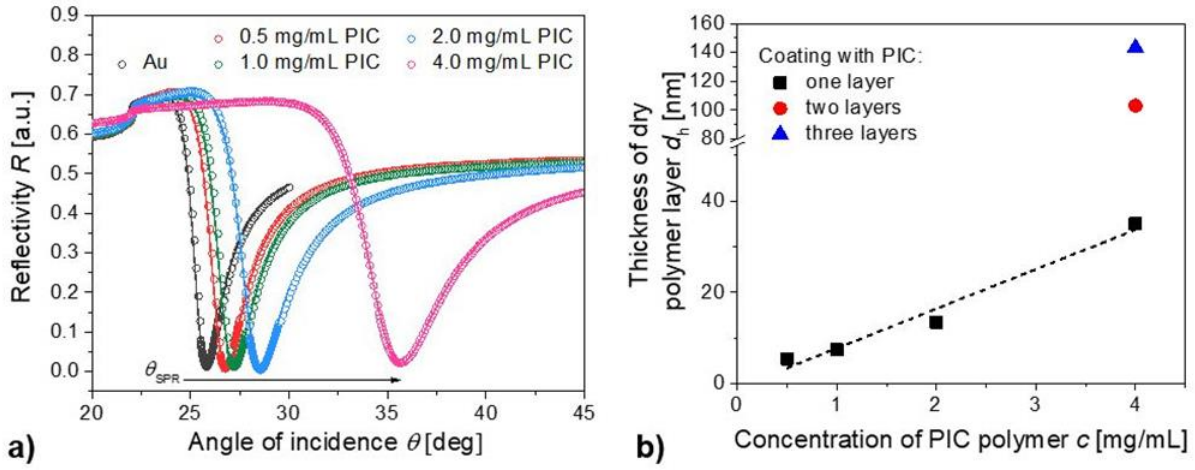

Figure 3. a) Reflectivity spectra R for dry polymer films prepared from a solution of PIC polymer at concentrations c and spun at 1000 rpm. b) Measured dependence of the fitted thickness on c for one (1000 rpm), two (1000, 500 rpm) and three (1000, 500, 500 rpm) sequential depositions. The points were fitted with the linear function where a = -0.93 ± 2.3 and b = 8.66 ± 1.0.

Swelling of thin PIC hydrogel layers

To prove that the grafted PIC polymer-based film forms a hydrogel, the layer was brought in contact with an aqueous liquid at room temperature (T = 22 °C that is above the PIC gel temperature T_{gel}). Combined surface plasmon resonance (SPR) and optical waveguide spectroscopy (OWS) were used for the SPR sensor chip carrying PIC film with a dry thickness of $d_{h\text{-}dry}$ = 101 nm and refractive index $n_{h\text{-}dry}$ = 1.4624. The polymer layer was contacted with phosphate-buffered saline (PBS) and angular reflectivity spectra $R(\vartheta)$ were measured for both transverse magnetic (TM) and transverse electric (TE) polarization, as showed in Figure 4a and b. Contrary to the measurement for a dry film (presented in Figure 3a), the angular spectra acquired from a film swollen in PBS show richer characteristics. The spectrum $R(\vartheta)$ exhibits two distinct resonances in TM polarization: besides the excitation of surface plasmons at ϑ_{SP} = 58.74°, we observed an additional dielectric waveguide mode TM_1 at ϑ_{TM1} = 47.42°. Moreover, $R(\vartheta)$ in the orthogonal TE polarization shows a faint resonance at ϑ_{TE0} = 47.50°, which is associated with a dielectric waveguide mode TE_0. The analysis of the reflectivity spectra allowed us to determine the thickness d_h and the refractive index n_h of the hydrated PIC layer. It reveals that thickness increased from $d_{h\text{-}dry}$ = 101 nm to d_h = 1558 nm and refractive index decreased to n_h = 1.3420, close to that of water. These data indicate that the PIC polymer layer did not dissolve and that the formed polymer networks swelled by the uptake of water with the swelling ratio of SR = 15.4 determined from equation (1). These data imply a decreased polymer volume fraction f = 6.3%, based on equation (2), using the measured refractive indices n_h, $n_{h\text{-}dry}$, and that of PBS buffer n_b=1.334. In addition, the respective surface mass density of the PIC-based hydrogel was calculated as Γ = 62.3 ng/mm^2 by using equation (3). This

value is slightly lower than Γ = 72.9 ng/mm^2 determined for the dry film, prior to the swelling, due to possible detachment of a small fraction of loosely bound polymer chains from the surface.

PIC-based hydrogel 3D binding matrix – post-modification

After establishing the protocol for the formation of a thin hydrogel layer on the gold substrate, we explored its application to serve as a three-dimensional binding matrix that can host biomolecules and allow for specific interactions with their affinity binding partners. In order to demonstrate this functionality, the azide groups on the PIC chains in the network were used for attaching functional biomolecules in a post-modification approach. The biofunctionalization steps were monitored by combined SPR and OWS for a pristine hydrogel film with a thickness of d_h = 1558 nm and a refractive index of n_h = 1.342.

We utilized the well-known biotin-streptavidin interaction for the coupling of functional proteins to PIC-based hydrogel.[33] In the first step, free azide moieties present on the PIC chains were reacted with the DBCO-biotin conjugate through the same catalyst-free click conjugation reaction that was used for substrate grafting (see Figure 2). After the reaction, the surface was rinsed with PBS and we observed corresponding shifts in the resonant angles ϑ_{TM1} and ϑ_{TE0} in the reflectivity scans $R(\vartheta)$. The acquired shifts to ϑ_{TM1}=47.46° and ϑ_{TE0}=47.53° indicate that the surface mass density of the PIC-based hydrogel layer increased by 4.07 ng/mm^2 to Γ = 66.40 ng/mm^2 due to the attachment of biotin groups conjugated with DBCO (molecular weight 0.75 kDa). In the next step, the biotin groups on the PIC were allowed to bind to neutravidin (molecular weight of 60 kDa). After the rinsing away excess protein with PBS, the dielectric waveguide mode resonances shifted to values ϑ_{TM1} = 47.58° and ϑ_{TE0} = 47.65°; these shifts correspond to a further increase of surface mass density by 15.57 ng/mm^2 to Γ = 81.97 ng/mm^2. It is worth noting that the measured surface mass density increase after the immobilization of neutravidin is 4-times higher

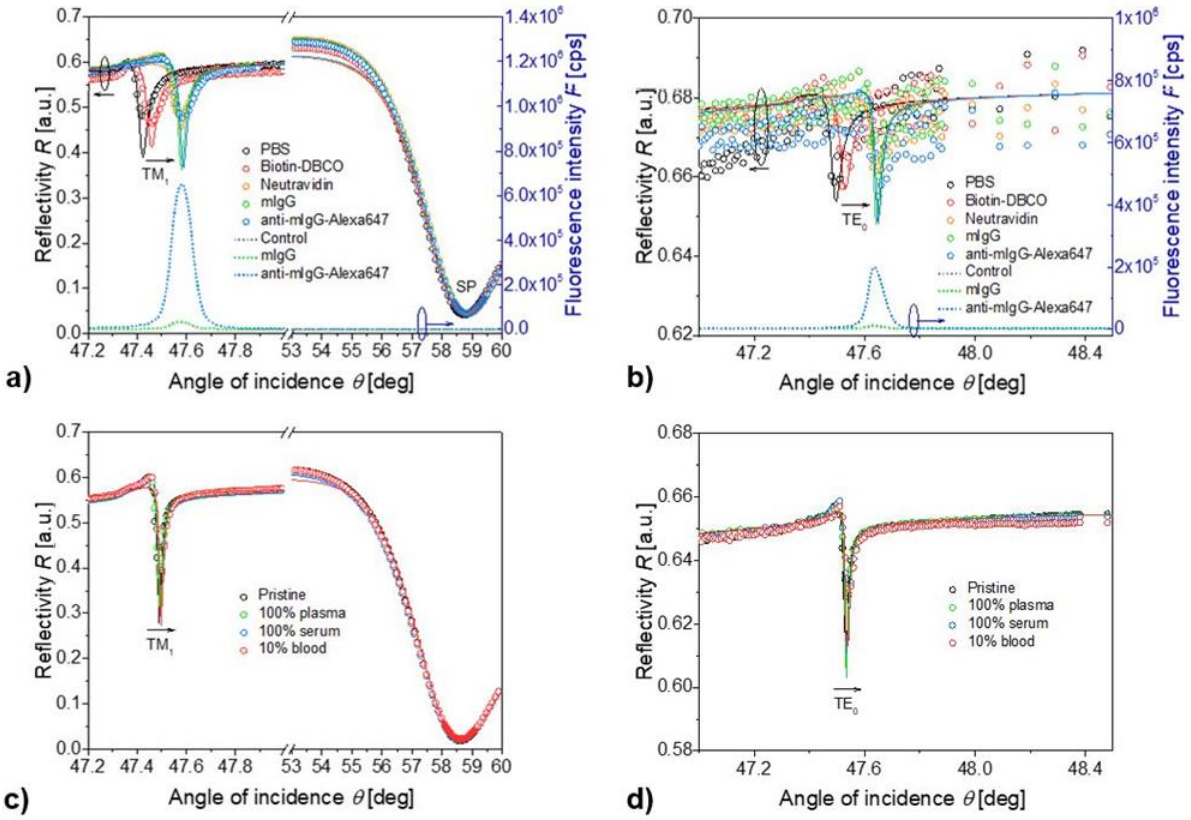

Figure 4. Changes in resonant coupling to a) SP and TM1 waves and b) TE0 wave upon a sequential reacting of the PIC hydrogel layer with biotin-DBCO, neutravidin, mouse IgG, and anti-mouse IgG conjugated with Alexa Fluor 647 fluorophore. Changes in resonant coupling to c) SP and TM1 waves and d) TE0 wave upon after the exposure of PIC-based hydrogel to 10% blood, undiluted plasma and undiluted serum.

compared to that for the biotin–DBCO conjugate. However, the molecular weight ratio of these molecules of 80 is much larger, which indicates that only a limited fraction of available biotin groups reacted with the neutravidin. A potential reason for this difference is that multiple biotin groups can bind one neutravidin molecule (carrying four binding pockets). This avidity is associated with additional crosslinking of the PIC hydrogel that may hinder the diffusion of molecules through the network and cause undesired crowding at the interface of the hydrogel film with the neutravidin solution. In line with this observation, we noticed a negligible shift in the SPR angle ϑ_{SP} after the coupling of biotin with neutravidin. The ϑ_{SP} angle probes about a 100 nm thin slice of the PIC-based hydrogel at its inner interface with the gold film. Therefore, the molecules reaching this interface need to diffuse through the whole PIC-based polymer network and may experience a more crowded environment due to the covalent attachment of the chains to the gold surface that thus hinders the affinity reaction.

PIC-based hydrogel as a 3D binding matrix – immunoassay and antifouling properties

In order to demonstrate the functionality of neutravidin-modified PIC coating as a binding matrix for immunoassays, a biotinylated mouse IgG (mIgG) was affinity bound into the PIC film with neutravidin

molecules, followed by the binding of its affinity partner - fluorophore-labeled anti-mIgG antibody. The first step was directly monitored by measuring a shift in the resonant angles ϑ_{TM1} and ϑ_{TE0} as can be seen in Figure 4. The increase in surface mass density to Γ = 82.45 ng/mm^2 was determined by the analysis of these changes. Considering the IgG molecular weight of about 160 kDa, this surface mass density change indicates that only a small fraction of neutravidin molecules inside the PIC-based hydrogel was available for reacting the mIgG-biotin molecules. A possible explanation for such decreased efficiency in the loading of this molecule to the PIC-based hydrogel layer is the crowding at the upper interface of the hydrogel occurring due to the densely packed neutravidin and, possibly, the additional crosslinking effect of reacting with mIgG carrying multiple biotin tags. The immobilized mIgG, however, allowed for the specific capture of anti-mIgG antibodies that were labeled with fluorophores Alexa Fluor 647 (A647), which allows for visualization by fluorescence spectroscopy. The fluorescence label was excited at λ_{ex} = 633 nm, coincident with the absorption band of A647 via the enhanced field intensity associated with the resonant excitation of the SP and dielectric waveguide modes TM_1 and TE_0. The binding of anti-mIgG conjugated with A647 gives rise to strong fluorescence peaks occurring in the angular scans $F(\vartheta)$ measured at the emission wavelength of λ_{em} = 670 nm at resonant angles ϑ_{TM1} and ϑ_{TE0}, see Figure 4a and b. These peaks show a strong intensity increase to $F = 6.5\times10^5$ cps for the TM_1 mode and 2×10^4 cps for the TE_0 mode, which corresponds to 20 times higher signal than the background indicating that, indeed, the PIC polymer gel can be used for sensing applications. Interestingly, no fluorescence signal increase was measured for ϑ_{SP}, which supports the hypothesis the binding of IgG molecules primarily occurred at the interface of PIC hydrogel films for the used neutravidin-biotin immobilization strategy.

As sensing is often required in complex (biological) fluids, sensor fouling is a recurring problem. The resistance to fouling of the PIC hydrogel was tested using blood serum, plasma, and 10 % diluted whole blood plasma. As seen in Figures 4c and d, a 15 min flow of these biological fluids followed by a 5 min rinse with PBS did not lead to a measurable shift in the resonances as measured for the surface plasmon modes SP or the dielectric waveguide modes TM_1 and TE_0 (Table 1 in SI). Overall, the 45 minutes exposure to various biological media resulted in the total shift of TM_1 and TE_0 modes by approximately 0.008° and an increase of surface mass density by less than $\Delta\Gamma$ = 1 ng/mm^2. The antifouling nature of the PIC hydrogel can be assigned to the high level of hydration and presence of the relatively inert oligo(ethylene glycol) chains [that in self-assembled monolayers of alkanethiols with oligo(ethylene glycol) headgroups are commonly used to prevent fouling of the sensor surfaces[34]]. Although the measurement of the resistance to nonspecific interactions of the PIC matrix shows its potential to serve as an efficient antifouling biointerface, the accuracy of the performed measurements does allow comparison with the best performing antifouling materials known to date. For instance, the zwitterionic

carboxybetaines and *N*-2-hydroxypropyl methacrylamide (HPMA) polymer brush layers were reported to prevent fouling of the complex media at a level of several pg/mm^2.[35] However, these biointerfaces exhibit a thickness that is about two orders of magnitude shorter than herein reported PIC-based architecture, which consequently affects the surface mass density of deposited biomolecules.

Conclusions

In this manuscript, we deposited a polyisocyanide-based hydrogel on a solid surface in form of a thin film and demonstrated that it can serve as an affinity binding matrix for sensing applications. The PIC gel is introduced on the chip in a two-step attachment procedure and the film thickness is readily controlled by the preparation conditions. The open fibrous structure of the hydrogel allows for diffusion of medium size protein molecules, which allows for post-modification of the polymer network with functional moieties. In our work, we demonstrated the functionalization with biotin and subsequent reaction with neutravidin, which is a frequently used platform for further conjugation of biomolecules and implementation of assays including the herein used immunoassay. Hydrogel swelling and successive conjugation steps were monitored in a label-free manner by the combined SPR and OWS. Our work demonstrates that the PIC gels can be used to form stable hydrogel layers without the need for chemical or photo-crosslinking chemistry, which simplifies preparation and is biomolecule compatible. Also, the antifouling properties of the gel are advantageous. This study is the first step for the future development of robust PIC-based 3D sensor matrices for efficient affinity biosensors. The use of evanescent optical techniques may provide a facile tool for the characterization of such thin films in order to tailor them also for other application fields. For example, one can envision using a PIC-functionalized SPR sensor for simultaneous cell culturing and monitoring of cellular secretion molecules of interest.

Associated content

Supporting Information include a Table with a calculation of the surface mass density of the hydrogel layers. This material is available free of charge via the Internet at http://pubs.acs.org.

Corresponding Author

* Dr. Paul Kouwer, E-mail: p.kouwer@science.ru.nl, Phone: +31 024 3652464

* Jakub Dostalek, PhD, E-mail: jakub.dostalek@ait.ac.at, Phone: +43 664 235 1773

Author Contributions

All authors have given approval to the final version of the manuscript.

Funding Sources

DK, KL and NGQ received funding from the European Union's Horizon 2020 research and innovation programme under grant agreement No 642787, Marie Sklodowska-Curie Innovative Training Network BIOGEL. J.D. was supported by Lower Austria project IKTHEUAP number WST3-F-5030820/010-2019 and the ESIF and MEYS (FZU researchers, technical and administrative staff mobility–CZ.02.2.69/0.0/ 0.0/18_053/0016627).

Abbreviations

SPR, surface plasmon resonance; OWS, optical waveguide spectroscopy; PIC, polyisocyanideisocyanide hydrogel; OEG, oligo(ethylene glycol) side chains; DBCO, dibenzocyclooctyne; SAM, self-assembled monolayer; TM, transverse magnetic; TE, transverse electric;

References

(1) Gibas, I.; Janik, H. Review : Synthetic Polymer Hydrogels for Biomedical. 2010, *4* (4).

(2) Zhang, X. Z.; Wang, F. J.; Chu, C. C. Thermoresponsive Hydrogel with Rapid Response Dynamics. *J. Mater. Sci. Mater. Med.* 2003, *14* (5), 451–455. https://doi.org/10.1023/A:1023219019500.

(3) Dai, S.; Ravi, P.; Tam, K. C. PH-Responsive Polymers: Synthesis, Properties and Applications. *Soft Matter* 2008, *4* (3), 435–449. https://doi.org/10.1039/b714741d.

(4) Zhao, Y. L.; Fraser Stoddart, J. Azobenzene-Based Light-Responsive Hydrogel System. *Langmuir* 2009, *25* (15), 8442–8446. https://doi.org/10.1021/la804316u.

(5) Katsuno, C.; Konda, A.; Urayama, K.; Takigawa, T.; Kidowaki, M.; Ito, K. Pressure-Responsive Polymer Membranes of Slide-Ring Gels with Movable Cross-Links. *Adv. Mater.* 2013, *25* (33), 4636–4640. https://doi.org/10.1002/adma.201301252.

(6) Reddy, N. N., Mohan, Y. M., Varaprasad, K., Ravindra, S., Joy, P. A., & Raju, K. M. Magnetic and Electric Responsive Hydrogel–Magnetic Nanocomposites for Drug-delivery Application. *J. Appl. Polym. Sci.* 2011, *122* (2), 1364–1375. https://doi.org/https://doi.org/10.1002/app.34016.

(7) Culver, H. R.; Clegg, J. R.; Peppas, N. A. Analyte-Responsive Hydrogels: Intelligent Materials for Biosensing and Drug Delivery. *Acc. Chem. Res.* 2017, *50* (2), 170–178. https://doi.org/10.1021/acs.accounts.6b00533.

(8) Cascone, S.; Lamberti, G. Hydrogel-Based Commercial Products for Biomedical Applications: A Review. *Int. J. Pharm.* 2020, *573* (May 2019), 118803. https://doi.org/10.1016/j.ijpharm.2019.118803.

(9) Homola, J.; Piliarik, M. Surface Plasmon Resonance (SPR) Sensors. In *Surface plasmon resonance based sensors*; Springer: Berlin, Heidelberg, 2006; pp 45–67.

(10) Löfås, S., & Johnsson, B. A Novel Hydrogel Matrix on Gold Surfaces in Surface Plasmon Resonance Sensors for Fast and Efficient Covalent Immobilization of Ligands. *J. Chem. Soc. Chem. Commun.* 1990, No. 21, 1526–1528. https://doi.org/10.1039/C39900001526.

(11) Howell, S.; Kenmore, M.; Kirkland, M.; Badley, R. A. High-Density Immobilization of an Antibody Fragment to a Carboxymethylated Dextran-Linked Biosensor Surface. *J. Mol. Recognit.* 1998, *11* (1–6), 200–203. https://doi.org/10.1002/(SICI)1099-1352(199812)11:1/6<200::AID-JMR423>3.0.CO;2-7.

(12) Wang, Y.; Huang, C. J.; Jonas, U.; Wei, T.; Dostalek, J.; Knoll, W. Biosensor Based on Hydrogel Optical Waveguide Spectroscopy. *Biosens. Bioelectron.* 2010, *25* (7), 1663–1668. https://doi.org/10.1016/j.bios.2009.12.003.

(13) Huang, C.-J.; Jonas, U.; Dostálek, J.; Knoll, W. Biosensor Platform Based on Surface Plasmon-Enhanced Fluorescence Spectroscopy and Responsive Hydrogel Binding Matrix. *Opt. Sensors 2009* 2009, *7356*, 735625. https://doi.org/10.1117/12.820988.

(14) Endo, T.; Ikeda, R.; Yanagida, Y.; Hatsuzawa, T. Stimuli-Responsive Hydrogel-Silver Nanoparticles Composite for Development of Localized Surface Plasmon Resonance-Based Optical Biosensor. *Anal. Chim. Acta* 2008, *611* (2), 205–211. https://doi.org/10.1016/j.aca.2008.01.078.

(15) Toma, M.; Jonas, U.; Mateescu, A.; Knoll, W.; Dostalek, J. Active Control of SPR by Thermoresponsive Hydrogels for Biosensor Applications. *J. Phys. Chem. C* **2013**, *117* (22), 11705–11712. https://doi.org/10.1021/jp400255u.

(16) Sharma, N.; Keshmiri, H.; Zhou, X.; Wong, T. I.; Petri, C.; Jonas, U.; Liedberg, B.; Dostalek, J. Tunable Plasmonic Nanohole Arrays Actuated by a Thermoresponsive Hydrogel Cushion. *J. Phys. Chem. C* **2016**, *120* (1), 561–568. https://doi.org/10.1021/acs.jpcc.5b10336.

(17) Zhang, Q.; Wang, Y.; Mateescu, A.; Sergelen, K.; Kibrom, A.; Jonas, U.; Wei, T.; Dostalek, J. Biosensor Based on Hydrogel Optical Waveguide Spectroscopy for the Detection of 17β-Estradiol. *Talanta* **2013**, *104*, 149–154. https://doi.org/10.1016/j.talanta.2012.11.017.

(18) Yang, W.; Xue, H.; Carr, L. R.; Wang, J.; Jiang, S. Zwitterionic Poly(Carboxybetaine) Hydrogels for Glucose Biosensors in Complex Media. *Biosens. Bioelectron.* **2011**, *26* (5), 2454–2459. https://doi.org/10.1016/j.bios.2010.10.031.

(19) Buzzacchera, I.; Vorobii, M.; Kostina, N. Y.; De Los Santos Pereira, A.; Riedel, T.; Bruns, M.; Ogieglo, W.; Möller, M.; Wilson, C. J.; Rodriguez-Emmenegger, C. Polymer Brush-Functionalized Chitosan Hydrogels as Antifouling Implant Coatings. *Biomacromolecules* **2017**, *18* (6), 1983–1992. https://doi.org/10.1021/acs.biomac.7b00516.

(20) Ahmed, E. M. Hydrogel: Preparation, Characterization, and Applications: A Review. *J. Adv. Res.* **2015**, *6* (2), 105–121. https://doi.org/10.1016/j.jare.2013.07.006.

(21) Kouwer, P. H. J.; de Almeida, P.; ven den Boomen, O.; Eksteen-Akeroyd, Z. H.; Hammink, R.; Jaspers, M.; Kragt, S.; Mabesoone, M. F. J.; Nolte, R. J. M.; Rowan, A. E.; et al. Controlling the Gelation Temperature of Biomimetic Polyisocyanides. *Chinese Chem. Lett.* **2018**, *29* (2), 281–284. https://doi.org/10.1016/j.cclet.2017.11.002.

(22) op 't Veld, R. C.; van den Boomen, O. I.; Lundvig, D. M. S.; Bronkhorst, E. M.; Kouwer, P. H. J.; Jansen, J. A.; Middelkoop, E.; Von den Hoff, J. W.; Rowan, A. E.; Wagener, F. A. D. T. G. Thermosensitive Biomimetic Polyisocyanopeptide Hydrogels May Facilitate Wound Repair. *Biomaterials* **2018**, *181*, 392–401. https://doi.org/10.1016/j.biomaterials.2018.07.038.

(23) Das, R. K.; Gocheva, V.; Hammink, R.; Zouani, O. F.; Rowan, A. E. Stress-Stiffening-Mediated Stem-Cell Commitment Switch in Soft Responsive Hydrogels. *Nat. Mater.* **2016**, *15* (3), 318–325. https://doi.org/10.1038/nmat4483.

(24) Zimoch, J.; Padial, J. S.; Klar, A. S.; Vallmajo-Martin, Q.; Meuli, M.; Biedermann, T.; Wilson, C. J.; Rowan, A.; Reichmann, E. Polyisocyanopeptide Hydrogels: A Novel Thermo-Responsive Hydrogel Supporting Pre-Vascularization and the Development of Organotypic Structures. *Acta Biomater.* **2018**, *70*, 129–139. https://doi.org/10.1016/j.actbio.2018.01.042.

(25) Weiden, J.; Voerman, D.; Dölen, Y.; Das, R. K.; Van Duffelen, A.; Hammink, R.; Eggermont, L. J.; Rowan, A. E.; Tel, J.; Figdor, C. G. Injectable Biomimetic Hydrogels as Tools for Efficient T Cell Expansion and Delivery. *Front. Immunol.* **2018**, *9* (NOV), 1–15. https://doi.org/10.3389/fimmu.2018.02798.

(26) Liu, K.; Mihaila, S. M.; Rowan, A.; Oosterwijk, E.; Kouwer, P. H. J. Synthetic Extracellular Matrices with Nonlinear Elasticity Regulate Cellular Organization. *Biomacromolecules* **2019**, *20* (2), 826–834. https://doi.org/10.1021/acs.biomac.8b01445.

(27) Schoenmakers, D. C.; Rowan, A. E.; Kouwer, P. H. J. Crosslinking of Fibrous Hydrogels. *Nat. Commun.* **2018**, *9* (1), 1–8. https://doi.org/10.1038/s41467-018-04508-x.

(28) Aulasevich, A.; Roskamp, R. F.; Jonas, U.; Menges, B.; Dostálek, J.; Knoll, W. Optical Waveguide Spectroscopy for the Investigation of Protein-Functionalized Hydrogel Films. *Macromol. Rapid Commun.* **2009**, *30* (9–10), 872–877. https://doi.org/10.1002/marc.200800747.

(29) Perlmann, G. E.; Longsworth, L. G. The Specific Refractive Increment of Some Purified Proteins. *J. Am. Chem. Soc.* **1948**, *70* (8), 2719–2724. https://doi.org/10.1021/ja01188a027.

(30) Vericat, C.; Vela, M. E.; Benitez, G.; Carro, P.; Salvarezza, R. C. Self-Assembled Monolayers of Thiols and Dithiols on Gold: New Challenges for a Well-Known System. *Chem. Soc. Rev.* **2010**, *39* (5), 1805–1834. https://doi.org/10.1039/b907301a.

(31) Kouwer, P. H. J.; Koepf, M.; Le Sage, V. A. A.; Jaspers, M.; Van Buul, A. M.; Eksteen-Akeroyd, Z. H.; Woltinge, T.; Schwartz, E.; Kitto, H. J.; Hoogenboom, R.; et al. Responsive Biomimetic Networks from Polyisocyanopeptide Hydrogels. *Nature* **2013**, *493* (7434), 651–655. https://doi.org/10.1038/nature11839.

(32) Vandaele, J.; Kouwer, P. H. J.; Louis, B.; Liu, K.; Camacho, R. Structural Characterization of Fibrous Synthetic Hydrogels Using Fluorescence Microscopy †. **2020**, 4210–4219. https://doi.org/10.1039/c9sm01828j.

(33) Mandal, S.; Eksteen-Akeroyd, Z. H.; Jacobs, M. J.; Hammink, R.; Koepf, M.; Lambeck, A. J. A.; van Hest, J. C. M.; Wilson, C. J.; Blank, K.; Figdor, C. G.; et al. Therapeutic Nanoworms: Towards Novel Synthetic Dendritic Cells for Immunotherapy. *Chem. Sci.* 2013, *4* (11), 4168–4174. https://doi.org/10.1039/c3sc51399h.
(34) Zhu, B.; Eurell, T.; Gunawan, R.; Leckband, D. Chain-Length Dependence of the Protein and Cell Resistance of Oligo (Ethylene Glycol)-Terminated Self-Assembled Monolayers on Gold. *J Biomed Mater Res.* 2001, *56* (3), 406–416. https://doi.org/10.1002/1097-4636(20010905)56:3<406::aid-jbm1110>3.0.co;2-r.
(35) Rodriguez-Emmenegger, C.; Houska, M.; Alles, A. B.; Brynda, E. Surfaces Resistant to Fouling from Biological Fluids: Towards Bioactive Surfaces for Real Applications. *Macromol. Biosci.* 2012, *12* (10), 1413–1422. https://doi.org/10.1002/mabi.201200171.

Supporting information

Table 1. Calculation of the surface mass density of the hydrogel layers.

	dh [nm]	nh	Γ [ng/mm2]
Pristine dry	101.13	1.4624	233.8126
Pristine in PBS	1558.26	1.3420	62.3304
Biotin-DBCO	1660	1.3420	66.4000
Neutravidin	1928.8	1.3425	81.9740
mIgG-biotin	1940	1.3425	82.4500
a-mIgG-A640	1963	1.3425	83.4275

Pristine in PBS	2167.04	1.3400	65.0112
Human plasma	2177	1.3400	65.3100
Human serum	2198	1.3400	65.9400
10% human blood	2200	1.3400	66.0000

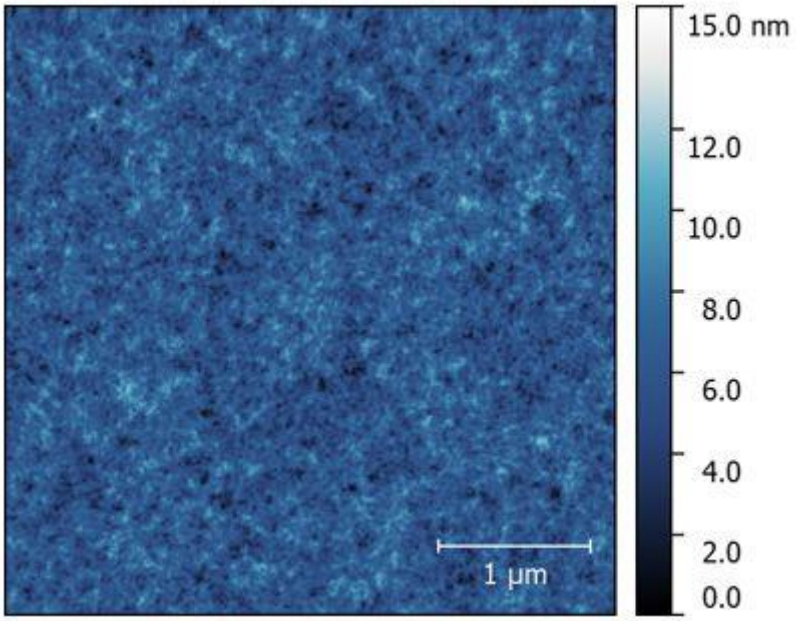

Figure S1. AFM topography of a dry PIC-based polymer film prepared from 4 mg/mL solution and spun at 1000 rpm. The black horizontal line indicates a measurement of the surface roughness.

3.4. COMPACT READER IMPLEMENTATION

Compact Grating-Coupled Biosensor for the Analysis of Thrombin

Daria Kotlarek,[†], Mariia Vorobii,[‡] Wojciech Ogieglo,[‡,§] Wolfgang Knoll[†], Cesar Rodriguez-Emmenegger,[‡] Jakub Dostálek[†,*].

[†] Biosensor Technologies, AIT-Austrian Institute of Technology GmbH, Konrad-Lorenz-Straße 24, 3430 Tulln an der Donau, Austria

[‡] DWI – Leibniz Institute for Interactive Materials and Institute of Technical and Macromolecular Chemistry, RWTH Aachen University, Forckenbeckstraße 50, 52074 Aachen, Germany

[§] Current address: Advanced Membranes & Porous Materials Center, 4700 King Abdullah University of Science and Technology (KAUST), Thuwal 23955-6900, Kingdom of Saudi Arabia

Keywords: surface plasmon resonance, grating-coupled surface plasmon resonance, biosensor, thrombin, antifouling brushes, aptamer, blood plasma, point of care

ABSTRACT

A compact optical biosensor for direct detection of thrombin in human blood plasma (HBP) is reported. This biosensor platform is based on wavelength spectroscopy of surface plasmons on a chip with a periodically corrugated gold film that carries an antifouling thin polymer layer consisting of poly[(*N*-(2-hydroxypropyl) methacrylamide)-*co*-(carboxybetaine methacrylamide)] poly(HPMA-*co*-CBMAA) brushes. This surface architecture provides superior resistance to nonspecific and irreversible adsorption of abundant compounds in the analyzed HBP samples in comparison to standard surface modifications. The carboxylate groups along the polymer brushes were exploited for the covalent immobilization of aptamer ligands. These ligands were selected to specifically capture target thrombin analyte from the analyzed HBP sample in a way that does not activate the coagulatory process at the biosensor surface with poly(HPMA-*co*-CBMAA) brushes. Direct label-free analysis of thrombin in the medically relevant concentration range (1 – 20 nM) is demonstrated without the need for diluting the HBP samples or using additional steps for signal enhancement. The reported platform constitutes the first step toward a portable and sensitive point-of-care (POC) device for direct detection of thrombin in human blood.

Introduction

Hemostasis is an indispensable physiological mechanism that maintains the integrity of the vascular system and circulation of the blood in the fluid state.[1] It relies on a number of highly regulated pro- and anti-thrombotic pathways that control the suppression of bleeding at the site of vessel injury, clot dissolution, and wound remodeling.[2] The delicate balance between coagulation and fibrinolytic activity can be disrupted by congenital and acquired coagulopathies,[1] anticoagulation therapy,[3] surgical procedures,[4,5] cardiopulmonary bypass,[6] and extracorporeal life support (ECLS).[7] In these cases, the patient is exposed to a risk of life-threatening hemorrhage or a thrombotic event that requires immediate medical intervention. The incidence of hemostatic complications and their consequences (mortality, number of transfusions, time spent in the intensive care, cost of the treatment) can be substantially reduced by routine clinical diagnostics complemented by self-testing of a patient's coagulation status.[8-10] Yet, because of the complexity of the hemostatic system with a plentiful positive and negative feedback controls, a generic and widely accepted method for the assessment of coagulation stage does not exist neither at patient´s home nor in the clinical practice.[11]

Affinity optical biosensors based on surface plasmon resonance (SPR) are considered as one of the prime candidates for the 'next generation' diagnostic devices.[12] The SPR biosensors hold potential to serve in emerging POC applications offering the advantage of fast response, real-time measurement, and already developed implementations to portable devices.[13] Up to now, portable systems based on SPR biosensor principle were pursued for the applications in food safety,[14,15] environmental monitoring, biodefense,[16,17] and medical diagnostics.[18,19] The majority of the reported portable SPR devices rely on the Kretschmann configuration of the attenuated total reflection (ATR) enabling resonant excitation of propagating surface plasmons (PSPs) on sensor surface with continuous metallic film.[20,21] In order to simplify the use of SPR sensor chips in compact or portable reader devices, diffraction grating-coupled surface plasmon resonance (GC-SPR) provides an alternative to ATR method.[22,23] The GC-SPR chips carry nanostructures which can be fabricated by scaled up means by injection molding,[24] roll-to-roll nanoimprint lithography,[25] or laser interference lithography.[26] These types of nanostructures were integrated to disposable sensor chips and used in the compact sensor designs supported by dedicated readers[27-29] as well as by optics integrated to smartphones.[30]

Throughout the last years, we witnessed a gradual progress in the development of thrombin biosensors based on electrochemical,[31] piezoelectric[32] and optical transducers.[33] Among these, SPR biosensors reached the limit of detection at pico- and attomolar concentrations[34,35] and relied on readers with miniature design by using plasmonic nanostructures[36] or optical fibers.[37] Although detection of thrombin in medically relevant range (5 – 20 nM) is well established in model samples, the operation in complex biological media such as human blood, plasma, and serum remains challenging due to the

unspecific adsorption of matrix proteins to the sensor surface - a phenomenon also called 'fouling'. The fouling from blood plasma is the result of complex cooperative intermolecular interactions,[38] which constitutes a multiscale process that begins with adsorption of smaller proteins that are subsequently replaced by more surface-affine ones (Vroman effect[39]) and followed by the activation of different coagulatory factors as well as thrombocytes. In the SPR affinity biosensors, fouling severely complicates the discrimination between the response originating from the capture of the target analyte and the unspecific protein adsorption on the sensor surface, and thus, impairs their performance. The most common approach to reduce the protein fouling is a modification of the metallic surface with self-assembled monolayers (SAM) carrying oligo(ethylene glycol) moieties.[40] This modification typically provides good resistance to the fouling from model samples, however, it is not sufficient when the sensor surface is challenged with more complex bodily fluids.[41] Often used strategy to mitigate the effect of unspecific interactions is diluting the analyzed sample ten to hundreds of times with a reaction buffer,[42,43] which lowers the concentration of the target analyte that is available for the detection by the same factor. In addition, there were reported multiple-step assays with the enhancement of specific response by using sandwich assay format combined with metallic nanoparticles[43] and advanced reference-compensated measurement strategies were pursued.[44] Despite these advances in SPR biosensor technology, only one of the aforementioned studies achieved sufficient limit of detection (LOD) of thrombin in 10% serum for the prediction of the thrombotic event by the combined aptamer-based rolling circle amplification and bio-bar-coded AuNP enhancement.[35]

Notably, the SPR analysis of complex biological media can be simplified by the implementation of anti-fouling biointerface architecture that will resist the biological matrix effect and thus enable the specific detection of the target analyte without the need of sample dilution or signal amplification. The poly[(*N*-(2-hydroxypropyl) methacrylamide)-*co*-(carboxybetaine methacrylamide)] poly(HPMA-*co*-CBMAA) brushes have become one of the most successful strategies for eliminating protein adsorption on the sensor surface from blood serum and plasma[45–47] and saliva.[48] Most importantly, the immobilization of the receptor molecules to these poly(HPMA-*co*-CBMAA) brushes induces only minute changes in their structure and thus it minimally impairs their anti-fouling properties. This functionality was demonstrated for brushes prepared by statistical copolymerization of two anti-fouling monomers HPMA and CBMAA (85:15%) that provides a small fraction of side groups available for functionalization with receptors.[45]

In this study, we address the important clinical need for a compact device to monitor the concentration of thrombin in biological media by developing a compact plasmonic biosensor. It should be emphasized that the detection of thrombin in the blood plasma is particularly challenging because its capture on the sensor surface locally increases its concentration and can trigger the coagulation cascade. Therefore,

the surface of a diffraction grating was coated with an advanced biointerface architecture comprising poly(HPMA-*co*-CBMAA) brushes that were post modified with aptamer ligand. The single-stranded DNA aptamer used in this study binds to exosite I of thrombin by adopting a G-quadruplex conformation leading to inhibition of thrombin-catalyzed clot formation.[49,50] In addition, we used an univalent thrombin inhibitor – argatroban in order to prevent the coagulation of the bulk human blood plasma (HBP) sample. The argatroban binds to the active site of thrombin blocking the catalytic activity of soluble and fibrin-bound thrombin and reducing thrombin-mediated activation of platelets.[51] By occupying the active site only, the argatroban does not impair the recognition of thrombin by the surface-attached aptamer. The importance of an anti-fouling sensor surface engineering is demonstrated by selective capture of medically relevant concentrations of thrombin in undiluted HBP.

Experimental

Materials

Thrombin purified from human plasma (M_W = 37 kDa) was purchased from Enzo Life Sciences (Switzerland). The thrombin binding aptamer HD1 (amino modifier C6 5'-TTT TTG GTT GGT GTG GTT GG-3') and control aptamer (scrambled sequence: amino modifier C6 5'- TTT TTG GTG GTG GTT GTG GT-3') were synthesized by Integrated DNA Technologies (Belgium). The pooled normal HBP samples were obtained from Innovative Research (USA). Alkane PEG-thiol with a carboxylic acid group (carboxyl PEG-thiol, TH 003-m11.n6-0.1) was purchased from Prochimia (Poland) and (11-mercaptoundecyl) triethyleneglycol (hydroxyl PEG-thiol, SPT-0011) was purchased from SensoPath Technologies Inc. (USA). Buffer solutions were prepared by using ultrapure water (arium pro, Sartorius Stedim) with all reagents used as received unless otherwise stated. 2-(*N*-Morpholino) ethanesulfonic acid (MES), acetic acid, sodium acetate (SA), sodium chloride, HEPES, PBS buffer tablets and argatroban monohydrate (M_W = 526.65 g/mol) were purchased from Sigma-Aldrich (Austria). 1-Ethyl-3-(3-dimethylaminopropyl)-carbodiimide (EDC) and *N*-hydroxysuccinimide (NHS) were obtained from Thermo Scientific (Austria). $CuCl_2$ (99.999%), 1,4,8,11-tetramethyl-1,4,8,11-tetraazacyclotetradecane (Me_4Cyclam, 98%) were purchased from Sigma-Aldrich (Germany). CuCl was purchased from abcr GmbH (Germany). Methanol (MeOH), ethanol (EtOH) were purchased from VWR Chemicals (Germany). Milli-Q water for the polymer synthesis was obtained using Elga™ US filter Purelab Plus UF purification system (PL5113 02) (United Kingdom).

Preparation of plasmonic gratings

A master structure of crossed relief grating was prepared by UV laser interference lithography as described before.[52] It was cast to polydimethylsiloxane (PDMS, Sylgard 184 from Dow Corning, USA),

which was cured overnight at 60 °C. The PDMS structure was detached from the master and used as a working stamp for further replication by UV-nanoimprint lithography. The UV-curable polymer Amonil MS10 (Amo GmbH, Germany) was spun on a BK7 glass substrate at 3000 rpm for 120 s. The PDMS working stamp was placed on the top of the Amonil layer and the polymer was irradiated with UV light at λ = 365 nm with the irradiation dose of 2 J/cm^2 (UV lamp Bio-Link 365, Vilber Lourmat). Then, the PDMS stamp was released from the UV-cured Amonil layer leaving an imprinted pattern of the master structure on the BK7 glass substrate. Subsequently, chromium (4 nm thickness) and gold (100 nm thickness) layers were deposited on the Amonil grating by vacuum thermal evaporation (HHV AUTO 306 from HHV LTD, UK) in vacuum better than 10^{-6} mbar. The prepared GC-SPR sensor chips comprised an area that was structured and area that was flat and served as a reference in the optical measurements.

Synthesis of poly(HPMA-co-CBMAA) brushes

Ω-mercaptoundecyl bromoisobutyrate and *N*-(2-hydroxypropyl) methacrylamide (HPMA) were synthesized according to the literature.[53,54] (3-methacryloylaminopropyl) - (2-carboxyethyl) - dimethylammonium (carboxybetaine methacrylamide, CBMAA) was synthesized using a modification of procedure reported earlier.[55] Shortly, the GC-SPR sensor chips with the gold film were immersed in 2.4 mM solution of ω-mercaptoundecyl bromoisobutyrate in EtOH overnight to form SAM of the initiator. For the atom transfer radical polymerization (ATRP), 8 mL of MeOH and 8 mL of Milli-Q water were degassed in separated Schlenk flasks via seven freeze-pump-thaw cycles. Simultaneously, catalyst [$CuCl_2$ (6.1 mg, 78 µmol), CuCl (20.5 mg, 207 µmol), and Me_4Cyclam (70.6 mg, 275 µmol)] and monomers [HPMA (1.4 g, 9.7 mmol) and CBMAA (409 mg, 1.7 mmol)] were placed in separated Schlenk flasks and degassed by a pump and refilled.

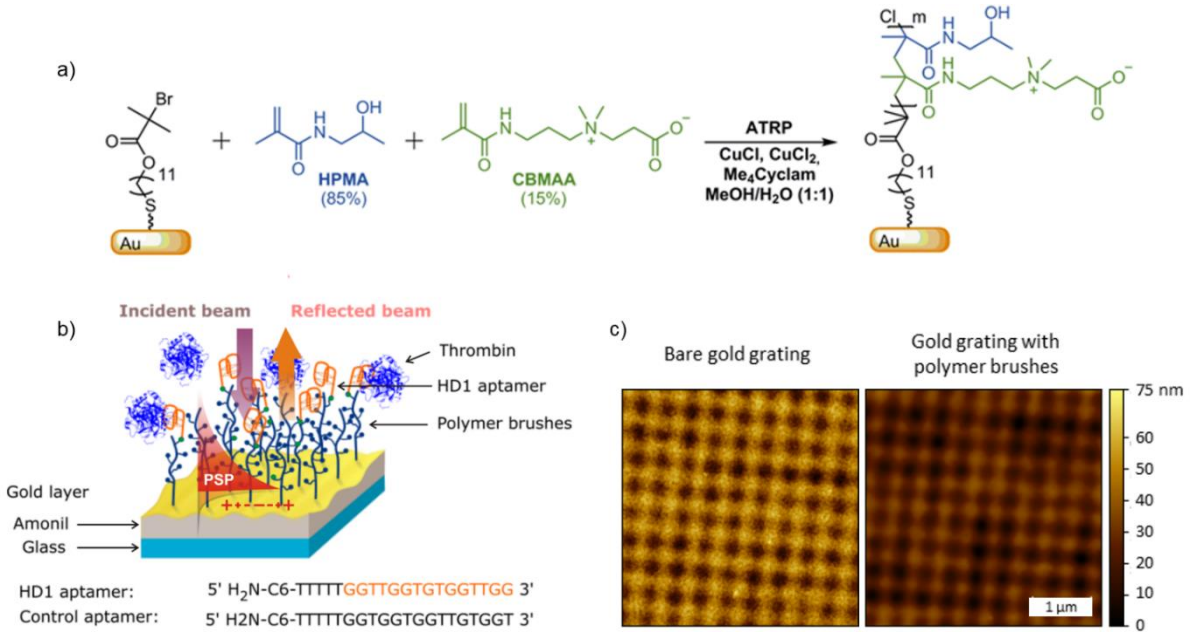

Figure 1. a) Synthesis and chemical structure of poly(HPMA-*co*-CBMAA) brushes on a gold surface by ATRP. b) Sensor chip surface with corrugated gold layer carrying nonfouling poly(HPMA-*co*-CBMAA) brushes for detection of thrombin. c) The AFM observation of the bare gold grating and the grating coated with polymer brushes.

Subsequently, 4 mL of MeOH and 7 mL of Milli-Q water together with 3 mL of MeOH were transferred to the Schlenk flasks containing catalyst and monomers, respectively, under N_2 atmosphere and were stirred until all solids were dissolved. Then, the obtained catalyst solution was mixed with the monomer solution using a gas-tight syringe under N_2 atmosphere and transferred to previously degassed reactors containing GC-SPR sensor chip with SAM. The polymerization was carried out at 30 °C for 2 h. The samples were taken out from the reactors, washed with EtOH, Milli-Q water and dried with N_2. The scheme of the polymerization is shown in Figure. 1a.

Morphology measurements

The morphology of the crossed relief grating before and after the modification with poly(HPMA-*co*-CBMAA) brushes was observed by using atomic force microscopy (AFM, PicoPlus from Molecular Imaging, Agilent Technologies, Germany) in the tapping mode with tips PPP-NCHR-50 (Nanosensors, Switzerland). The acquired images were analyzed with the open-source software Gwyddion (version 2.47 from gwyddion.net). The grafting of polymer brushes was monitored by measuring the thickness of dried polymer film using a spectroscopic ellipsometer M2000 (J.A.Woollam Co., USA) operated in rotating compensator mode. All measurements were performed in air at room temperature in the wavelength range of 350–1000 nm with a Xe-arc lamp light source and angle of incidence of 65, 70 and 75°. The obtained data were analyzed with the CompleteEASE software using a transparent Cauchy-type optical dispersion to model the polymer brushes.

Optical setup of GC-SPR biosensor

The *in situ* probing of the sensor surface was performed by using an in-house developed compact instrument (Figure. 2). The polychromatic light from a halogen light source (12V, HL-2000, Mikropack, USA) was coupled to an input arm of Y-optical fiber splitter (Ø 400 µm core, 0.39 NA, Thorlabs, UK). The light emitted from the output arm of Y-optical splitter was collimated by using a lens (focal length of 11 mm, Thorlabs, UK) and made normally incident at the sensor surface in order to resonantly excite PSPs on its corrugated gold surface. A flow-cell with a chamber depth of 100 µm, length 10 mm, and width 5 mm was clamped against the gold sensor surface in order to contain aqueous samples. The flow cell consisted of a thin PDMS gasket and a transparent glass with drilled input and output ports. The analyzed liquid samples were flowed through the flow-chamber by using a peristaltic pump (Ismatec, Switzerland) with a flow rate of 50 µL/min. The light reflected from the sensor surface was coupled back to the Y-optical fiber splitter that was connected to a spectrometer (HR4000, OceanOptics Inc., USA).

The measured spectrum of the light beam reflected from the grating surface was normalized with that acquired from the reference flat area on the sensor chip. The normalized reflectivity spectra $R(\lambda)$ were processed by a dedicated LabView software[56] and the spectral position of the resonant coupling to PSPs λ_{SPR} was tracked as a function of time t (Figure 2). The acquisition time of the SPR reflectivity spectra was set at 7 ms and in each measurement spot, 100 spectra were accumulated.

The changes in the spectral position of GC-SPR reflectivity dip $\delta\lambda_{SPR}$ were determined by fitting with an analytical function. The resonant wavelength changes $\delta\lambda_{SPR}$ were calibrated by the measuring of sensor response to the flow of 1, 2 and 4 wt% water solutions of sucrose with known refractive indices (δn_s=1.4 × 10^{-3}; 2.8 × 10^{-3}; 5.6 × 10^{-3} RIU, respectively) in order to convert the sensor signal to refractive index units RIU. The refractive index sensitivity was determined as $S=\delta\lambda_{SPR}/\delta n_s$. From the SPR signal baseline, the standard deviation $\sigma[\lambda_{SPR}(t)]$ of its noise was obtained and the refractive index resolution was obtained as σ/S.

Immobilization of aptamers

The HD1 or control aptamers with amine terminal group were covalently coupled to the carboxylic groups carried by the poly(HPMA-*co*-CBMAA) brushes. The coupling was monitored *in situ* by the use of GC-SPR and firstly, the baseline in $\lambda_{SPR}(t)$ was established upon a flow of PBS (pH 7.4). Then, the surface was incubated with 10 mM SA buffer (pH 5.0) for 5 min and freshly prepared solution of EDC (0.4 M) and NHS (0.1 M) in 50 mM MES buffer (pH 6.0) was reacted with the brushes for 10 min in order to activate the carboxylic groups. Subsequently, the surface was rinsed with 10 mM SA (pH 5.0) and HEPES (pH 7.5) for 1 min each. The activated surface was exposed to 1 μM solution of the aptamer for 30 min and rinsed with HEPES (pH 7.5) for 5 min. Finally, the functionalized sensor surface was washed with PBS (pH 7.4) for 90 min to let the unreacted active ester groups hydrolyze.

Observation of the fouling

The fouling from undiluted HBP was monitored by using GC-SPR instrument. Four types of GC-SPR sensor chips with different surface chemistry were examined: unmodified gold, gold surface with a mixed SAM (form up overnight incubation in ethanolic solution with dissolved carboxyl PEG-thiol and hydroxyl PEG-thiol at ratio 1:10, respectively, and 1 mM total concentration), gold surface with pristine poly(HPMA-*co*-CBMAA) brushes and gold surface with poly(HPMA-*co*-CBMAA) brushes that were functionalized with HD1 aptamer. For each surface chemistry, a baseline in SPR signal λ_{SPR}(t) in PBS (pH 7.4) was established for 5 min. Then, undiluted HBP that was spiked with 1 μL of argatroban monohydrate (stock 10 mg/ml) in final volume of 500 μL was flowed over each surface for 15 min, followed by the rinsing with PBS for 5 min. The amount of unspecifically bound species from HBP on the

sensor surface was determined in ng/mm^2 from the difference in the sensor signal before λ_{SPR} and after the contact with the HBP by using the formula $\Gamma = 1.5 \cdot \delta\lambda_{SPR}$ for polymer brushes and $0.85 \cdot \delta\lambda_{SPR}$ for bare gold (SPR wavelength shift $\delta\lambda_{SPR}$ is in nm) based on numerical simulations discussed in the supporting information.

Detection of thrombin

The sensor chip with poly(HPMA-*co*-CBMAA) brushes functionalized with an aptamer ligand (specific HD1 or scrambled HD1 sequence) were used to detect thrombin in analyzed liquid samples (Figure 1b). There were prepared two types of samples that were spiked with a known concentration of thrombin. The PBS sample was spiked with thrombin at a concentration of c=1, 2.5, 5, 7.5, 10, 12.5, 15, 17.5, 20, 22.5, and 25 nM. 1 µL of argatroban stock solution (10 mg/ml, c=19 mM) was added to the analyzed HBP sample, gently mixed and incubated for 5 min. Afterwards, the HBP sample was spiked with thrombin (stock 500 nM) to obtain c=5, 10, 15 and 20 nM in the final sample volume of 500 µL and gently mixed prior to the analysis by using GC-SPR. The measurement baseline in SPR sensor signal $\lambda_{SPR}(t)$ was established upon a 5 min flow of PBS. Then, the sensor surface was exposed to the analyzed sample for 15 min and subsequently rinsed with PBS for 5 min. In order to regenerate the surface and release the affinity bound thrombin, aqueous solution with 2 M NaCl was flowed for 2 min. The sensor response ΔSPR was determined in µRIU from the difference in the SPR signal divided by refractive index sensitivity $\delta\lambda_{SPR}(t)/S$ before and after the target analyte binding. Similarly, two types of control experiments were performed. All measurements carried in HBP were repeated three times in order to determine the standard deviation of the sensor response ΔSPR. The measured dependence of sensor response ΔSPR on the thrombin concentration c was fitted with Langmuir isotherm analytical function $\Delta SPR = \Delta SPR_{max} \times c/K_d/(1+c/K_d)$ and where ΔSPR_{max} states for the response in saturation, K_d is the equilibrium dissociation affinity constant. The limit of detection (LOD) was defined as a concentration where 3 times the standard deviation of the baseline signal $3\times\sigma[\lambda_{SPR}(t)]$ intersects the Langmuir fit of the calibration curve.

Results and discussion

Characterization of the compact sensor and its chips

The crossed relief grating structure was fabricated by using the UV-nanoimprint lithography followed by the coating with 100 nm thick gold layer in order to resonantly couple incident light beam to PSPs. The polymer brushes were subsequently synthesized on top of the gold film in order to provide biointerface resistant to fouling from HBP. The surface of the diffraction grating with and without polymer brushes was analyzed by AFM as shown in Figure 1c. The period of the gold-coated grating with

sinusoidal profile was determined as Λ=434 ± 16 nm and the corrugation depth h=29.5 ± 3.5 nm. After the synthesis of the polymer brushes with a thickness of d=35 ± 7 nm, the grating corrugation depth decreased to d=13.2 ± 1.6 nm and reduced roughness of the topography was observed (Figure S1). These phenomena can be explained by the fact that after their drying, the flexible polymer chains rearrange and tends to fill the concave areas of the grating.

The plasmonic grating structure on the top of the sensor chip was attached to a flow cell and loaded to the compact optical reader (see Figure 2a). The resonant excitation of PSPs on the bare gold grating is manifested as a narrow dip in the wavelength reflectivity spectrum $R(\lambda)$. It occurs at a wavelength λ_{SPR}, where the normally incident wave and PSPs are phase-matched due to the diffraction on the grating periodic corrugation. The momentum of the PSP waves is equal to the grating momentum $\mathrm{Re}\{k_{PSP}(\lambda)\} = 2\pi/\Lambda$ for the herein used first diffraction order coupling, which is fulfilled at a wavelength λ_{SPR} = 635.8 nm (see the spectral position of the reflectivity dip in Figure 2b). After the synthesis of poly(HPMA-*co*-CBMAA) brushes on the top of the gold grating, the resonant wavelength shifts to λ_{SPR} = 655.1 nm due to an increase of the surface mass density Γ.

Importantly, the presence of polymer brushes (with a thickness of d=35 nm) affects the sensitivity of the SPR sensor S to the refractive index changes occurring on its surface. The reason is that the polymer occupies part of the volume that is probed by the evanescent field of PSPs with a decay length of about L_p~100 nm. By measuring the detuning of λ_{SPR} due to the refractive index change n_s of an aqueous solution spiked with sucrose (Figure S2), the sensitivity of S = 459 ± 20 nm/RIU was determined for the GC-SPR chip without the polymer brushes. This value agrees with previous GC-SPR measurements at a similar wavelength.[56] On the same chips that carried the polymer brushes biointerface architecture the sensitivity decreased about twice to S = 238.3 ± 5.4 nm/RIU. The baseline of the SPR sensor signal exhibited the noise with the standard deviation of $\sigma = 3\times10^{-3}$ nm, which translates to the instrument refractive index resolution of 6×10^{-6} RIU without the brushes and 1.1×10^{-5} ± RIU with the brushes. It is worth of noting that more than an order of magnitude better resolution can be achieved with more advanced engineering of GC-SPR sensor instrument, however, then more sophisticated stabilization (e.g. temperature) has to be implemented.[29]

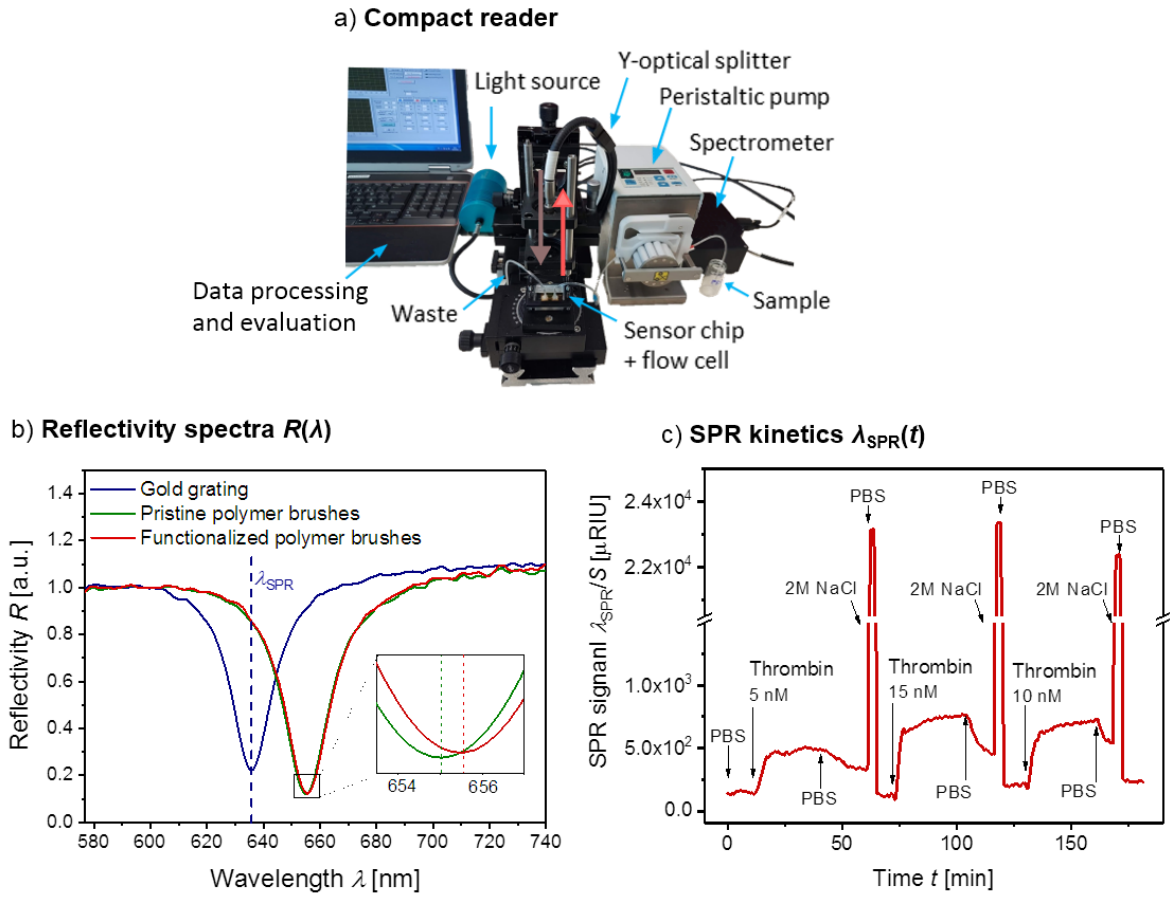

Figure 2. a) A photograph of the compact GC-SPR instrument. b) The SPR spectra obtained from the gold grating, grating modified with pristine polymer brushes and after the immobilization of the aptamer and c) The sensorgram showing detection of thrombin in PBS by using a plasmonic grating chip modified with poly(HPMA-*co*-CBMAA) brush and HD1 aptamer.

Immobilization of the aptamers

In order to allow for the specific capture of target analyte at the sensor surface, the aptamer receptors were tethered to polymer brushes. The immobilization of thrombin-specific HD1 aptamer or scrambled control aptamer was performed *in-situ* and monitored by GC-SPR. The reflectivity spectra $R(\lambda)$ (Figure 2b) and respective SPR sensor signal kinetics $\lambda_{SPR}(t)$ (Figure S3a) show that after the immobilization of the aptamer, the resonance shifts to longer wavelengths. After 30 min, non-covalently bound aptamers were washed from the surface with a PBS buffer. A shift in the position of the SPR resonance $\Delta\lambda_{SPR}$ of about 0.5 nm was observed after the immobilization of the HD1 aptamer on the sensor surface which corresponds to the 2.3 ± 0.9 mRIU for HD1 thrombin specific aptamer and 2.4 ± 0.1 mRIU for the scrambled sequence of HD1 aptamer (Figure S3b).

Investigation of the fouling of biointerface architectures

The fouling from undiluted HBP was observed from SPR signal measured upon the contact of the sensor surface with a sample and it was quantified in terms of the surface mass density change Γ determined after the rinsing of the surface with PBS. Besides the polymer brushes-coated gold grating surfaces, also a sensor chips carrying a layer of bare gold and gold modified with PEG-thiol SAM were examined for comparison. Figure 3a shows the SPR sensor signal measured upon the 15 min flow of HBP over each type of surface followed by the rinsing. These data show that the injection of HPB rapidly shifts the SPR wavelength due to the bulk refractive index change Δn_s. Afterwards, there is observed a slower gradual increase in the SPR signal on the bare and PEG-thiol modified gold surface due to the adsorption of HPB constituents. Importantly, much smaller gradual changes in SPR signal are measured on the polymer brushes, which indicates weaker unspecific interaction with HBP. After the rinsing with PBS, the SPR signal rapidly decreases owing to a change in the bulk refractive index Δn_s and it reaches an equilibrium after 5 min. The surface mass density of the irreversibly deposited constituents Γ was determined from the change in the SPR signal baseline before and after the exposure to HBP as summarized in Figure 3b. In agreement with the previous studies,[46] there was observed no measurable change in Γ for pristine brushes demonstrating that the anti-fouling properties are not affected by the grating topology. These characteristics are superior to the bare gold (Γ=0.66 ng/mm^2) and conventional gold modified with PEG-thiol SAM (Γ=0.59 ng/mm^2).

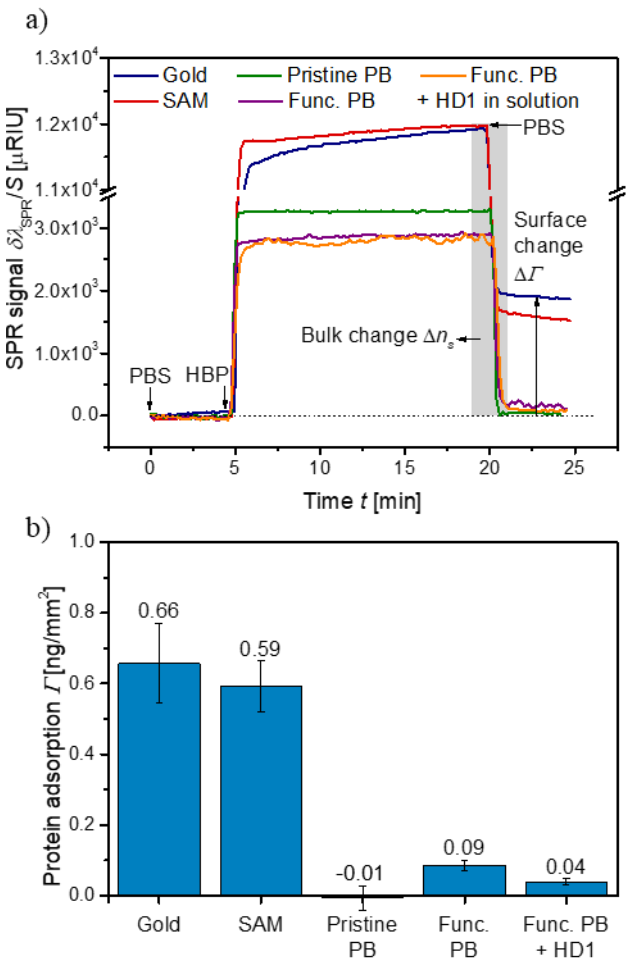

Figure 3. a) The sensorgram showing fouling of the examined surfaces to 100% plasma with 38 μM argatroban: gold - bare gold, SAM - gold modified with a thiol-based SAM, pristine PB - gold modified with polymer brushes, func. PB - gold modified with polymer brushes that were functionalized with HD1 aptamer. b) The averaged protein adsorption Γ reflecting fouling of each surface to 100% plasma with 38 μM argatroban.

However, in contrast to previous study[45] (in which a protein ligand was immobilized to similar brushes) we observed a significant increase in the surface mass density (Γ=0.09 ng/mm^2) for the brushes that were functionalized with the HD1 DNA aptamer. This observation indicates that the presence of negatively charged DNA strands can impair more severely the anti-fouling properties, but it also can be attributed to the capture of endogenous thrombin that is natively present in the tested pooled HBP at pM concentrations.[57,58] In order to elucidate between these two possible contributions, we also measured the fouling for the HD1 aptamer-functionalized brushes from HBP that was spiked with the same HD1 aptamer. Then, we observed about two-times lower surface mass density increase (Γ=0.04 ng/mm^2), which can be ascribed to the blocking of the thrombin present in the sample and thus preventing its specific capture by the sensor HD1 aptamer tethered to the surface. Therefore, about 50% of the observed SPR response can be ascribed to the fouling and it should be highlighted that it

corresponds to about 7% of the value observed on (even non-functionalized) PEG-thiol SAM that is widely accepted as standard low-fouling surface architecture.

Detection of thrombin

The developed GC-SPR sensor chip with poly(HPMA-*co*-CBMAA) brushes was used for the detection of thrombin in model PBS and undiluted HBP samples. The polymer brushes were functionalized either with thrombin-specific aptamer HD1 or by an aptamer with a scrambled sequence of nucleotides in order to serve as a negative control. There were prepared a series of HBP samples spiked with 38 μM argatroban and thrombin in the concentration range from c=1 to 25 nM. The impact of argatroban on a thrombin detection assay was investigated and it was confirmed that the argatroban does not interfere with the aptamer binding site (Figure S4). As can be seen in Figure 2c and Figure 4a, prepared samples were subsequently analyzed with the SPR sensor signal λ_{SPR}/S aquired in time. Each sample was flowed through the sensor for 15 min followed by rinsing with PBS and regeneration of the surface by introducing an aqueous solution of NaCl (2 M), which weakens the thrombin-HD1 affinity binding. Importantly, the regeneration has been complete and lead to washing off all of the specifically captured thrombin as well as unspecifically adsorbed abundant HBP constituents. The control experiment was performed analogously in sensor chips with the polymer brushes functionalized with a scrambled sequence of the HD1 aptamer that does not form a G-quadruplex structure which is indispensable for the binding of thrombin.

As there is indicated in Figure 4a, the sensor response ΔSPR due to the binding of thrombin was determined from the SPR signal changes before the injection of a sample and after the rising with PBS prior to the regeneration step. The calibration curves were established for detection of thrombin in PBS (blue symbols in Figure 4b) and HBP (red symbols in Figure 4b). These data were fitted by using the Langmuir isotherm and the obtained dissociation equilibrium constant were of K_d=3.7 and 22 nM for the PBS and HBP samples, respectively. Such variation can be attributed to potential interaction of immobilized HD1 aptamer with other constituents that are present in HBP and not in PBS. These can include the background thrombin level in used pooled plasma (which would lead to false concentration of thrombin) and to the presence of ions and macromolecules that amend the balance of aptamer intermolecular interactions. It is worth of noting that the obtained K_d values fall in the range that was reported in the literature and measured by using the aptamers utilized for heterogeneous assays[59,60] as well as homogeneous assays.[61,62] By taking into account the noise of the sensor signal, the limit of detection was determined as LOD=0.15 and 1.1 nM for the PBS and HBP, respectively. In addition, squares in Figure 4b represent two control experiments obtained with the scrambled aptamer sequence in PBS (blue color) and human plasma (red color). An additional control experiment was performed by

using HBP samples containing 38 µM argatroban that were spiked with 1 µM HD1 or scrambled control aptamer (Figure S5). The obtained data are in the good agreement with the values that were obtained in the direct assay in HBP.

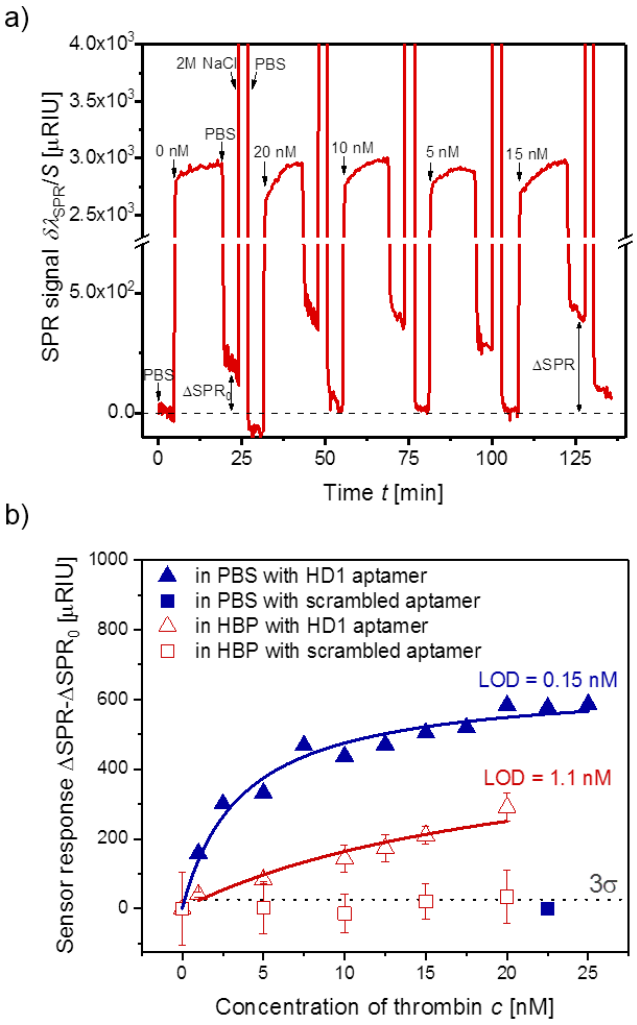

Figure 4. a) The sensorgram showing detection of thrombin in 100% plasma. b) The normalized SPR response vs. concentration of thrombin measured in PBS (blue) (n = 1) and 100% plasma (red) (n = 3) by using the brushes functionalized with HD1 aptamer (triangles) or with control aptamer (squares).

Conclusions

An optical biosensor platform for rapid direct monitoring of thrombin in HBP was established based on grating-coupled SPR readout. The specific detection of thrombin that is not impeded by the interfering adsorption of proteins from HBP was achieved by using the thrombin aptamers and advanced biointerface architecture comprising nonfouling poly(HPMA-*co*-CBMAA) brushes. We demonstrated the label-free detection of thrombin content in undiluted human blood plasma is possible in 15 min with LOD of 1.1 nM. The grating-coupled SPR sensor was implemented to a compact portable system making

its deployment outside specialized optical laboratories possible. The further miniaturization of each individual component of the optical system can be pursued by future opto-electrical engineering paving the way towards hand-held POC device. Despite further investigations are needed to carry out (including tests on clinical samples) in order to evaluate the diagnostic value of the presented biosensor, the reported performance shows that the implementation of this technology to a diagnostic tool to monitor coagulation status of patients at risk of thrombosis is possible. The coagulation process occurs once the level of thrombin in blood has reached approximately 5 – 20 nM[63,64] and at the end of the clot formation, the concentration of thrombin can reach several hundred nM.[65] Therefore, it is postulated that the level of thrombin in the range of 5 – 20 nM indicates a high risk of thrombosis and these values are within the detection range of reported sensor.

Associated content

Supporting Information Available: The following files are available free of charge. Kotlarek_ACS Sensors_supporting information.pdf. It contains information on the topography changes of grating corrugation after the coating with antifouling polymer brushes and calibration of the sensor. In addition, GC-SPR sensorgrams for the functionalization of sensor chips are provided together with an impact of argatroban to the assay performance and control thrombin assay.

Corresponding Author

Jakub Dostalek, PhD, E-mail: jakub.dostalek@ait.ac.at, Phone: +43 (0) 50550 4470, Fax: +43 (0) 50550 4450.

Acknowledgment

This project has received funding from the European Union's Horizon 2020 research and innovation programme under grant agreement No 642787, Marie Sklodowska-Curie Innovative Training Network BIOGEL. CR-E and M.V. acknowledge the support of the Deutsche Forschungsgemeinschaft (DFG) in the framework of the priority programme 2014 "Towards an Implantable Lung", project numbers: 346972946 and 347367912".

References

(1) Rasche, H. Haemostasis and Thrombosis: An Overview. *Eur. Hear. Journal, Suppl.* 2001, *3* (Q), 3–7.
(2) Sira, J.; Eyre, L. Physiology of Haemostasis. *Anaesth. Intensive Care Med.* 2016, *17* (2), 79–82.
(3) Miyares, M. A.; Davis, K. Newer Oral Anticoagulants: A Review of Laboratory Monitoring Options and Reversal Agents in the Hemorrhagic Patient. *Am. J. Heal. Pharm.* 2012, *69* (17), 1473–1484.
(4) Adams, G. L.; Manson, R. J.; Turner, I.; Sindram, D.; Lawson, J. H. The Balance of Thrombosis and Hemorrhage in Surgery. *Hematol. Oncol. Clin. North Am.* 2007, *21* (1), 13–24.

(5) Falck-Ytter, Y.; Francis, C. W.; Johanson, N. A.; Curley, C.; Dahl, O. E.; Schulman, S.; Ortel, T. L.; Pauker, S. G.; Colwell, C. W. Prevention of VTE in Orthopedic Surgery Patients: Antithrombotic Therapy and Prevention of Thrombosis. *Chest* 2012, *141* (2), e278S-e325S.
(6) Edmunds, L. H.; Colman, R. W. Thrombin During Cardiopulmonary Bypass. *Ann. Thorac. Surg.* 2006, *82* (6), 2315–2322.
(7) Mazzeffi, M.; Greenwood, J.; Tanaka, K.; Menaker, J.; Rector, R.; Herr, D.; Kon, Z.; Lee, J.; Grif, B.; Rajagopal, K.; et al. Bleeding, Transfusion, and Mortality on Extracorporeal Life Support: ECLS Working Group on Thrombosis and Hemostasis. *Ann. Thorac. Surg.* 2016, *101(2)*, 682–689.
(8) Cortelazzo, S.; Finazzi, G.; Viero, P.; Galli, M.; Remuzzi, A.; Parenzan, L.; Barbui, T. Thrombotic and Hemorrhagic Complications in Patients with Mechanical Heart Valve Prosthesis Attending an Anticoagulation Clinic. *Thromb. Haemost.* 1993, *70* (04), 316–320.
(9) Despotis, G. J.; Joist, J. H.; Goodnough, L. T. Monitoring of Hemostasis in Cardiac Surgical Patients: Impact of Point- of-Care Testing on Blood Loss and Transfusion Outcomes. *Clin. Chem.* 1997, *43* (9), 1684–1696.
(10) Heneghan, C.; Alonso-Coello, P.; Garcia-Alamino, J. M.; Perera, R.; Meats, E.; Glasziou, P. Self-Monitoring of Oral Anticoagulation : A Systematic Review and Meta-Analysis. *Lancet* 2006, *367* (9508), 404–411.
(11) Bashaw, M. Coagulopathy In and Outside the Intensive Care Unit. *Crit. Care Nurs. Clin. NA* 2017, *29 (3)*, 353–362.
(12) Zheng, R.; Cameron, B. D. Surface Plasmon Resonance: Recent Progress toward the Development of Portable Real-Time Blood Diagnostics. *Expert Rev. Mol. Diagn.* 2012, *12* (1), 5–7.
(13) Tokel, O.; Inci, F.; Demirci, U. Advances in Plasmonic Technologies for Point of Care Applications. *Chem. Rev.* 2014, *114* (11), 5728–5752.
(14) Feltis, B. N.; Sexton, B. A.; Glenn, F. L.; Best, M. J.; Wilkins, M.; Davis, T. J. A Hand-Held Surface Plasmon Resonance Biosensor for the Detection of Ricin and Other Biological Agents. *Biosens. Bioelectron.* 2008, *23* (7), 1131–1136.
(15) Wang, S.; Xie, J.; Jiang, M.; Chang, K.; Chen, R.; Ma, L.; Zhu, J.; Guo, Q.; Sun, H.; Hu, J. The Development of a Portable SPR Bioanalyzer for Sensitive Detection of Escherichia Coli O157:H7. *Sensors (Switzerland)* 2016, *16* (11), 1–9.
(16) Mauriz, E.; Calle, A.; Montoya, A.; Lechuga, L. M. Determination of Environmental Organic Pollutants with a Portable Optical Immunosensor. *Talanta* 2005, *69* (2 SPEC. ISS.), 359–364.
(17) Soelberg, S. D.; Furlong, C. E. Biosensors and Bioassays for Ecological Risk Monitoring and Assessment. In *Environmental Toxicology*; Springer: New York, 2013; pp 121–142.
(18) Prabowo, B. A.; Wang, R. Y. L.; Secario, M. K.; Ou, P. T.; Alom, A.; Liu, J. J.; Liu, K. C. Rapid Detection and Quantification of Enterovirus 71 by a Portable Surface Plasmon Resonance Biosensor. *Biosens. Bioelectron.* 2017, *92*, 186–191.
(19) Trzaskowski, M.; Napiórkowska, A.; Augustynowicz-Kopeć, E.; Ciach, T. Detection of Tuberculosis in Patients with the Use of Portable SPR Device. *Sensors Actuators, B Chem.* 2018, *260*, 786–792.
(20) Naimushin, A. N.; Soelberg, S. D.; Bartholomew, D. U.; Elkind, J. L.; Furlong, C. E. A Portable Surface Plasmon Resonance (SPR) Sensor System with Temperature Regulation. *Sensors Actuators, B Chem.* 2003, *96* (1–2), 253–260.
(21) Stevens, R. C.; Soelberg, S. D.; Near, S.; Furlong, C. E. Detection of Cortisol in Saliva with a Flow-Filtered, Portable Surface Plasmon Resonance Biosensor System. *Anal. Chem.* 2008, *80* (17), 6747–6751.
(22) Dostálek, J.; Homola, J.; Miler, M. Rich Information Format Surface Plasmon Resonance Biosensor Based on Array of Diffraction Gratings. *Sensors Actuators, B Chem.* 2004, *107* (1 SPEC. ISS.), 154–161.
(23) Wang, Y.; Dostalek, J.; Knoll, W. Magnetic Nanoparticle-Enhanced Biosensor Based on Grating-Coupled Surface Plasmon Resonance. 2011, 6202–6207.
(24) Arachchillage, D. R.; Passariello, M.; Laffan, M.; Aw, T. C.; Owen, L.; Banya, W.; Trimlett, R.; Morgan, C.; Patel, B. V.; Pepper, J.; et al. Intracranial Hemorrhage and Early Mortality in Patients Receiving Extracorporeal Membrane Oxygenation for Severe Respiratory Failure. *Semin. Thromb. Hemost.* 2018, *44* (03), 276–286.
(25) Kooy, N.; Mohamed, K.; Pin, L. T.; Guan, O. S. A Review of Roll-to-Roll Nanoimprint Lithography | Nanoscale Research Letters | Full Text. *Nanoscale Res. Lett.* 2014, *9* (1), 1.
(26) Lu, C.; Lipson, R. H. Interference Lithography: A Powerful Tool for Fabricating Periodic Structures. *Laser Photonics Rev.* 2010, *4* (4), 568–580.
(27) Vala, M.; Chadt, K.; Piliarik, M.; Homola, J. High-Performance Compact SPR Sensor for Multi-Analyte Sensing. *Sensors Actuators, B Chem.* 2010, *148* (2), 544–549.

(28) Fernández, F.; Hegnerová, K.; Piliarik, M.; Sanchez-Baeza, F.; Homola, J.; Marco, M. P. A Label-Free and Portable Multichannel Surface Plasmon Resonance Immunosensor for on Site Analysis of Antibiotics in Milk Samples. *Biosens. Bioelectron.* 2010, *26* (4), 1231–1238.
(29) Piliarik, M.; Homola, J. Surface Plasmon Resonance (SPR) Sensors: Approaching Their Limits? *Opt. Express* 2009, *17* (19), 16505.
(30) Zhang, J.; Khan, I.; Zhang, Q.; Liu, X.; Dostalek, J.; Liedberg, B.; Wang, Y. Lipopolysaccharides Detection on a Grating-Coupled Surface Plasmon Resonance Smartphone Biosensor. *Biosens. Bioelectron.* 2018, *99* (April 2017), 312–317.
(31) Centi, S.; Tombelli, S.; Minunni, M.; Mascini, M. Aptamer-Based Detection of Plasma Proteins by an Electrochemical Assay Coupled to Magnetic Beads. *Anal. Chem.* 2007, *79* (4), 1466–1473.
(32) Bini, A.; Minunni, M.; Tombelli, S.; Centi, S.; Mascini, M. Analytical Performances of Aptamer-Based Sensing for Thrombin Detection. *Anal. Chem.* 2007, *79* (7), 3016–3019.
(33) Pavlov, V.; Xiao, Y.; Shlyahovsky, B.; Willner, I. Aptamer-Functionalized Au Nanoparticles for the Amplified Optical Detection of Thrombin. *J. Am. Chem. Soc.* 2004, *126* (38), 11768–11769.
(34) Baek, S. H.; Wark, A. W.; Lee, H. J. Dual Nanoparticle Amplified Surface Plasmon Resonance Detection of Thrombin at Subattomolar Concentrations. *Anal. Chem.* 2014, *86* (19), 9824–9829.
(35) He, P.; Liu, L.; Qiao, W.; Zhang, S. Ultrasensitive Detection of Thrombin Using Surface Plasmon Resonance and Quartz Crystal Microbalance Sensors by Aptamer-Based Rolling Circle Amplification and Nanoparticle Signal Enhancement. *Chem. Commun.* 2014, *50* (12), 1481–1484.
(36) Li, S.; Zhang, D.; Zhang, Q.; Lu, Y.; Li, N.; Chen, Q.; Liu, Q. Electrophoresis-Enhanced Localized Surface Plasmon Resonance Sensing Based on Nanocup Array for Thrombin Detection. *Sensors Actuators, B Chem.* 2016, *232*, 219–225.
(37) Lao, J.; Han, L.; Wu, Z.; Zhang, X.; Huang, Y.; Tang, Y.; Guo, T. Gold Nanoparticle-Functionalized Surface Plasmon Resonance Optical Fiber Biosensor: In Situ Detection of Thrombin with 1 NM Detection Limit. *J. Light. Technol.* 2019, *37* (11), 2748–2755.
(38) Andrade, J. D. *Surface and Interfacial Aspects of Biomedical Polymers: Volume 1 Surface Chemistry and Physics*; Springer Science & Business Media, 2012.
(39) Vroman, L.; Adams, A. L.; Fischer, G.; Munoz, P. Interaction of High Molecular Weight Kininogen, Factor XII, and Fibrinogen in Plasma at Interfaces. *Blood* 1980, *55* (1), 156–159.
(40) Ostuni, E.; Chapman, R. G.; Holmlin, R. E.; Takayama, S.; Whitesides, G. M. A Survey of Structure-Property Relationships of Surfaces That Resist the Adsorption of Protein. *Langmuir* 2001, *17* (18), 5605–5620.
(41) Emmenegger, C. R.; Brynda, E.; Riedel, T.; Sedlakova, Z.; Houska, M.; Alles, A. B. Interaction of Blood Plasma with Antifouling Surfaces. *Langmuir* 2009, *25* (11), 6328–6333.
(42) Polonschii, C.; David, S.; Tombelli, S.; Mascini, M.; Gheorghiu, M. A Novel Low-Cost and Easy to Develop Functionalization Platform. Case Study: Aptamer-Based Detection of Thrombin by Surface Plasmon Resonance. *Talanta* 2010, *80* (5), 2157–2164.
(43) Bai, Y.; Feng, F.; Zhao, L.; Wang, C.; Wang, H.; Tian, M.; Qin, J.; Duan, Y.; He, X. Aptamer/Thrombin/Aptamer-AuNPs Sandwich Enhanced Surface Plasmon Resonance Sensor for the Detection of Subnanomolar Thrombin. *Biosens. Bioelectron.* 2013, *47*, 265–270.
(44) Špringer, T.; Bocková, M.; Homola, J. Label-Free Biosensing in Complex Media: A Referencing Approach. *Anal. Chem.* 2013, *85* (12), 5637–5640.
(45) Riedel, T.; Surman, F.; Hageneder, S.; Pop-Georgievski, O.; Noehammer, C.; Hofner, M.; Brynda, E.; Rodriguez-Emmenegger, C.; Dostálek, J. Hepatitis B Plasmonic Biosensor for the Analysis of Clinical Serum Samples. *Biosens. Bioelectron.* 2016, *85*, 272–279.
(46) Riedelová, Z.; Májek, P.; Pečánková, K.; Kučerová, J.; Surman, F.; De Los Santos Pereira, A.; Riedel, T. SPR Biosensor for Quantification of Fetuin-A as a Promising Multibiomarker. 2018, *67*, 367–375.
(47) Vorobii, M.; Kostina, N. Y.; Rahimi, K.; Grama, S.; Söder, D.; Pop-Georgievski, O.; Šturcová, A.; Horák, D.; Grottke, O.; Singh, S.; et al. Antifouling Microparticles to Scavenge Lipopolysaccharide from Human Blood Plasma. 2019, *20* (2), 959–968.
(48) Riedel, T.; Hageneder, S.; Surman, F.; Pop-Georgievski, O.; Noehammer, C.; Hofner, M.; Brynda, E.; Rodriguez-Emmenegger, C.; Dostálek, J. Plasmonic Hepatitis B Biosensor for the Analysis of Clinical Saliva. *Anal. Chem.* 2017, *89* (5), 2972–2977.
(49) Bock, L. C., Griffin, L. C., Latham, J. A., Vermaas, E. H., & Toole, J. J. Selection of Single-Stranded DNA Molecules That Bind and Inhibit Human Thrombin. *Nature* 1992, *355* (6360), 564–566.
(50) Paborskys, L. R.; Mccurdy, S. N.; Griffin, L.; Toole, J. J.; Lawrence, L.; Leung, K. The Single-Stranded DNA Aptamer-Binding Site of Human Thrombin. 1993, 20808–20811.

(51) Di Nisio, M.; Middeldorp, S.; Büller, H. R. Direct Thrombin Inhibitors. *N. Engl. J. Med.* 2005, *353* (10), 1028–1040.
(52) Bauch, M.; Hageneder, S.; Dostalek, J. Plasmonic Amplification for Bioassays with Epi-Fluorescence Readout. *Opt. Express* 2014, *22* (26), 32026.
(53) Jones, D. M.; Brown, A. A.; Huck, W. T. S.; Street, P.; Cb, C. Surface-Initiated Polymerizations in Aqueous Media: Effect of Initiator Density. 2002, No. 13, 1265–1269.
(54) Ulbrich, K.; Šubr, V.; Strohalm, J.; Plocová, D.; Jelínková, M.; Říhová, B. Polymeric Drugs Based on Conjugates of Synthetic and Natural Macromolecules. *J. Control. Release* 2000, *64* (1–3), 63–79.
(55) Rodriguez-Emmenegger, C.; Schmidt, B. V. K. J.; Sedlakova, Z.; Šubr, V.; Alles, A. B.; Brynda, E.; Barner-Kowollik, C. Low Temperature Aqueous Living/Controlled (RAFT) Polymerization of Carboxybetaine Methacrylamide up to High Molecular Weights. *Macromol. Rapid Commun.* 2011, *32* (13), 958–965.
(56) Reiner, A. T.; Ferrer, N. G.; Venugopalan, P.; Lai, R. C.; Lim, S. K.; Dostálek, J. Magnetic Nanoparticle-Enhanced Surface Plasmon Resonance Biosensor for Extracellular Vesicle Analysis. *Analyst* 2017, *142* (20), 3913–3921.
(57) Hemker, H. C.; Beguin, S. The Clotting Mechanism and How to Determine Its Phenotype. *Arch. Hell. Med.* 2000, *17*, 13–18.
(58) Müller, J.; Becher, T.; Braunstein, J.; Berdel, P.; Gravius, S.; Rohrbach, F.; Oldenburg, J.; Mayer, G.; Pötzsch, B. Profiling of Active Thrombin in Human Blood by Supramolecular Complexes. *Angew. Chemie - Int. Ed.* 2011, *50* (27), 6075–6078.
(59) Müller, J.; Freitag, D.; Mayer, G.; Pötzsch, B. Anticoagulant Characteristics of HD1-22, a Bivalent Aptamer That Specifically Inhibits Thrombin and Prothrombinase. *J. Thromb. Haemost.* 2008, *6* (12), 2105–2112.
(60) Pasternak, A.; Hernandez, F. J.; Rasmussen, L. M.; Vester, B.; Wengel, J. Improved Thrombin Binding Aptamer by Incorporation of a Single Unlocked Nucleic Acid Monomer. *Nucleic Acids Res.* 2011, *39* (3), 1155–1164.
(61) Li, J. J.; Fang, X.; Tan, W. Molecular Aptamer Beacons for Real-Time Protein Recognition. *Biochem. Biophys. Res. Commun.* 2002, *292* (1), 31–40.
(62) Zavyalova, E.; Tagiltsev, G.; Reshetnikov, R.; Arutyunyan, A.; Kopylov, A. Cation Coordination Alters the Conformation of a Thrombin-Binding G-Quadruplex DNA Aptamer That Affects Inhibition of Thrombin. *Nucleic Acid Ther.* 2016, *26* (5), 299–308.
(63) Hemker, H. C.; Beguin, S. Thrombin Generation in Plasma: Its Assessment via the Endogenous Thrombin Potential. *Thromb. Haemost.* 1995, *74* (1), 134–138.
(64) Mann, K. G.; Brummel, K.; Butenas, S. What Is All That Thrombin For? *J. Thromb. Haemost.* 2003, *1* (7), 1504–1514.
(65) Brummel, K. E.; Paradis, S. G.; Butenas, S.; Mann, K. G. Thrombin Functions during Tissue Factor–Induced Blood Coagulation. *Blood* 2002, *100 (1)*, 148–152.

Supporting information

Morphology measurements of poly(HPMA-co-CBMAA) brushes

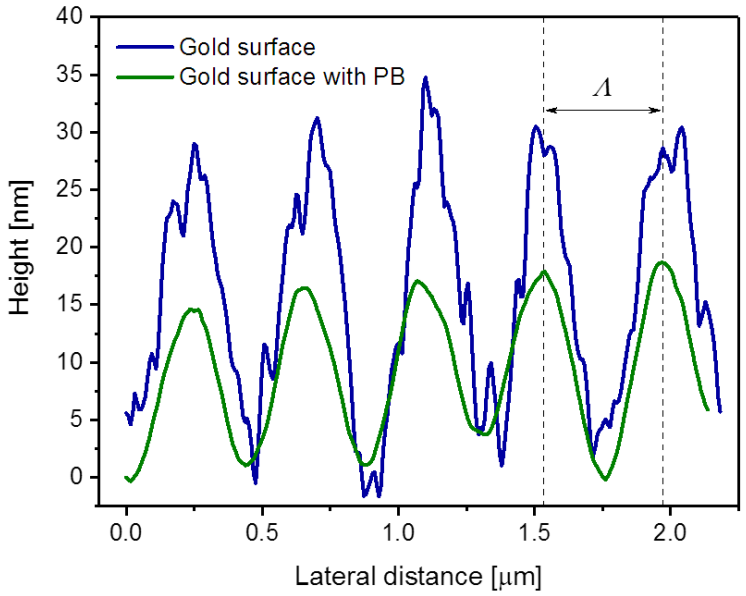

Figure S1. The cross-section of the structure profile of the bare gold grating and grating coated with polymer brushes observed by AFM.

Calibration of the SPR response with sucrose solutions

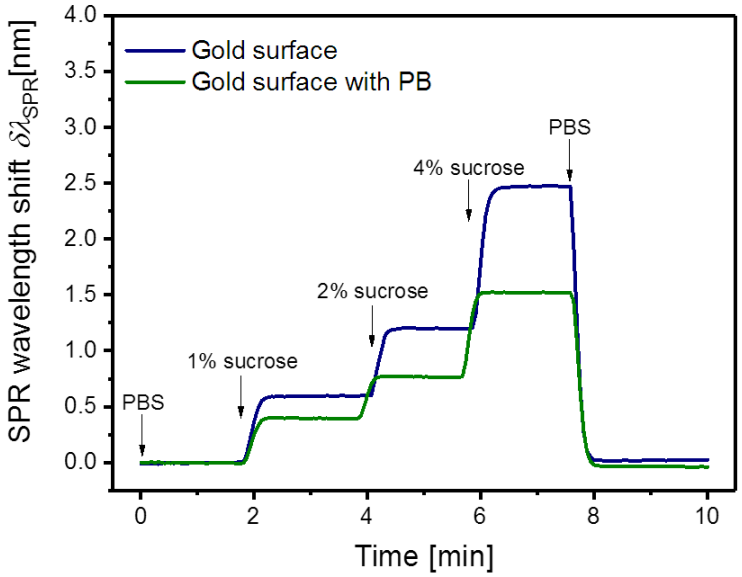

Figure S2. The sensorgram showing the SPR response to 1, 2 and 4% sucrose solutions by using bare gold grating (blue) and gold grating modified with polymer brushes (green).

Immobilization of HD1 and control aptamer on poly(HPMA-co-CBMAA) brush

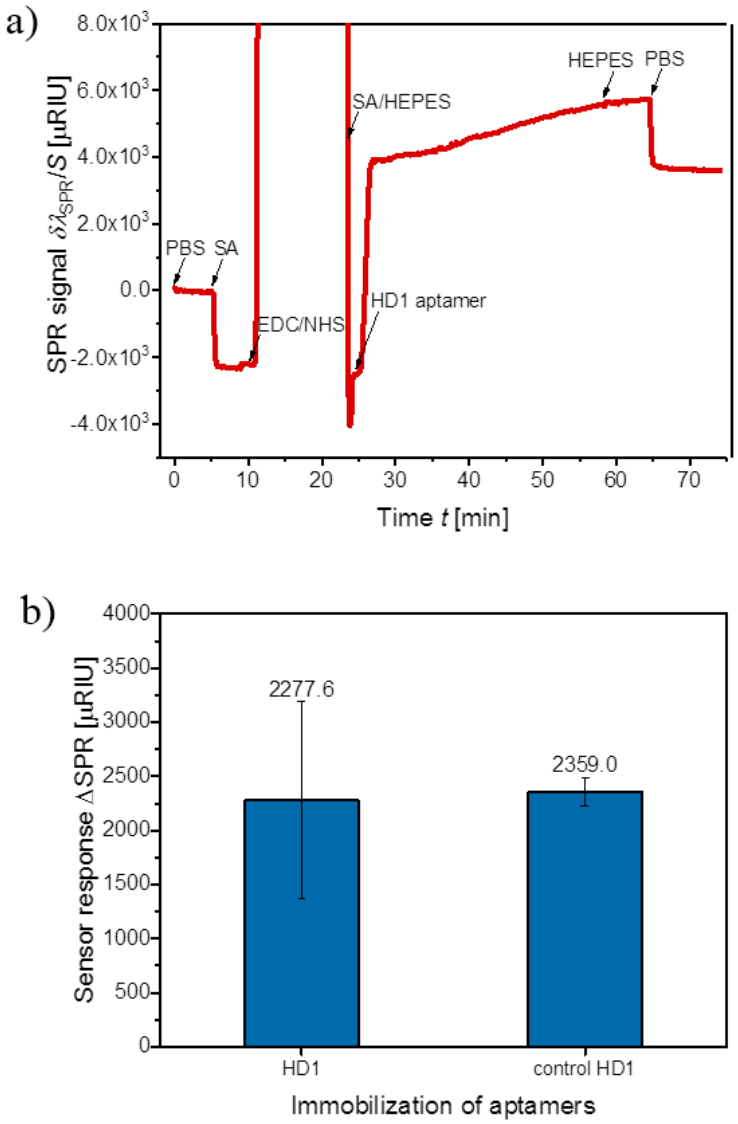

Figure S3. a) The sensorgram showing immobilization of the HD1 aptamer on the polymer brushes. b) The averaged SPR response reflecting immobilization of the HD1 specific thrombin aptamer (n = 7) and scrambled HD1 control aptamer (n = 3).

Impact of argatroban on the thrombin detection assay

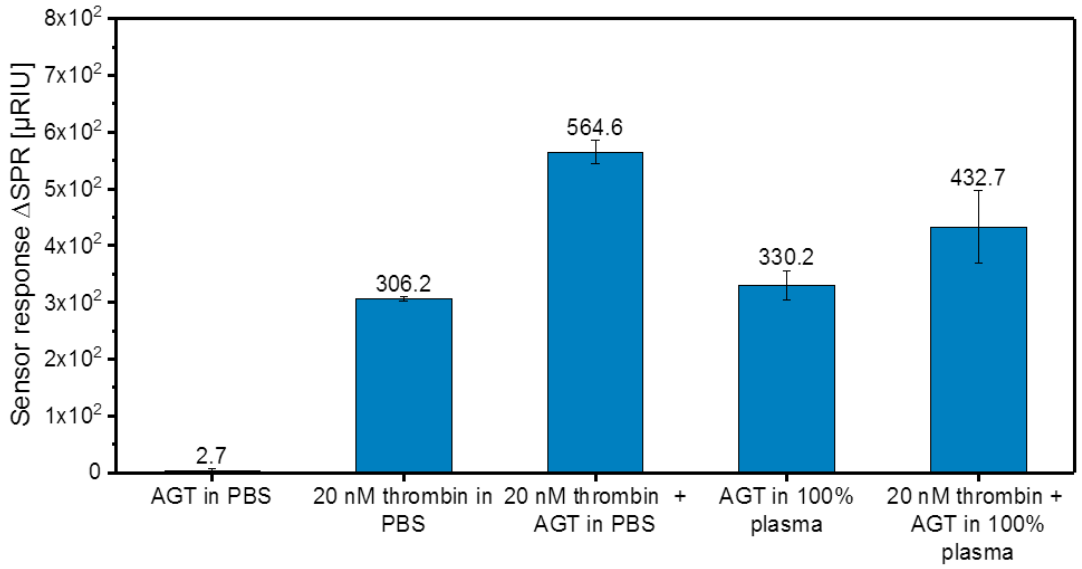

Figure S4. The averaged SPR response obtained by contacting indicated samples with plasmonic grating chip modified with poly(HPMA-*co*-CBMAA) brush and HD1 aptamer. AGT corresponds to addition of 38 μM argatroban to the sample (n = 3).

Control experiment in HBP by using functionalized poly(HPMA-co-CBMAA) brush

In this approach the analyzed plasma samples containing 38 μM argatroban were spiked with a known concentration of thrombin and additionally 1 μM HD1 or scrambled control aptamer. The samples were analyzed on the SPR chip comprising polymer brushes that were functionalized with HD1 aptamer. Fig. S5 illustrates the calibration curves for each assay. As it was expected the HD1 aptamer in the solution competes with the receptor that is coupled to the surface of polymer brushes and prevents binding of thrombin. In contrast, the scrambled aptamer in the solution does not bind to thrombin and allows for its capture on the surface by the HD1 aptamer. The LOD = 1.4 nM was determined for the curve with the scrambled aptamer in the solution. This data are in the good agreement with the values that were obtained in the direct assay in plasma (Fig. 4).

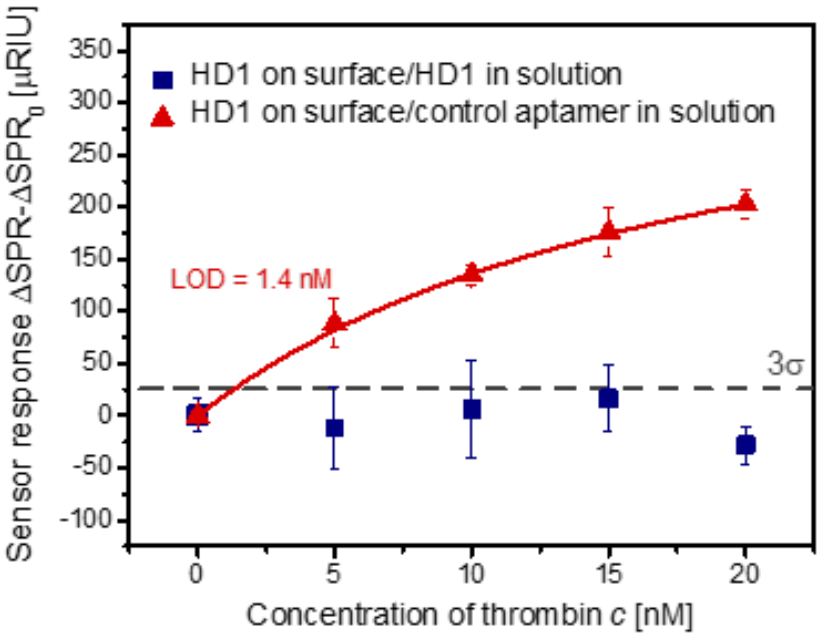

Figure S5. The normalized SPR response vs. concentration of thrombin measured in 100% plasma with addition of HD1 aptamer (red) or control aptamer (blue) by using the brushes functionalized with HD1 aptamer.

Table S1. Comparison of the K_d values reported in the literature for HD1 aptamers in solution.

Aptamer	Sequnece	Kd [nM]	Medium	Method	Reference
HD1	5′-FAM- **GGT-TGG-TGT-GGT-TGG**-DABCYL-3′	5.20 ± 0.49	Physiological buffer*	Fluorescence	Li et al., (2002)
HD1	5′-**GGT-TGG-TGT-GGT-TGG**-3′	16 ± 2	2 µM fibrinogen solution	Turbidimetric assay	Zavyalova et al., (2016)
HD1	5′-Cy5-**GGT-TGG-TGT-GGT-TGG**-3′	104.7	Reaction buffer	MicroScale Thermophoresis	Breitsprecher et al., (2016)
HD1	5′-**GGT-TGG-TGT-GGT-TGG**-3′	123.1±7.2	PBS	Filter retention experiments	Müller et al., (2007)
HD1	5′-Cy5-**GGT-TGG-TGT-GGT-TGG**-3′	132.1	Fetal calf serum	MicroScale Thermophoresis	Breitsprecher et al., (2016)

* 20 mM Tris–HCl (pH 7.4), 140 mM NaCl, 5 mM KCl, 1 mM CaCl2, 1 mM MgCl2, 5% (v/v) glycerol

Simulations of GCSPR sensitivity

Optical simulations of shifts of GC-SPR dip in the wavelength reflectivity spectrum was simulated for the geometry consisting of sinusoidal gold corrugation grating (modulationd depth 30 nm, period Λ=434 nm), polymer brushes described by a dielectric layer with a thickness of d=30 nm and refractive index of n_b=1.45, and water with refractive index n_s=1.33 on the top. The presence of biomolecules on the top of a bare gold surface and on the top of the brushes was manifested as a dielectric adlayer with the thickness of d_l=5 nm and refractive index n_l=1.45. This adlayer correspondes to a surface mass density of biomolecules of Γ=3 ng/mm^2 based on the the equation $\Gamma=(n_l-n_s)\times d_l/(\partial n/\partial c)$, where the factor $\partial n/\partial c$=0.2 mm^3/mg relates the changes in refractive index and concentration c of molecules in the layer. From the results presented in Figure S5 follows that the GC-SPR dip shifts with the presence of the adlayer by $\delta\lambda_{SPR}$=2 mn for the polymer brushes and $\delta\lambda_{SPR}$=3.5 mn for the bare gold surface. Therefore the GC-SPR wavelength shift due to the surface mass density increase on the polymer brushes was determined as $\Gamma/\ \delta\lambda_{SPR}$ =0.66 ng mm^{-2}nm^{-1} and $\Gamma/\ \delta\lambda_{SPR}$ =1.2 ng mm^{-2}nm^{-1} for the bare gold. These simulations were carried out by the numerical model based on the finite element method that was implemented in a diffraction grating solver DiPoG (Weierstrass Institute, Germany).

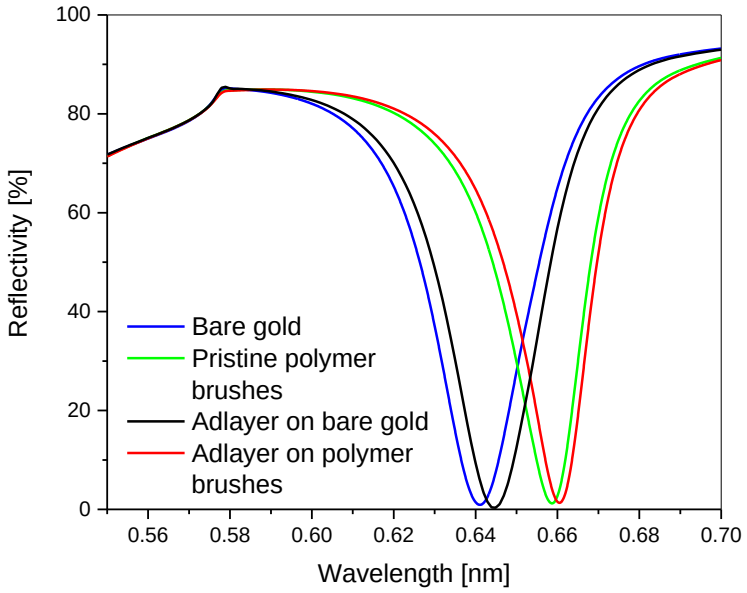

Figure S6. Reflectivity spectra simulated for GC-SPR on gold grating with and without polymer brushes on the top and an ad-layer with thickness of d_l=5 nm and refractive index of 1.45 (corresponding to surface mass density of Γ=3 ng/mm^2) on the top.

References

Breitsprecher, D., Schlinck, N., Witte, D., Duhr, S., Baaske, P., & Schubert, T. (2016). Aptamer binding studies using microscale thermophoresis. In *Nucleic Acid Aptamers* (pp. 99-111). Humana Press, New York, NY

Li, J. J., Fang, X., & Tan, W. (2002). Molecular aptamer beacons for real-time protein recognition. *Biochemical and biophysical research communications*, *292*(1), 31-40.

Müller, J., Wulffen, B., Pötzsch, B., & Mayer, G. (2007). Multidomain Targeting Generates a High-Affinity Thrombin-Inhibiting Bivalent Aptamer. *ChemBioChem*, *8*(18), 2223-2226.

Zavyalova, E., Tagiltsev, G., Reshetnikov, R., Arutyunyan, A., & Kopylov, A. (2016). Cation coordination alters the conformation of a thrombin-binding G-quadruplex DNA aptamer that affects inhibition of thrombin. *Nucleic acid therapeutics*, *26*(5), 299-308.

4. SUMMARY AND OUTLOOK

This multidisciplinary project capitalizes on plasmonics, surface chemistry, and assay development to design and implement the plasmonic biosensor device for thrombin detection in human blood samples.

On the route to achieving this ultimate goal, firstly, three aptamer sequences have been tested for their affinity to thrombin. Two of them, HD1 and HD22, exhibited single-digit nanomolar K_d values, which predisposed them to serve as biorecognition elements in the subsequent assay development. Then, these aptamers were exposed to the buffer solutions spiked with selected proteins such as albumin, IgG, and prothrombin to check the possible cross-reactivity of the sensor with other species abundant in blood. This experiment revealed that HD1 aptamer interacts with prothrombin with the relatively high affinity of K_d=39 nM, while HD22 was selective only to thrombin. In the next step, two distinct sensor coatings (thiol-SAM and polymer brushes) with anti-fouling properties were compared for their capacity to immobilize aptamers and detect thrombin in buffer and diluted human blood. The polymer brushes turned to be superior in terms of surface packing, amount of detected thrombin molecules, and prevention of sensor contamination from a complex biological sample.

In the second part of this project, an in-depth study of the optical properties of a novel to state-of-the-art plasmonic nanostructure supported by a thermo-responsive hydrogel was carried out. Periodic nanohole arrays (NHA) coupled with arrays of nanoparticles (NP) were designed and manufactured to advance the following aspect of the biosensor:

- minimize the size of the sensor chip by using the nanometer-scale structures coated by a gold layer
- simplify the optical setup by replacing the angular interrogation with a transmission wavelength spectrum readout
- introduce additional optical properties such as multiple plasmonic modes that can be monitored simultaneously and modulated by the thermo-responsive hydrogel cushion for signal enhancement
- replacement of the microfluidics by wettable properties of the underneath hydrogel layer

The multiple plasmonic modes were achieved by combining nanohole arrays and nanoparticles into one NHA+NP structure. Three plasmonic modes were identified and assigned to the particular areas of the NHA+NP throughout the experimental work aided by computational simulations. Also, the temperature-dependent spectral positions of the modes were investigated to actively tune the plasmonic properties

by swelling and collapsing the thermo-responsive polymer network. Finally, the developed nanostructures were used to probe the binding events in the model assay with IgG molecules by transmission wavelength spectroscopy and 4-MBA in the SERS experiment. Although the time restrictions of the project did not allow for the optimization of the aptamer-thrombin assay on the developed nanostructure, these results constitute a concrete step toward implementing this thrombin assay on the miniaturized sensor chip with the advanced plasmonic properties.

As this project aimed at detecting medically relevant molecules in bodily fluids such as blood and plasma, the new type of hydrogel, polyisocyanide (PIC) copolymer, was tested for its implementation to the SPR-based sensor. Although the PIC polymer is fully synthetic, it was reported to mimic naturally occurring polymers by its stress-stiffening and excellent biocompatibility with cells and tissues. Therefore, this material bridges a fully controllable synthesis and shelf-life of artificial polymers with comprehensive bio-properties of natural hydrogels. Up to our knowledge, PIC copolymer was used for biosensing for the first time in this study. Firstly, the deposition and the optical properties of the PIC thin layers on the senor surface were tested. Then, these layers were postmodified and used for sensing with a model bioassay based on the fluorescently labeled anti-mouse IgG molecules and optical waveguide spectroscopy combined with fluorescence spectroscopy. Finally, the antifouling properties were tested in undiluted serum and plasma and 10% human blood. After 45 min exposure to various blood-derived samples, PIC showed a satisfactory prevention level from the biological contaminates. Future studies with PIC polymer applied as a biocompatible active surface can bring exciting developments in the field of *in vitro* and *in vivo* sensing.

In the last stage of the project, the gathered information was used to build up a complete portable plasmonic device for detecting thrombin in undiluted plasma. Instead of the standard flat sensor chip coupled to the prism, the periodically corrugated surface of a metallic grating was used. This allowed for excitation of the surface plasmons without needing a bulky prism with a rotation stage for the angular interrogation. As a result, the optical setup was miniaturized to a sample stage with an integrated fiber optic splitter, a light source, and the spectrophotometer. To assure the resistance to fouling from the biological matrices, the sensor grating was coated with up-to-date best-performing anti-fouling material: poly[(N-(2-hydroxypropyl)-methacrylamide)-co-(carboxybetaine methacrylamide)] brushes. The brushes were then functionalized with the HD1 aptamer to investigate thrombin levels in the undiluted plasma samples. As a result, the presented sensor device provides a low nanomolar limit for detecting thrombin that is sufficient to monitor the risk of thrombotic events.

The presented device is a prototype that has been constructed in academic settings leaving room for further improvements. For instance, the biosensor can be miniaturized to the hand-held size with the help of more sophisticated optical, microfluidic, and electrical systems. In addition, one can envision

a parallel measurement of multiple blood samples. The indisputable advantage of the SPR sensor chips is that the measurement area is small and size down to the propagation length of surface plasmon modes. Thus, a chip with the dimensions of 1x1 cm can accommodate tens of separate channels to measure multiple samples (providing an appropriate construction of optical and microfluidic components).

The other important aspect worth pointing out is the detection assay based on aptamer biorecognition elements. In this study, the stability of the aptamers immobilized on the sensor surface and exposed to the biological samples was not impaired throughout more than 120 minutes of the experiment. This result is satisfactory giving that screening measurements of patients will be relatively short, e.g., 15 min. However, being aware of the presence of the endogenous DNases in the biological samples, the stability of the aptamers should be routinely controlled at different time points by introducing a reference sample. As the HD1 aptamer showed cross-reactivity with prothrombin (a proenzyme cleaved upon coagulation start), the HD22 aptamer is recommended as a biorecognition element to avoid false-positive signals. Importantly, detection of thrombin with HD22 aptamer resulted in a worse detection limit (less thrombin could be detected) than with HD1 aptamer. However, the refractive index resolution of the presented instrument can be improved by one order of magnitude by the implementation of temperature stabilization and more sensitive optics.

Finally, to validate the assay for the diagnostics setting, a study should be performed on a significant number of patients suffering from thrombosis, and the results should be compared to the group of healthy individuals. Moreover, a stringent protocol for blood preparation, loading of the sample, readout, and reference values should be established across all diagnostic centers. The proposed sensing approach with a portable SPR-based detection setup holds the potential to be readily applicable to other medically relevant molecules present in the biological fluids.

LIST OF ABBREVIATIONS

AFM	atomic force microscopy
APC	activated protein C
aPTT	activated partial thromboplastin time
ATIII	antithrombin III
ECLS	extracorporeal life support
ECM	extracellular matrix
F1+2	prothrombin fragment 1+2
FDPs	fibrin degradation products
FPA	fibrinopeptide A
IHD	ischemic heart disease
IS	ischemic stroke
LMWH	low-molecular-weight heparin
LSPR	localized surface plasmon resonance
NOACs	non-vitamin K antagonist oral anticoagulants
OEG	(oligo)ethylene glycol
PAI-1	plasminogen activator inhibitor type 1
PCR	polymerase chain reaction
PEG	poly(ethylene glycol)
PT	prothrombin time
PTE	pulmonary thromboembolism
PT/INR	prothrombin time/international normalized ratio method
ROTEM®	thromboelastometry
SAM	self-assembled monolayer
SELEX	Systematic Evolution of Ligands by Exponential Enrichment
SIP	surface-initiated polymerization
TAFI	thrombin-activatable inhibitor of fibrinolysis
TAT	thrombin-antithrombin complex
TEG®	thromboelastography
TF	tissue factor
TFPI	tissue factor pathway inhibitor
TM	thrombomodulin

tPA	tissue-type plasminogen activator
uPA	urokinase-type plasminogen activator
VKAs	vitamin K antagonists
vWF	von Willebrand factor